

Characterization of Perfluorocompound Emission and Abatement Kinetics in Plasma Processes

by

Vivek Mohindra

Bachelor of Engineering (Chemical)
University of Roorkee, Roorkee, India
(1989)

M.S. Chemical Engineering Practice
Massachusetts Institute of Technology
(1990)

M.B.A.
MIT Sloan School of Management
(1996)

Submitted to the Department of Chemical Engineering
in Partial Fulfillment of the Requirements for the Degree of

DOCTOR OF PHILOSOPHY in CHEMICAL ENGINEERING

at the

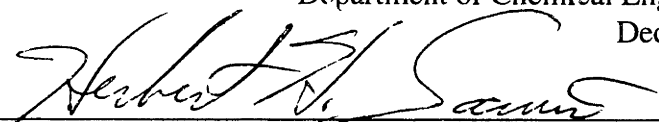
MASSACHUSETTS INSTITUTE OF TECHNOLOGY

February 1996

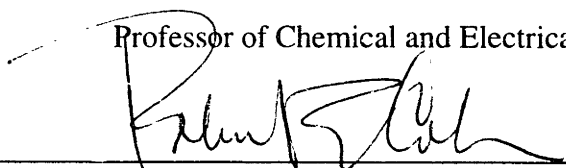
© 1996 Massachusetts Institute of Technology. All rights reserved

Signature of Author 

Department of Chemical Engineering, MIT
December 5, 1995

Certified by 

Herbert H. Sawin
Professor of Chemical and Electrical Engineering, MIT
Thesis Supervisor

Accepted by 

Robert E. Cohen
Professor of Chemical Engineering, MIT
Chairman, Departmental Committee on Graduate Students

MASSACHUSETTS INSTITUTE
OF TECHNOLOGY

MAR 22 1996

LIBRARIES

1

ARCHIVES

Characterization of Perfluorocompound Emission and Abatement Kinetics in Plasma Processes

by

Vivek Mohindra

Submitted to the Department of Chemical Engineering
on December 5, 1995 in Partial fulfillment of the
Requirements for the Degree of Doctor of Philosophy
in Chemical Engineering

Abstract

The goal of this thesis is the characterization of Perfluorocompound (PFC) emission and abatement kinetics in plasma processes used for fabricating Integrated Circuits (IC). The thesis work was divided into three parts.

The first part dealt with the feasibility of substituting PFCs with hydrofluorocarbons (HFCs) in SiO_2 plasma etching processes. Two HFCs were investigated — C_2HF_5 (HFC-125) and $\text{C}_2\text{H}_2\text{F}_4$ (HFC-134a). The HFCs were combined with O_2 and Ar, and SiO_2 etching was characterized in the Applied Materials Precision 5000 commercial etcher. The experiments showed that these HFCs can replace PFCs for anisotropic SiO_2 etching with high etch selectivity towards Si and photoresist.

The second part of the thesis characterized the kinetics of SiO_2 etching with CF_4 . RF modulated power relaxation technique was used, and three plasma chemistries — CF_4 , $\text{CF}_4 + \text{O}_2$ and $\text{CF}_4 + \text{SiO}_2$ — were compared. The dominant species (F, CF_2 , O) loss rates were found to vary for each system. Residence time was found to have an impact on the species loss rates for the $\text{CF}_4 + \text{SiO}_2$ system. The dominant SiO_2 etching behavior with CF_4 was captured using a well-mixed reactor model with seven elementary reactions.

The last part of the thesis characterized PFC abatement kinetics in a microwave tubular reactor. The abatement was carried out using O_2 as an additive gas, and was studied as a function of O_2 :PFC ratio, Flowrate, Power, and Pressure. Close to 100% abatement was achieved for all PFCs investigated. A detailed characterization of C_2F_6 abatement showed the major abatement products to be CO_2 , COF_2 and F_2 . A well-mixed reactor model was developed for C_2F_6 abatement using 13 elementary reactions and it gave good qualitative agreement with the experimental trends. The parameteric dependence of CF_4 , SF_6 and CHF_3 abatement was also characterized experimentally. The major products from CF_4 abatement were similar to C_2F_6 . The main products for SF_6 were SO_2F_2 , SO_2 , and F_2 , while those for CHF_3 were CO_2 , COF_2 , F_2 and HF. Additional

experiments indicated that the unit can be successfully used to abate a wide range of PFCs in the IC fabrication facilities.

Thesis Supervisor: Herbert H. Sawin

Title: Professor of Chemical and Electrical Engineering

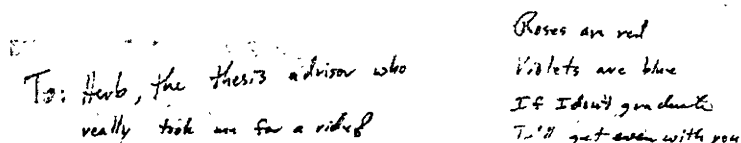
Dedication

To My Parents,
For always sacrificing their present for our future,
and supporting me in all my endeavors.

Acknowledgments

It is hard to believe that this segment of my life is finally coming to an end. It is equally hard to believe that I spent approximately 8% of my expected life-span on acquiring the privilege of prefixing two letters (Dr.) to my name. That works out to more than 3 years per letter!!

There were many ups and downs in this journey. I often had doubts on whether this was worth doing. But the fact is — it's coming to an end now. And there are many characters who played the role of the supporting cast in my endeavor to get a PhD. First among them is my advisor Herb, who really took me for a ride (in his airplane, that is!). I am thankful to Herb for supporting me all these years. He was always very supportive and understanding of my needs and goals. I do not know of any advisor who would even consider the idea of his/her student pursuing other interests while engaged in a PhD — Herb actually provided me a letter of reference when I applied to Sloan for an MBA! Perhaps the greatest compliment I can pay Herb is that if I had to do it all over again, I would still select him as my advisor. After all, how can you not like an advisor who even pitches in and tries to help you with your thesis writing?! Here's Herb's contribution to the Dedication and Acknowledgment sections of my thesis in his own handwriting:



To: Herb, the thesis advisor who
really took me for a ride!

Roses are red
Violets are blue
If I don't graduate
I'll get even with you

I also gratefully acknowledge Ronnie's contribution to me and the group. She made sure I was well-fed at all of Herb's parties, and her refreshing sense of humor seems to have rubbed off on Herb (much to the group's delight!).

I am also thankful to my thesis committee members — Prof. Klavs Jensen, Prof. Karen Gleason, Dr. Ed Gleason and Dr. Mike Mocella. I am particularly thankful to Mike for all the technical and financial support over the years. He was deeply involved with all phases of my PhD, and provided me with the real world anchor for my thesis. He truly is the guardian angel for our group, and also most responsible for what has to be one of the longest-running sponsored research accounts at MIT!

I owe thanks to many METLites for their contributions over the years:

- Heeyeop for helping with the abatement reactor construction, and experiments on the modulation reactor. We were a good team!
- Dave for showing me the ropes and introducing me to Taekwondo
- Linda and Bill for teaching me all about optics and modulation
- Subodh for “guiding” me towards plasma research during my first term at MIT
- John and Gib for the countless philosophical discussions and pitchers of beer
- Scott for inviting me to Gloryhound (R.I.P.) concerts and squawking on demand

- Tim for demonstrating the loudest burps I have ever heard
- Gil for helping me with my code and baking me the Weight Gain 2000 brownies
- Igor for providing sagely advice on how to graduate from the group
- Joanne for answering questions about her setup even 2 years after graduating
- Minh for being so gullible and ready to help
- Jane for livening up the office/group and organizing the birthday parties
- Yong-Pil (YP) for erecting the obstacle course (new table) to my apparatus
- Frank and Tony for trying to deposit when everybody else was trying to etch
- Colin for trying to grow diamonds for an engagement ring (in case....)
- Arpan for getting me home-cooked *parathas* and proofing the entire thesis
- Anthony and Han for being calm, measured voices (even though they knew that Herb doesn't really like post-docs!)
- And Sze for being Sze (need I say more?!)

I am also deeply thankful to Arline, Carol and Nancy for keeping me on their speed-dial for the times there was leftover food anywhere in the department. Thanks to them, I have been able to stay alive on the measly amount they call the graduate student stipend! I also thank Peter Romanow (straight from Jeffrey Archer's "A Matter of Honor") for the numerous enriching discussions on the meaning of life, universe and everything, and for trying to educate me on the American ways. Thanks to my discussions with him, I have given up my ambitions of becoming a *sadhu* and retiring to the Himalayas after my PhD. Instead, my new mission is to go to New York and become known as Broadway Vivek!

This phase of my life would have been very difficult without the constant support and encouragement of my family away from home — The Mohindras of Boston. Uncle Suniti and Aunt Karuna kept constant check on my spirits and kept them up during my entire stay here. I will remember those dinners and dinnertime conversations for a long time to come. I will forever be thankful for all they have done for me. Atul, Dhruv and Kapil also were great friends and supporters.

I cannot even begin to find words suitable enough to thank my dear friends Raghav, Ketu bhabhiji, Tarun and Sharmila. They are the best friends I have ever had. I little realized the goldmine of friendship I stumbled into when I pounced upon Raghav and Tarun at the MIT off-campus housing office in 1989. Since then we have become a closely knit family. We have gone through a lot together, and seen each other grow over the years (along multiple dimensions!). I only hope we can continue to do so the rest of our lives.

I could not have reached this stage of life without the support of my parents and siblings. I have learnt a lot from my parents over the years. I am constantly reminded of the quote, "When I was 10, I was surprised how little my parents knew. By the time I reached 20, I was surprised at all they had learnt in 10 years." Since 1980, I have been seeing my parents about once a year for about a month (less in the last 6 years). Ever since, I have been acutely aware of how little I know in their comparison. They have taught me things which no school in the world can teach. This PhD is for them. Not only do they deserve this doctorate, they also deserve the doctorates of their other two children. I am thankful

to my older brother Ajay for showing me the path ever since I was young. I would have surely strayed in boarding school had it not been for his constant supervision. He clearly is the smarter one in the family and I have always been inspired by his achievements. Priya is very lucky to have a dad like him and a mom like Reena bhabhi. I am also thankful to my sister Deepali for being there for me over the years. It was with a twinge of sadness I attended her wedding on 19th Nov — I can no longer monopolize her time as much as I would like to. While at NYU, she provided me with a lot of emotional support during the tough periods of my PhD.

I convey my heartfelt thanks to Debbie — my best friend of last 1½ years. She has provided me with more emotional support than she realizes, and has made the last phase of my PhD bearable. What started off as a membership of the South Pacific Seagulls flock at Sloan has blossomed into an enriching and rewarding friendship. I have learnt a lot about life from my discussions with her, and I am sure she will continue to educate me for the rest of my life!

Lastly, I acknowledge the contributions of countless others who have made me who I am today. I may not have named you here, but you know who you are! Thank you!

Table of Contents

ABSTRACT	2
ACKNOWLEDGMENTS	5
TABLE OF CONTENTS	8
LIST OF FIGURES	11
LIST OF TABLES	15
CHAPTER 1: INTRODUCTION	16
1.1 Plasma Processing	16
1.2 Perfluorocompounds (PFCs) in Plasma Processing	18
1.3 Mitigating the impact of PFCs	21
1.4 Goals of this Thesis	23
CHAPTER 2: EQUIPMENT AND DIAGNOSTICS	25
2.1 Applied Material Precision-5000 Reactor (AME-5000)	25
2.1.1 Laser Interferometry	26
2.1.2 Optical Emission Spectroscopy and Actinometry	28
2.1.3 Profilometry using Atomic Force Microscopy/Scanning Electron Microscopy	31
2.2 Modulation Reactor	33
2.2.1 RF Power Modulation Technique	33
2.2.2 Modulation Reactor Design	35
2.3 Abatement Reactor	38
2.3.1 Portable Gas Chromatograph	41
2.3.2 Gas Chromatograph/Mass Spectrometer (GC/MS)	43

2.3.3 Inline Mass Spectrometer (MS)	46
CHAPTER 3: ALTERNATIVES TO PFCS FOR PLASMA ETCHING	48
3.1 Experimental Setup and Methodology.....	48
3.1.1 Experimental Setup.....	48
3.1.2 Design Experiments	49
3.2 Results and Discussion	50
3.2.1 C ₂ HF ₅ /O ₂ Experiments.....	50
3.2.2 C ₂ HF ₅ /Ar/O ₂ Experiments.....	56
3.2.3 C ₂ H ₂ F ₄ /O ₂ Experiments	59
3.2.4 C ₂ H ₂ F ₄ /Ar/O ₂ Experiments	63
3.2.5 C ₂ F ₆ /O ₂ , C ₂ HF ₅ /O ₂ and C ₂ H ₂ F ₄ /O ₂ Comparative Experiments	65
3.3 Conclusions	66
CHAPTER 4: KINETICS OF PFC CONSUMPTION: CHARACTERIZATION OF CF₄ ETCHING OF SiO₂.....	68
4.1 Experimental Setup	69
4.2 Results and Discussion	71
4.3 Reactor Modeling	76
4.4 Conclusions	82
CHAPTER 5: KINETICS OF C₂F₆ ABATEMENT	83
5.1 Introduction	83
5.2 Preliminary Experiments	84
5.3 Parametric Dependence of C ₂ F ₆ Abatement.....	85
5.3.1 Design Experiments	85
5.3.2 Contribution of Surface Reactions to Abatement.....	87
5.3.3 Reactor Flow Issues	89

5.4 Characterization of Byproducts	92
5.4.1 GC/MS Characterization.....	92
5.4.2 Inline Mass Spectrometry	95
5.4.3 Plasma Induced Emission	99
5.5 Contribution of Pyrolysis to Abatement.....	101
5.6 Mechanism for C₂F₆ Abatement.....	105
5.6.1 Interpretation of Mass Spectrometer Data	106
5.6.2 Results and Discussion.....	109
5.7 Well-Mixed Reactor Model for Abatement.....	113
5.8 Use of Abatement Unit in Integrated Circuit (IC) Fabrication Facilities	119
5.8.1 Deposition on Reactor Walls	119
5.8.2 Other Issues for Manufacturing.....	122
5.9 Conclusions	123
CHAPTER 6: ABATEMENT OF OTHER PERFLUOROCOMPOUNDS	125
6.1 Abatement of CF ₄	125
6.2 Abatement of SF ₆	130
6.3 Abatement of CHF ₃	134
6.5 Conclusions	135
REFERENCES	136
APPENDIX A: DRAWINGS FOR THE MODULATION REACTOR	143
APPENDIX B: DRAWINGS FOR THE UTI 100C MASS SPECTROMETER ASSEMBLY.....	168
APPENDIX C: COMPUTER CODE FOR STEADY STATE SOLUTION FOR C₂F₆ + O₂ WELL-MIXED REACTOR MODEL.....	181

List of Figures

<i>Figure 1-1: Subtractive Processing for IC processing.....</i>	<i>17</i>
<i>Figure 1-2 Atmospheric Lifetimes and Global Warming Potentials of PFCs and HFCs</i>	<i>19</i>
<i>Figure 1-3: Goals and Components of this Thesis.....</i>	<i>24</i>
<i>Figure 2-1: Applied Materials Precision 5000 Etcher and Diagnostics</i>	<i>26</i>
<i>Figure 2-2: Sample trace from Laser Interferometry.....</i>	<i>27</i>
<i>Figure 2-3: Snapshot from 0.27m monochromator equipped with a linear diode array.....</i>	<i>31</i>
<i>Figure 2-4: AFM SuperTip™ used for characterizing feature wall profiles</i>	<i>32</i>
<i>Figure 2-5: Topographic and Lateral Force AFM images showing near wall artifacts</i>	<i>33</i>
<i>Figure 2-6: RF Modulated Power Relaxation technique</i>	<i>34</i>
<i>Figure 2-7: RF Power Modulation experimental setup</i>	<i>36</i>
<i>Figure 2-8: Schematic diagram of the Abatement Reactor.....</i>	<i>39</i>
<i>Figure 2-9: Modification of standard ASTeX applicator for air cooling.....</i>	<i>39</i>
<i>Figure 2-10: Microwave components in the Abatement Reactor.....</i>	<i>41</i>
<i>Figure 2-11: Countercurrent water scrubber for plasma effluent</i>	<i>43</i>
<i>Figure 3-1: SiO₂ etching rate dependence on Pressure and O₂ flowrate</i>	<i>51</i>
<i>Figure 3-2: F concentration dependence on Pressure and O₂ flowrate.</i>	<i>53</i>
<i>Figure 3-3: SiO₂ Etching rate dependence on Power and Pressure.</i>	<i>53</i>
<i>Figure 3-4: F concentration dependence on Power and Pressure</i>	<i>54</i>
<i>Figure 3-5: Photoresist etching rate dependence on Pressure and O₂ flowrate.</i>	<i>55</i>

<i>Figure 3-6: SiO₂ etching rate as a function of Ar and O₂ flowrates.....</i>	<i>57</i>
<i>Figure 3-7: Photoresist etching rate as a function of Ar and O₂ flowrates.</i>	<i>57</i>
<i>Figure 3-8: Etched SiO₂ grating in C₂HF₄/O₂/Ar mixtures.....</i>	<i>58</i>
<i>Figure 3-9: Etched SiO₂ grating in C₂H₂F₄/O₂/Ar mixtures.....</i>	<i>59</i>
<i>Figure 3-10: SiO₂ etching rate as a function of Pressure and O₂ flowrate.</i>	<i>61</i>
<i>Figure 3-11: SiO₂ etching rate as a function of Power and O₂ Flowrate.</i>	<i>62</i>
<i>Figure 3-12: Profile of features etched in C₂H₂F₄/Ar/O₂ mixtures.</i>	<i>65</i>
<i>Figure 3-13: Comparison of SiO₂ etching in C₂F₆/O₂, C₂HF₄/O₂ and C₂H₂F₄/O₂.</i>	<i>66</i>
<i>Figure 4-1: Effect of electrode material on characteristic breakpoint frequency.....</i>	<i>71</i>
<i>Figure 4-2: Bode plot depicting the effect of adding O₂ to CF₄.....</i>	<i>74</i>
<i>Figure 4-3: Effect of placing SiO₂ wafer on one of the electrodes</i>	<i>75</i>
<i>Figure 4-4: Effect of changing residence time in the reactor.....</i>	<i>76</i>
<i>Figure 4-5: Comparison of transfer functions from experiments and model for SiO₂ etching.....</i>	<i>82</i>
<i>Figure 5-1: C₂F₆ Abatement as a function of Power and Flowrate.....</i>	<i>86</i>
<i>Figure 5-2: C₂F₆ Abatement as a function of Power and Pressure.</i>	<i>86</i>
<i>Figure 5-3: Comparison of C₂F₆ abatement in quartz and alumina reactors.....</i>	<i>88</i>
<i>Figure 5-4: Physical appearance of the plasma in the microwave tubular reactor.....</i>	<i>89</i>
<i>Figure 5-5: Equipment modification to eliminate annular flow in the reactor.....</i>	<i>91</i>
<i>Figure 5-6: Effect of annular flow modification on C₂F₆ abatement.....</i>	<i>91</i>
<i>Figure 5-7: GC/MS analysis of effluent from C₂F₆ plasma abatement process.....</i>	<i>94</i>

<i>Figure 5-8: Location of inline mass spectrometer in the Abatement Reactor setup</i>	96
<i>Figure 5-9: Baseline Mass Spectrum for C₂F₆ and O₂ in the absence of plasma)</i>	97
<i>Figure 5-10: C₂F₆ + O₂ Mass Spectrum with and without plasma</i>	97
<i>Figure 5-11: Plasma induced emission (PIE) scan for C₂F₆ + O₂ system.</i>	100
<i>Figure 5-12: Gas phase axial temperature distribution in the microwave tubular reactor</i>	102
<i>Figure 5-13: C₂F₆ Abatement and Extents ϵ_{CO_2} and ϵ_{COF_2} as a function of Power and Fraction of C₂F₆ in the Gas Mixture.</i>	110
<i>Figure 5-14: Extents ϵ_{CO_2} and ϵ_{COF_2} as a function of Flowrate and Fraction of C₂F₆ in the gas mixture.</i>	111
<i>Figure 5-15: C₂F₆ abatement and O₂ Consumption as a function Flowrate and Fraction of C₂F₆ in the gas mixture</i>	112
<i>Figure 5-16: Comparison of Extents of reaction for model and experiments as a function of Power and Fraction C₂F₆ in inlet.</i>	117
<i>Figure 5-17: Comparison of Extents of reaction from model and experiments as a function of Flowrate and Fraction C₂F₆ in inlet.</i>	118
<i>Figure 5-18: XPS analysis of black deposit on the inside of non-cooled alumina reactor wall.</i>	120
<i>Figure 5-19: Experimental setup to determine the genesis of tube deposition</i>	121
<i>Figure 6-1: C₂F₆ vs. CF₄ abatement as a function of Fraction of PFC in Inlet and Flowrate.</i>	126
<i>Figure 6-2: C₂F₆ vs. CF₄ abatement as a function of Pressure and Flowrate.</i>	127
<i>Figure 6-3: C₂F₆ vs. CF₄ abatement as a function of Power and Flowrate.</i>	128
<i>Figure 6-4: Mass spectrum for CF₄ + O₂ with and without plasma</i>	129
<i>Figure 6-5: C₂F₆ vs. SF₆ abatement as a function of Flowrate and Fraction of SF₆ in inlet...</i>	131

Figure 6-6: C₂F₆ vs. SF₆ abatement as a function of Pressure and Flowrate..... 131

Figure 6-7: C₂F₆ vs. SF₆ abatement as a function of Power and Flowrate. 132

Figure 6-8: Mass spectrum for SF₆ + O₂ system with and without plasma 133

Figure 6-9: Abatement of CHF₃ in the microwave tubular reactor 134

Figure 6-10: Mass spectrum for CHF₃ + O₂ system with and without plasma..... 135

List of Tables

<i>Table 2-1: Wavelengths used for actinometry and their corresponding transitions.....</i>	<i>38</i>
<i>Table 2-2: Recipes used to quantify abatement of gases using MTI P200 GC</i>	<i>42</i>
<i>Table 2-3: Recipe for C₂F₆ detection using the HP GC/MS.....</i>	<i>45</i>
<i>Table 4-1: Comparison of Experimental Conditions for this work with that of Kiss.....</i>	<i>70</i>
<i>Table 4-2: Reaction Network used for modeling CF₄ Etching of SiO₂.....</i>	<i>80</i>
<i>Table 5-1: Reference cracking patterns for reactants and potential products for C₂F₆ + O₂</i>	<i>98</i>
<i>Table 5-2: Thermodynamic data used for equilibrium calculations(Burgess et al., 1995).....</i>	<i>103</i>
<i>Table 5-3: Extents of reactions from thermodynamic equilibrium calculation — C₂F₆ + O₂</i>	<i>104</i>
<i>Table 5-4: Reactions included in the C₂F₆ + O₂ abatement model.....</i>	<i>115</i>
<i>Table 5-5: Steady state species concentrations for C₂F₆ + O₂ from the reactor model.....</i>	<i>119</i>

Chapter 1: Introduction

1.1 Plasma Processing

Silicon processing for the production of very large scale integrated (VLSI) circuits has made tremendous progress since the invention of a germanium integrated circuit (IC) by J.S. Kilby in 1958. The ICs manufactured nowadays are highly complex devices incorporating millions of components connected by wires only a few thousand Å in diameter.

Many steps go into the making of a device. Some of the major ones are — Crystal growth (for making crystal from raw materials), Chemical Vapor Deposition (CVD) and Epitaxy (for producing thin films), Lithography (for defining the areas for selective processing), Wet and Dry etching (for selective removal of material), and Diffusion and Ion implantation (for doping). As many as 60 of these basic steps can go into the making of a simple device like a MOS transistor (Tedrow and Sodini, 1988).

The ever-increasing complexity of ICs demands the incorporation of more and more devices on a single wafer. This is achieved either by stacking up multiple layers of devices, or by building smaller devices. Fabrication lines ("Fab") are also moving towards larger wafers to increase throughput. Fab lines working with 8" wafers are common, and researchers are already working towards 12" wafer processing. The trend towards larger wafers and smaller devices (which translates to smaller linewidths) places particularly stringent demands on the Lithographic and Etching steps. These two processes together constitute the "subtractive processing" step, which is repeated multiple times in the fabrication of any device.

The steps involved in the subtractive processing of a film (e.g. SiO₂) over a substrate (e.g. Si) are shown in Fig 1-1. The first step involves spin-coating of a photoresist over the film, which has been already been deposited (e.g. via Plasma

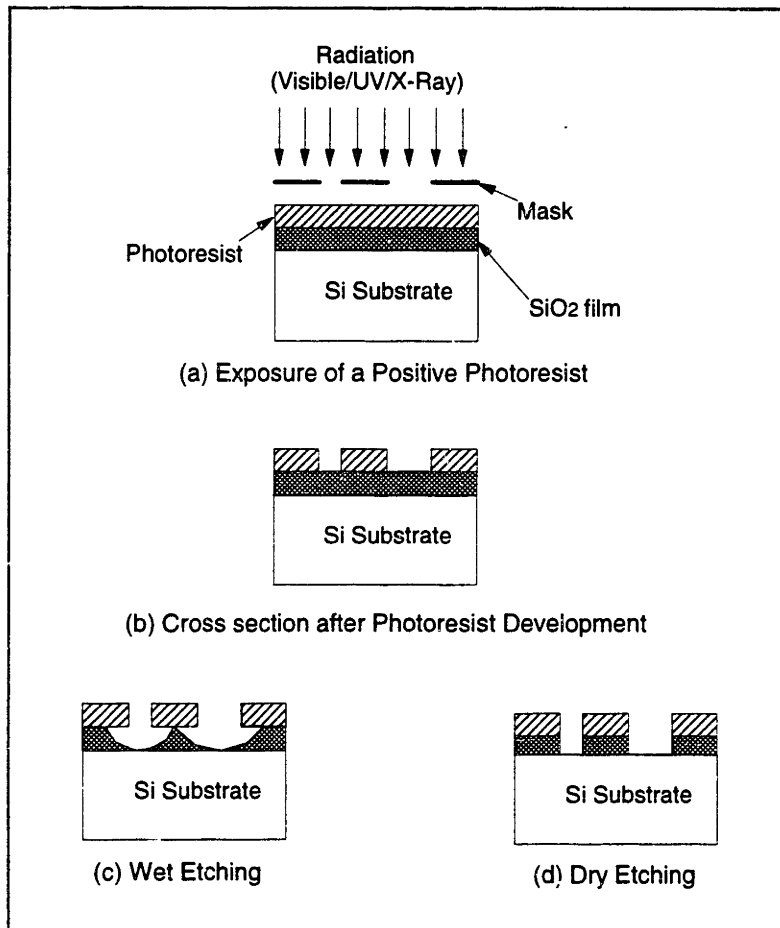


Figure 1-1: Subtractive Processing for IC processing

Enhanced CVD). The photoresist (PR) is a polymeric material, and undergoes changes upon exposure to radiation (visible light, UV or X-ray). A “mask” (made of glass or silicon nitride, depending on the radiation) containing the pattern to be transferred is then placed over the PR, and the PR is exposed (Fig 1-1(a)). Depending on the nature of the PR, the exposed (for positive PR) or the unexposed (for negative PR) areas of the resist are removed in the subsequent developing step (Fig 1-1(b)). Next step is the transfer of the PR pattern to the underlying silicon dioxide film. This can be accomplished by either

wet or dry etching. Wet etching is done using chemical solutions and produces isotropic etching (Fig 1-1(c)). A plasma glow discharge is used for dry etching and this technique results in anisotropic etching (Fig 1-1(d)). As is obvious from the figure, dry etching is preferred to wet etching especially for high fidelity transfer of small patterns to the underlying film.

Plasma processing, as used in this thesis, refers to any processing step which requires the use of plasma glow discharges in IC production. There are two main plasma processing steps in IC production — dry etching (also referred to as Plasma etching), and plasma enhanced CVD (PECVD). While plasma etching relies on plasmas to selectively remove material (see Fig 1-1), PECVD uses plasmas to aid film deposition on substrates. This thesis focuses on the plasma processes for SiO₂ deposition and etching.

1.2 Perfluorocompounds (PFCs) in Plasma Processing

Most of the SiO₂ plasma etching is currently based on fluorocarbon chemistry. Amongst the gases and gas mixtures used have been CF₄, CHF₃, CF₄/H₂, CF₄/O₂, CHF₃/CF₄ and CHF₃/CF/Ar. Since most of SiO₂ etching is over a Si substrate, selectivity of SiO₂ to Si etching is important. This selectivity is normally controlled by varying the Fluorine to Carbon (F/C) ratio in the gas mixtures used, as originally proposed by Coburn and Winters (1979). While additives like H₂ scavenge F radicals (thus reducing the effective F/C ratio) and reduce Si etching rate, additives like O₂ enhance Si etching rate by scavenging C. For this reason CHF₃ has been a popular additive to CF₄ for SiO₂ to Si selectivity control. The selectivity mainly arises due to the formation of CF₂ from the dissociation of CF₄. This radical is a major precursor of fluorocarbon polymer and can passivate surfaces against further etching (Kitamura *et al*, 1989). The oxygen released from SiO₂ due to ion-enhanced etching reacts with the carbon in CF₂, forming gaseous products and preventing the formation of polymer. However, Si lacks any O₂ to prevent the polymer formation, and thus the polymer forms

as soon as SiO₂ is etched away, thereby preventing etching of underlying Si. This is how the selectivity of SiO₂ to Si etching is obtained.

Perfluorocompounds (PFCs) have been popular sources of F and C for SiO₂ etching. This is mainly because of their non-toxicity, ready availability and the existence of a vast body of literature documenting the fundamentals of PFC etching of SiO₂. All the gases listed above for SiO₂ etching (except O₂ and Ar) are PFCs, and are extensively used commercially. These gases have long atmospheric lifetimes. In addition, they have a high global warming potential (GWP) since they are excellent absorbers of infrared radiation. Figure 1-2 shows the lifetimes and the GWPs for some of the PFCs.

Comparable numbers for the HFCs (Hydrofluorocarbons) are also shown. The GWPs are relative to CO₂ and are calculated on a 100 year integrated time horizon (ITH) basis.

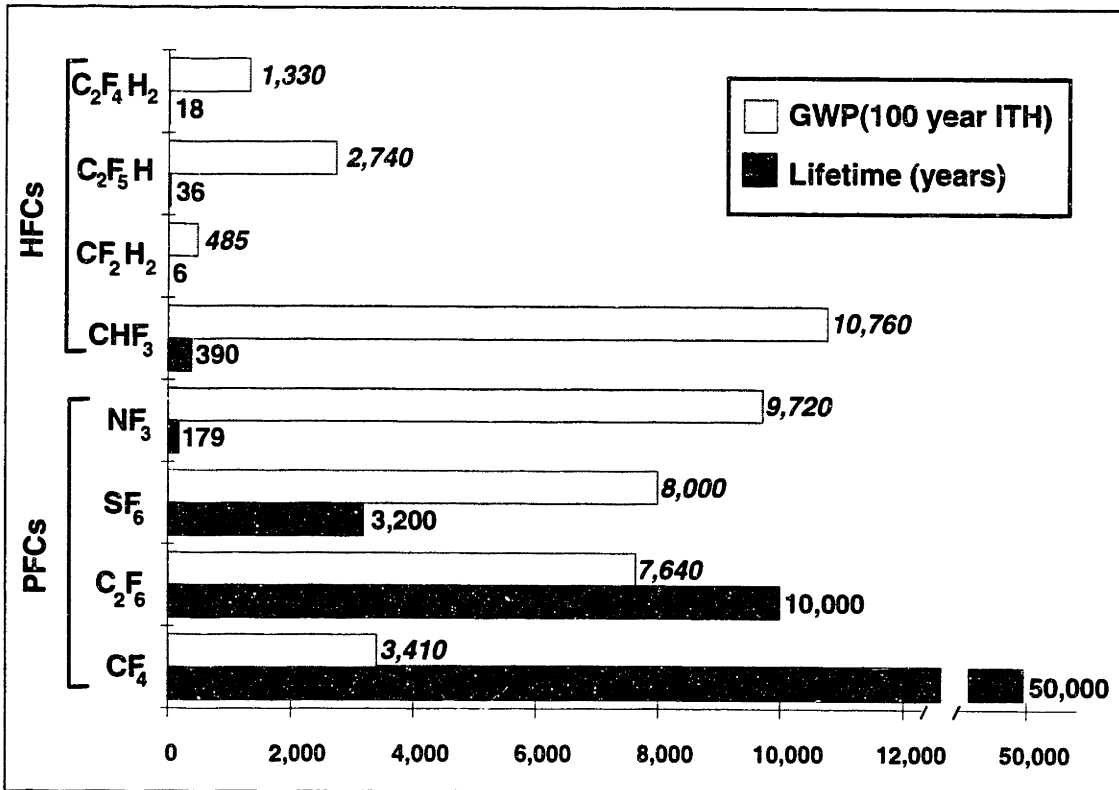


Figure 1-2 Atmospheric Lifetimes and Global Warming Potentials of PFCs and HFCs

The lifetime and GWP figures are calculated from kinetic and atmospheric flow models and thus have many in-built assumptions. The data shown in Fig 1-2 are from Ravishankara *et al.* (1993). The lifetimes for C₃ HFCs (not shown in the figure) are comparable to C₂ HFCs (Cooper and Cunningham, 1993). The underlying assumptions and the calculation methodology for the numbers in Fig 1-2 is elucidated in Gierczak *et al.* (1991) and Orlando *et al.* (1991).

It is clear from Fig 1-2 that the PFCs have very long lifetimes and high GWPs. Despite these high values, these PFCs have seen an increased use in the semiconductor industry in the last ten years. This increased usage is largely due to their low Ozone Depleting Potential (ODP), which resulted in their use as a substitute for chlorofluorocarbons (CFCs). CFCs were widely used in the semiconductor industry till 1985. Their main uses were as dry etching gases, as a source of chloride in Si oxidation and for cleaning of components (Newboe, 1993). The Upper Atmosphere Research Satellite (UARS) launched by NASA in 1991 showed conclusively that CFCs were to blame for ozone depletion (Chemistry & Industry, 1995). Due to the increasing concern about ozone depletion, many countries became signatories of the Montreal Protocol on Substances That Deplete the Ozone Layer in 1990 and decided to phase out the production and use of CFCs by the year 2000. This deadline was later moved up to 1996 (Zurer, 1994). Consequently, PFCs, HFCs and HCFCs (hydrochlorofluorocarbons) were proposed as alternatives to CFCs. The presence of H in HCFCs allows the Cl to be dissipated at levels below the ozone layer in the atmosphere, thereby greatly reducing the ODP. PFCs and HFCs on the other hand have zero ODP (since they contain no Cl). Although there were initial doubts that the HFCs might also contribute to ozone depletion, it was subsequently shown that HFCs do not destroy ozone (Science, 1994).

While the industry action against CFCs was swift due to the visible reduction in ozone evident in NASA pictures, the issue of global warming is only recently gaining attention. The long lifetimes of PFCs and their high GWP are of particular concern. Due to the long lifetimes, even if all PFC emission were to cease today, these gases would

continue to reside in the atmosphere and contribute to global warming for thousands of more years (*e.g.* see system dynamics models of Nordhaus (1992) and Rotmans (1990)). In addition, there is a possibility that these gases might have other yet-unknown environmental impacts. In such an eventuality, the long lifetimes would pose an additional problem. Recognizing this issue, DuPont, a major supplier of PFCs, mandated that it will not sell PFCs unless users can prove that suitable PFC emission control mechanisms are installed in-house. EPA has recently taken note of this policy and is trying to reach a consensus PFC regulation policy which will ensure significant emission reduction. Therefore, PFCs are likely to follow the CFCs and either be eliminated or, at the minimum, tightly regulated in the near future.

1.3 Mitigating the impact of PFCs

One way to mitigate the impact of PFC/CFCs would be to remove them directly from the atmosphere (see *e.g.* Stix (1989) on the removal of CFCs from atmosphere). However, a more desirable approach would be to mitigate the impact of PFCs before their release into the atmosphere. There are three approaches to ensuring that VLSI fabrication processes do not contribute to the PFC level in the atmosphere — (i) substitution, (ii) recovery and optimization, and (iii) abatement. The substitution approach aims at using PFC alternatives, which hopefully have short lifetimes and minimal ODPs and GWPs, as process gases. There have been efforts to find substitutes both for Plasma Etch and CVD chamber clean applications. While some efforts for plasma etching using HFCs (like those discussed in Chapter 3 of this thesis) appear promising, the wide diversity of existing plasma etching processes makes it difficult to achieve blanket substitution for all cases (Arnold and Hartman, 1995). In addition, the cumbersome procedure for process qualification required by the fabs makes it difficult to employ a new process without significant process development. Even for the case of silicon dioxide etching discussed in Chapter 3, the substitutes (HFCs) are not completely benign to the environment. Instead, they are merely less of a concern than the current PFCs. On the CVD chamber

cleaning front, some efforts have recently been made to substitute C_2F_6 . However, most of these efforts appear to be driven by business economic considerations. For example, the two substitutes investigated — C_3F_8 (Stone, 1995) and NF_3 (Ridgeway *et al*, 1995) — are long-lived global warmers in their own respect. The availability of a non-PFC, low ODP and low GWP source of F (the primary etchant of SiO_2 and Si_3N_4 in CVD chamber cleans) seems to be the primary obstacle to achieving this substitution. Even if such a source is found, one has to ensure that PFCs are not generated during the cleaning process. This is particularly difficult for plasma etching applications, where the carbon (*e.g.* in the Photoresist) present in the system can combine with F in the feed gas to form a long-lived PFC.

A second approach to minimizing the impact of PFCs would be optimizing the processes to minimize usage, or recovering the unreacted PFCs before venting to the atmosphere. Titanium chemical traps have been used successfully for some gases (*e.g.* CCl_4) but have proven unsuccessful for C_2F_6 (Hu, 1988). Dow Chemicals and Air Products have recently launched efforts to design a system for C_2F_6 recovery. ASPEN PLUS simulations on idealized feed streams have shown promising results. However, the system is not expected to be economical for existing fabs due to the prohibitive cost of piping all process exhaust gases to the recovery unit outside the fab. In addition, the tendency of PFCs to form azeotropes may create problems when the feed gas consists of multiple PFCs. These concerns will probably be addressed when a unit is installed in a commercial fab.

The third approach to mitigating the impact of PFCs is destructive abatement. There are various approaches to this *e.g.* combustion, chemical-thermal and plasma assisted abatement (Mocella, 1995). Combustion and Chemical-Thermal systems operate on post-pump effluent, a significant fraction of whose volume is made of the N_2 used for pump purges. Therefore, these units suffer from dilution of feed and the associated high cost of effluent treatment. In addition purge N_2 can react with the O_2 present in the feed (*esp.* for PECVD chamber cleans which typically use 50:50 mix of

C_2F_6 and O_2) to generate NO_x which are pollutants in their own right. Plasma units operating post-pump will also suffer from the same drawbacks. A plasma assisted abatement unit which processes gases before the pump can circumvent both these problems. The unit discussed in this thesis operates before the pump thereby avoiding the dilution and potential NO_x formation problems.

1.4 Goals of this Thesis

The main goal of this thesis is to characterize the emission and abatement kinetics of PFCs used in SiO_2 plasma processing. The thesis approach and its components are summarized in Fig 1-3. The first part of the thesis deals with the substitution of PFCs like CF_4 and CHF_3 with environmentally more benign HFCs — C_2HF_5 (HFC-125) and $C_2H_2F_4$ (HFC-134a) — for anisotropic SiO_2 etching. The second part concentrates on elucidating the etching kinetics within the process chamber. In any PFC process, a portion of the gas is consumed, and the remaining exits the reactor unused. Also, some of the products of the process themselves might be PFCs. Therefore, the second part of the thesis deals with the characterization of dominant plasma kinetics in CF_4 etching of SiO_2 . These chemical kinetics are a necessary input to understanding and modeling the emission of PFCs (both unreacted and newly formed as a process by-product) from a process. The third part of the thesis looks at the process effluent. Once the PFCs are emitted in a process, they have to be treated before venting to the atmosphere. This part of the thesis deals with the abatement kinetics of PFCs in a microwave tubular reactor. The abatement of C_2F_6 , which is used extensively in SiO_2 and Si_3N_4 PECVD chamber cleans, is characterized in detail in the microwave reactor. In addition, abatement behavior for other PFCs — CF_4 , SF_6 and CHF_3 — is also discussed and characterized as a function of parameter space.

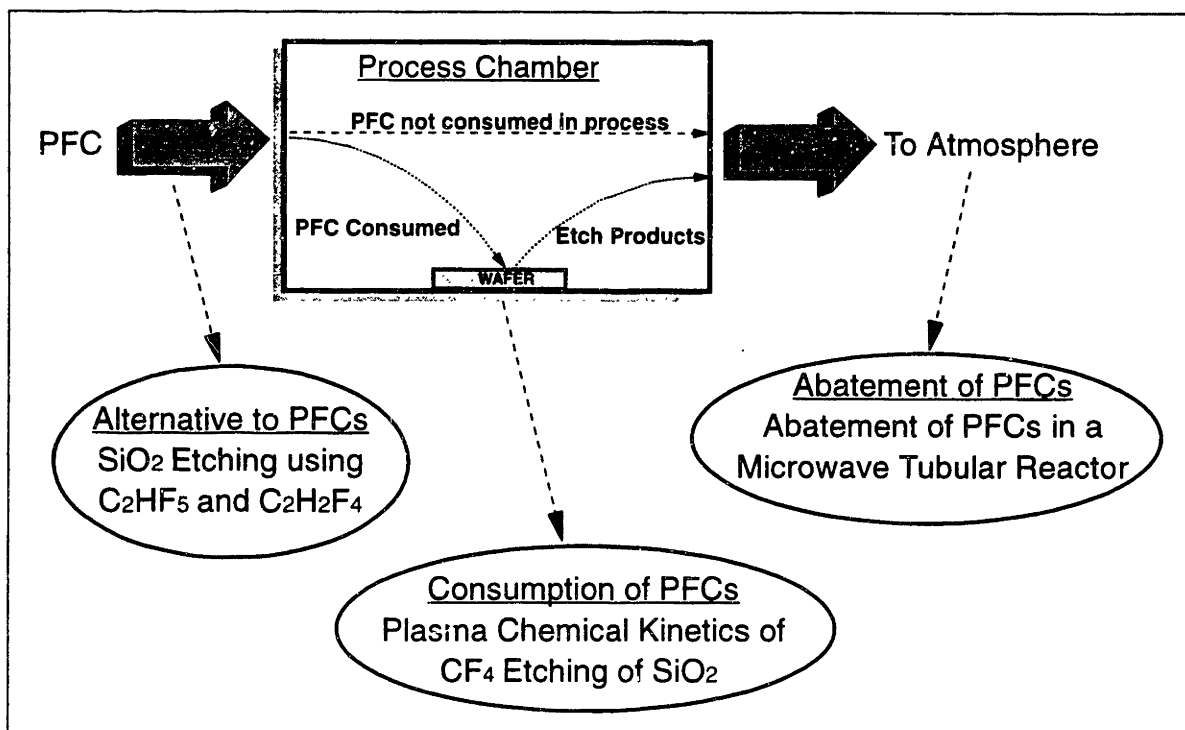


Figure 1-3: Goals and Components of this Thesis

The thesis is organized as follows. Chapter 2 describes the equipment and diagnostics used in this work. The feasibility of substituting HFCs for PFCs in anisotropic SiO₂ etching is discussed in Chapter 3. The characterization of dominant chemical kinetics in CF₄ etching of SiO₂ is detailed in Chapter 4. The abatement of C₂F₆ is discussed in Chapter 5, and the abatement of CF₄, SF₆ and CHF₃ in Chapter 6.

Chapter 2: Equipment and Diagnostics

The work for this thesis was carried out on three different sets of apparatus. The first part, which evaluated the feasibility of using C_2HF_5 (HFC-125) and $C_2H_2F_4$ (HFC-134a) for SiO_2 plasma etching, was carried out in a commercial reactor — the Applied Material Precision 5000 Etcher (AME-5000). The second part dealt with the kinetics of consumption of a PFC (CF_4) during SiO_2 etching, and was carried out in a laboratory scale capacitively-coupled parallel-plate reactor ("Modulation Reactor"). The last part of this thesis was carried out in a microwave tubular reactor, referred to here as the "Abatement Reactor." These equipment and the associated diagnostics are described below.

2.1 Applied Material Precision-5000 Reactor (AME-5000)

AME-5000 is a commercial, capacitively-coupled, asymmetric, magnetically enhanced, single-wafer etcher. The reactor and the diagnostics are shown in Fig 2-1. The 4" wafer was clamped on the smaller, powered electrode. The larger electrode was defined by the grounded walls and the chamber volume was approximately 6 litres. Helium at a pressure of 6 torr was used at the wafer backside to facilitate heat transfer from the wafer to the water cooled electrode. Power was supplied by a 13.56 MHz RF generator capable of supplying up to 1000W. The process chamber was equipped with four 2" quartz optical ports — one at the top of the chamber and three on the sides. Since the quartz ports frosted with extended use and adversely impacted laser interferometry and optical emission spectroscopy, the top and one of the side ports were replaced with MgF_2 windows. The chamber also had four magnetic coils on each side to provide a rotating magnetic field. The pumping system consisted of a 150 l/s turbomolecular pump, backed by a corrosive service roughing pump.

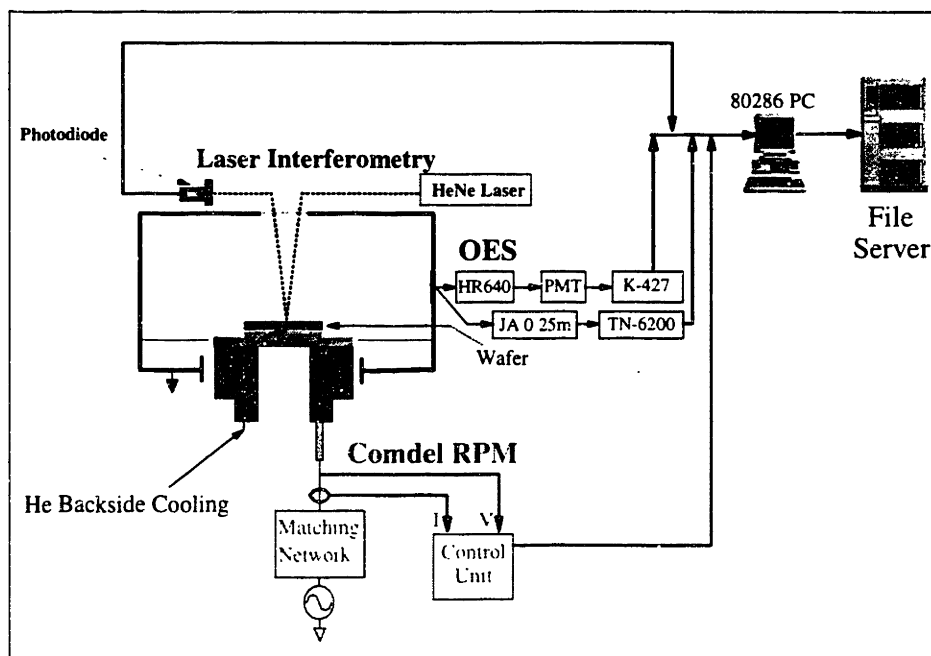


Figure 2-1: Applied Materials Precision 5000 Etcher and Diagnostics

The reactor was modified to incorporate a number of diagnostics. A Comdel real power monitor (RPM-1) probe was attached at the copper RF power feedthrough into the chamber to monitor the electrical characteristics (I, V, Z, ϕ , and Real Power) of the plasma. This probe has been shown to be accurate in the electrical characterization of the plasma (Zau *et al.*, 1991). In addition to the Comdel RPM-1, a single point laser interferometry system was also constructed to measure the etching rate.

2.1.1 Laser Interferometry

The laser interferometry system used a 0.95 mW HeNe laser (632 nm wavelength) as incident light, and a photodiode to detect the light reflected from the wafer surface. The interference between the beam reflecting from the top of the film, and from the film-substrate interface, gives rise to a sinusoidal signal which can be used to calculate the etching rate. A sample trace from the laser interferometer is shown in Fig 2-2. The periodicity of the signal is directly related to the etching rate of the film by the formula

$$ER = \frac{\lambda/2}{\sqrt{n^2 - \sin^2 \theta}} \left[\frac{1}{\Delta t} \right] \quad (2-1)$$

where λ is the wavelength in Å, ER is the etching rate in Å/min, n is the refractive index of the film, θ is the angle of the laser from the normal, and Δt is the time period of the observed waveform in minutes. The refractive indices for the films were calibrated by comparing the etching rates obtained from laser interferometry with the ones obtained using a NanoSpec — a film thickness measuring instrument. The refractive indices used were: 1.45 for SiO₂, 3.0 for polysilicon and 1.6 for photoresist. The sample trace shown in Fig 2.2 is for the etching of 5000 Å SiO₂ over 5000 Å polysilicon over 100Å SiO₂. Using time periods of 78 seconds for SiO₂ and 143 seconds for polysilicon, the etching rates are calculated to be 1688 Å/min and 355 Å/min for SiO₂ and polysilicon respectively.

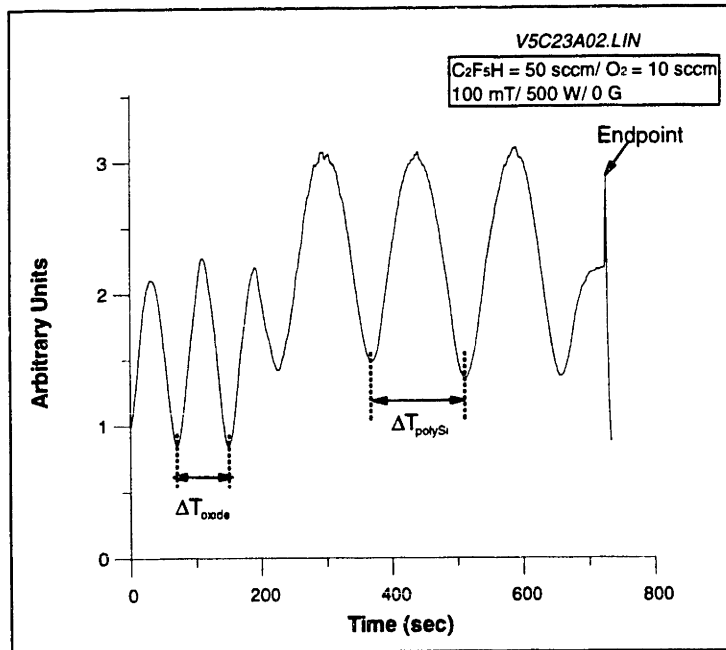


Figure 2-2: Sample trace from Laser Interferometry

2.1.2 Optical Emission Spectroscopy and Actinometry

The other two diagnostics employed on the AME studies were Optical Emission Spectroscopy (OES) and Actinometry. Both these diagnostics use monochromators. Optical emission spectroscopy was conducted using a high resolution 0.64m focal length f/7 monochromator — Jobin Yvon HR640 — manufactured by Instruments SA. This monochromator was equipped with two gratings — one optimized for 1800-4500 Å and the other for 4500-10000 Å. Plasma emission was coupled into the entrance slit of the monochromator using a fused silica fiber optic bundle. Although the wavelength transmission for fiber optics was inferior to UV lens based optics especially at lower wavelengths (≤ 2400 Å), it allowed for a flexible positioning of monochromator with respect to the chamber. A photomultiplier tube (Hamamatsu R955) was used at the exit aperture of the monochromator to monitor individual wavelengths. The resolution of this monochromator was determined to be about 0.3 Å.

The concentration of F during the etching runs was monitored using actinometry. The technique was pioneered by Coburn and Chen (1981). The main condition for actinometry to work is that the monitored species emission (in this case F) should result from the relaxation of direct electron impact ground state excitation. Even if the monitored emission is not solely from ground state excitation relaxation, actinometry can be used if the ratio of the emission from ground state excitation to the emission from all other mechanisms is constant.

The principle of actinometry is summarized below. The plasma induced emission (PIE) from any excited species, say X, is a complex function of many factors and can be written as

$$I_x = \Gamma_x k_x [e^-] [X] \quad (2-2)$$

where I_X is the emission intensity from species X, Γ_X is the branching ratio for the monitored emission relative to all other de-excitation paths, k_X is the excitation efficiency, $[e^-]$ is the electron density, and $[X]$ is the concentration of X. The excitation efficiency k_X is in turn a function of the electron energy distribution and the excitation cross section, and is related to the two by the relation

$$k_x = \int_0^{\infty} v(\epsilon) \sigma_x(\epsilon) f(\epsilon) d\epsilon \quad (2-3)$$

where $v(\epsilon)$ is the electron velocity, $\sigma_x(\epsilon)$ is the collision cross section for the excitation of X, and $f(\epsilon)$ is the electron energy distribution function.

The quantities required to compute $[X]$ from the above equations are difficult to determine in any given system. Actinometry allows for the tracking of the relative change in the concentration of species of interest via the introduction of an inert species (“actinometer”) into the system. The emission intensity from the actinometer is also governed by Eqn 2-2. Therefore the ratio of the two intensities (for X and actinometer) can be written as

$$\frac{I_X}{I_{Act}} = \frac{\Gamma_X k_X [e^-] [X]}{\Gamma_{Act} k_{Act} [e^-] [Act]} \quad (2-4)$$

If the actinometer is chosen such that the same set of electrons is responsible for the emission from both X and the actinometer, then the ratio k_X/k_{Act} can be taken to be constant. Similarly, Γ_X/Γ_{Act} is constant under conditions where collisional de-excitation (i.e. de-excitation by molecular collision) is unimportant. This is expected to hold true for the low pressures used in these experiments. Under these conditions, Eqn 2-4 reduces to

$$[X] \propto \frac{I_X}{I_{Act}} [Act] \quad (2-5)$$

Since the concentration of the actinometer [*Act*] is a constant for a fixed addition of actinometer to the reacting gas mixture, the ratio of I_X to I_{Act} gives an idea about the concentration of X. Therefore, the concentration of species X can be tracked.

The concentration of F in the AME-5000 experiments was tracked using Ar as an actinometer. The 7037Å transition of F*, which has an excitation threshold of 14.8 eV, was scaled with the 7030Å transition of Ar* (excitation threshold 13.5 eV) to track the ground state concentration of F. Since the etching runs typically lasted on the order of minutes, it was important to monitor both the emissions simultaneously. This was accomplished by using a 0.27m focal length f/3.8 Jarrell-Ash Monospec-27 monochromator equipped with a linear diode array at the exit aperture. The resolution of this monochromator was about 10Å. The linear diode array used on the system was the TN-6112 DARSS manufactured by TracorNorthern. It was a 1024 element linear diode array, and allowed for simultaneous recording of 600Å of the spectrum when used with a 1200 groove/mm ruled grating. The grating used was blazed at 5200Å, and had a range of 3800-9000Å. A sample scan from the diode array is shown in Fig 2-3. This scan is for the commercial recipe for AME-5000 for etching anisotropic vias in oxide. Both 7037Å F* and 7030Å Ar* lines are visible in the scan. In addition, other transitions related to Ar and F are also visible, and can be identified by comparing with the standard transitions listed in many sources (*e.g.* Striganov and Sventitskii, 1968; Herzberg, 1966).

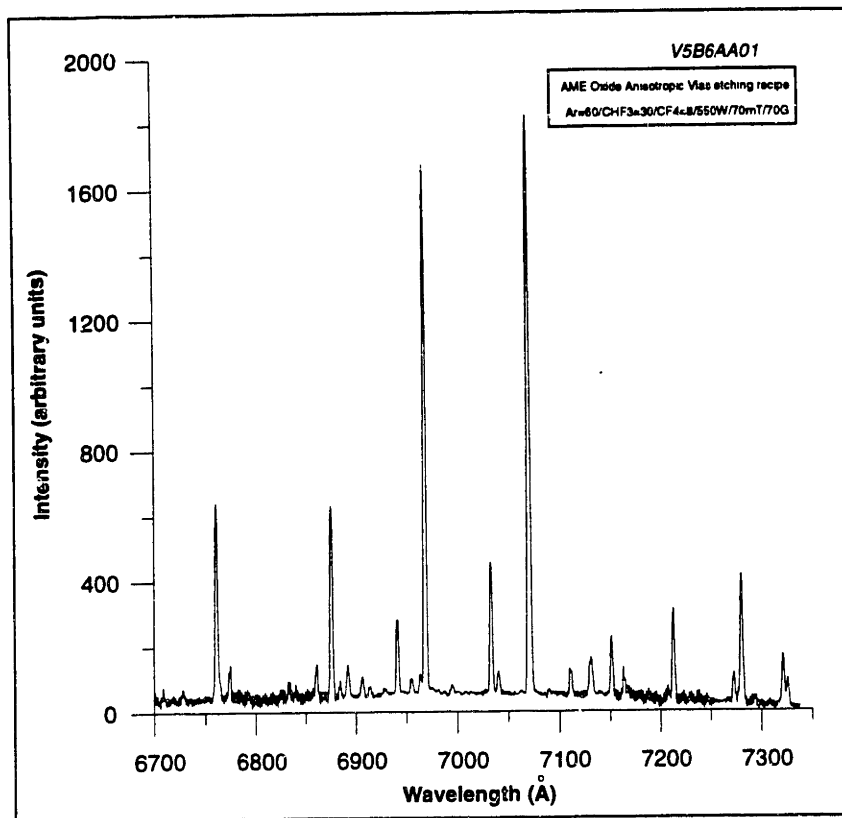


Figure 2-3: Snapshot from 0.27m monochromator equipped with a linear diode array

2.1.3 Profilometry using Atomic Force Microscopy/Scanning Electron Microscopy

The experiments on the AME-5000 were carried out both on unpatterned and patterned wafers. Two types of patterned wafers were used. The first type were those patterned using the experimental test mask developed by Hah and Dalton (Dalton, 1994). The other set of patterned wafers used were donated by Motorola. The patterns on the Motorola wafers consisted of a variety of ruled gratings and vias ranging in pitch from $0.1\mu\text{m}$ to $1\mu\text{m}$. The etched patterns were initially characterized using an Atomic Force Microscope (AFM). The AFM - TMX 2000 - was manufactured by TopoMetrix (Santa Clara, CA). Since the interest was in profiling sidewalls and feature bottoms, high aspect-ratio SuperTipsTM were used. A scanning electron micrograph of a SuperTipTM is shown in Figure 2.4. Although the tips were high aspect ratio, they suffered from a lack

of mechanical rigidity. This made them error prone due to the lateral forces experienced when the tip was in close proximity of the sidewall, and led to a distortion in the topographic information. This lateral force effect is depicted in Fig 2-5 where the top image is the topographic image and the bottom is the lateral force image. Lateral force induced artificial trenches can be seen near the sidewalls in the topographic (top) image. The lateral force map shown at the bottom clearly shows that the artifact is indeed due to the interaction of the tip with the sidewall. This phenomenon is well documented in the literature (*e.g.* Griffith *et al.*, 1991; Lee *et al.*, 1991; and Griffith *et al.* 1992) and seriously affected our ability to image and quantify the anisotropy of the etched features. Another limitation of the AFM was the finite size of the tip used to image the feature. Since the tip dimensions ($\sim 1.5 \mu\text{m}$ long and $\sim 0.3 \mu\text{m}$ diameter at the base) were comparable to the feature sizes being imaged, the tip frequently was unable to penetrate the feature to profile its bottom.

Due to these two major limitations, a scanning electron microscope (SEM) was used to image and characterize all the feature profiles discussed in this thesis.

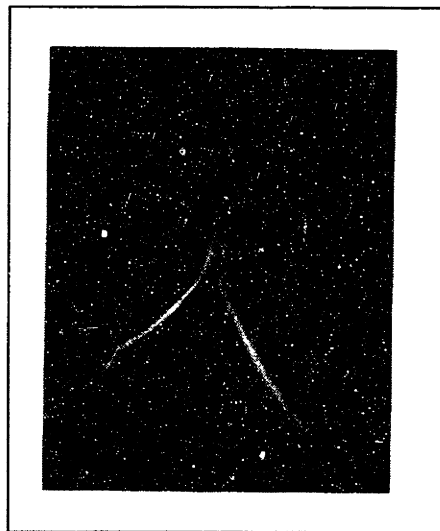


Figure 2-4: AFM SuperTipTM used for characterizing feature wall profiles

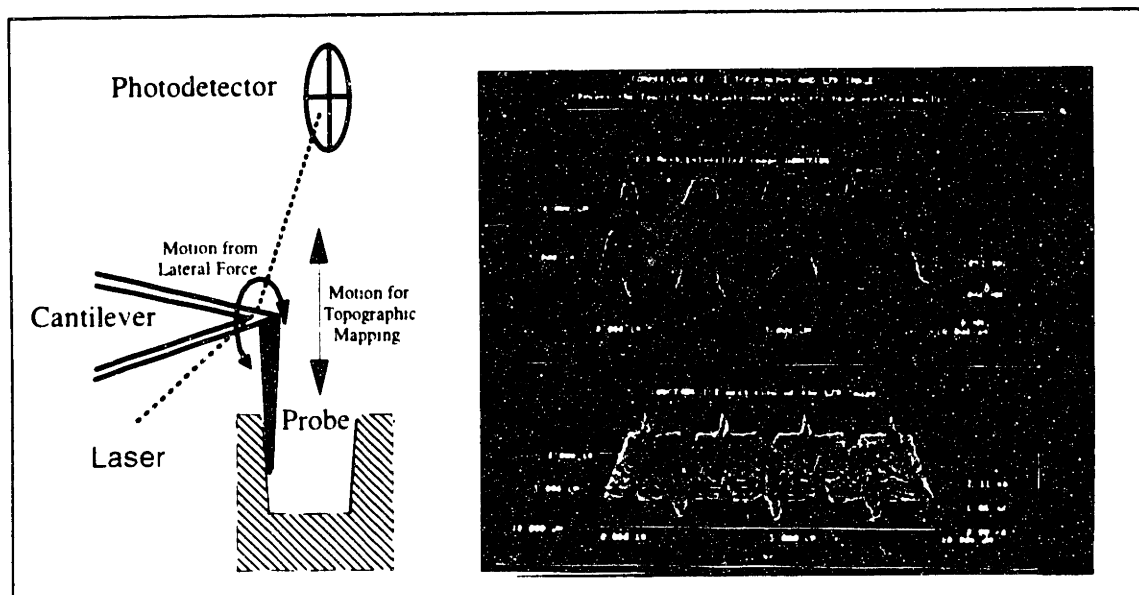


Figure 2-5: Topographic and Lateral Force AFM images showing near wall artifacts

2.2 Modulation Reactor

The second set of experiments for this thesis, dealing with the plasma chemical kinetics of PFC consumption and emission in a process, were carried out in another reactor referred to as the “Modulation Reactor”. The technique used for determination of dominant chemical kinetics was the RF Modulated Power Relaxation technique (also referred to as the Power Modulation technique).

2.2.1 RF Power Modulation Technique

The RF Power Modulation technique was pioneered in our laboratory by Linda Kiss (Kiss and Sawin, 1992a; Kiss and Sawin, 1992b). She used this technique to determine and model the chemical kinetics of CF_4 , CF_3Cl and $\text{C}_2\text{F}_6 + \text{Cl}_2$ chemistries in a parallel plate research reactor. The basic technique relies upon the validity of actinometry (see section 2.1.2) and is summarized in Fig 2-6.

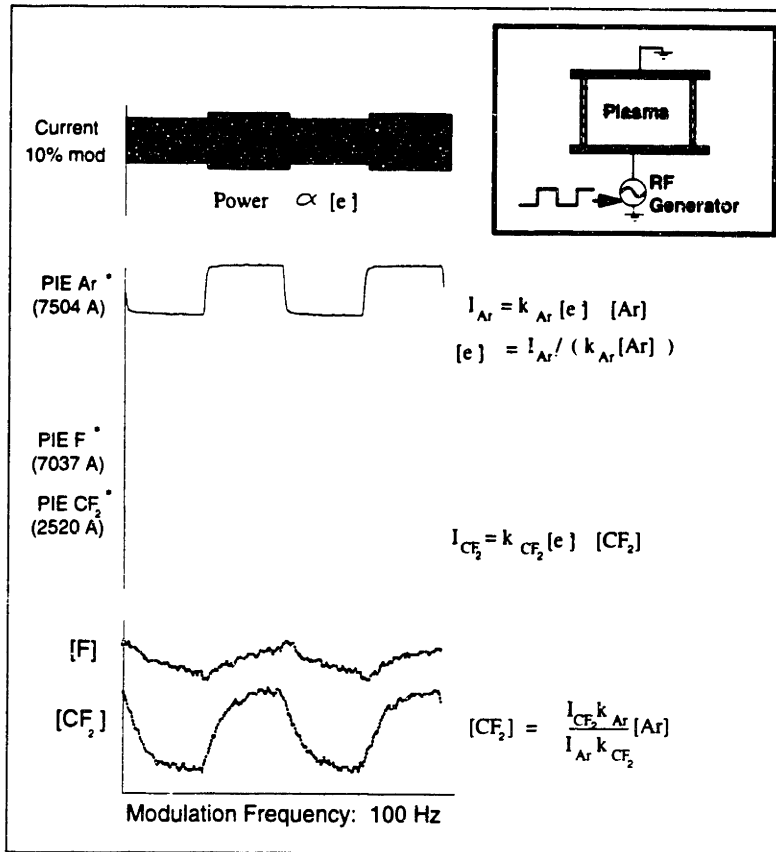


Figure 2-6: RF Modulated Power Relaxation technique for determination of dominant plasma kinetics

The RF power into the plasma is square wave modulated (5-10% typically) at frequencies from 1-1000 Hz, and species emissions are observed using a monochromator. The perturbation is purposely kept small to minimize the perturbation in chemistry, and to allow the linearization of the response analysis. This modulation in power results in a perturbation in electron density. Since many gas phase reactions in plasmas are electron impact driven, the perturbation in electron density in turn affects the concentrations of chemical species in the plasma. By the addition of an actinometer like Ar into the system, the perturbation in electron density due to RF power modulation can be tracked. In addition, by dividing the species emission waveforms (e.g. for F and CF₂) by actinometer waveform, the change in species concentration in response to the perturbation in electron density can also be monitored. These response waveforms can then be analyzed in the frequency domain. By conducting the experiments at different modulation frequencies,

Bode and Nyquist plots can be constructed for each species. The characteristic shapes of these plots give an insight into the dominant kinetics, which can then be modeled. The detailed theory of this technique is well documented in Kiss (1992c).

The main criteria for this technique to work is the applicability of actinometry (see Section 2.1.1). In addition, the plasma volume needs to be well-defined and confined. If the volume is not well-confined, the modulation in power could result in a modulation in plasma volume instead of a modulation in electron density. Although the modulation in plasma volume does not limit the applicability of this technique, it significantly complicates the analysis. Therefore, a well-confined plasma volume is highly desirable.

Since one goal of this thesis was to determine the chemical kinetics of PFC consumption and emission in a commercial process, an attempt was made to apply the RF modulation technique to the SiO₂ etching process on the AME-5000 etcher. Despite many months of system optimization, this technique failed to yield results on the AME. The main reason for the failure was the poor optical access to the plasma due to the presence of wafer clamping pedestal in the chamber. This pedestal made it impossible to ensure that the sampled emission was from the plasma bulk and not the sheaths. In addition, it degraded the signal-to-noise (S/N) to a point where the signal was unusable. Therefore, a new reactor — the Modulation Reactor — was constructed to study the chemical kinetics of SiO₂ etching.

2.2.2 Modulation Reactor Design

The modulation reactor was constructed on the skeleton of another reactor — the Scaling Reactor — constructed by Joanne Liu (1992). The water utilities, gas manifold and the basic setup from the scaling reactor were retained. The main features of the modulation reactor were the well-confined and defined plasma volumes, and the simplicity of design. The reactor was built to provide for an easy configuration change. It consists of a water-cooled top flange where the gas and the power feedthroughs are

connected. The top electrode has a gas showerhead, and can be either 3", 4.5" or 6" in diameter. The bottom water-cooled electrode can similarly be either 3", 4.5" or 6" in diameter. The design allows for both symmetric and asymmetric reactor configurations. In an asymmetric configuration, the powered top electrode is larger than the bottom by design. The gap between the electrodes is also adjustable using quartz reactor shells of different heights. This flexibility of reactor design also facilitates the use of this reactor for other studies. The machine drawings for the reactor are documented in Appendix A.

The experimental setup for the RF power modulation experiment is shown schematically in Fig 2-7.

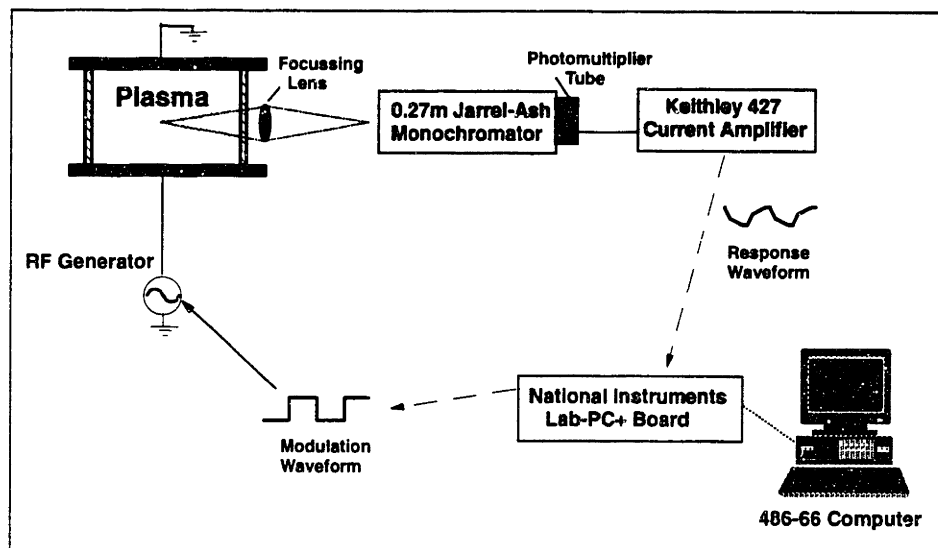


Figure 2-7: RF Power Modulation experimental setup

A Stanford Research Systems (SRS Model DS345) function generator was used for the 13.56 MHz signal. An ENI 3200L RF Power amplifier, capable of supplying up to 300 W, amplified the signal from the DS345 to the desired power level. A National Instruments Lab PC⁺ computer plug-in board was used for modulating the 13.56 MHz signal, and for acquiring the data. Another National Instruments Counter/Timer board (PC-TIO-10) was used to synchronize the output (modulation pulse) and the input (response) signals. Both the HR640 and MonoSpec27 monochromators were used to

observe the emissions. However, the MonoSpec27 had a higher throughput (due to shorter focal length) at an acceptable resolution. Therefore it was used for the experiments. The entrance and exit slits were fixed at 250 μm . The current from the photomultiplier tube detector at the exit of the monochromator was routed to the Keithley 427 current amplifier, which converted it to a voltage. This signal was then stored on a 486-66DX2 computer using the analog input ports on the Lab PC⁺. Since the phase relationship between the modulation signal and the observed relaxation is important in determining the kinetics, the output (modulation) and the input (emission) signals were synchronized to have a constant phase lag/lead which was then accounted for in the analysis.

The reactor configuration was held constant for all the experiments. A 3'' symmetric configuration was used at a gap spacing of 1 cm. The smallest configuration was chosen to maximize the range of residence time in the reactor, given the limited range of the mass flow controllers. The sheath width was visually observed to be about 1 mm on each electrode for this configuration. The optics were aligned to ensure exclusion of any sheath emission. Two circular apertures in series were used to achieve that. Both a fused silica fiber optic bundle and a plano-convex UV lens were tried for coupling light into the monochromator. The transmission from the fiber optic bundle was found to be slightly better than the lens for wavelengths greater than about 2400 \AA . However, the transmission rolled off dramatically for all wavelengths below that. Since some wavelengths of interest were below 2400 \AA , a 30.6 cm focal length plano-convex UV lens was used for imaging the plasma.

All experiments were carried out at a pressure of around 500 mT (same as Kiss, 1992). The three plasma systems studied were CF_4 , CF_4+O_2 and CF_4 with an SiO_2 wafer on the electrode (referred to here as CF_4+SiO_2 system). The plasma with CF_4 and SiO_2 exhibited some striations at 500 mT, so the pressure was lowered to around 400 mT for that system. The power was fixed at about 40 W nominal, corresponding to a setting of

0.25V_{pp} (peak-to-peak voltage) output from the SRS DS345 function generator. This power level corresponded to about 0.58 W/cc of the plasma volume.

The dominant species in each system were observed using the monochromator. Argon was added (5% by volume) to each system for actinometry. The wavelengths used for different species and their corresponding transitions are tabulated in Table 2-1. The background was subtracted from each signal to define the net emission.

Table 2-1: Wavelengths used for actinometry and their corresponding transitions

Species	Signal (Å)	Background (Å)	Transition
Ar*	7503 Å	7490 Å	4s'(1/2) ^o - 4p'(1/2)
F*	7037 Å	7055 Å	3p ² P _{3/2} ^o - 3s ² P _{3/2}
CF ₂ *	2520 Å	2530 Å	A ¹ B ₁ (0,5,0) - X ¹ A ₁ (0,0,0)
O*	8446 Å	8443 Å	3p ³ P - 3s ³ S

The validity of actinometry for F*, CF₂* and CF* using Ar* has been established by Kiss *et al.* (1992d) using laser induced fluorescence. The emission from O* at 8446Å has also been shown to give the right trends in O atom concentration (Walkup *et al.*, 1986).

2.3 Abatement Reactor

The third set of experiments for this thesis dealing with the kinetics of PFC abatement were carried out in the Abatement Reactor. The initial experiments for this phase of the thesis were carried out in a McCarrol microwave cavity using a 0.25" OD quartz tube. After promising results were obtained in this setup, a new scaled-up reactor was constructed. The reactor is schematically shown in Fig 2-8.

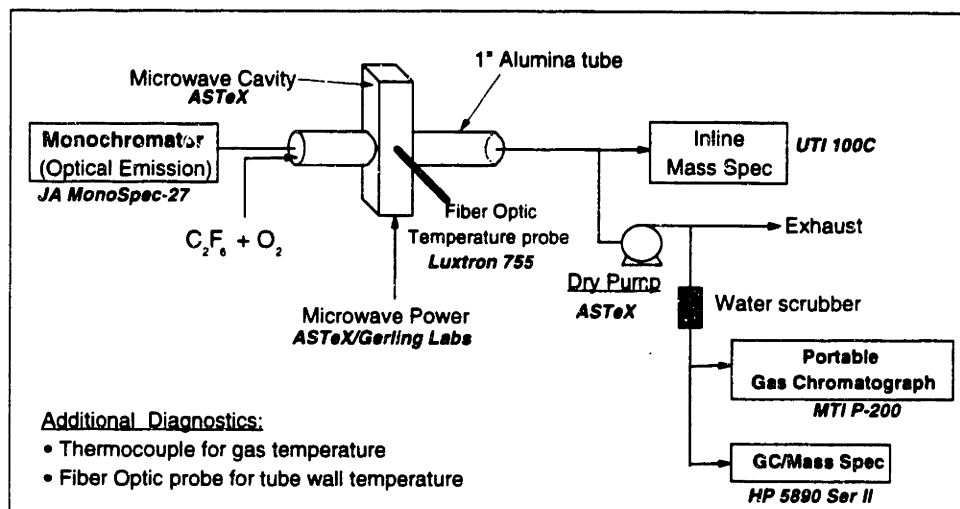


Figure 2-8: Schematic diagram of the Abatement Reactor

The basic reactor consists of a 10" long, 1" OD/0.875" ID alumina tube. A quartz tube with similar dimensions was also used for some experiments. The tube was housed in either a standard or a special ASTeX microwave applicator. The standard ASTeX applicator was modified to allow for efficient air cooling of the reactor tube walls. This modification is depicted in Fig 2-9.

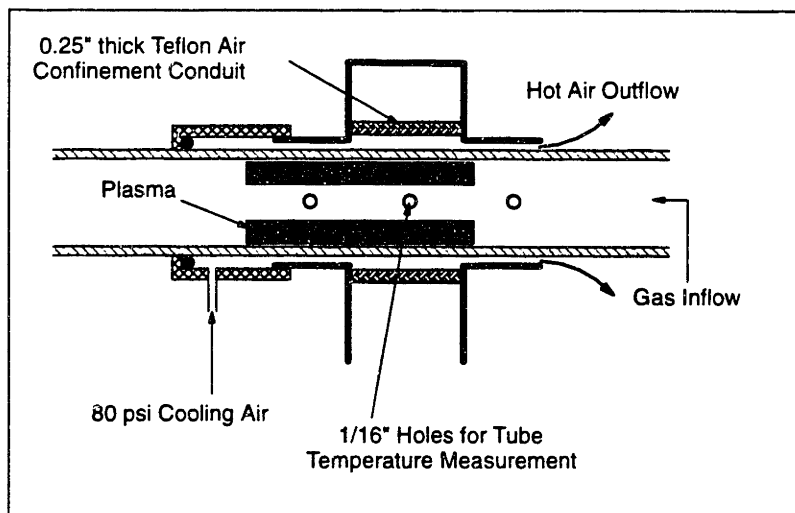


Figure 2-9: Modification of standard ASTeX applicator for air cooling

Air flowing at 80 psi was used to cool the tube, which heated up to nearly 200°C during the experiments. Three 0.07" diameter holes were drilled into the Aluminum applicator jacket to facilitate the measurement of the tube wall temperature. A Luxtron 755 Multichannel Fluoroptic thermometer was used for these temperature measurements. The thermometer probe consisted of a 0.0625" diameter ceramic-sheathed fiber optic bundle (MIH-2) with a temperature sensitive phosphor in its tip. This probe is capable of measuring temperatures up to 400°C continually, or up to 460°C intermittently. In addition to this probe, a 0.25" diameter ceramic-sheathed thermocouple was used to measure the gas phase axial temperature profile in the plasma. The thermocouple used was a type C W/Rh (T5R-010-19) manufactured by Omega Engineering. This thermocouple was encased in a ceramic protection tube (PTRA-53214-18), and the temperature was recorded using DP21-TC thermocouple indicator.

The microwave power at 2.45 GHz was coupled into the applicator using various microwave equipment shown in Fig 2-10. The power supply used was a 1 kW low ripple power supply manufactured by Gerling Laboratories. This power was delivered to a GL135 Magnetron head, which launched the microwaves into a circulator (ASTeX AX3120). The circulator had a water cooled dummy load (ASTeX LS) on one of its ports to absorb the reflected power. On its other port was a three stub tuner (TS) to tune the power into the plasma. The applicator was placed immediately after this three stub tuner. As mentioned above, the modified standard applicator from ASTeX was used for most of the experiments. Some of the later experiments were conducted using a proprietary ASTeX water cooled microwave applicator. This applicator had 0.25" diameter copper tube running along the 1" OD reactor tube wall. This copper tube carried cooling water directly along the reactor tube wall, thus cooling it more effectively. The proprietary design allowed for the coupling of the microwaves into the reactor without heating the cooling water, which is a strong microwave absorber.

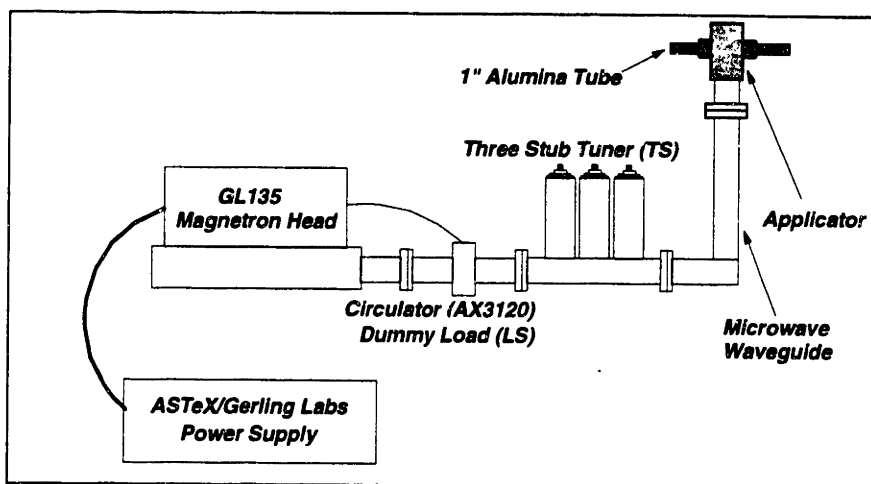


Figure 2-10: Microwave components in the Abatement Reactor

The tubular reactor was pumped using an Edwards Dry Star DP180 dry pump. This pump had a pumping speed of about 105 cfm, and could pump the system down to a base pressure of about 75 mT. The pressure in the reactor was maintained using an MKS Baratron 10 torr range capacitance manometer (122AA-00010AB) in feedback with a MKS 253A-1-40-1 throttle valve.

As shown in Fig 2-8, many other diagnostics were used on this system. These diagnostics are briefly discussed below.

2.3.1 Portable Gas Chromatograph

A portable GC (P200 Gas Analyzer) made by MTI Analytical was used in the initial studies to quantify the abatement of various gases. This GC was equipped with a 10 m long Al_2O_3 column, a thermal conductivity detector (TCD) and its own supply of He (carrier gas) in an internal tank. Due to short column length, the GC gave acceptable separation for PFCs in less than two minutes. The column was usually operated at 13 psig pressure, and the recipes for different PFCs usually differed only in column temperature.

The recipes for various gases were created by injecting known gases into the GC, and adjusting the GC parameters to achieve a reasonable gas elution time. Since purge N₂ was always introduced at the pump inlet, the GC recipes were created to ensure the separation of N₂ from the gas peaks. The recipes used for various gases were:

Table 2-2: Recipes used to quantify abatement of gases using MTI P200 Gas Chromatograph

Gas	Temperature (°C)	Pressure (psig)
C ₂ F ₆	33	13.2
CHF ₃	100	13.2
SF ₆	36	13.2

Typically, while observing C₂F₆/O₂/N₂ mixtures, the O₂ peak gets subsumed in the N₂ peak (the first one), and the second peak is due to C₂F₆. This GC could not be used for measuring the abatement of CF₄ since CF₄ retention time is same as N₂, and thus CF₄ peak also gets subsumed in the N₂ peak.

The abatement for the gases was quantified by measuring the peak areas with and without the plasma. The peak areas were taken to represent the concentrations, and the difference gave the extent of abatement. Once the conditions were changed (*e.g.* turning on the power or changing the gas flow rates), the system took about 5-7 minutes to come to the new steady state. Thus after changing any condition a time of 10 minutes was allowed to lapse before the collection of next data point. The reaction products from the plasma were expected to be corrosive, and HF was a very likely product. Since the GC injection port was fused silica and F or HF in the stream corroded the inlet, the plasma effluent was scrubbed with water before injecting into the GC. Initially, a water bubbler system was used for scrubbing. However, due to the large gas flow rates involved (~1000 sccm), and the low volume of water in the bubbler (~150 cc), the water saturated with HF fairly rapidly. In some cases, entrained water (HF) reached the GC inlet and corroded the

inlet valve. To alleviate this problem, a countercurrent water scrubber shown in Fig 2-11 was designed.

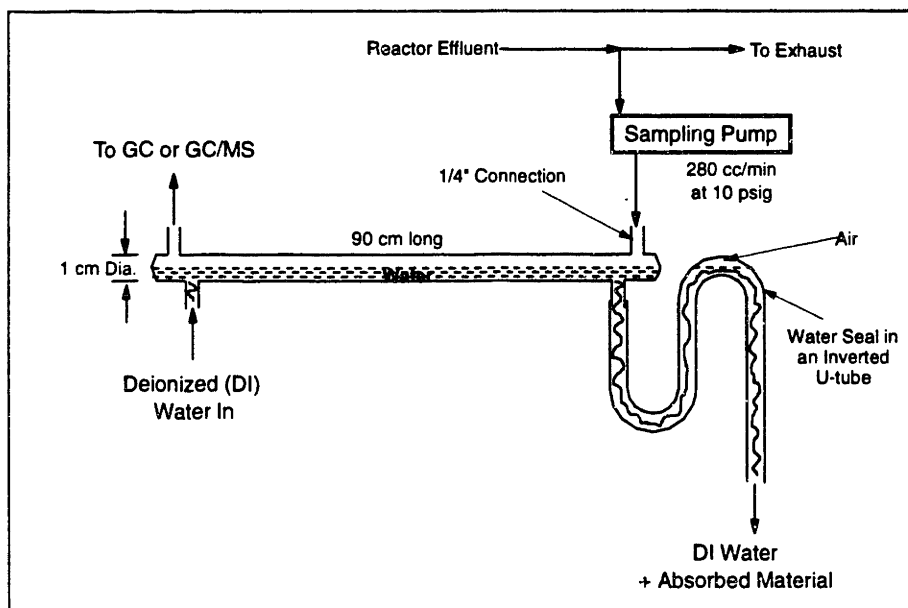


Figure 2-11: Countercurrent water scrubber for plasma effluent

This scrubber was fashioned out of 1 cm ID glass tube and was 90 cm long. The plasma effluent flowed in from one side, and exited the other. Deionized (DI) water was introduced in a countercurrent fashion, and occupied the bottom half of the circular cross section of the tube. The 90 cm scrubbing length ensured that all water soluble species (including HF) were scrubbed out of the gas phase. The DI water was also cooled using crushed ice before introduction into the scrubber to minimize the evaporation of water into the gas stream. The GC inlet corrosion was eliminated after the installation of this scrubber.

2.3.2 Gas Chromatograph/Mass Spectrometer (GC/MS)

The GC described above does an adequate job of separating out pre-identified gases. However, one of the concerns while quantifying the abatement is whether any

other PFC byproducts are created during the process. Even if additional peaks are observed with a GC once the plasma is turned on, there is no way of positively identifying these peaks unless prior calibration has been carried out. This difficulty is partially alleviated through the use of a GC/MS. The GC/MS uses a Mass Spectrometer (MS) as a detector after the column, instead of the TCD used in the P200. Therefore, the mass spectra at each elution point are available for aiding the identification of unknown GC peaks.

The GC/MS system from Hewlett-Packard (HP) was used for by-product identification. The GC used was HP 5890 Series II, and the mass spectrometer detector was HP 5972. The gas stream was sampled using a heated 6-port gas sampling valve with a 2 cc gas sampling loop. Splitless injection was used into the GC since the concentration of species was expected to be relatively large. The GC was also equipped with Electronic Pressure Control (EPC) which allowed for constant volumetric flows through the column when pressure programming was used at the inlet (HP Operating Manual, 1994). In contrast to the MTI P200 portable GC, this GC has a number of degrees of freedom in creating recipes. The temperature of the column can be programmed as a function of time using a programmable GC oven. The temperature of the injection port is also independently programmable. In addition, the pressure at the injection port can also be programmed.

The Mass Spectrometer detector (MSD) used was a standard heated quadrupole mass spectrometer. It was pumped using an oil diffusion pump backed by a roughing pump. It could scan from 1.2 to 700 amu, and gave good sensitivity even at a scanning rate of 500 amu/second. The entire flow from the GC (up to 2 sccm) was injected into the MS without witnessing a significant rise in the pressure and the MS was tuned automatically using an internal reference (PFTBA).

The column used for the separation of the PFCs was an HP Al₂O₃ M-deactivated Porous Layer Open Tubular (PLOT) column. It had a diameter of 0.32 mm and was 50 m

long. PLOT columns show good separations for many C-H-F type PFCs, but cannot separate chlorofluorocarbons (Bersotti, 1995). Additional columns (PoraPLOT “Q”) were purchased for used with CFCs.

Similar to MTI GC, recipes had to be developed for the HP GC/MS for the separation of C₂F₆ from N₂. This task was complicated by the presence of multiple degrees of freedom including pressure programming, temperature programming and choice of column. The recipe used for C₂F₆ is detailed in Table 2-3.

Table 2-3: Recipe for C₂F₆ detection using the HP GC/MS

Parameter	Value
Column	HP-PLOT/Al ₂ O ₃ “M” Deactivated. 50 m. 0.32 mm ID
Inlet	HP 5890 GC
Tune File	ATUNE.U
Mode	Scan
Solvent Delay	0:00 min
Scan from	1.2 to 200 amu. Threshold of 3.
Inlet B	250 °C for 480 min (constant)
Inlet B Pressure	3 psi for 480 min.
Splitless Mode	Splitless
Aux Channel E	25 psi for 480 min.
Zone Temperature	Injector B = 250 °C. Detector B = 280 °C
Oven Program	Initial Temperature = 30 °C for 2 min. Level 1: 50 °C/min rate; Final Temperature = 90 °C for 10 min. Oven equilibration time = 0.50 min
Injector Information	Source: Manual Purge A/B: Init. Value = Off; On Time 1:00; Off Time 0:00

Since CF₄ abatement could not be quantified using MTI GC, this GC/MS was used for the purpose. Various recipes were tried to achieve a separation of CF₄ and N₂, but all failed. Finally m/e 69 (CF₃⁺) was used as a proxy for CF₄, and CF₄ abatement was

characterized using the Extracted Ion chromatogram (EIC) peak area for m/e 69 before and after the plasma was turned on.

2.3.3 Inline Mass Spectrometer (MS)

After the initial experiments for C_2F_6 abatement indicated the importance of plasma gas phase reactions, the equipment was modified to add a differentially pumped inline mass spectrometer — UTI 100C. A new chamber was constructed to house the mass spectrometer. The drawings for this chamber are documented in Appendix B. The chamber consists of two sections. The gas from the process (typically at 5-10 torr) is sampled through a 0.005" diameter orifice into the front section. This section is pumped through a Balzers TPU 240C corrosive service 210 l/sec turbo pump. This turbo pump is backed by an Edwards E2M12 roughing pump. The abstracted beam is then channeled through a beam skimmer cone (Ni with 0.05" orifice; Model 1 manufactured by Beam Dynamics, Inc.) into the second section with the mass spectrometer. A beam chopper (UHV compatible CH-10 manufactured by Electro-Optical Products Corp. of NY) with a resonant frequency of 400 Hz is used at the entrance of the mass spectrometer chamber to distinguish the beam signal from the background. The mass spectrometer chamber is equipped with a Granville-Philip ionization gauge for measuring the pressure in the chamber. In addition, both the front and the main sections are equipped with a 2 $\frac{3}{4}$ " quartz optical port for visually observing the mass spectrometer.

The UTI 100C mass spectrometer is capable of scanning a pre-programmed range of masses. The ramp signal and the mass signal are available at the mass spectrometer controller and are plotted in X-Y format on an oscilloscope (Tektronix 7603). A National Instruments Lab PC⁺ Analog I/O board was used to provide a computer generated ramp signal, and store the mass intensities directly on the computer. The beam chopper signal was used as a reference in a lock-in amplifier (EG&G Princeton Applied Research Model 124A) to ensure that the mass spectrometer signal was not corrupted by the chamber background. The chopper frequency was fixed at about 400 Hz. The ramp used for

scanning the mass spectrometer was at 1 amu/sec. A 0.1 amu step was used, which gave 10 points per amu and acceptable peak resolutions (<1 amu). The mass intensity signals were typically averaged 10-20 times to increase the signal-to-noise ratio.

The output from the mass spectrometer electron multiplier is a current (\sim nA range). This current is converted to a voltage in the mass spectrometer control unit. The current amplifier built into the control unit, however, is not fast enough to respond to a 400 Hz modulation imposed by the chopper. Therefore, the signal from the electron multiplier was diverted from the mass spectrometer control unit to an isolated fast current amplifier (EG&G PARC Model 181), and then fed to the lock-in amplifier. The current amplifier was normally operated at a gain of 10^{-6} A/V. The time constant of the lock-in amplifier was fixed at 30 ms.

The mass spectrometer was placed immediately after the microwave cavity. There was about a 10-12" length of stainless steel fittings from the exit of the reactor to the entrance of the mass spectrometer. The presence of this wall area facilitated the recombination of free radicals. Therefore only stable species could be detected in the mass spectrometer. Both the inlet and the outlet flanges of the mass spectrometer were water cooled to prolong the life of the O-ring used to seal the front section. Right angle valves were used at each end to isolate the mass spectrometer from the rest of the equipment. This ensured that the mass spectrometer remained under vacuum even when the rest of the apparatus was open to air.

Chapter 3: Alternatives to PFCs for Plasma Etching

The gases currently used in SiO₂ etching, like CF₄ and C₂F₆, are members of the PFC family. It would be prudent to minimize (and ultimately eliminate) emissions of all PFCs due to the reasons mentioned in Chapter 1. One route to emissions control would be to develop alternative processes using non-PFC gases. Several gases being developed as CFC alternatives, including hydrofluorocarbons like C₂HF₅ (HFC-125) and C₂H₂F₄ (HFC-134a), could be suitable as replacement gases for PFCs in the current processes for plasma etching and CVD chamber cleaning. The presence of H in the molecules of these gases greatly reduces their lifetimes in the atmosphere, and so reduces their global warming potential.

The first part of this thesis involved characterizing the replacement potential of these gases for conventional PFCs in SiO₂ etching. The etching studies were carried out using O₂ and Ar as additive gases to the HFCs. In addition, the etching characteristics of SiO₂ in C₂F₆/O₂ plasmas were compared with the etching in C₂HF₅/O₂ and C₂H₂F₄/O₂ plasmas. This comparison was carried out to explore the applicability of these gases to CVD chamber cleaning, which is currently carried out using C₂F₆/O₂ mixtures.

3.1 Experimental Setup and Methodology

3.1.1 Experimental Setup

All experiments were carried out in the Applied Materials Precision 5000 (AME-5000). The reactor and the associated diagnostics are described in Chapter 2.

The wafers used in the experiments were 10 cm p-type Si (0.5-2 ohm-cm resistivity) with 2 μm thick patterned thermal oxide (SiO₂). The photoresist used was

Shibley-821. To monitor the selectivity of SiO₂ to Si etching, a 1 cm² die with 2 μm undoped polysilicon was bonded to the wafers using silver paint. While the etching rate of SiO₂ was monitored *in-situ* using laser interferometry, polysilicon and photoresist etching rates were determined *ex-situ* by dividing the change in thickness (as measured using Nanospec) by the total etching time.

3.1.2 Design Experiments

The experiments were designed and analyzed using NNAPER — a neural network based program developed by DuPont. The program uses statistical design (central composite) to generate a design matrix, and employs a back-propagation neural network (BPN) to analyze the responses. The modeling approach is as follows. The matrix of generated experiments is divided into two groups- "Training" and "Test" points. "Training" data points correspond to the experiments generated using the Central Composite design. "Test" data points are randomly generated experimental points, and are used to validate the model. For example, the 3 parameter design used in the current study consisted of 20 "training" points and 4 "test" points.

NNAPER is a 3 layer neural network, with one layer each consisting of "input" nodes (corresponding to the design variables), "output" nodes (corresponding to response variables), and "hidden" nodes (a layer between the input and output layers, used to generate a model). The number of hidden nodes in the network can be varied to generate different models. The software first generates a model based on the "training" data points. It then tests the validity of the generated model using the "test" data points. The fit of the test points to the model indicates the general applicability of the model. Generally speaking, increasing the number of hidden nodes leads to a better fit of the model to the "training" points. However, it can also lead to overparametrization of the model, whereby the noise in the data is also fit in the model, leading to a poor fit of the model to the "test" points. Thus the number of hidden nodes is optimized to yield a

model which best fits the "test" data points. Details of this modeling approach are documented in Mocella *et al.* (1992).

It is worth mentioning that since the experimental points correspond to a matrix based on a Central Composite Design, the responses can also be modeled using a conventional statistical approach. However, a neural network based analysis is amenable to a more flexible model generation. Researchers have shown that neural networks, employing at least one hidden layer, can serve as global approximators of any function to arbitrarily desired accuracy (Bishop(1994), Moody and Darken (1989), Bhagat (1990)). Thus the present analysis was carried out using the neural network approach. One drawback of the neural network approach, however, is that the analysis does not yield individual coefficients for each design variable. Therefore, the generated model only exists as a look-up table at best.

3.2 Results and Discussion

The etching characteristics of both HFCs were first evaluated using O₂ as an additive gas. Subsequently, Ar was also used in the gas mixture. The results from C₂HF₅ (HFC-125) are discussed first, followed by results from C₂H₂F₄ (HFC-134a).

3.2.1 C₂HF₅/O₂ Experiments

Some exploratory experiments were carried out to determine the parameter space of interest for the design experiments. Magnetic field was found to influence the SiO₂ etching rate dramatically. For example, while the SiO₂ etching rate was 1600 Å/min with no magnetic field (50 sccm C₂HF₅/ 20 sccm O₂/ 2 sccm Ar/ 100 mT/ 500 W nominal power), it increased to 3000 Å/min with 75 G magnetic field under the same conditions. The design variables chosen for the study were Power, Pressure and O₂ flowrate while the fixed variables were C₂HF₅ flowrate (50 sccm), Magnetic field (75 G), and Ar flowrate

(2 sccm for F actinometry). The ranges of parameters investigated were Power: 300-700 W, Pressure: 50-150 mT and O₂ flowrate: 0-20 sccm. A 24-experiment design matrix was generated on NNAPER using these ranges. The responses (SiO₂ etching rate, Photoresist etching rate, F concentration, Polysilicon etching rate and RF Voltage indicative of ion bombardment energy) were analyzed using the same software.

The test data R² were all greater than 0.95, and the F-factor for the model was high (39), indicating that the model captures the behaviors of the responses accurately and can be used for quantitative predictions. The high F value also indicates that there is practically no lack of fit to the model. The results from the model are shown in Fig 3-1 to 3-4. The default setpoints for all the plots are power=500 W, pressure= 50 mT, and O₂ flowrate= 10 sccm. The plots are in terms of nominal power. The real power deposited in the plasma as measured using the Comdel RPM-1 was about 80% of the nominal under all conditions.

The model predictions for SiO₂ etching rate dependence on pressure and O₂ flowrate is shown in Fig 3-1.

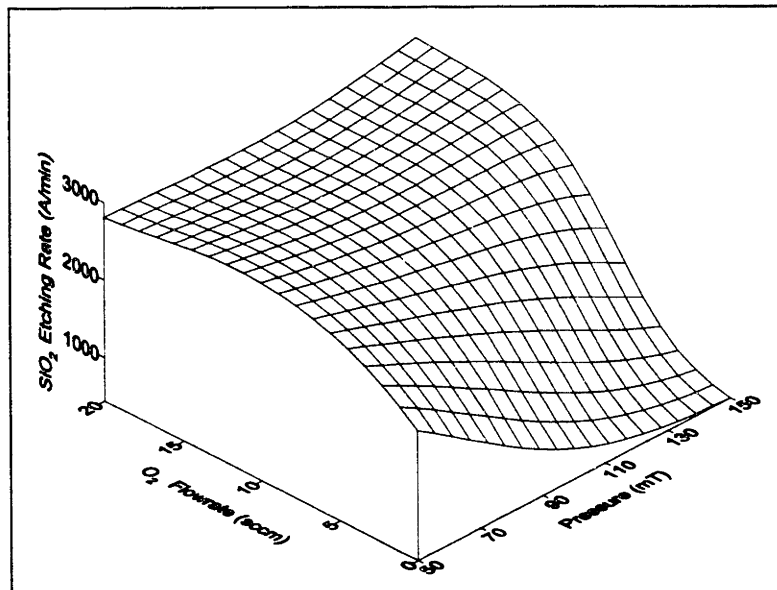


Figure 3-1: SiO₂ etching rate dependence on Pressure and O₂ flowrate. Fixed conditions for plot: Power at 500W and C₂HF₅ flowrate at 50 sccm

At a given pressure, SiO₂ etching rate initially increases rapidly with increase in O₂ flowrate. However, the increase saturates at higher O₂ flowrates. SiO₂ etching rate decreases with increasing pressure, but the effect is less pronounced at higher O₂ flowrates (>10 sccm). The ion-bombardment energy (assumed to equal the RF voltage since the reactor configuration is highly asymmetric) is almost invariant with O₂ flowrate and pressure and varies between 385 and 433 V for the conditions in Fig 3-1.

The addition of O₂ to C₂HF₅ has two effects. It scavenges the C from CF_x type species liberating F which enhances SiO₂ etching. In addition, increasing O₂ flowrate also tends to decrease the residence time for gas species in the reactor. Since O₂ is added to a fixed amount of C₂HF₅ (50 sccm), the change in residence time with O₂ addition is about a factor of 1.4. This decrease in residence time could reduce the concentration of neutral species available for etching. The combined effect (residence time and scavenging of C) leads to a net enhancement of F, which leads to the observed SiO₂ etching behavior. This is corroborated by the F concentration (from actinometry) shown in Fig 3-2, where some saturation is evident especially at lower pressures. Therefore, the behavior observed in Fig 3-1 is mainly related to the neutral etchant (F) density.

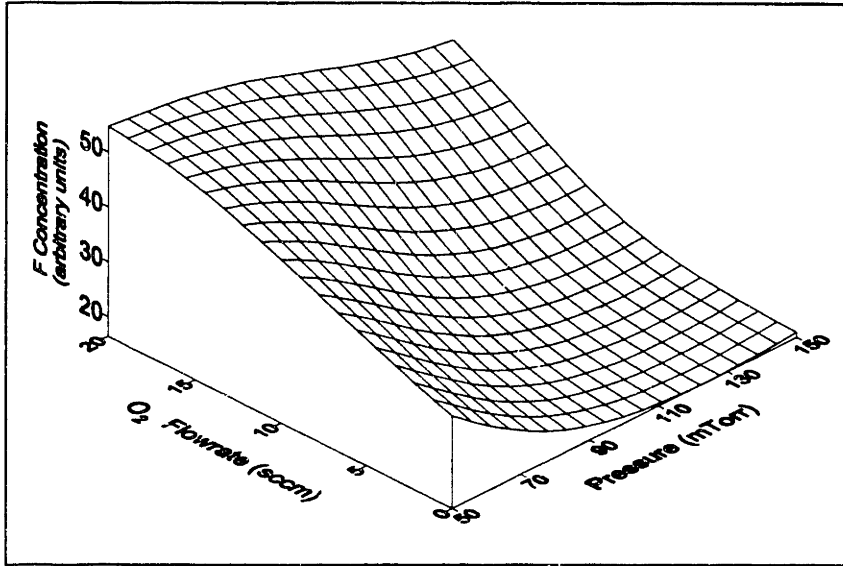


Figure 3-2: F concentration dependence on Pressure and O₂ flowrate. Fixed conditions for plot: Power at 500W and C₂HF₅ flowrate at 50 sccm

Fig 3-3 and Fig 3-4 show the predicted dependence of SiO₂ etching rate, and F concentration on pressure and power respectively.

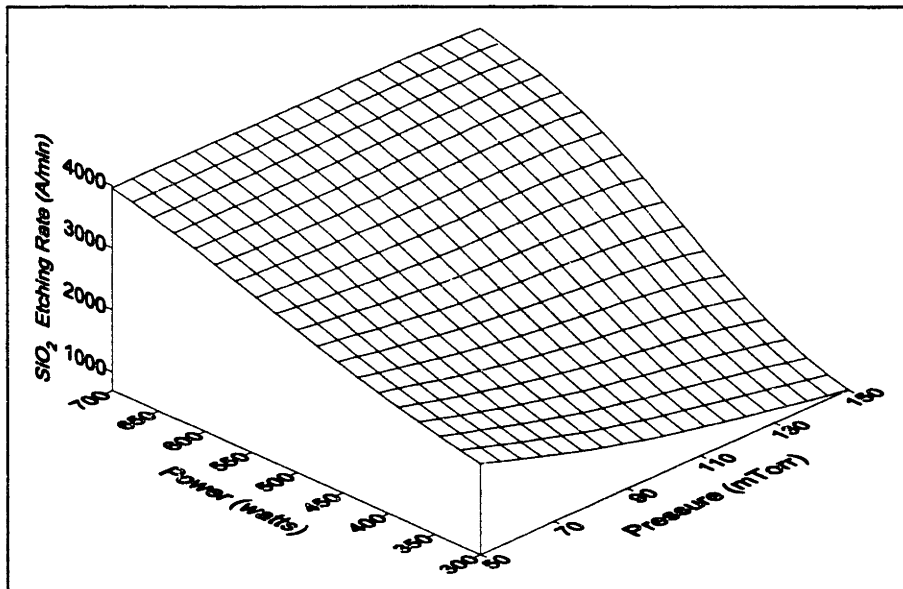


Figure 3-3: SiO₂ Etching rate dependence on Power and Pressure. Fixed conditions for plot: O₂ flowrate at 10 sccm and C₂HF₅ flowrate at 50 sccm

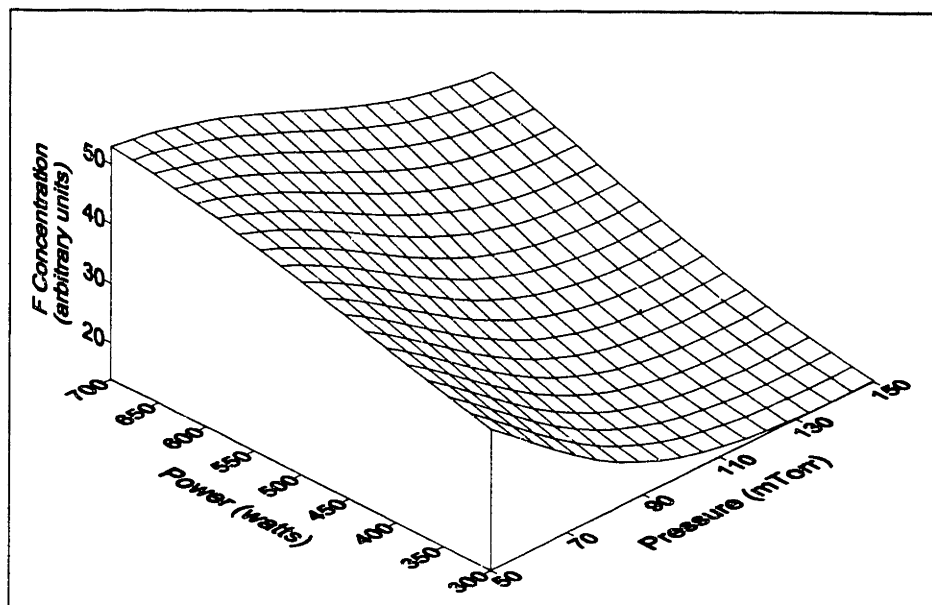


Figure 3-4: F concentration dependence on Power and Pressure. Fixed conditions for plot: O_2 flowrate at 10 sccm and C_2HF_5 flowrate at 50 sccm

The plots are for a fixed O_2 flowrate of 10 sccm, and indicate that oxide etching rate increases almost linearly with increasing power, at all pressures. This trend is also reflected in both F concentration (Fig 3-4) and V_{rf} (it changes from 300 to 494 V over the plot range). Therefore, increasing power enhances SiO_2 etching rate both by making more F available and by increasing the ion bombardment energy..

To summarize the observed trends, SiO_2 etching rate shows a rapid enhancement with O_2 addition at any given pressure, but the enhancement saturates at approximately 10-13 sccm O_2 addition (to 50 sccm C_2HF_5). However at higher powers (>500 W) and lower pressures (50 mT), SiO_2 etching rate is relatively insensitive to O_2 addition. In general SiO_2 etching rate drops with increasing pressure, with the decrease being particularly pronounced for low O_2 additions. SiO_2 etching rate increases linearly with power, but shows a shifting trend with pressure. Increasing pressure decreases the etching rate at lower powers, but a slight increase is seen at higher powers.

In addition to the model results presented above, photoresist etching rate were also monitored for all experimental conditions, and analyzed using NNAPER. Photoresist etching rate dependence is particularly important when the main goal is high-fidelity pattern transfer. Fig 3-5 shows the photoresist etching behavior as a function of pressure and O₂ flowrate.

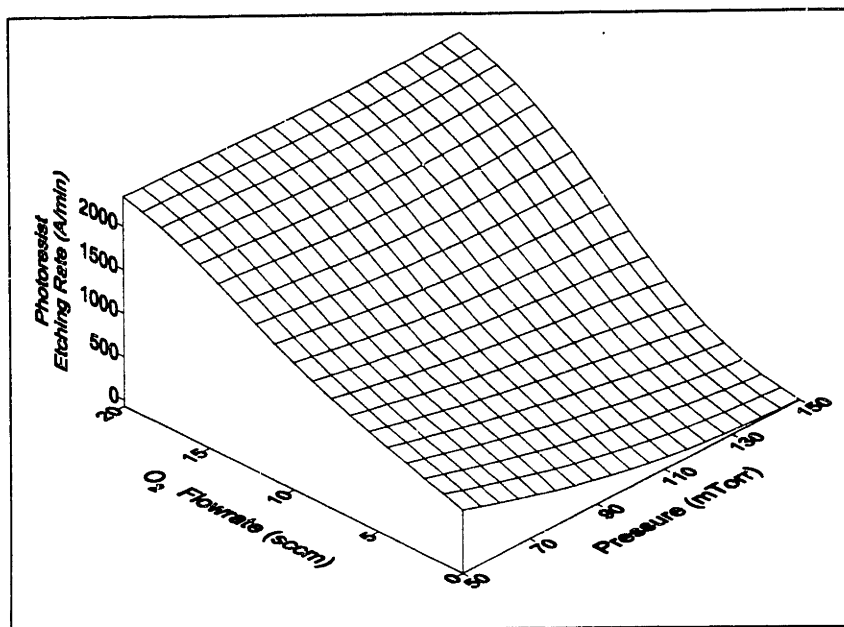


Figure 3-5: Photoresist etching rate dependence on Pressure and O₂ flowrate. Fixed conditions for plot: Power at 500W and C₂HF₅ flowrate at 50 sccm

The parametric dependence of photoresist etching rate on pressure, power, and O₂ flowrate is identical to F concentration. The etching rate varied from 50 Å/min to 2500 Å/min, over the parameter-space investigated. In general, high powers, moderate pressures and moderate O₂ flowrates give a high SiO₂ etching rate and good selectivity with respect to the photoresist. For example, SiO₂ etching rate at 615 W/ 80 mT/ 75 G/ 50 sccm C₂HF₅/ 5 sccm O₂/ 2 sccm Ar was 3300 Å/min, with the resist etching rate being 1100 Å/min. The best selectivity to photoresist obtained for the design experiments was 4, with oxide etching rate of 2850 Å/min. It is also worth mentioning that an attempt to etch oxide with pure C₂HF₅ led to a brown polymer deposition on the wafer surface. Assuming the same refractive index for this film as for a positive photoresist (1.6), the

polymer deposition rate at 50 sccm C_2HF_5 / 500 W/ 200mT/100 G was estimated at 150 Å/min.

3.2.2 C_2HF_5 /Ar/ O_2 Experiments

Although the above set of experiments was carried out using C_2HF_5/O_2 mixtures, the commercial SiO_2 etching recipe for anisotropic vias on the AME-5000 suggested that a mixture of Ar/ C_2HF_5/O_2 might be better (the commercial recipe employs a mixture of Ar, CHF_3 and CF_4). Therefore, three parameters were investigated in the next set of experiments: Ar flowrate (0-50 sccm), O_2 flowrate (5-15 sccm) and Pressure (20-140 mT). The fixed variables were nominal power (600 W), magnetic field (100 G) and C_2HF_5 flow rate (50 sccm). The monitored responses were SiO_2 etching rate, polysilicon etching rate, photoresist etching rate, F concentration (monitored actinometrically using Ar), and electrical characteristics of the plasma. In addition scanning electron micrographs were taken at each point to characterize the etched profiles. Due to the qualitative nature of the observed profiles, this data was not modeled, but the results are summarized at the end of this section. The quality of F actinometry was very marginal, and hence it was not fit in the model. The real power deposited into the plasma was 80-83% of nominal under all experimental conditions.

A 24-experiment design matrix was generated on NNAPER using the design variable ranges mentioned above. In general the responses were consistent with those discussed in the previous section. The effect of Ar addition is depicted in Fig 3-6. As seen in the figure, the addition of Ar to the mixture leads to an enhancement in SiO_2 etching rate. However, as shown in Fig 3-7, Ar addition also increases the photoresist etching rate, which could lead to a loss of anisotropy. The enhancement in both SiO_2 and photoresist etching rates are directly attributable to the increase in ion flux (and possibly energy) with the increase in Ar flowrate.

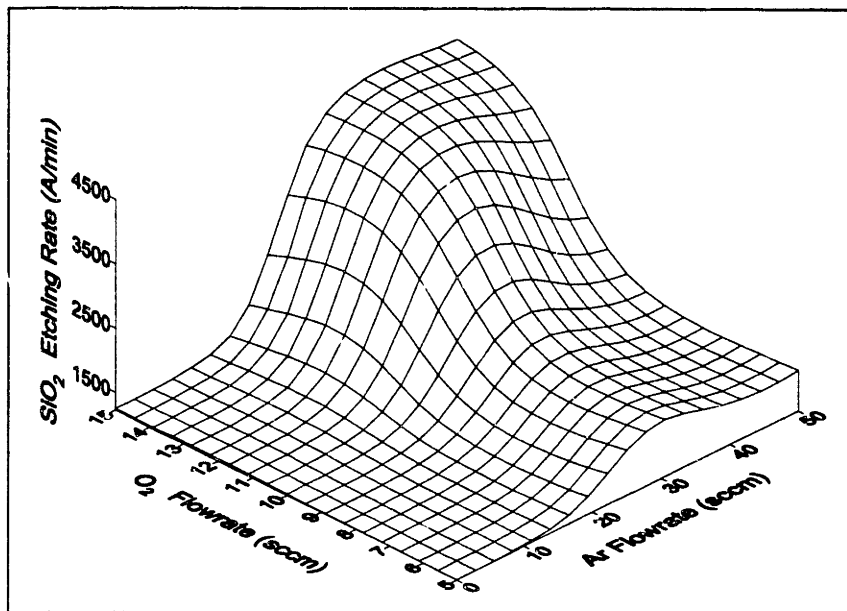


Figure 3-6: SiO₂ etching rate as a function of Ar and O₂ flowrates. Fixed conditions for plot: Pressure at 80 mT and C₂HF₅ flowrate at 50 sccm

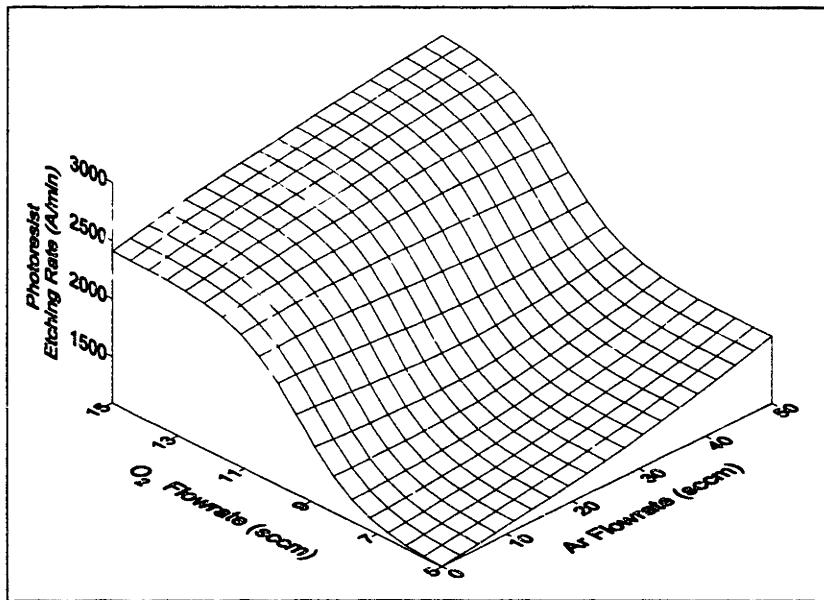


Figure 3-7: Photoresist etching rate as a function of Ar and O₂ flowrates. Fixed conditions for plot: Pressure at 80 mT and C₂HF₅ flowrate at 50 sccm.

As mentioned earlier, scanning electron micrographs (SEM) were taken for each experimental condition. The dies were cleaved after immersing in liquid N₂ to preserve

photoresist integrity. The test pattern consisting of submicron gratings was observed under each condition. The SEMs showed a wide range in the quality of the etched profiles. Under some conditions, phenomena like RIE lag (or Aspect Ratio Dependent Etching - ARDE) and microtrenching were clearly observed. The quality of the etched sidewalls varied anywhere from ragged to smooth, and various sidewall angles were observed. The sidewall angles were hard to quantify and were not fit to the model. Fig 3-8 shows one of the profiles obtained with the gratings. The conditions of etching are listed in the caption. Under the conditions for Fig 3-8, SiO₂ etching rate was 2420 Å/min, selectivity to undoped polysilicon was 3, and selectivity to photoresist was 1.10. In comparison, the commercial recipe using Ar/CHF₃/CF₄ mixture was found to result in SiO₂ etching rate of 4125 Å/min, selectivity to undoped polysilicon of 12, and selectivity to photoresist of 1.13. Fig 3-9 shows the cross section of another profile etched under different conditions using the same Ar/CHF₅/O₂ mixture.

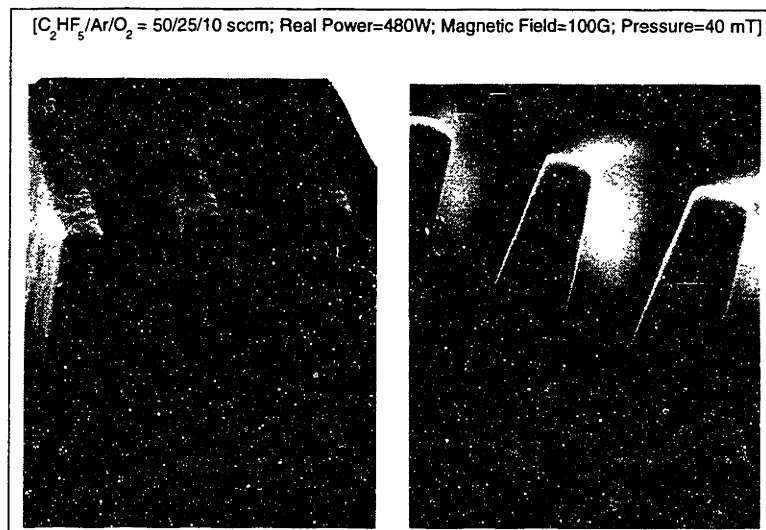


Figure 3-8: Etched SiO₂ grating in C₂HF₅/O₂/Ar mixtures

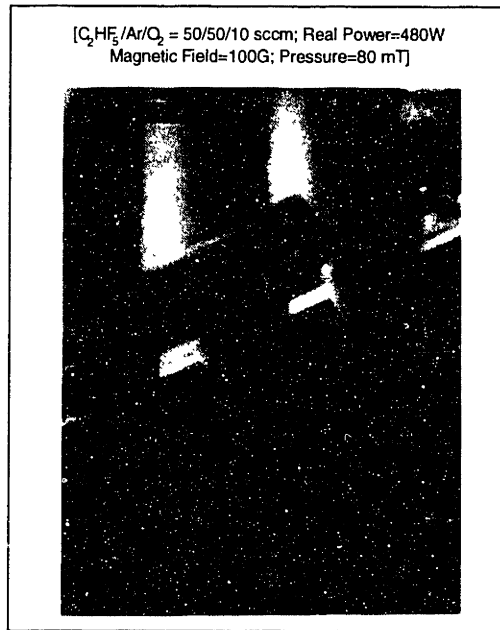


Figure 3-9: Etched SiO₂ grating in C₂HF₅/O₂/Ar mixtures

3.2.3 C₂H₂F₄/O₂ Experiments

A set of design experiments similar to those for C₂HF₅/O₂ were carried out to determine the parametric dependence of oxide etching in C₂H₂F₄/O₂ RF plasmas. A preliminary set of exploratory experiments again indicated a strong enhancement in SiO₂ etching rate with increasing magnetic field. For example, while the SiO₂ etching rate was 1100 Å/min with no magnetic field (500 W/ 100 mT/ 20 sccm O₂/ 50 sccm C₂H₂F₄), it jumped to 2200 Å/min with 75 G magnetic field, and to 2600 Å/min with 140 G magnetic field. To maximize SiO₂ etching rate, the magnetic field was fixed at 140 G for all experiments. There was a lot of noise in the plasma induced emission (PIE) and the quality of F actinometry was marginal. The exploratory experiments also indicated that C₂H₂F₄ was a much more polymerizing gas than C₂HF₅. Significant deposition was observed (even on SiO₂), even with as much as 5 sccm O₂ addition to 50 sccm C₂H₂F₄. This deposition also got enhanced at higher pressures.

Similar to C_2HF_5/O_2 experiments, the effects of Power, Pressure and O_2 flowrate on SiO_2 etching were investigated. The ranges for the experiments were — Power: 300-700 W, Pressure: 10-290 mT and O_2 flowrate: 4 to 20 sccm. The fixed conditions were — $C_2H_2F_4$ flowrate: 50 sccm, magnetic field: 140 G, and Ar flowrate: 2 sccm (for actinometry). The monitored variables were SiO_2 , polysilicon and photoresist etching rates, the electrical characteristics and F actinometry. The real power deposited in the plasma, as determined using the Comdel RPM-1, was again about 80% under all conditions.

The responses for the 24 design experiments generated on NNAPER were analyzed. It should be mentioned that visible polymer deposition was observed on the wafer for some runs. The oxide etching rate was set to a low value (100-200 Å/min) for the experimental points where deposition was observed. The abrupt drop seen in the SiO_2 etching rate involving O_2 flowrate is most probably a consequence of this. It is also worth mentioning that the SiO_2 etching rate continually decreased for the center point in the design matrix, as the experiments proceeded. The oxide etching rate for the center point at the beginning of the experiments was 3118 Å/min and had dropped to 2808 Å/min at the end. This drift was probably due to a modification in the chamber wall conditions due to polymer formation.

The quality of the model generated by NNAPER was not as good as for C_2HF_5 experiments. The test data R^2 were in the vicinity of 0.9 for both the oxide etching rate and RF voltage, as compared to 0.99 for the C_2HF_5/O_2 experiment. Test data R^2 values for polysilicon and photoresist etching rates, and F concentration were close to 0, indicating a poor model for their functional dependence. Thus these responses were not analyzed on NNAPER. Due to low test data R^2 and the method for adjusting the oxide etching rate for the points where deposition was occurring, the interpretation of the model results can be qualitative at best, and quantitative interpretations should be made with caution. The model predicted functionalities are discussed below.

Fig 3-10 shows the saturation in SiO_2 etching rate with O_2 addition, similar to behavior observed with C_2HF_5 . Again increasing pressure decreases the SiO_2 etching rate, but the effect is substantially mitigated for higher O_2 additions. O_2 flowrate in excess of 11 sccm does not seem to affect the SiO_2 etching rate significantly. Fig 3-11 shows the SiO_2 etching behavior as a function of Power and O_2 flowrate. The oxide etching rate increases almost monotonically with increasing power. The drop seen at low O_2 flowrates is caused by polymerization. The RF voltage also follows a similar trend, and all trends are analogous to those observed for $\text{C}_2\text{HF}_5/\text{O}_2$ experiments.

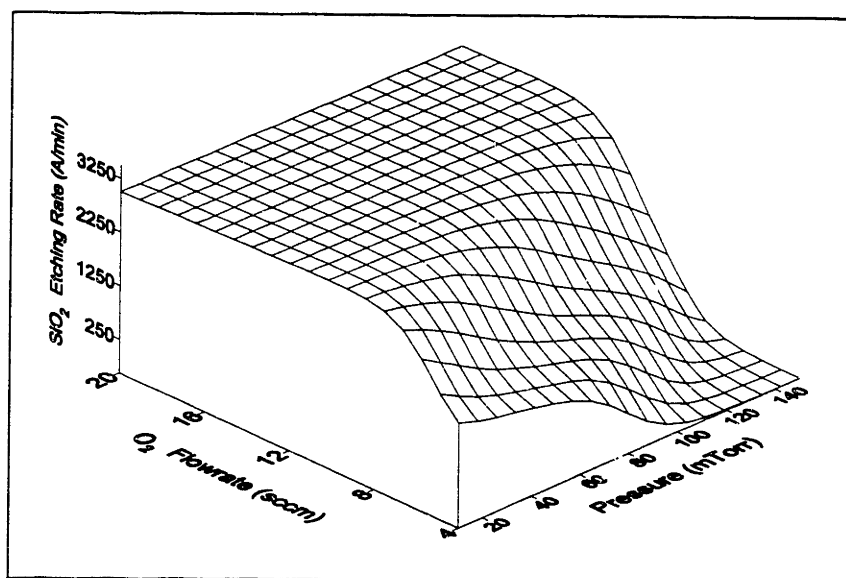


Figure 3-10: SiO_2 etching rate as a function of Pressure and O_2 flowrate. Fixed conditions for the plot: Power at 500 W and $\text{C}_2\text{H}_2\text{F}_4$ flowrate at 50 sccm.

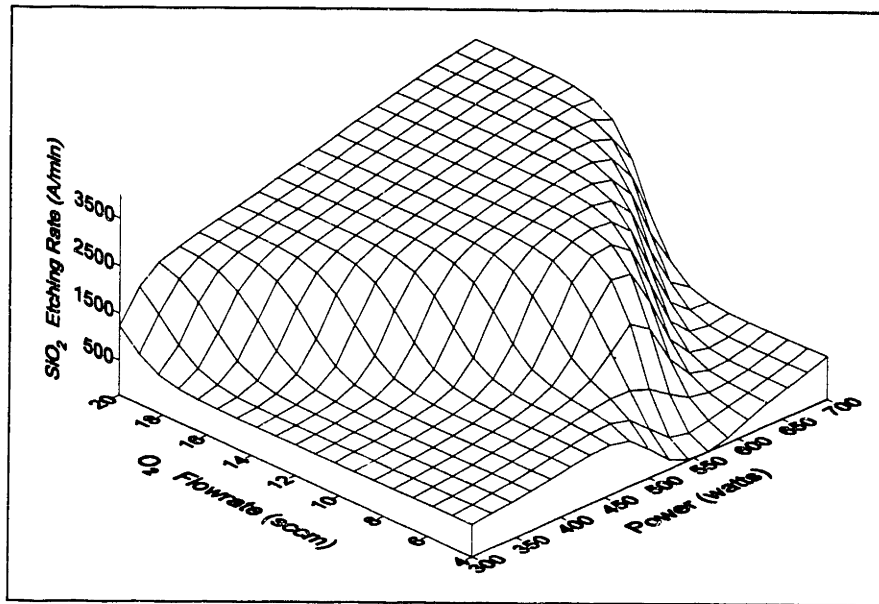


Figure 3-11: SiO_2 etching rate as a function of Power and O_2 Flowrate. Fixed conditions for the plot: Pressure at 80 mT and $\text{C}_2\text{H}_2\text{F}_4$ flowrate at 50 sccm.

To summarize the observed trends, SiO_2 etching rate seems to increase dramatically for O_2 additions of about 10 sccm to 50 sccm $\text{C}_2\text{H}_2\text{F}_4$, but minimal increase is seen with further addition. The SiO_2 etching rate also shows an increase with increasing power, and decreases with increasing pressure, especially at lower O_2 flowrates. The trends observed in oxide etching rate correspond closely to the trends in RF Voltage.

As mentioned previously, photoresist and polysilicon etching rates were also monitored during the design experiments. These etching rates were not analyzed using NNAPER due to poor model fits for the test data. In general, polysilicon etching rate was low (100-500 Å/min) for all the points except for those at lower pressures and high O_2 flowrates (17 sccm or more). This was mainly due to the excellent surface passivation by the CF_x polymerizing precursors. Higher pressures lead to an enhancement in the polymer deposition behavior of the plasma. Photoresist etching rate is generally in the range of 500-800 Å/min, but increases with O_2 flowrate, especially at lower pressures. In general, to get a high SiO_2 etching rate with good selectivity to polysilicon and

photoresist, a high power with moderate pressure and moderate O₂ flowrate is required. For example, SiO₂ etching rate for 615 W/ 50 mT/ 140 G/ 50 sccm C₂H₂F₄/ 9 sccm O₂ / 2 sccm Ar was 3600 Å/min with polysilicon etching rate being 100 Å/min, and photoresist etching rate being 250 Å/min. This corresponds to a selectivity of 36 to polysilicon and 14 to photoresist, both of which are superior to those observed for the commercial anisotropic vias recipe on the AME-5000.

3.2.4 C₂H₂F₄/Ar/O₂ Experiments

The results of the above set of experiments, and some additional exploratory runs were used to define the parameter space to be investigated. The design variables used were: Ar flow rate (0 to 50 sccm), O₂ flow rate (8-20 sccm), and pressure (20-140 mT). The fixed variables were nominal power (600 W), magnetic field (100 G) and C₂H₂F₄ flow rate (50 sccm). The response variables were SiO₂ etching rate, Polysilicon etching rate, Photoresist etching rate, F concentration (using actinometry), and electrical characteristics of the plasma. Similar to the C₂HF₅ experiments, the quality of F actinometry was poor, and thus was not fit in the model. The real power deposited into the plasma was about 80% under all conditions. Scanning electron micrographs of submicron gratings were taken at each point to characterize the etched profiles.

The responses — SiO₂ etching rate, polysilicon etching rate, photoresist etching rate and RF voltage — were again modeled on NNAPER. The number of hidden nodes was varied to optimize the model parameters. The 3-parameter 24-experiment design matrix consisted of 6 center point replicates to track the variability across the experimental run. Due to the extreme polymerizing nature of the plasma, large process variation (esp. for SiO₂ etching rate) were observed for the replicates over the course of the experiments. Consequently, even SiO₂ etching rate could not be fit with reasonable confidence using any network structure. Only polysilicon and photoresist etching rates could be fit with good confidence.

Both polysilicon and photoresist etching rates exhibit similar behaviors. The etching rates increase monotonically with O₂ addition, probably due to increasing F concentration. The etching rates also show a maxima along the pressure axis, with the maximum etching rate at about 50 mT for both polysilicon and photoresist. The etching rates initially increase with increasing Ar flow rates (probably due to increased ion bombardment), but decrease with further Ar addition. This decrease is probably a result of decreased F concentration at higher Ar flow rates due to a dilution effect.

Scanning electron micrographs of the etched profiles were also taken for each experimental condition. The dies were again cleaved after immersing in liquid nitrogen to preserve photoresist integrity, and the test pattern consisting of submicron gratings was observed under each condition. As for C₂HF₅/Ar/O₂ experiments, a wide variety of etched profiles were realized across the experimental domain. The quality of the sidewalls again was anywhere from ragged to smooth. Fig 3-12 shows one representative profile etched under different conditions. The bowing seen in Fig 3-12 is caused by photolithography errors. As representative numbers, under the conditions for Fig 3-12, SiO₂ etching rate was 2825 Å/min, selectivity to undoped polysilicon was 3, and selectivity to photoresist was 1.42.

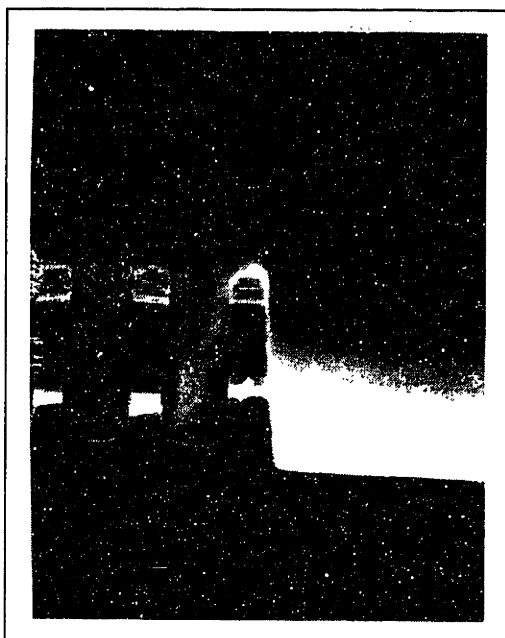


Figure 3-12: Profile Etched in $C_2H_2F_4/Ar/O_2$ mixtures. Conditions were: $C_2H_2F_4$ flowrate at 50 sccm, Ar flowrate at 25 sccm, O_2 flowrate at 14 sccm, Pressure at 70 mT, Power at 600W, and Magnetic Field at 100G.

3.2.5 C_2F_6/O_2 , C_2HF_5/O_2 and $C_2H_2F_4/O_2$ Comparative Experiments

PFCs like C_2F_6 are frequently used in conjunction with O_2 for cleaning chambers employed for SiO_2 (and tungsten) chemical vapor deposition (CVD). Typical commercial cleaning recipes for oxide CVD chamber use 1000 sccm each of C_2F_6 and O_2 at pressures of several torrs and powers on the order of 1 kW. Although these conditions could not be emulated in the Precision 5000 etcher, it was still felt that a comparative study investigating SiO_2 etching rates in C_2F_6/O_2 , C_2HF_5/O_2 and $C_2H_2F_4/O_2$ plasmas would be useful to gauge the applicability of C_2HF_5 and $C_2H_2F_4$ to chamber cleaning. For the purposes of this limited investigation, the fluorocarbon flow rate was fixed at 50 sccm, the power at 750 W nominal, pressure at 100 mT and the magnetic field at 0 G (i.e. no magnetic field). Oxygen was added in increasing amounts to the fluorocarbon, and the SiO_2 etching rate was monitored on a wafer using laser interferometry.

Fig 3-13 depicts the SiO₂ etching rate behavior for different gases, as a function of O₂ addition. While SiO₂ etching rate decreases monotonically with O₂ addition to C₂F₆ (from 3325 Å/min at no O₂ to 2700 Å/min at 30 sccm O₂), it increases significantly for initial O₂ addition to both C₂H₂F₄ and C₂HF₅ and then decreases again. SiO₂ etching rate in C₂F₆/O₂ is about 3 times that in C₂H₂F₄/O₂ at 5 sccm O₂ addition, and about twice the rate at higher O₂ additions (10 sccm and above). Correspondingly, the oxide etching rate in C₂F₆/O₂ mixtures is about 1.2 to 1.4 times the oxide etching rate in C₂HF₅/O₂. Of course these rates are under conditions significantly different from CVD chamber conditions, and apply to oxide which is under significant ion bombardment.

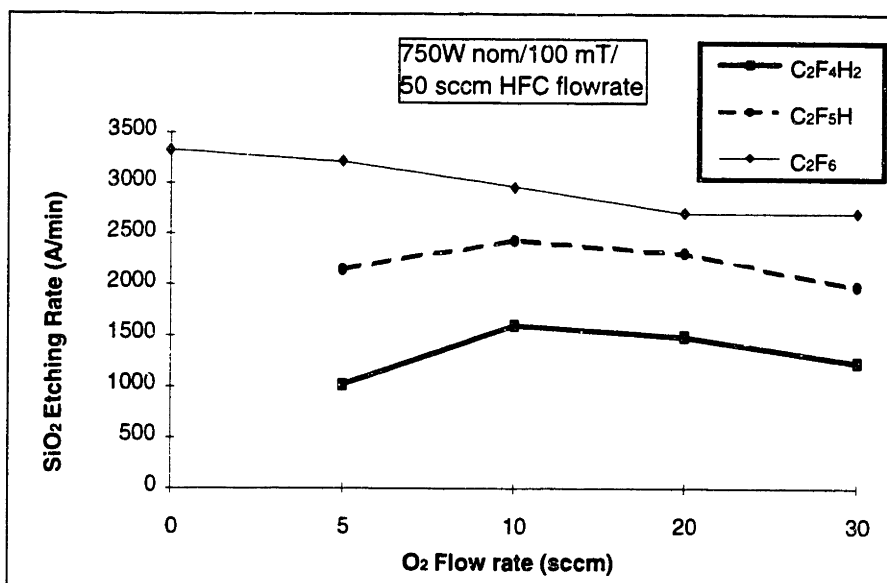


Figure 3-13: Comparison of SiO₂ etching in C₂F₆/O₂, C₂HF₅/O₂ and C₂H₂F₄/O₂ mixtures for potential CVD chamber clean application.

3.3 Conclusions

The parametric dependence of SiO₂ etching rate on power, pressure and O₂ flowrate has been characterized in C₂HF₅/O₂/Ar and C₂H₂F₄/O₂/Ar RF plasmas in a commercial reactor. C₂H₂F₄ was found to be a much more "polymerizing" than C₂HF₅. A significant enhancement in oxide etching rate was seen for both gases with O₂ addition,

but the enhancement saturated at higher flowrates. A dramatic increase in SiO₂ etching rate was also observed for both gases in the presence of magnetic field. High oxide etching rates (~ 4000 Å/min) were realized for both gases with good etching selectivity to polysilicon and photoresist.

This part of the thesis work indicates that C₂HF₅ and C₂H₂F₄ are viable as potential replacement gases for conventional PFCs like C₂F₆ and CF₄, both for anisotropic etching of patterned oxide features and for use in CVD chamber cleaning recipes. Significant process development and characterization would have to be undertaken before these gases can be routinely used for etching and cleaning. The parameter space investigated in the current study would provide a good starting point for further process development (Mohindra *et al.*, 1994).

Chapter 4: Kinetics of PFC Consumption: Characterization of CF₄ Etching of SiO₂

The first part of this thesis dealt with the possibility of using hydrofluorocarbons (HFCs) instead of PFCs as process gases. However, blanket PFC substitution is not possible in the short term. For the processes where substitution is infeasible, another approach would be to reduce the PFC usage in the process. This reduction can either be achieved experimentally (*e.g.* using designed experiments and response surface methodology), or via the use of a model. The model would consist of a reactor flow model incorporating the plasma physics, coupled to the gas phase kinetics and surface kinetics. Researchers have recently started to create such models (Mantzaris *et al.*, 1995). Of course, a prerequisite to such a model is the availability of the gas phase chemical kinetics model and the surface kinetics model.

The second part of this thesis deals with the characterization of plasma gas phase kinetics for a PFC etch process. The model system studied was CF₄ etching of SiO₂. This system was selected due to the wide use of CF₄ as a process gas for SiO₂ etching. As shown in Fig 1-1 CF₄ has an extremely long lifetime (>50,000 years), and a substantial global warming potential. Therefore a reduction in its use is highly desirable.

The technique used for characterizing the kinetics was the plasma RF power modulation technique, pioneered in our lab by Linda Kiss. A study carried out by Kiss and Sawin (1992a) had characterized the gas phase kinetics of a CF₄ plasma in the absence of any substrate. One goal of this thesis was the characterization of a commercial process. Therefore a CF₄ plasma in the presence of a substrate was characterized. The first step in this characterization was to repeat the experiments of Kiss with CF₄ in the absence of a substrate. Then the system complexity was increased by the addition of O₂ to the gas mixture. Finally, SiO₂ was added to the system in the form of a quartz wafer placed on one

of the electrodes. The plasma chemistry was characterized and compared for each of these cases.

4.1 Experimental Setup

An attempt was first made to characterize the CF_4 etching of SiO_2 in an industrial reactor - the Applied Precision 5000 etcher. However, poor optical access and low signal-to-noise frustrated that effort. Subsequently, another reactor (referred to here as the “Modulation Reactor”) was constructed for this study. This reactor consisted of two parallel electrodes separated by a quartz shell which formed the reactor wall. The reactor design allowed for a well-confined plasma (which facilitates the analysis), and ready optical access for the purpose of sampling plasma emission. The setup and the RF power modulation methodology are discussed in greater detail in Chapter 2.

All the experiments described in this chapter were carried out in a 3" symmetric reactor configuration, which means both the electrodes were 3" in diameter. The gap spacing was fixed at 1 cm, which is same as in the work of Kiss. Smaller electrodes and a small gap allowed us to achieve power densities similar to those found in commercial reactors using the limited output from the RF generator. Table 4-1 compares the experimental conditions for this work with those of Kiss.

Table 4-1: Comparison of Experimental Conditions for this work with that of Kiss

Parameter	Experiments of Kiss	This Work
Reactor Geometry	Parallel Plate	Parallel Plate
Electrode Material	Anodized Aluminum	Anodized Aluminum with SiO ₂ ^a
Feed Gas	CF ₄ , with 5% Ar	CF ₄ or CF ₄ +O ₂ , with 5% Ar
Pressure	500 mT	500 mT or 400 mT
Frequency	13.56 Mhz	13.56 MHz
Residence Time	20 ms and 200 ms	20 ms and 1.23 s
Electrode Separation	1 cm	1 cm
Nominal Power/Volume	0.81 W/cm ³	0.58 W/cm ³
Estimated Temperature	313 K ^b	313 K ^b
Electron Density	6x10 ⁸ cm ⁻³	6x10 ⁸ cm ^{-3c}

^a Experiments with CF₄ and CF₄+O₂ used Anodized Aluminum.
CF₄+SiO₂ experiments had a quartz wafer bonded on the bottom electrode

^b Both estimated

^c Assumed to be same as Kiss

As seen in the table, the basic setup was very similar. The main differences are in the feed gas composition, electrode material and the range in residence time.

Plasma induced emissions (PIE) was sampled using a 0.27m monochromator and UV lens optical setup, and actinometry was carried out by dividing the species waveforms by Ar waveforms. The species observed for the CF₄ and CF₄+SiO₂ system were F and CF₂. With the addition of O₂ to CF₄, CF₂ could no longer be detected; instead F and O were observed. The experiments were carried out at various modulation frequencies ranging from 0.25 Hz to 100 Hz. The actinometrically processed waveforms were analyzed in the frequency domain, and transfer functions were constructed for each species. Both Nyquist and Bode plots were generated for all the species, but only Bode plots are shown here. Each experiment generates multiple data points since the square wave modulation used consists of multiple fourier harmonics. Only the first two harmonics were used in the Bode plots, since the signal-to-noise becomes unacceptable for the higher harmonics.

4.2 Results and Discussion

As mentioned above, a stepwise approach was taken to characterize SiO₂ etching in CF₄. First the experiments with CF₄ alone (with anodized aluminum electrodes) were carried out. Then O₂ was added to CF₄ (40% O₂), and the responses re-analyzed. The fraction of O₂ was deliberately high to highlight the difference in CF₄ chemistry from CF₄+O₂ chemistry. Lastly, a quartz (SiO₂) wafer was placed on the bottom electrode and the responses analyzed while it etched in pure CF₄. The results from these three sets of experiments are shown below.

The work of Kiss showed that while the species generation was governed by gas phase reactions, the losses are driven by surface reactions. Therefore the first step was to test the sensitivity of the observed responses to the surface conditions. Fig 4-1 shows the Bode plot for the case where different electrode materials were used in the reactor. It is obvious that the response for F is different for the two electrodes. Before quantitative numbers can be derived, it is useful to review the underlying theory. This theory is summarized directly from Kiss (1992d).

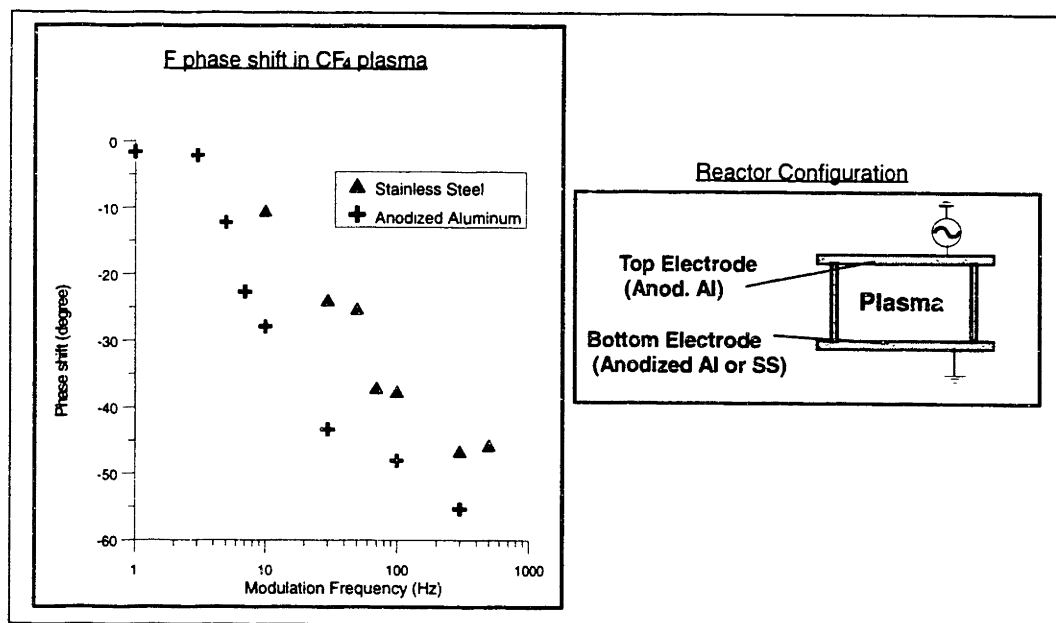


Figure 4-1: Effect of electrode material on characteristic breakpoint frequency

The Bode plot is a semi-log plot with the x-axis being the \log_{10} of the modulation frequency, and y-axis being the negative of the phase between the species and Ar waveform. Since the Ar waveform is assumed to track the electron density (see Section 2.2.1 of this thesis), the y-axis really depicts the phase between the species (response) and the electron density (perturbation). If all the species losses are assumed to be lumped into a first order loss mechanism, the characteristic breakpoint frequency of the Bode plot is indicative of this first order homogeneous loss rate coefficient for that species. Since the primary loss mechanism for the species of interest is the surface loss (Kiss and Sawin, 1992a), the breakpoint frequency is related to the surface loss rate coefficient k_{surf} , which can in turn be used to calculate the sticking probability γ of that species on the surface. If the surface reaction is taken to be characterized by a Boltzmann flux to the surface and then a reaction probability on that surface, then the surface loss coefficient k_{surf} can be written as

$$k_{surf} = \frac{\gamma |\bar{v}|}{4} \quad (4-1)$$

where $|\bar{v}|$ is the mean speed (Sawin and Reif, 1995) of the molecules and is given by the relation

$$|\bar{v}| = \sqrt{\frac{8k_B T}{\pi m}} \quad (4-2)$$

where k_B is the Boltzmann constant, T is the temperature and m is the mass of the molecule. This surface loss rate can be converted to a homogeneous loss rate k_L by multiplying it by the area (A) to volume (V) ratio

$$k_L = \frac{A}{V} k_{surf} \quad (4-3)$$

This homogeneous loss rate is experimentally determined from the breakpoint frequency f_B as

$$k_L = 2\pi f_B \quad (4-4)$$

and thus the sticking coefficient (or probability) γ can be calculated from the relation

$$\gamma = 2\pi k_L \frac{4V}{|v|A} f_B \quad (4-5)$$

From the Bode plot in Fig 4-1 it can be seen that the curve for stainless steel electrodes (SS) lies to the right of that for anodized aluminum (AA). Therefore, the breakpoint frequency is higher for SS than for AA, and so is the sticking coefficient for F. The sticking coefficient for F on SS is calculated to be 0.012, while it is 0.005 on anodized aluminum electrode. Thus while 1 out of every 80 F radicals recombines (and is lost) on the SS surface, only 1 in 200 is lost on the anodized aluminum surface. This sensitivity of loss rates to surface conditions was also observed by Kiss and Sawin (1992a). Fig 4-1 captures the sensitivity of this technique to the surface conditions.

Fig 4-2 shows the effect of adding O₂ to CF₄. The fraction of O₂ in the feed gas was 40%. The Bode plot for F shows a significant shift in the curve towards lower frequencies when O₂ is added. The F sticking coefficient calculated from the curves in CF₄ alone (over AA electrodes) was 0.012, while that in presence of O₂ is 0.001. This dramatic decrease in F recombination rate is due to some surface modification caused by O₂ addition. One important implication of the observed behavior is that O₂ addition to C_xF_y type gases not only affects the etchant (F) generation in the gas phase (probably via the reaction of C_xF_y with O to liberate F), but it also affects the surface loss rate. Therefore the traditional view attributing the change in etching behavior with the addition of O₂ on gas phase species generation alone is incomplete.

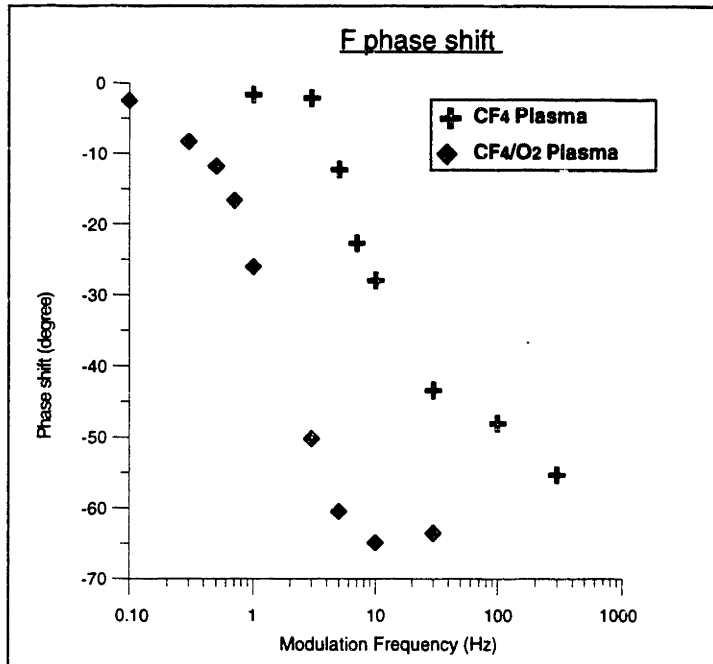


Figure 4-2: Bode plot depicting the effect of adding O_2 to CF_4

The effect of placing an SiO_2 wafer on the bottom electrode is shown in Fig 4-3. The upper electrode in this configuration is anodized aluminum. The figure shows that the F loss rate increases when SiO_2 wafer is placed on the electrode. It is important to distinguish that in the presence of SiO_2 , F is indeed lost to a surface reaction instead of merely recombining on the surface to form other species. The effective sticking probability increases back to 0.015 when SiO_2 is placed on the electrode. This increase in loss rate in the presence of SiO_2 is consistent with other experiments (Gray, 1992; Butterbaugh *et al.*, 1991) which show that the sticking probability of reacting species like F on reacting materials (Si, SiO_2) increases in presence of ion bombardment. The quartz wafer placed on the electrode in this case is also under significant ion bombardment.

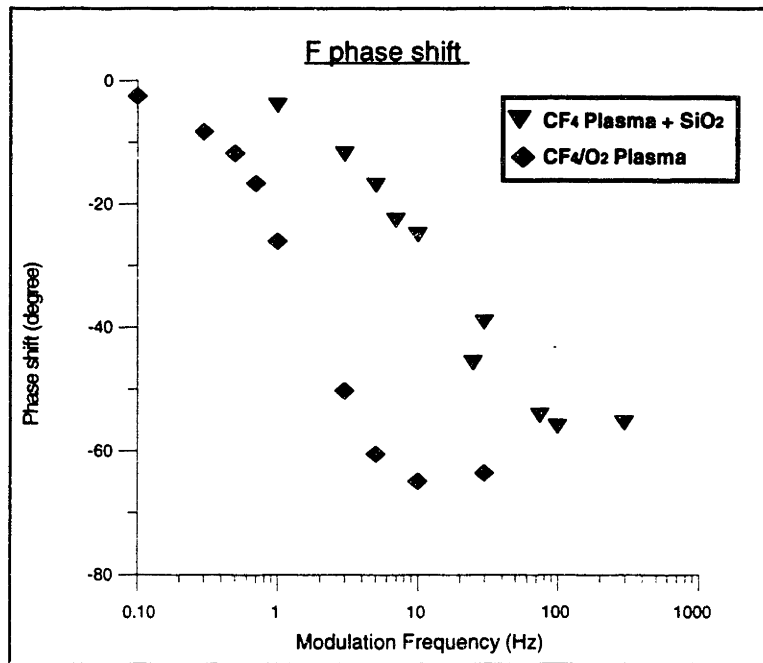


Figure 4-3: Effect of placing SiO_2 wafer on one of the electrodes

The Bode plot in Fig 4-4 shows the change in F loss rate with a change in residence time. The experiment was carried out in the presence of a quartz wafer on the lower electrode. The sticking coefficient decreases from 0.012 at lower residence time (higher flowrate) to 0.001 at higher residence time (lower flowrate). Since the losses are primarily surface driven, the change in residence time leads to a surface modification which decreases the loss rate. One such mechanism could be increased gas fragmentation at higher residence times to form CF_x species which lead to polymeric deposition on the electrode (Bariya *et al.*, 1991). Another cause of surface modification could be an increase in the product concentration in the gas phase, which could in turn re-deposit on the surface from the plasma.

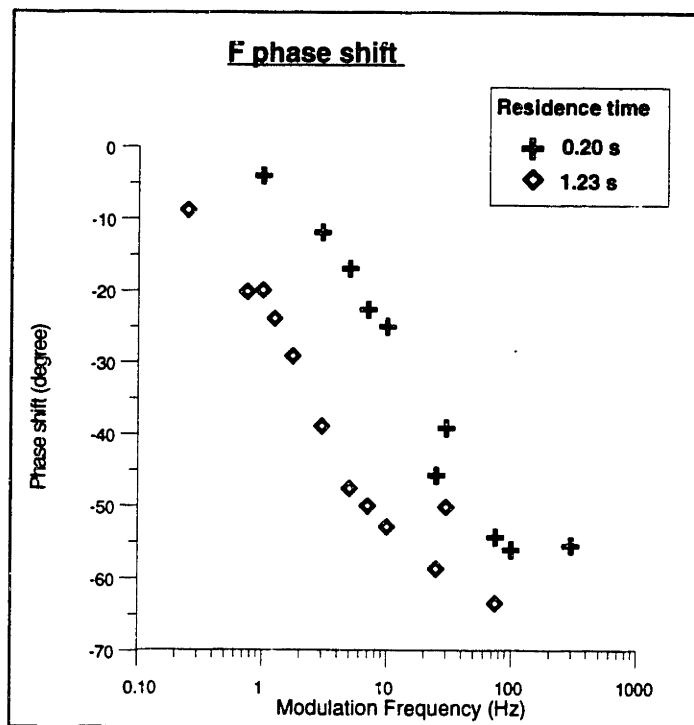


Figure 4-4: Effect of changing residence time in the reactor

There are two implications of the data in Fig 4-4. First, a reduction in PFC consumption cannot be achieved simply by cutting down the flowrates to economize on the gas usage. This is because a change in process parameters not only affects the generation rate of species (in the gas phase), but also the loss rates by modifying the surfaces. The second implication of the data is that chemical kinetics models being used by researchers cannot be taken as invariant. It is very important to use the chemical kinetics data measured under similar conditions to those being modeled.

4.3 Reactor Modeling

The dominant gas phase chemical kinetics is determined by comparing the experimentally observed transfer function with that generated from the postulated mechanism. To compare the experimental data from section 4.2 to a model, the modulation reactor was modeled as a well mixed reactor. The use of a well mixed reactor

(or a CSTR — a Continuously Stirred Tank Reactor) for a plasma system is justified under three conditions:

- $Pe \rightarrow 0$
- $Da_s \rightarrow 0$, and
- Penetration time scale for species be much smaller than kinetic time scales

The Peclet Number Pe is defined as

$$Pe = \frac{v}{(D_{AB} / \ell)} \quad (4-6)$$

where v is the convective gas velocity, D_{AB} is the diffusivity of component A in B and ℓ is the length scale for diffusion. In words, Pe is the ratio of the convective velocity to diffusion velocity. A well mixed reactor is characterized by $Pe \rightarrow 0$ (diffusion is much faster than convection and smears out any concentration gradients due to flow), while a system with $Pe \rightarrow \infty$ is classified as a plug flow reactor or PFR.

When a system has surface reactions, the evaluation of Pe is no longer adequate. Another dimensionless number, Damköhler number or Da_s , also has to be evaluated. The Da_s is defined as

$$Da_s = \frac{k_{surf}}{(D_{AB} / \ell)} \quad (4-7)$$

where k_{surf} is the surface reaction rate for a first order heterogeneous reaction. The system is considered well mixed when there are no surface reaction induced concentration gradients in the reactor. Therefore, when $Da_s \rightarrow 0$ the reaction controls the loss of species, and the system can be regarded well mixed. Similarly, for $Da_s \rightarrow \infty$ the system is characterized as a PFR.

Whenever the generation of the species in the reactor is spatially non-uniform, the evaluation of Pe and Da is no longer sufficient to characterize a reactor. The penetration time, which is the time required by the system to reach a new steady state after a perturbation, also has to be considered. If the penetration time scale is smaller than the kinetic time scale, then reaction controls the loss of species and a well mixed reactor model can be used. The analysis by Kiss (1992d) was used to calculate the penetration time scales for this system. As an extremely simplified case, all the generation was assumed to take place at the bulk-sheath interface. The penetration time T under such conditions is given by the equation

$$T = \frac{1}{\lambda_n^2 D} \quad (4-8)$$

where D is the diffusivity and λ_n are the characteristic roots given by the equation

$$\lambda_n \tan\left[\left(\frac{\ell}{2}\right)\lambda_n\right] = \frac{k_{surf}}{D}, \quad n = 0, 1, 2, \dots \quad (4-9)$$

Since λ_0 represents the slowest response of the system, the penetration time needs to be evaluated only for λ_0 . This time can be calculated for each species of interest and compared with its dominant kinetic rate to determine if the well mixed reactor assumption is justified.

All three quantities Pe , Da_s and T were evaluated for our system to confirm that the CSTR model could be used for modeling the transfer functions. The diffusivities were evaluated using the Chapman and Enskog equation (Reid *et al.*, 1977), which uses the Lennard-Jones potentials. The Pe calculated for all species were less than 0.02 under all conditions of pressure and flowrate, indicating that there are no diffusion related concentration gradients. The Da_s were calculated using the sticking coefficients found from the experiments. Taking the lengthscale as half the gap spacing, the maximum Da_s was about 0.5 (for CF_2), indicating that some concentration gradients might exist for CF_2 .

This assumes that the primary non-uniformity is due to the surface loss at the electrode. Most of the concentration gradient in these plasmas is confined to the sheaths. Therefore the more appropriate lengthscale for Da_s computation is the sheath width. The Da_s using the sheath width as the length scale were all less than 0.1, indicating that the reactor has negligible concentration gradients due to surface reactions. The penetration time scales T were calculated for all species at around 3-5 ms. The kinetic time scales assuming the maximum sticking probability observed (0.012) were also around 2-4 ms. Although these two are similar, the penetration time scales were calculated assuming a delta production function at the bulk-sheath interface. This assumption is likely to be mitigated in an actual reactor, leading to the penetration timescales being smaller than kinetic time scales. Therefore, the transfer functions were generated using the CSTR model for the reactor.

The reaction network used for CF_4 etching of SiO_2 is shown in Table 4-2. Only seven reactions were considered - four electron impact reactions for production of species and three surface loss reactions. The rate constants for the electron impact reactions were taken from literature. The loss rates for F and CF_2 were determined experimentally using the breakpoint frequency from the Bode plots. SiO_2 etching was assumed to occur in the CF_3^+ ion flux limited regime (true for a high-pressure low-density plasma, Gray 1992), and the reaction rate was taken as the surface loss rate of CF_3^+ . This loss rate is estimated using the Bohm sheath criteria (Chapman, 1980) and is given by

$$k_{Bohm} = \frac{A}{V} 0.6 \sqrt{\frac{kT_e}{m_{CF_3}}} \quad (4-10)$$

where T_e is the electron temperature (assumed to be 4.5 eV for this work), k is the Boltzmann constant and m_{CF_3} is the mass of a CF_3 molecule, A is the area of the electrodes and V is the volume of the reactor.

Table 4-2: Reaction Network used for modeling CF₄ Etching of SiO₂

Reaction	Rate	Comments
$\text{CF}_4 \xrightarrow{e^-} \text{CF}_3 + \text{F}$	$20\text{s}^{-1} \frac{[\text{e}^-]}{[\text{e}^-]_0} \frac{1.2}{4.2}$	a
$\text{CF}_4 \xrightarrow{e^-} \text{CF}_2 + 2\text{F}$	$20\text{s}^{-1} \frac{[\text{e}^-]}{[\text{e}^-]_0} \frac{3}{4.2}$	a
$\text{CF}_3 \xrightarrow{e^-} \text{CF}_2 + \text{F}$	$20\text{s}^{-1} \frac{[\text{e}^-]}{[\text{e}^-]_0}$	a
$\text{CF}_4 \xrightarrow{e^-} \text{CF}_3^+ + \text{F} + e^-$	$1.2 \times 10^{-12} \text{ cm}^3 / \text{s}$	b
$\text{F} \xrightarrow{\text{wall}} \text{loss}$	γ_{F}	c
$\text{CF}_2 \xrightarrow{\text{wall}} \text{loss}$	γ_{CF_2}	c
$\text{SiO}_2 + 2\text{F} + \text{CF}_2 \xrightarrow{k_{\text{CF}_3^+}} \text{SiF}_4 + 2\text{CO}$	k_{Bohm}	d

^a Plumb and Ryan (1986). Branching ratios for the two reactions adjusted for the absence of CF in the model. The unimolecular rate is adjusted for the electron density for Plumb and Ryan. $[\text{e}^-]_0 = 6 \times 10^{10} \text{ cm}^{-3}$ and $[\text{e}^-]$ for this work = $6 \times 10^8 \text{ cm}^{-3}$ (same as Kiss, 1992a).
^b Stephen *et al.* (1985)
^c From experiments
^d Bohm Criteria (Chapman 1980)

The approach described in Kiss (1992a) is used to generate the transfer functions for comparison with experiments. This approach is briefly described below. The well mixed reactor can be modeled by the equation

$$\frac{d[j]}{dt} = \frac{1}{\tau} ([j]_0 - [j]) + \sum_l \sum_{m \geq l} \nu_{lm} k_{lm} [l][m] + \sum_l \nu_l k_l [l] \quad (4-11)$$

where $[j]_0$ is the feed concentration of species j , $[j]$ is the instantaneous concentration of species j , k_{lm} are the reaction rates for second order reactions involving species l and m , and ν_{lm} are the corresponding stoichiometric coefficients for the second order reactions. The first order analogues of k_{lm} and ν_{lm} are k_l and ν_l respectively.

The transfer functions are developed by linearizing the flow and reaction terms using the perturbation variable

$$[j]_{(t)} = [\bar{j}] + \Delta[j]_{(t)} \quad (4-12)$$

where $[j]_{(t)}$ is the instantaneous concentration of j , $[\bar{j}]$ is the steady state concentration and $\Delta[j]_{(t)}$ is the instantaneous perturbation to the concentration. The flow and reaction problem thus reduces to

$$\frac{d\Delta[j]}{dt} = -\frac{1}{\tau}(\Delta[j]) + \sum_l \sum_{m \geq l} v_{lm} k_{lm} ([\bar{l}][\Delta m] + [\bar{m}][\Delta l]) + \sum_l v_l k_l [\Delta l] \quad (4-13)$$

The steady state values $[\bar{l}]$ and $[\bar{m}]$ are determined by setting the time derivative in equation to 0. The linear perturbation equation, Eqn 4-13, is transformed to the frequency domain and written as

$$i\omega[\hat{j}] = -\frac{1}{\tau}[\hat{j}] + \sum_l \sum_{m \geq l} v_{lm} k_{lm} ([\bar{l}][\hat{m}] + [\bar{m}][\hat{l}]) + \sum_l v_l k_l [\hat{l}] \quad (4-14)$$

where $[\hat{j}]$ is the complex frequency domain concentration of species j . This equation can be rearranged to generate the transfer function for the relaxation of species j to the modulation in electron density $[e^-]$:

$$\frac{[\hat{j}]}{[e^-]} = \frac{\sum_{l \neq j} \sum_{m \neq j} v_{lm} k_{lm} [\bar{l}] \frac{[\hat{m}]}{[e^-]} + \sum_{l \neq j} (v_l k_{lj} [\bar{j}] + v_l k_l) \frac{[\hat{l}]}{[e^-]}}{\frac{1}{\tau} + \sum_m v_{jm} k_{jm} [\bar{m}] + v_j k_j + i\omega} \quad (4-15)$$

This equation can be used to generate transfer functions either analytically or numerically.

Equation 4-15 was used to generate the transfer functions numerically for the reaction network shown in Table 4-2. The modeled transfer function is compared to the experimental data points in Fig 4-5. As can be seen in the figure, the modeled transfer

function closely matches the experimentally observed one. Therefore the simple reaction network proposed for SiO_2 etching adequately captures the dominant plasma chemical kinetics.

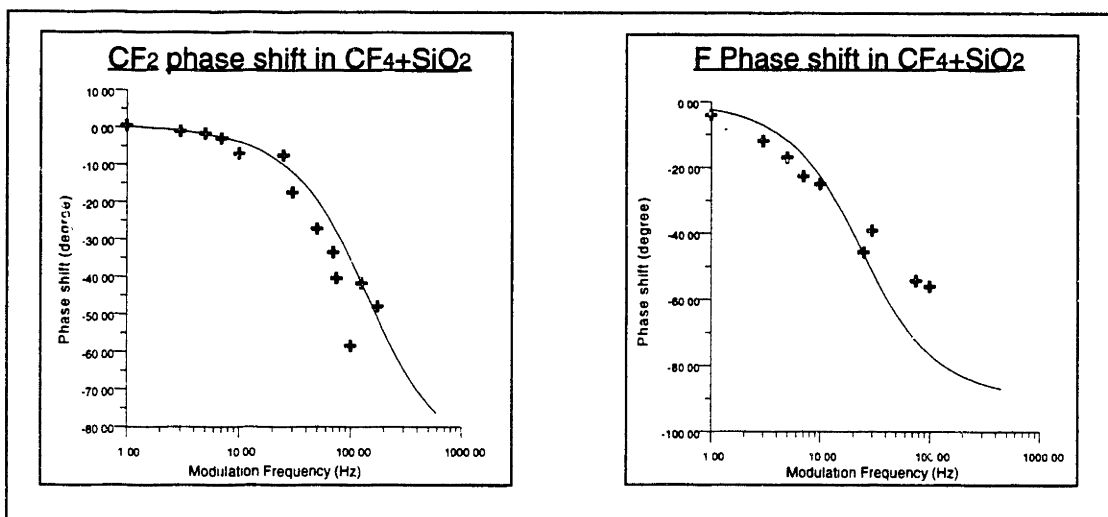


Figure 4-5: Comparison of transfer functions from experiments and model for SiO_2 etching with CF_4

4.4 Conclusions

This part of the thesis was involved with elucidating the mechanism of the consumption and subsequent emission of a PFC (CF_4) during a process (SiO_2 etching). The experiments indicate that a simple reduction in the PFC flowrate (and therefore consumption) not only changes the species generation mechanism, but also alters the species loss rates by affecting the surface. Therefore chemical kinetics has to be characterized for specific process conditions before any models can be used to optimize the processes. Lastly this part of the thesis explained the dominant chemical kinetics of SiO_2 etching with CF_4 using seven elementary reactions.

Chapter 5: Kinetics of C₂F₆ Abatement

5.1 Introduction

Hexafluoroethane (C₂F₆) is used in VLSI fabrication for plasma etching and PECVD chamber cleans. PECVD (silicon dioxide, silicon nitride, silicon oxynitride and tungsten) chamber cleans account for about 95% of C₂F₆ use while etching accounts for the rest. Although consumption varies in different processes, it is estimated that 70-80% of the feed gas passes through the whole process unreacted (Ridgeway *et al.*, 1995). The exhaust gases are chemically scrubbed before being vented to the atmosphere. The chemical scrubber efficiency is dependent on the components of the process exhaust, and the scrubber may not completely remove all of the unreacted PFC. This unscrubbed C₂F₆ reaches the atmosphere and raises the overall PFC level.

As mentioned in Chapter 1 of this thesis, there are three approaches to mitigating the impact of PFCs - substitution, recovery and optimization, and abatement. This chapter considers the last option - destructive abatement. There are various approaches to abatement *e.g.* combustion, chemical-thermal abatement and plasma assisted abatement (Mocella *et al.*, 1994; Mocella, 1995). Of these, combustion and chemical-thermal systems operate on post-pump effluent, a significant fraction of which is N₂ used as pump purge. This feed dilution increases the cost of effluent treatment. In addition to the high cost, another drawback of these systems is that the purge N₂ can react with the O₂ present in the feed (*esp.* for PECVD chamber cleans which typically use 50:50 mix of C₂F₆ and O₂) to generate NO_x which are pollutants in their own right. The plasma unit discussed in this chapter, in contrast, operates upstream of the pump thereby eliminating the dilution and potential NO_x formation problem. This is similar to the surface wave based plasma abatement unit (Arno *et al.*, 1995) which also operates before the pump. This chapter

outlines the characterization of a microwave plasma based unit, and addresses some issues for the manufacture of a commercial unit.

5.2 Preliminary Experiments

After the promising results for PFC substitution by HFCs for SiO₂ plasma etching (see Chapter 3), an attempt was made in industry to use the HFCs for CVD chamber cleans. However, all these attempts were unsuccessful due to significant loss of chamber cleaning rate, which led to an unacceptable increase in the clean time. After this failure, it became clear that a blanket PFC substitution might not be possible, at least in the short run. Similarly, the possibility of reclaiming unreacted C₂F₆ from the exhaust remains to be commercially demonstrated. Even if the technology for reclamation could be perfected, it was recognized that prohibitive re-plumbing costs would make it an uneconomical option for existing IC fabrication facilities. At this point, we turned our attention to the possibility of destructive abatement using microwave plasmas. A plasma based unit had the potential to be economical, both in terms of fixed and variable costs. In addition, if the unit worked, it could be designed with a footprint small enough that it could be placed after each tool, thereby eliminating the plumbing problems.

Some initial experiments were carried out using a 0.25" diameter tubular McCarrol microwave cavity (Mocella *et al.*, 1994). Subsequently, experiments were also carried out in a 1" tubular quartz reactor. These experiments achieved greater than 95% abatement for C₂F₆, indicating that the plasma based technology had potential. The results indicated that C₂F₆ abatement varied inversely with residence time in the reactor, almost linearly with microwave power input, and seemed to work best for a 50:50 mixture of O₂ and C₂F₆. The other two additive gases studied, H₂ and NH₃, did not aid abatement and merely acted as diluents. The tubular quartz reactor used for the experiments etched away with use, and it was thought that the main mechanism for C₂F₆ abatement was probably the scavenging of the F by SiO₂ to form SiF₄. A preliminary

material balance taking into account the amount of SiO_2 consumed and total C_2F_6 abated, and assuming SiF_4 to be the main product failed to account for all F. Less than one-tenth of all F disappearing from C_2F_6 (corresponding to its abatement) could be accounted for by the formation of SiF_4 . To test the hypothesis that quartz was unimportant to the abatement mechanism, an alumina (ceramic) reactor was used instead of quartz. It gave similar abatement to that obtained in the quartz reactor. Since a reactor that does not get consumed in the process is much more desirable than one that does, all subsequent experiments were carried out using an alumina reactor.

5.3 Parametric Dependence of C_2F_6 Abatement

5.3.1 Design Experiments

The first step towards the understanding of C_2F_6 abatement in the microwave tubular reactor was the characterization of abatement as a function of different parameters. Therefore an experimental design was constructed using NNAPER. The design variables were Total flowrate (400-1200 sccm), Power (300-700 W) and Pressure (4-8 torr). The flowrate regime was picked to represent typical industrial flowrates from C_2F_6 CVD chamber cleaning recipes. The pressure was also picked to reflect the pressures used in industry, with the minimum being dictated by the pumping capacity. The power was limited by the microwave power supply. Based on the preliminary experiments, the $\text{O}_2:\text{C}_2\text{F}_6$ ratio was fixed at 50:50 for all experiments. All experiments were carried out in the abatement reactor described in Chapter 2. The standard ASTeX applicator (without annular air cooling) was used to couple the power into the reactor. The C_2F_6 abatement was computed from the difference in the C_2F_6 peak areas when the plasma was off and when it was on, using the MTI portable P200 gas chromatograph (GC). The process effluent was scrubbed in a countercurrent water scrubber before injection into the GC. Unless otherwise mentioned, the effluent was always water scrubbed prior to injection whenever a GC or GC/MS was used.

The results from the design experiments are depicted in Fig 5-1 and Fig 5-2.

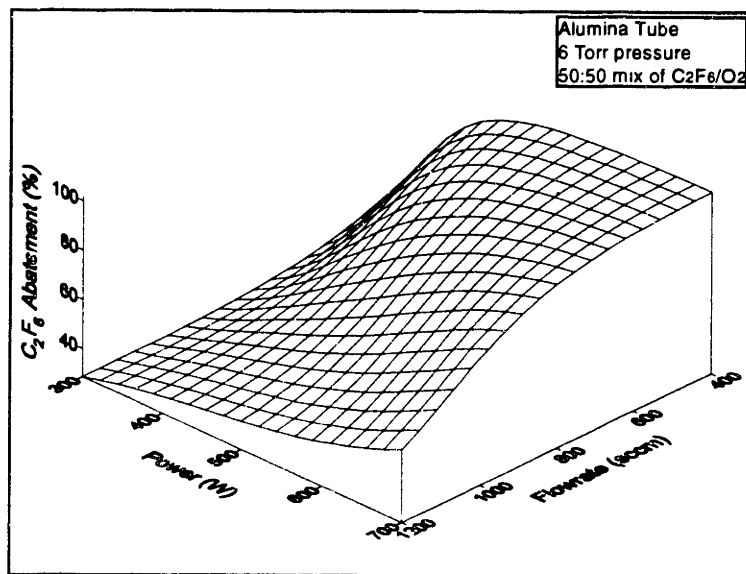


Figure 5-1: C₂F₆ Abatement in the microwave tubular reactor as a function of Power and Flowrate. Fixed conditions for the plot: Pressure at 6 torr and C₂F₆:O₂ ratio 1:1

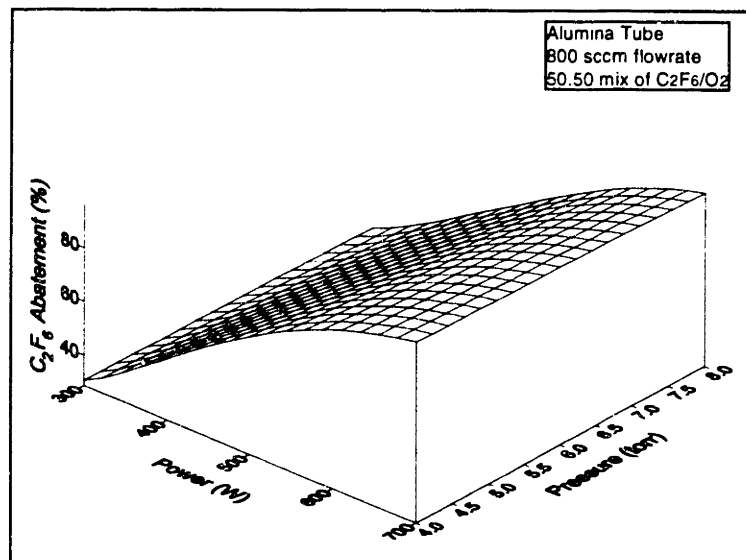


Figure 5-2: C₂F₆ Abatement in the microwave tubular reactor as a function of Power and Pressure. Fixed conditions for the plot: Flowrate at 800 sccm and C₂F₆:O₂ ratio 1:1

As indicated in the figures, high C_2F_6 abatement was obtained especially at low flowrates and high powers. There was a saturation effect in power at lower flowrates. However, at higher flowrates, the abatement scaled linearly with power. This suggests that a critical parameter for abatement is power deposition per C_2F_6 molecule. Fig 5-1 also shows that abatement falls off as the flowrate increases (or equivalently, as the residence time decreases). Also, pressure does not have an impact on abatement for the regime studied (Fig 5-2). Therefore, using an equimolar mixture of C_2F_6 and O_2 , high powers and long residence times, one should be able to achieve near complete C_2F_6 abatement for any flowrate.

5.3.2 Contribution of Surface Reactions to Abatement

As mentioned in section 5.2, it was initially thought that the mechanism for C_2F_6 abatement was the scavenging of F in C_2F_6 by the SiO_2 in the quartz reactor. This hypothesis was rejected when not all the F could be accounted for by the formation of SiF_4 , and when similar abatement was obtained in quartz and alumina reactors. To confirm this conclusion, four distinct experimental points were picked from the matrix of design experiments, and the experiments were repeated for both quartz and alumina reactors. The results are depicted in Fig 5-3.

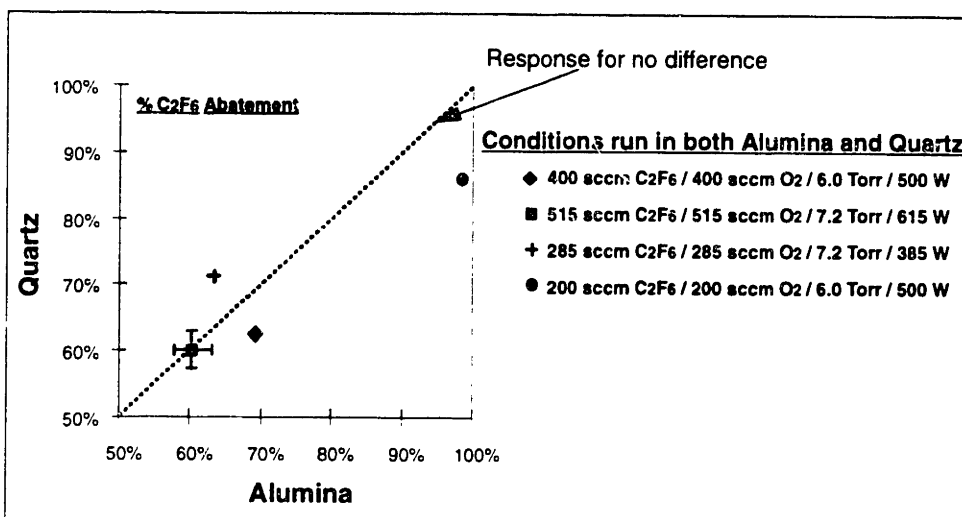


Figure 5-3: Comparison of C_2F_6 abatement in quartz and alumina reactors

The figure shows the abatement obtained for quartz on the y-axis, and that obtained in alumina on the x-axis. The dotted line (drawn at 45°) represents the condition for no difference in the abatement observed in the two reactors. As seen in the figure, all the four points approximately lie near the 45° line, indicating that the reactor surface makes no difference in the abatement obtained. In fact, the alumina reactor performed slightly better than quartz under some conditions. This effect was also observed when a mass spectrometer was used to characterize the product stream (see Section 5.4). The mass spectrometer showed that the mass spectrums for the two reactors (under similar conditions) were identical, with only trace amounts of SiF_4 present for the quartz reactor.

The importance of the surface was also tested by varying the temperature of the reactor walls. If the walls contribute significantly to the abatement, a change in reactor wall temperature is expected to affect the degree of abatement. Three different reactor configurations were tested to check the effect of reactor wall temperature - Standard ASTeX applicator without air cooling, Standard ASTeX applicator with air cooling, and the water cooled ASTeX applicator. The centerpoint of the design matrix (400 sccm C_2F_6 , 400 sccm O_2 , 6 torr and 500 W) was run in each case. The outside temperature of the wall was above $250^\circ C$ for applicator without any cooling, about $120^\circ C$ for the air

cooled applicator, and 50°C for water cooled applicator. Since the temperature drop across alumina wall is approximately constant for each applicator (assuming no difference in power coupling), the difference in the outside tube wall temperature is indicative of the difference in the inside tube temperature for each reactor. The abatement obtained for all three cases was similar ($70 \pm 5\%$), thereby confirming that the surface plays an insignificant role in C_2F_6 abatement. This was also tested by varying the cooling air flowrate for the air cooled applicator (and thus holding the microwave coupling constant). The abatement was same for tube temperatures ranging from 120 °C to 250 °C, thereby validating the earlier conclusion.

5.3.3 Reactor Flow Issues

The physical shape of the plasma in the reactor probably has an impact on the degree of abatement. The plasma, as shown in Fig 5-4, appeared annular for all conditions studied.

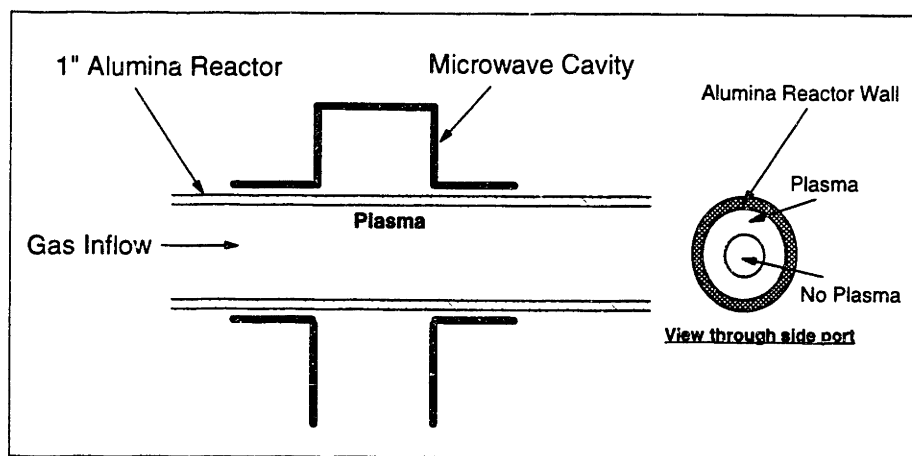


Figure 5-4: Physical appearance of the plasma in the microwave tubular reactor

It was confined mainly to the periphery of the reactor, and clung to the reactor walls. There was no plasma along the axis of the tube, giving the plasma a “donut” like appearance when viewed from the side port. This shape is not entirely unexpected given

the nature of the power coupling into the plasma. The sleeves on the ASTeX applicator act like the grounded shield, while the plasma acts like the inner conductor of a coaxial cable. As the power is coupled in, the plasma is generated near the walls, and is able to carry almost all the current, effectively shielding out the center of the reactor. Therefore, no plasma is generated at the center. The annular “hole” at the center visibly diminished as the power was increased probably because more of a conductor was required to handle the enhanced current. The plasma completely filled the cross section at pressures lower than about 1.5 torrs, presumably due to increased skin depth (of power penetration). Because of this nature of the plasma, the enhanced abatement seen at higher powers is probably a convolution of both the increased power per molecule and residence time.

One consequence of plasma annularity is that a part of the gas can potentially bypass the reactor (defined by the plasma volume) and escape unreacted, leading to a lower effective abatement. This possibility can be estimated by comparing the characteristic diffusion time for a species from the center of the tube to the plasma zone, with the residence time in the reactor. The residence time for a flowrate of 800 sccm and a pressure of 6 torr, assuming the reactor (plasma) length to be 4” and taking the ID of the reactor as 0.75” is about 17 ms. The diffusivity was calculated using the Chapman and Enskog theory (Reid *et al.*, 1977) which uses Lennard-Jones potentials. The Lennard-Jones potentials for F, CF₃, CO, O and O₂ were obtained from Svhela (1962), and the stationary phase was taken as C₂F₆. The properties for C₂F₆ were approximated by those for CF₄ for this estimate. The characteristic diffusion time was based on half the inner diameter of the tube (0.375”). The calculated diffusion times for the species ranged from 4-11 ms, with the self diffusion time for C₂F₆ estimated at about 11 ms. This characteristic diffusion time (11 ms) is of the same order as the residence time (17 ms), thereby indicating that the possibility of gas bypassing the reactor through the annular region exists.

This possibility was tested by conducting an experiment. Two solid alumina rods — 0.25”OD and 0.5” OD — were inserted into the reactor axially, as shown in Fig 5-5.

These alumina rods served to block out the annular portion of the plasma, forcing the gas to flow through the plasma. The abatement was measured with and without these rods and the results are shown in Fig 5-6.

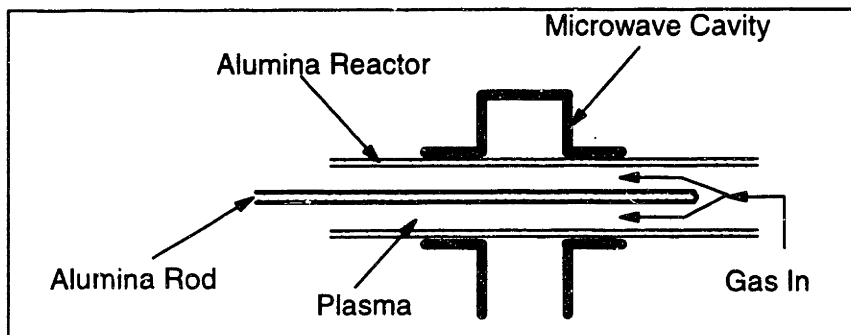


Figure 5-5: Equipment modification to eliminate annular flow in the reactor

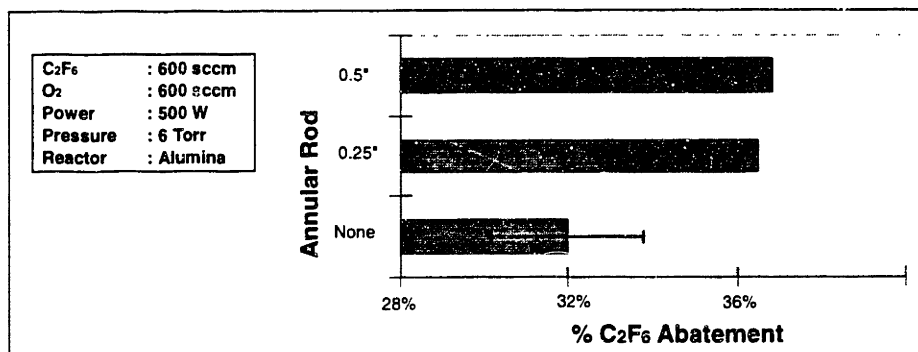


Figure 5-6: Effect of annular flow modification on C_2F_6 abatement

The figure indicates that the elimination of annular flow aids the abatement. However, the change in abatement from the “No rod” to “0.25” Rod” is only about 5%. In addition, one necessary condition for this comparison to be valid was not met during the experiment. It was expected that the alumina rod inserted into the plasma would only serve to modify the flow, and not the reaction. However, this did not hold during the experiments. The alumina rods suffered severe erosion, with the 0.5” OD rod also accumulating some black deposition on the surface. In addition some colorless, hygroscopic crystals (probably AlF_3) were formed on the rod immediately downstream of the erosion. Thus, since the rods did not remain inert during this experiment, it is not

clear if the small enhancement in abatement is attributable to elimination/reduction of annular flow or not.

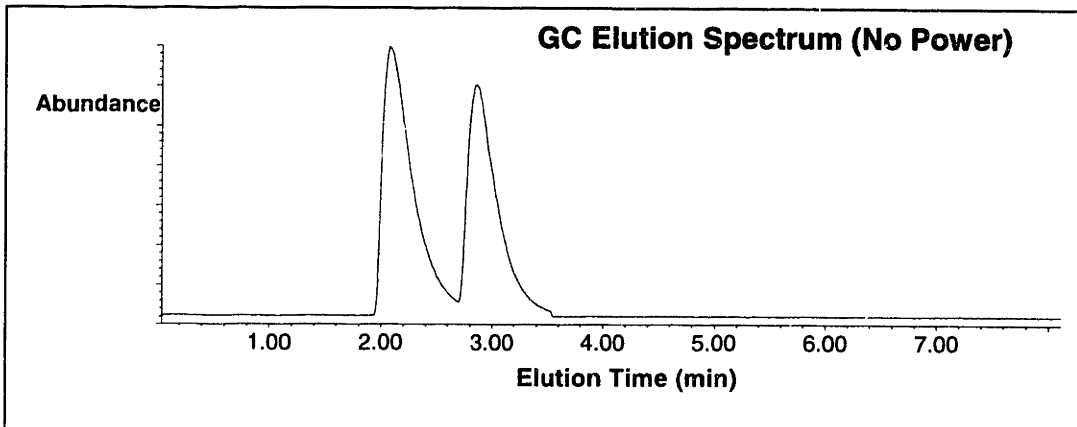
An attempt was also made to quantify the change in plasma volume (due to both a change in annularity and length of the plasma) as a function of pressure and power. A sapphire reactor was fabricated at a substantial cost. It was hoped that this reactor could be used to visually observe the change in volume as a function of parameters. However, the reactor cracked within the first 5 minutes of operation, probably due to severe temperature stress (in an air cooled cavity). Therefore that attempt was abandoned. As mentioned before, visual observation did indicate a substantial change in annularity with pressure and power.

5.4 Characterization of Byproducts

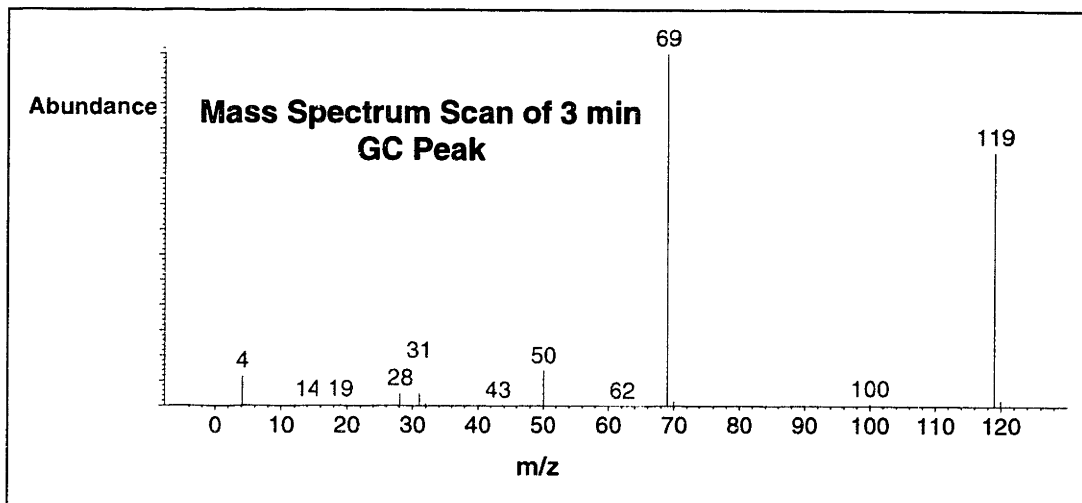
One important question for any abatement is — What are the products of the abatement process? If the abatement products have a higher GWP/ODP/lifetime than the species being abated, then the process may not be that useful. Three different diagnostics were used to characterize the products of the plasma abatement process - GC/MS, inline Mass Spectrometry and optical emission spectroscopy.

5.4.1 GC/MS Characterization

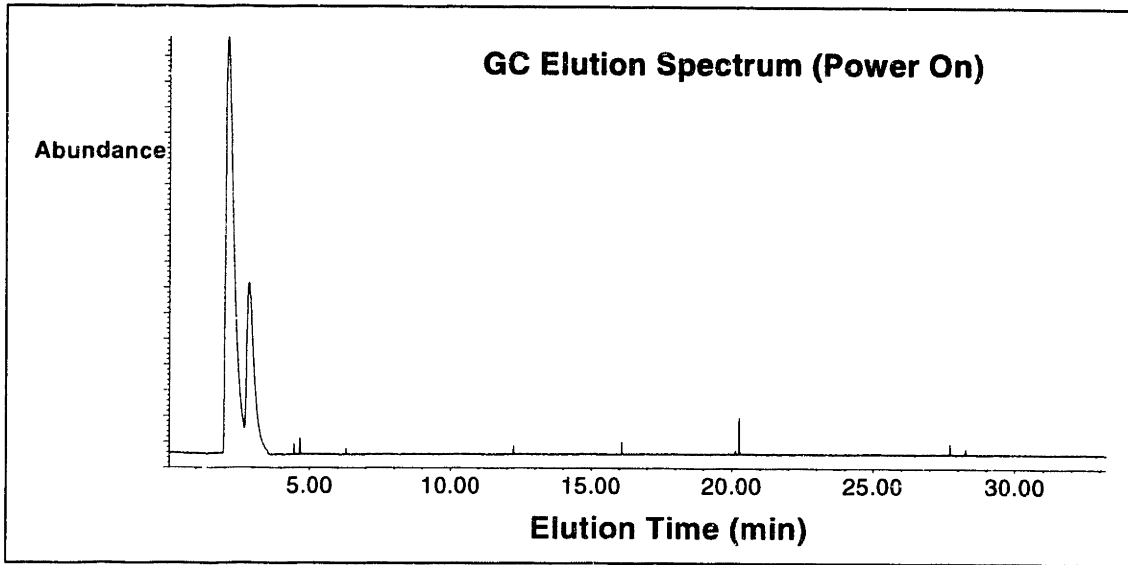
A GC/MS was used to identify the stable compounds in the effluent. As mentioned before, the plasma process effluent was scrubbed in the countercurrent water scrubber (to remove any HF) before injection into the GC. Also since the sampling was done post-pump, the injected stream contained N₂ which was used as a pump purge. A baseline was first established for the case when there was no plasma (with just gases flowing through). Then the plasma was turned on, and the effluent was analyzed. Fig 5-7 shows the results from the GC/MS characterization.



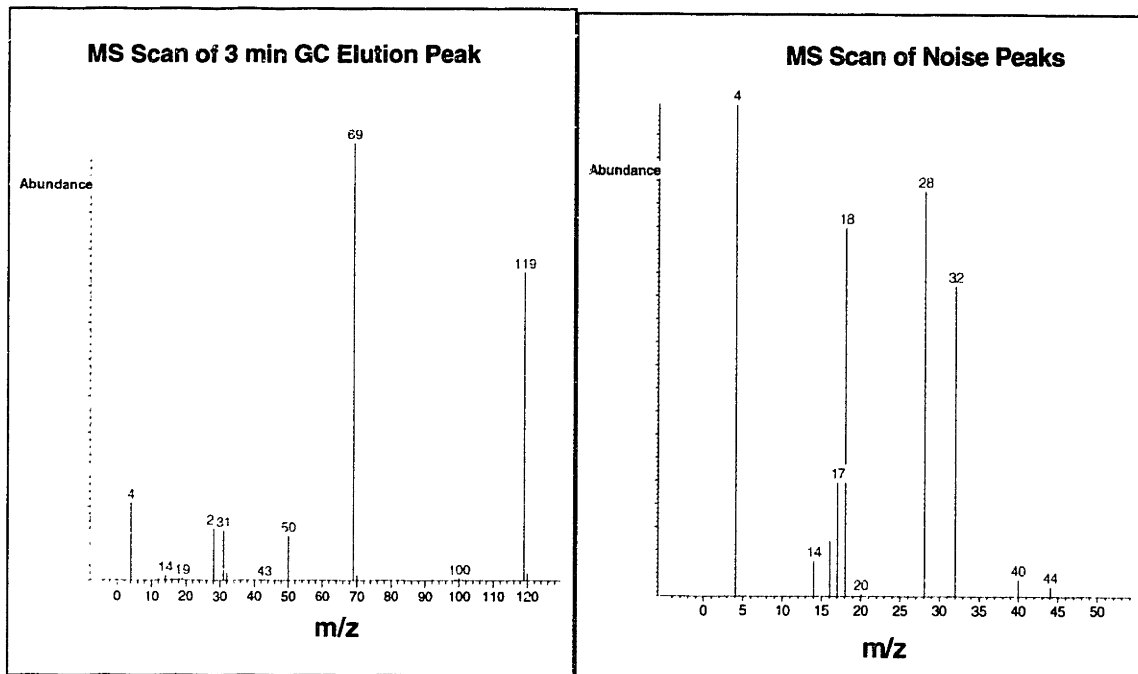
(a)



(b)



(c)



(d)

Figure 5-7: GC/MS analysis of effluent from C_2F_6 plasma abatement process. Both the Total Ion Chromatogram (TIC) and mass spectra are shown. Figure 5-7(a) and 5-7(b) are without plasma, and 5-7(c) and 5-7(d) for when the plasma was turned on.

Fig 5-7(a) shows the baseline when the power is not on. The GC Total Ion Chromatogram (TIC) trace in Fig 5-7(a) shows two peaks . The first peak corresponds to

N_2 (from pump purge), while the latter is from C_2F_6 . This is confirmed by the mass spectrum shown in Fig 5-7(b). The fragments from the cracking of C_2F_6 (CF_3^+ at m/e 69 and $C_2F_5^+$ at m/e 119) are clearly evident in the spectra. Fig 5-7(c) shows the result when the power is turned on. As expected, the TIC shows a diminished C_2F_6 peak, indicating that some abatement has taken place. There are no other significant peaks in the TIC trace. There are a few spikes present, but all of those arise from a minor air leak at the GC/MS interface. The MS shown in Fig 5-7(d) indicates that the major components in the other spikes are carrier gas He (m/e 4), H_2O (m/e 18), N_2 (m/e 28) and O_2 (m/e 32). The m/e of 28 could also be attributed to CO, but the similarity in the mass spectrum in all the spikes, and the corruption of that peak by m/e of 4, 18 and 32 strongly suggests that peak 28 is attributable to N_2 . The GC/MS data was collected for 35 minutes. Both C_2F_6 and N_2 elute in the first 4 minutes. Since no other peaks were detected in 35 minutes, we can conclude that no byproducts made it past the water scrubber before the GC/MS. Since PFCs do not scrub out in the water scrubber, we can rule out the possibility of CF_4 as a byproduct based on the GC/MS scan. CF_4 sometimes tends to elute with N_2 , but the Extracted Ion Chromatogram (EIC) for m/e 69 (CF_3^+) — which is the primary peak of CF_4 — indicated that this was not the case. The EIC for m/e 69 looked exactly the same as the TIC for C_2F_6 , thereby indicating that all m/e 69 was due to C_2F_6 . In addition, for the cases where C_2F_6 abatement was close to 100%, there was no evidence of m/e 69 either in GC/MS or in the inline mass spectrometer. Therefore, we can conclude that no CF_4 (and other PFCs) or CO are being produced in this process. This is important since these gases are harmful to the atmosphere due to their high GWP and long atmospheric lifetimes.

5.4.2 Inline Mass Spectrometry

The GC/MS scans showed that the byproducts from the plasma abatement of C_2F_6 are all water soluble. A logical step would be to inject the effluent directly into the GC/MS without any water scrubbing. However, since the materials in the GC/MS were incompatible with high levels of HF (expected from the hydrolysis of F species), we did

not use the GC/MS to ascertain the nature of products. Therefore, an inline Mass Spectrometer (MS) was used for identifying stable species in the effluent (Fig 5-8). This inline MS was located about 12" from the exit of the reactor. Since that length represents significant wall area for collision and recombination, the MS is only capable of identifying stable products. A beam chopper with a lock-in amplifier was used to ensure that the mass spectra were not corrupted by the background species already present in the MS chamber.

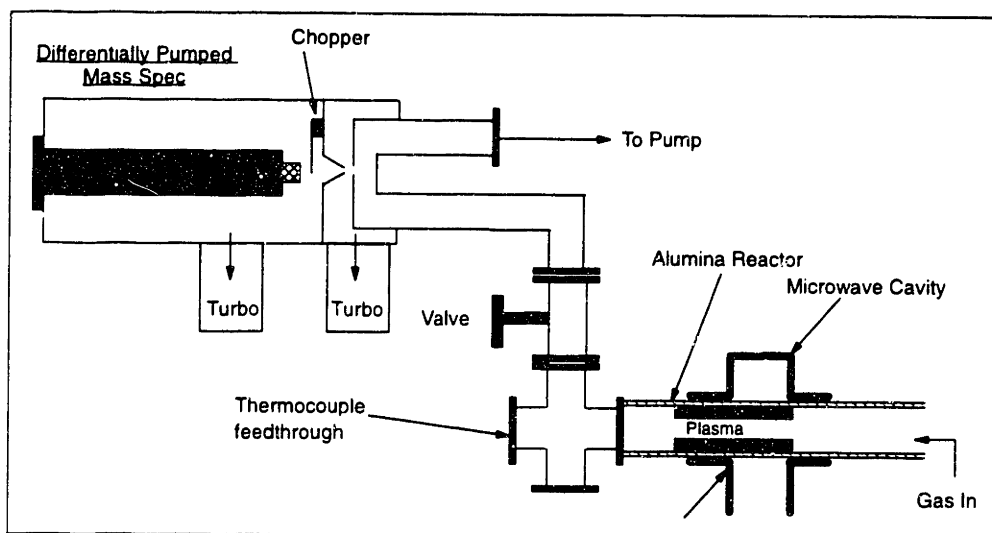


Figure 5-8: Location of inline mass spectrometer in the Abatement Reactor setup

Since the interpretation of mass spectra is always complicated by the convolution of different peaks, a stepwise approach was adopted. First the cracking patterns of C_2F_6 and O_2 alone were characterized. Then, a baseline spectra for a mixture of the two (without a plasma) was collected. Subsequently, the power was turned on and the spectrum was compared to the baseline to determine the products. Fig 5-9(a) shows a sample C_2F_6 baseline spectrum. The spectrum in Fig 5-9(a) shows m/e peaks 12 (C^+), 19 (F^+), 31 (CF^+), 50 (CF_2^+), 69 (CF_3^+) and 119 ($C_2F_5^+$). Fig 5-9(b) shows the analogous spectrum for O_2 . There are only two peaks in the cracking pattern of O_2 - m/e 16 (O^+) and 32 (O_2^+). The light line in Fig 5-10 shows the spectrum when both C_2F_6 and O_2 are fed in equimolar mixtures into the chamber. This base spectrum is a combination of the

spectra for individual components. The heavy line in Fig 5-10 is the spectrum when the plasma was turned on at 700 W.

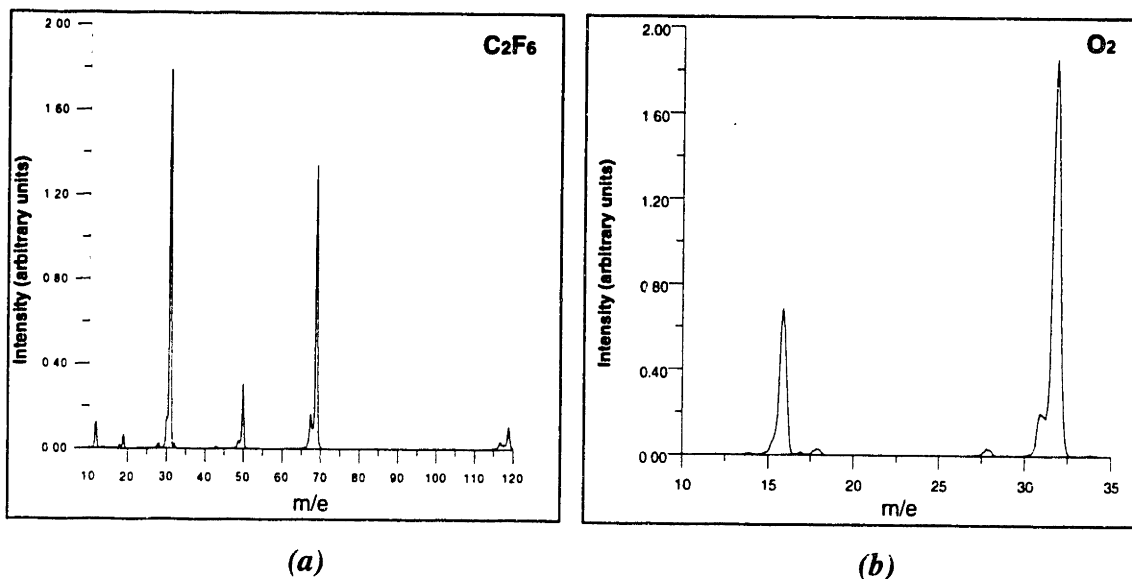


Figure 5-9: Baseline Mass Spectrum for C_2F_6 and O_2 in the absence of plasma

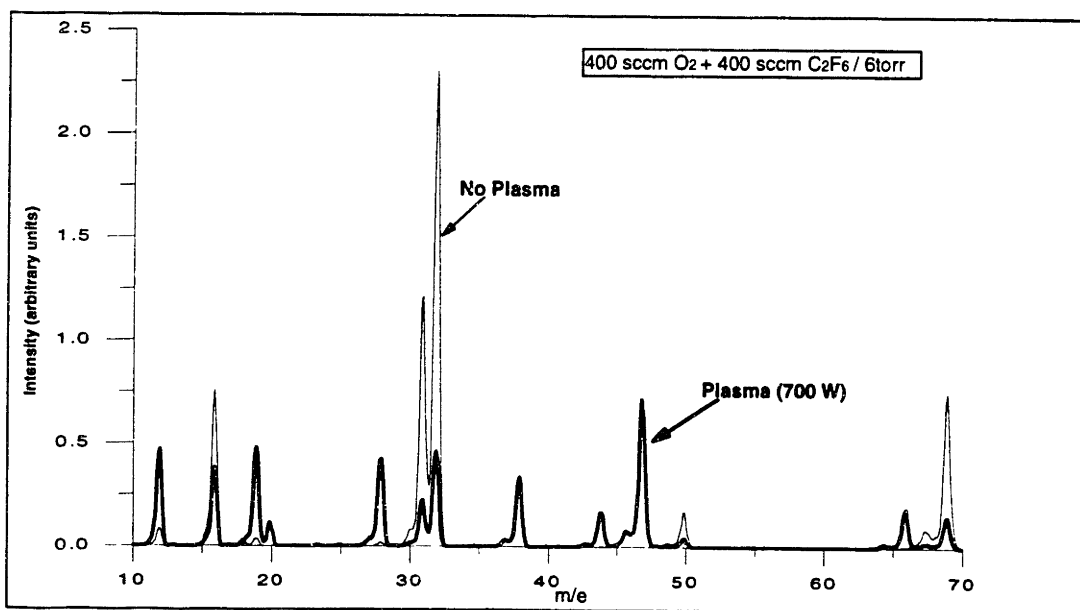


Figure 5-10: $C_2F_6 + O_2$ Mass Spectrum with and without plasma

All the peaks in the spectra showed a small shoulder to the left (most evident for peak 32 in Fig 5-9 (b)). The intensity of the shoulder peak was about 10% of the main peak intensity and is attributable to charging within the quadrupole. The presence of this shoulder peak does not affect any of the conclusions presented in this thesis. Basic linearity checks were carried out for a mixture of C₂F₆ and O₂ by changing both the composition and pressure. All primary peaks scaled perfectly in the expected direction with pressure and composition changes.

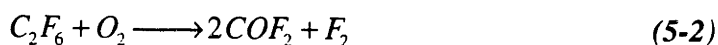
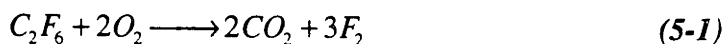
Fig 5-10 shows the impact of turning the plasma on for a C₂F₆ + O₂ mixture. The m/e axis has been truncated at 70 to highlight the important portion of the spectrum. There is another peak at 119 (C₂F₅⁺), which is not shown. As seen in Fig 5-10, peaks 16 (O⁺), 31 (CF⁺), 32 (O₂⁺), 51 (CF₂⁺) and 69 (CF₃⁺) decrease when the power is turned on. Other peaks like 12 (C⁺) and 19 (F⁺) increase, while peaks 20 (HF⁺), 28 (CO⁺), 38 (F₂⁺), 44 (CO₂⁺), 47 (COF⁺) and 66 (COF₂⁺) appear in the mass spectrometer when plasma is on. The intensity of peak 20 (HF⁺) is low as expected since residual H₂O is the only H source in the system. Table 5-1 shows the reference cracking patterns from Eight Peak Spectra (1995) for the reactants (C₂F₆ and O₂) and the postulated products.

Table 5-1: Reference cracking patterns for reactants and potential products for C₂F₆ + O₂

Species	Cracking Pattern (with relative intensities in parenthesis)
C ₂ F ₆	69(100); 119(41); 31(18); 50(10)
O ₂	32(100); 16(9)
COF ₂	47(100); 66(55); 28(14); 31(4); 50(3); 48(2)
CO ₂	44(100); 16(9); 28(8); 12(7)
F ₂	19(100); 38(55)

Comparing the cracking pattern observed in Fig 5-10 with the reference spectra in Table 5-1, it is clear that a minimum of three products from the reaction of C₂F₆ with O₂ — CO₂, COF₂ and F₂ — can explain all of the peaks. Another product, OF₂, was considered but eliminated due to the absence of m/e 35, which is the main peak from OF₂. CO could be a potential product, but its absence in the GC/MS indicates that it is not

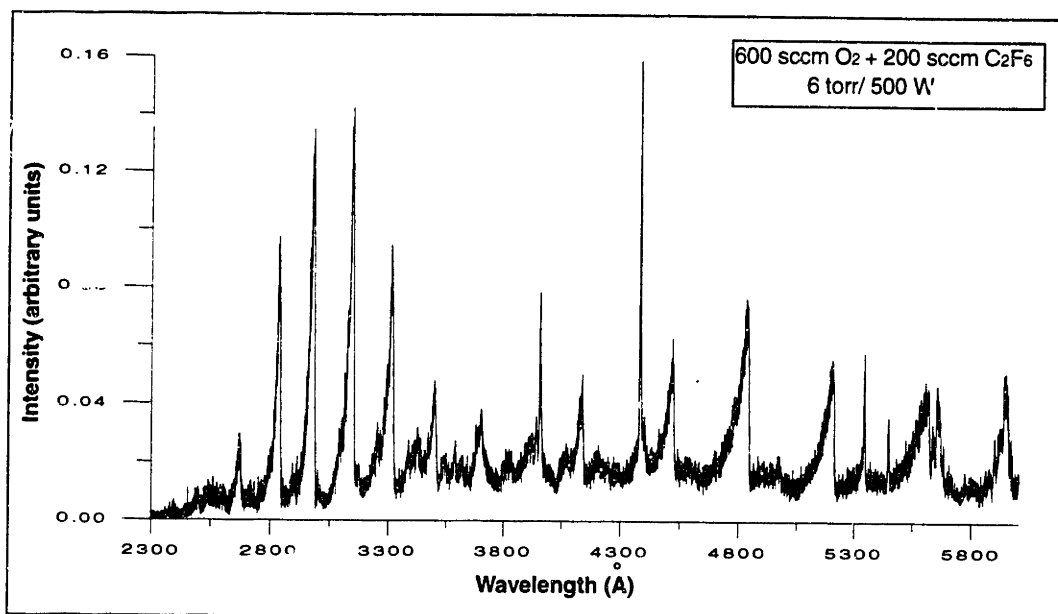
being produced to an appreciable extent. If CO were a stable product, it would be detected in the GC/MS since its solubility in water is low. The possibility of observing O and F is diminished due to the presence of significant stainless steel wall area, which facilitates the wall recombination process before the species reach the mass spectrometer. Therefore, C₂F₆ abatement can be characterized as proceeding via two competing reactions:



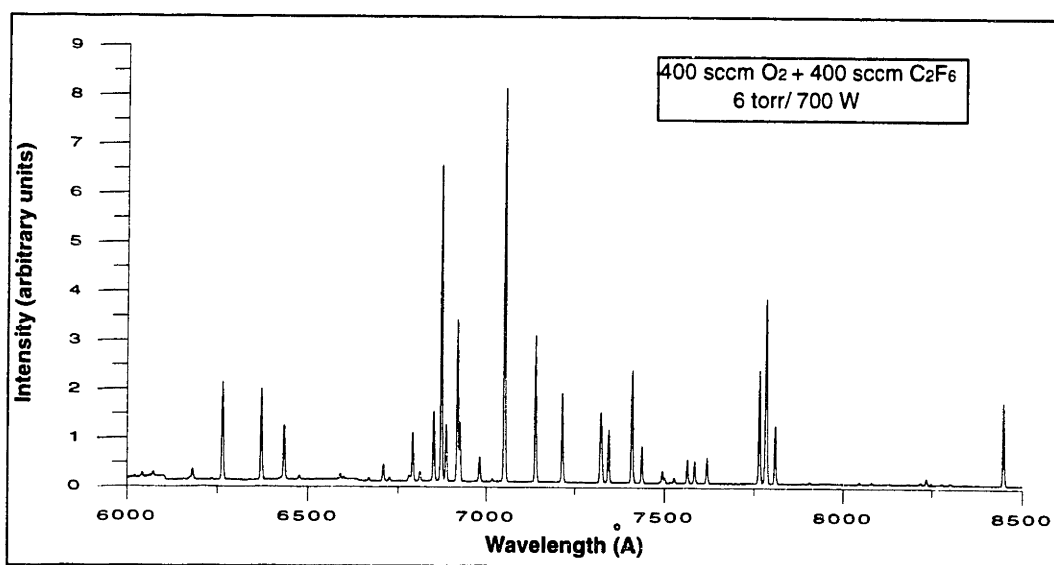
Of course, the exact reaction sequence is much more complicated. This is discussed in greater detail in section 5.7.2.

5.4.3 Plasma Induced Emission

Plasma induced emission (PIE) provides quick and useful information on the species present in the plasma. A 0.27m monochromator (Jarrell-Ash) was used to image the plasma in an attempt to identify the dominant species. A 2m long fiber optic cable was used to image the plasma axially and couple the light into the monochromator. A scan from 2000Å to 8500Å was conducted. The fiber optic cable was unable to transmit any emission below about 2400Å. Fig 5-11(a) shows the PIE scan from 2300 to 6000Å, while Fig 5-11(b) shows the scan from 6000-8500Å. There was only one peak beyond 8000Å — that for O at 8446Å. The scan in Fig 5-11(a) is for a 1:3 mixture of C₂F₆ and O₂ while that in Fig 5-11(b) is for a 1:1 mixture of C₂F₆ and O₂. The scan in Fig 5-11(a) was carried out under O₂ rich conditions to maximize the chance of observing CO in the mixture.



(a)



(b)

Figure 5-11: Plasma induced emission (PIE) scan for $C_2F_6 + O_2$ system. Fig 5-11(a) shows the spectrum from 2300-6000Å for a 1:3 mixture of $C_2F_6 + O_2$. The O_2 rich feed was used to maximize the probability of observing CO. Fig 5-11(b) shows the spectrum from 6000-8500Å for a 1:1 mixture of $C_2F_6 + O_2$.

All, except one, of the peaks in Fig 5-11(a) are from CO. The only exception is the peak at 3961Å which is from CO_2^+ . No peaks for CF and CF_2 were observed, which is expected due to excess O_2 . In summary, PIE scans showed the existence of F, O, CO and

CO₂ in the reacting mixture. It is impossible to estimate the absolute concentrations of these species from the PIE data though. The concentrations of F, O and CO₂ are expected to be significant since F₂ (from recombination of F), O₂ (from recombination of O) and CO₂ are detected in the mass spectrometer. Although CO cannot be identified with certainty in the mass spectrometer (due to interference in cracking pattern from COF₂), its concentration in the effluent is probably much lower than CO₂ concentration since it is not detected in the GC/MS. In addition, since the formation of CO₂ from the recombination of CO and atomic O is thermodynamically favored (particularly at temperatures less than about 2000 °C), all the CO in the effluent probably recombines with O in the post-plasma region. This possibility is also enhanced by the low activation energy (3 kcal/mol) for the three-body recombination reaction of CO with O (Burgess *et al.*, 1995). Therefore, the only stable products from the process are CO₂, COF₂ and F₂.

5.5 Contribution of Pyrolysis to Abatement

The gas phase temperature in the plasma zone was measured using a ceramic sheathed thermocouple. The thermocouple was introduced axially, and the temperature was measured along the axis at various points. The measured temperature distribution is shown in Fig 5-12.

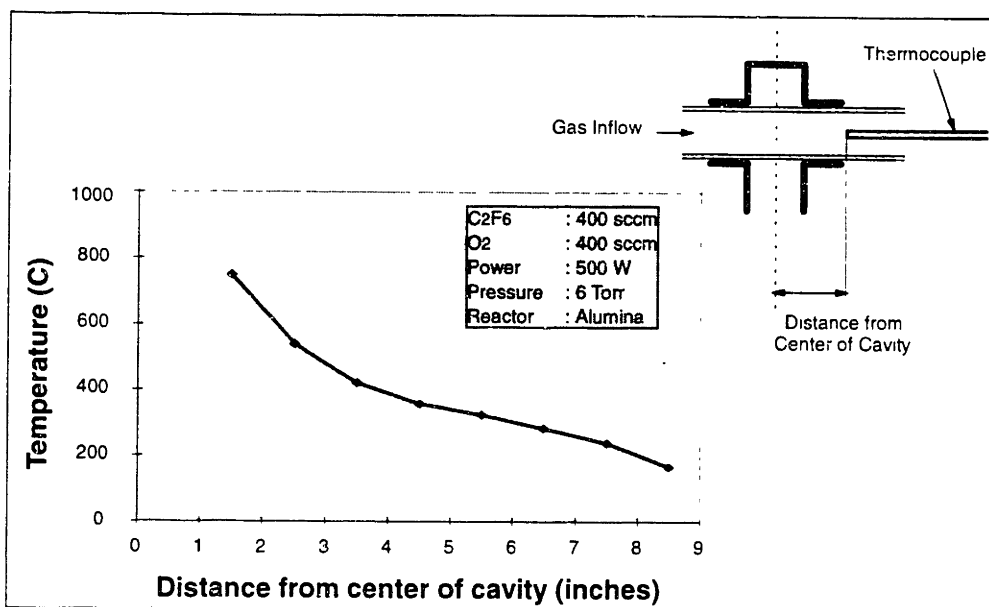
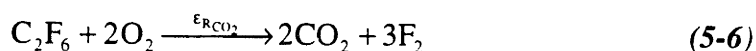
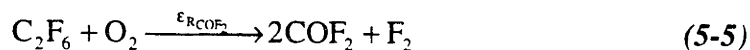


Figure 5-12: Gas phase axial temperature distribution in the microwave tubular reactor

The x-axis in the figure is the distance of the thermocouple from the center of cavity. The thermocouple was placed 8.5" from the cavity center and moved in 1" steps towards the center during a run. The temperature could not be measured closer than 1.5" from the center since the thermocouple acted like an antenna and started transmitting microwaves at that point. The temperature was measured at about 800°C 1.5" from the center, and is expected to be much higher at the center. The sublimation temperature of AlF_3 , which we suspect was formed during the annular flow modification experiments discussed in section 5.2.3, is 1300°C. Therefore, the temperature at the center could be as high as 1300°C. At these elevated temperatures, one could suspect some pyrolysis of C_2F_6 . Thermodynamic equilibrium calculations were carried out for the following reactions to estimate the potential for thermal decomposition to C_2F_6 abatement.



The first two reactions are for the decomposition of C₂F₆ and O₂ respectively, while the last two are for the overall reactions. The respective extents of reactions are : $\epsilon_{D_{C_2F_6}}$, $\epsilon_{D_{O_2}}$, $\epsilon_{R_{COF_2}}$ and $\epsilon_{R_{CO_2}}$. Thus if an extent equals 1, then the reaction essentially goes to completion for the conditions at which the extent is calculated. The extents were calculated at four temperatures — 1000°C, 1200°C, 1500°C and 2000°C. The thermodynamic data used in the calculations is summarized in Table 5-2. The mean heat capacity C_{pm} at other temperatures were determined from Burgess *et al.* (1995). The standard heat of formation $\Delta H_{f,298K}^{\circ}$ for COF₂ was taken from the calculations of Schneider and Wallington (1994).

Table 5-2: Thermodynamic data used for equilibrium calculations(Burgess et al., 1995)

Species	$\Delta H_{f,298K}^{\circ}$ (kJ/mol)	$S_{f,298K}^{\circ}$ (J/mol. K)	$C_{pm, 800K}$ (J/mol. K)
C ₂ F ₆	-1343.9	332.1	160.34
O ₂	0	205	33.75
CO ₂	-393.5	213.7	51.54
COF ₂	-607.9	258.8	70.82
F	78.9	158.7	21.46

The calculation methodology for 1000°C is illustrated here. First the ΔH_{1300K} and ΔS_{1300K} for the two reactions were computed using the equations (see Benson, 1976 for details)

$$\Delta H_T = \Delta H_{T_o} + \Delta C_{p_{T_m}} (T - T_o) \quad (5-7)$$

and

$$\Delta S_T = \Delta S_{T_o} + \Delta C_{p_{T_m}} \ln \frac{T}{T_o} \quad (5-8)$$

where T_o is the reference temperature (298 K), T is the temperature of interest (1300 K), $\Delta C_{p,Tm}$ is the heat capacity at mean temperature (800 K), ΔH_T and ΔS_T are the enthalpy

and entropy change respectively for the reaction at temperature T . Then the change in Gibbs free energy (ΔG) for the reaction was computed using the equation

$$\Delta G = \Delta H - T\Delta S \quad (5-9)$$

and the equilibrium constant K_c was computed from

$$K_c = e^{\left[-\frac{\Delta G}{RT}\right]} \quad (5-10)$$

which was then converted to pressure units using the formula

$$K_p = K_c (R T)^{\Delta n} \quad (5-11)$$

where K_p is the equilibrium constant in pressure units, R is the universal gas constant and Δn is the change in number of moles from the reactant to the product.

The extents of reactions at various temperatures are summarized in Table 5-3.

Table 5-3: Extents of reactions from thermodynamic equilibrium calculation — $C_2F_6 + O_2$

	1000°C	1200°C	1500°C	2000°C
$\epsilon_{D_{C_2F_6}}$	4%	33%	97%	100%
$\epsilon_{D_{O_2}}$	0	0	1%	19%
$\epsilon_{R_{COF_2}}$	100%	100%	100%	100%
$\epsilon_{R_{CO_2}}$	0	0	0	76%

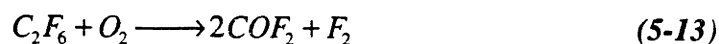
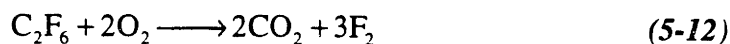
The calculation show that C_2F_6 could start to decompose at about 1000°C, while O_2 could not start decomposing till about 1500°C. However, the decomposition product of C_2F_6 (CF_3) could spontaneously react with O_2 at lower temperatures (all equilibrium K_p are greater than 10^5). The extent of reaction for COF_2 formation is 100% for all temperatures

(>1000°C); however, a significant kinetic barrier prevents the spontaneous reaction of C₂F₆ with O₂ to form COF₂. The formation of CO₂ is not favored thermodynamically until the temperature is in excess of 1500°C. It is important to point out that these calculations are thermodynamic equilibrium calculations. Plasmas are inherently non-equilibrium, and thus it is hard to be definitive about the role of pyrolysis in plasma abatement.

There is data from burn-box studies however, showing that heating alone does not decompose C₂F₆ and a flame is necessary for its decomposition (Worth, 1995). This is probably because of the high kinetic barrier to PFC decomposition (Burgess *et al.*, 1995). In the burn-box studies (carried out on the Delatech CDO™ unit at Motorola), heating C₂F₆ to 850-900°C did not result in decomposition; however, rapid C₂F₆ decomposition was observed in the presence of a flame (Worth, 1995). A flame may initiate free radical reactions, which lower the kinetic barrier for C₂F₆ decomposition. A plasma could act similarly to a flame, and facilitate "free radical" reactions which also lower the effective kinetic barrier for decomposition. Thus pyrolysis probably does not play a role in C₂F₆ abatement in the microwave tubular reactor described in this thesis.

5.6 Mechanism for C₂F₆ Abatement

As mentioned in section 5.4, the three main products identified in the abatement process effluent were CO₂, COF₂ and F₂. Therefore, on a lumped basis, the overall C₂F₆ abatement can be characterized as a competition between two reactions:



The actual abatement mechanism is obviously much more complicated, with elementary reactions like electron impact dissociation of species, and gas phase radical

recombination. However, the above lumped sequence is helpful in explaining the abatement behavior more intuitively.

A set of experiments was carried out, and mass spectra collected under each condition, to identify the dominant pathway for abatement as a function of parameter space. The parameters varied during the experiments were: Total Flowrate (200-1600 sccm), Fraction of C₂F₆ in feed gas (10-50%), Power (300-700W) and Pressure (3-9 torr). The degree of C₂F₆ abatement from the GC and the GC/MS were found to be in excellent agreement with that from the mass spectrometer (using the peak 69 (CF₃⁺) intensity). Since the GC data takes much longer to collect due to longer acquisition time and volume holdup issues in the pump, only the Mass Spectrometer data was collected during these runs. The data from these experiments was interpreted using an extent of reaction approach.

5.6.1 Interpretation of Mass Spectrometer Data

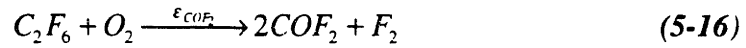
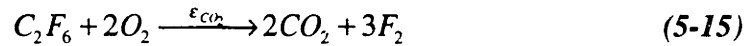
The mass spectrometer data was interpreted as follows. The cracking pattern for various species shown in Table 5-1 indicated that peaks 38, 44 and 47 arose mainly from the cracking of F₂, CO₂ and COF₂ respectively. Therefore the intensities of peaks 38, 44 and 47 were taken to represent the concentrations of F₂, CO₂ and COF₂ respectively. The absolute concentrations (in terms of partial pressures) could be ascertained easily for the reactants C₂F₆ and O₂. Peak 69 was used to track C₂F₆ concentration (peak 119 was generally too low-intensity and therefore prone to error), and 32 was used for oxygen. The partial pressures for both C₂F₆ and O₂ were calculated using the relation

$$PP_i = K_i I_i \quad (5-14)$$

where PP_i is the partial pressure of species i , I_i is the intensity of the peak used to track the concentration, and K_i is a constant. This relation holds provided the cracking patterns for various species do not change with a change in the gas composition. The constant K_i

for C_2F_6 and O_2 was determined by sampling pure gases into the mass spectrometer at known pressures. This constant was then verified by sampling a mixture of these two gases in various proportions and pressures. This constant K_i was found to be quantitatively accurate to within $\pm 5\%$ for both C_2F_6 and O_2 .

The extents of different reactions were computed as following. Three pathways for C_2F_6 loss were taken:



The extents of the three reactions are ϵ_{CO_2} , ϵ_{COF_2} and ϵ_{loss} as shown. These extents are denominated in fractions, and the fractional abatement of C_2F_6 is simply the sum of the three extents. The last reaction for C_2F_6 loss signifies the uncertainty in the closure of mass balance. Assuming we start with 1 mole of C_2F_6 and y moles of O_2 , the number of moles of different species in the system can be written as

$$C_2F_6 = 1 - \epsilon_{CO_2} - \epsilon_{COF_2} - \epsilon_{loss} \quad (5-18)$$

$$O_2 = y - 2\epsilon_{CO_2} - \epsilon_{COF_2} \quad (5-19)$$

$$CO_2 = 2\epsilon_{CO_2} \quad (5-20)$$

$$COF_2 = 2\epsilon_{COF_2} \quad (5-21)$$

$$F_2 = 3\epsilon_{CO_2} + \epsilon_{COF_2} \quad (5-22)$$

$$Total = 1 + 2\epsilon_{CO_2} + \epsilon_{COF_2} - \epsilon_{loss} + y \quad (5-23)$$

The partial pressure of any component is given by the number of moles of that component divided by the total moles, multiplied by the total pressure P . The total pressure in the system is always constant since the abatement is carried out at constant pressure using a throttle valve in feedback with a pressure sensing capacitance manometer. Therefore, the partial pressures of C_2F_6 and O_2 can be written as

$$PP_{C_2F_6} = m = \frac{1 - \epsilon_{CO_2} - \epsilon_{COF_2} - \epsilon_{loss}}{1 + 2\epsilon_{CO_2} + \epsilon_{COF_2} - \epsilon_{loss} + y} P \quad (5-24)$$

$$PP_{O_2} = n = \frac{y - 2\epsilon_{CO_2} - \epsilon_{COF_2}}{1 + 2\epsilon_{CO_2} + \epsilon_{COF_2} - \epsilon_{loss} + y} P \quad (5-25)$$

The quantities m and n are explicitly known at each experimental condition from equation 5-14. Since we are solving for three unknowns (ϵ_{CO_2} , ϵ_{COF_2} and ϵ_{loss}), we need a third equation.

The third equation relates the concentration of CO_2 with COF_2 , and is derived as following (see UTI 100C Manual for details). The partial pressure of any species J is related to the mass spectrometer intensity of its fragments by

$$PP_J \propto \frac{I_j^+}{G S_B} \quad (5-26)$$

where I_j^+ is the intensity of j^{th} fragment of J , G is the electron multiplier gain for each fragment, and S_B is the basic sensitivity. The basic sensitivity S_B in turn is a function of ionization efficiency ϵ and transmission T of an ion through the quadrupole filter, and is related by the equation

$$S_B(J) = \epsilon_J T_J S_B(N_2) \quad (5-27)$$

The transmission T depends upon the m/e of the fragment and falls off linearly with an increase in m/e . It can be assumed to be same for the two fragments 44 and 47 (for CO_2 and COF_2 respectively), since they are very close. $S_B(\text{N}_2)$ is the sensitivity for nitrogen and is obviously a constant. The only factor expected to be significantly different for CO_2 and COF_2 is the ionization efficiency ϵ . It is empirically related to the sum of atomic numbers Z of a compound's constituent atoms by the formula

$$\epsilon_j = 0.6 \left(\frac{\sum Z}{14} \right) + 0.4 \quad (5-28)$$

Therefore, combining equations 5-26, 5-27 and 5-28 we get,

$$\text{PP}_{\text{CO}_2} = 1.32 \left[\frac{I_{\text{CO}_2}}{I_{\text{COF}_2}} \right] \text{PP}_{\text{COF}_2} \quad (5-29)$$

This is the third equation needed to solve for ϵ_{CO_2} , ϵ_{COF_2} and ϵ_{loss} . This equation ensures that the solution for ϵ_{CO_2} , ϵ_{COF_2} and ϵ_{loss} considers the formation of both CO_2 and COF_2 . We could have solved for ϵ_{CO_2} and ϵ_{COF_2} only, using the partial pressure equations for C_2F_6 and O_2 (Eqns 5-24 and 5-25). However, that approach was error prone and sometimes predicted very little of one product, when in fact that product's intensity was significant in the mass spectrum. By forcing the third equation on the system of equations, the mass balances were very reasonable and ϵ_{loss} gave an idea of the uncertainty in the mass balance.

5.6.2 Results and Discussion

The extents of reactions ϵ_{CO_2} , ϵ_{COF_2} and ϵ_{loss} were calculated at each data point. These extents were then analyzed using NNAPER. For almost all experimental conditions, the extent for loss of C_2F_6 (ϵ_{loss}) was less than 5% in absolute magnitude. It

was greater than 5% (8%) for only two experimental conditions out of 28. Therefore, we can conclude that the mass balance was closed to within 5% for all conditions.

The extents ϵ_{CO_2} and ϵ_{COF_2} are shown as a function of different parameters in Fig 5-13 and Fig 5-14.

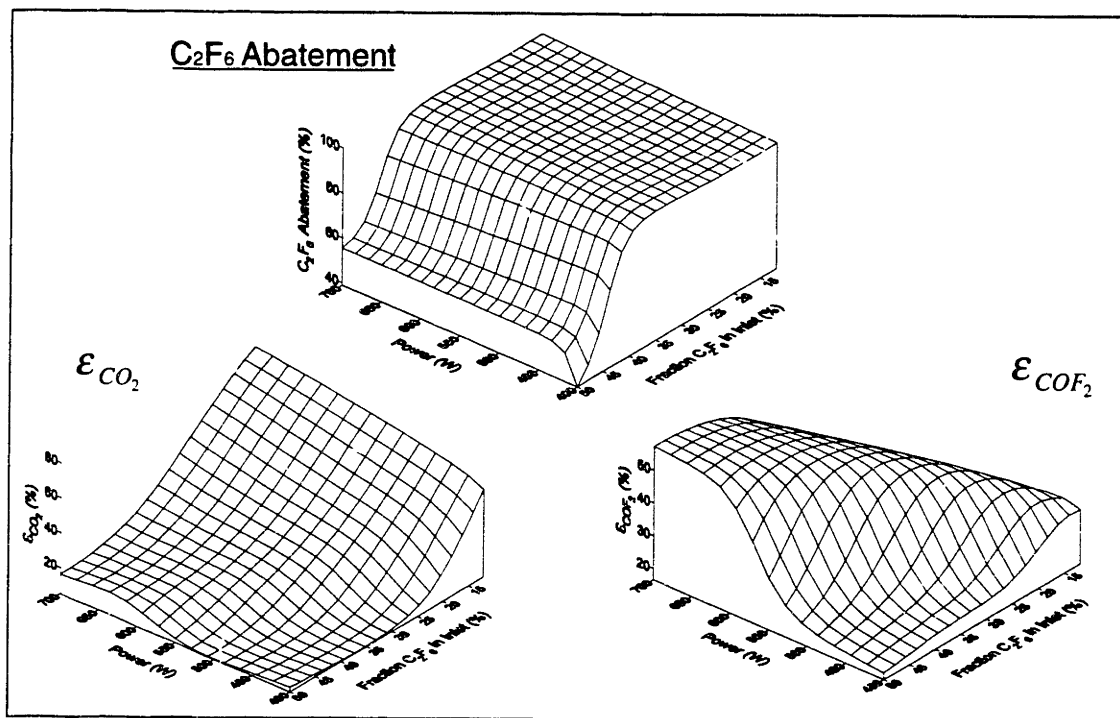


Figure 5-13: C₂F₆ Abatement and Extents ϵ_{CO_2} and ϵ_{COF_2} as a function of Power and Fraction of C₂F₆ in the Gas Mixture. Fixed conditions for the plots: Pressure at 6 torr and Flowrate at 800 sccm

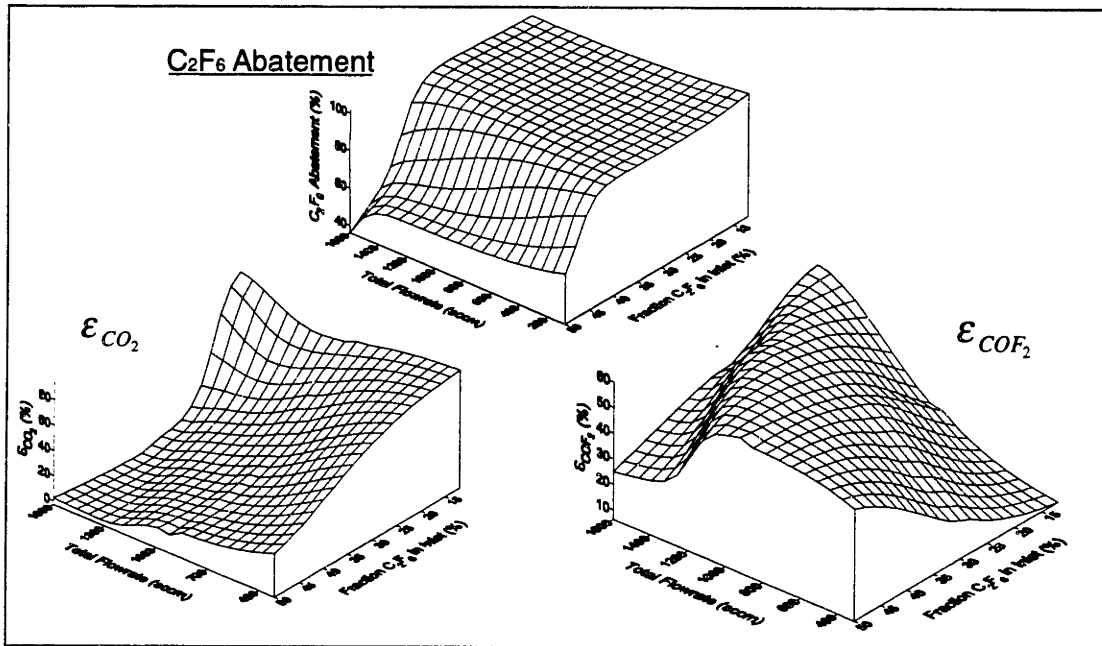


Figure 5-14: Extents ϵ_{CO_2} and ϵ_{COF_2} as a function of Flowrate and Fraction of C_2F_6 in the gas mixture. Fixed conditions for the plots: Pressure at 6 torr and Power at 700W

Fig 5-13 shows the shifts in the abatement mechanism as the conditions are varied. With oxygen rich feed, more CO_2 is produced relative to COF_2 as the power is increased. However, as the percentage of C_2F_6 in the feed gas is increased, more of it goes to form COF_2 than CO_2 . This pattern also makes intuitive sense since CO_2 is expected to be the final product when there is an excess of O_2 in the reacting mixture. Even though the abatement mechanism shifts as a function of parameters, overall abatement remains high over the parameter space. Fig 5-14 shows the shift in extents of reaction as a function of flowrate and fraction of C_2F_6 in the feed gas. The behavior with increasing C_2F_6 in the feed gas observed in Fig 5-14 is again borne out in the figures. Increasing the C_2F_6 in feed again leads to a preferential production of COF_2 over CO_2 . The same effect is seen with increasing flowrate especially under oxygen rich feed composition (Fig 5-13). Presumably, the higher flowrate does not give enough residence time for the O_2 to decompose to the extent required for CO_2 formation. When the proportion of C_2F_6 in increased in the feed, increasing flowrate also depresses the

production of COF_2 . Therefore, there is a maximum along the flowrate axis for the extent ϵ_{COF_2}

The extents of reaction do not vary with pressure for the pressure range (3-9 torr) studied. Even C_2F_6 abatement and O_2 consumption are nearly invariant over this pressure range. Fig 5-15 shows the C_2F_6 abatement and O_2 consumption as a function of flowrate and fraction of C_2F_6 in feed. Although individual extents of reaction vary with changes in process variables, the overall abatement shows relatively simple behavior with a change in parameters. Since all the products (CO_2 , COF_2 and F_2) from this process can be scrubbed with water, the shift in extents of reaction under different process conditions has relatively little impact on the practical issues involving the unit design. The plots do however show that a mix of about 40:60 C_2F_6 : O_2 is optimum for maximizing abatement with minimum power. Less than 60% O_2 in the feed leaves too little O for reaction with C_2F_6 , and anything over that results in feed dilution. This is similar to other studies where maximum F concentration (corresponding to maximum C_2F_6 dissociation) is observed at a 40:60 ratio of C_2F_6 : O_2 (Flamm, 1981).

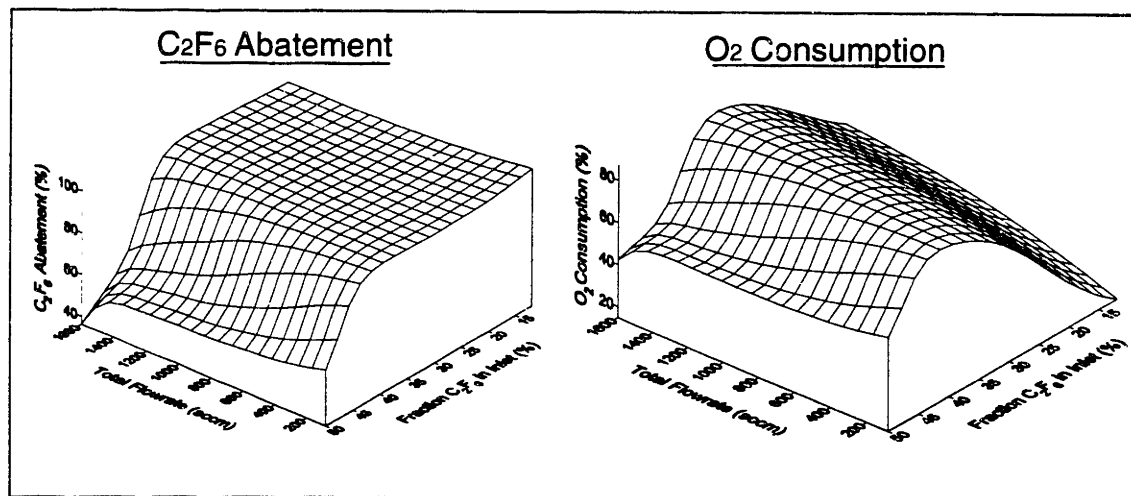


Figure 5-15: C_2F_6 abatement and O_2 Consumption as a function Flowrate and Fraction of C_2F_6 in the gas mixture . Fixed conditions for the plots: Power at 500W and Pressure at 6 torr.

5.7 Well-Mixed Reactor Model for Abatement

There are four general conclusions from C₂F₆ abatement experiments.

- Abatement is directly proportional to power.
- Abatement is inversely proportional to residence time.
- Pressure has no effect on abatement, at least over the parameter space explored.
- A C₂F₆ to O₂ ratio of 40:60 seems to be the most advantageous for abatement.

We wanted to create a model which would adequately capture this performance, and also give some predictive ability for fine tuning the process. However, coming up with a simple Plug Flow Reactor (PFR) model was not easy because of the complicated nature of the plasma. The axial Peclet numbers were on the order of 1, thereby precluding the use of a PFR approach. The reactor had severe axial temperature gradients (25°C at inlet to about 1300°C at the center of reactor), which impacted all physical properties. The plasma itself was annular requiring the need for its rigorous treatment for an accurate model. In addition, the plasma annularity and length were an unknown function of power and pressure. The plasma also had a tendency to be displaced downstream due to the convective flow. In short, an accurate model of abatement would have been very complicated and required many hours on a supercomputer for solution. As such, 2-D continuum models for Ar accounting for only the plasma physics already require multiple Cray hours to give solutions (Huppert, 1995). The attempts to couple plasma physics to plasma chemistry are fairly recent, and confined to one dimensional treatment of the plasma (Mantzaris *et al.*, 1995).

For all the reasons outlined above, a detailed kinetic and transport model was not attempted. Instead a well-mixed reactor model with a simplified reaction set was created using the important variables identified in the experiments. This well mixed reactor had four exogenous variables — Power, Flowrate, Inlet gas composition and Pressure (The code is included in Appendix C). The temperature for the reaction was fixed at 1000K, and the reactor volume was also fixed by its dimensions (0.75” diameter, 4” long with no

annularity). The elementary reactions considered in the model are listed in Table 5-4. The reaction sequence begins with the electron-impact disassociation of C_2F_6 and O_2 to give CF_3 and O respectively. CF_3 reacts with O to give COF_2 and F . COF_2 leads to CO_2 formation via an electron-impact and a radical recombination reaction. The formation of CO from electron-impact disassociation of CO_2 is also included in the reaction sequence. The rate coefficients are all taken from the literature.

Table 5-4: Reactions included in the C₂F₆ + O₂ abatement model

Reaction	Rate	Comments
$C_2F_6 \xrightarrow{e^-} CF_3 + CF_3$	$20s^{-1} \frac{[e^-]}{[e^-]_0}$	a
$CF_3 + CF_3 + M \longrightarrow C_2F_6 + M$	$k_0=2.8 \times 10^{-23} \text{ cm}^6/\text{s}$ $k_\infty=8.3 \times 10^{-12} \text{ cm}^3/\text{s}$ $Fc=0.32$	b
$O_2 \xrightarrow{e^-} O + O$	$18s^{-1} \frac{[e^-]}{[e^-]_0}$	a
$O + O + M \longrightarrow O_2 + M$	$2.7 \times 10^{-33} [M] \text{ cm}^3/\text{s}$	c
$CF_3 + O \longrightarrow COF_2 + F$	$3.1 \times 10^{-11} \text{ cm}^3/\text{s}$	d
$COF_2 \xrightarrow{e^-} COF + F$	$13.5s^{-1} \frac{[e^-]}{[e^-]_0}$	a
$COF + F + M \longrightarrow COF_2$	$k_0=6.5 \times 10^{-29} \text{ cm}^6/\text{s}$ $k_\infty=1.4 \times 10^{-11} \text{ cm}^3/\text{s}$ $Fc=0.68$	b
$COF + O \longrightarrow CO_2 + F$	$4.98 \times 10^{-11} \text{ cm}^3/\text{s}$	d
$F + F + M \longrightarrow F_2 + M$	$2.8 \times 10^{-34} [M] \text{ cm}^3/\text{s}$	e
$F_2 \xrightarrow{e^-} F + F$	$13.5s^{-1} \frac{[e^-]}{[e^-]_0}$	a
$CO_2 \xrightarrow{e^-} CO + O$	$18s^{-1} \frac{[e^-]}{[e^-]_0}$	a
$CO + F + M \longrightarrow COF$	$k_0=8.1 \times 10^{-32} \text{ cm}^6/\text{s}$ $k_\infty=9.4 \times 10^{-11} \text{ cm}^3/\text{s}$ $Fc=0.73$	b
$CO + O + M \longrightarrow CO_2 + M$	$2.25 \times 10^{-10} \frac{P(\text{in torr})}{760} \text{ cm}^3/\text{s}$	d

^a Plumb and Ryan (1986). Unimolecular constants were adjusted for our electron density.

$[e^-]_0=6 \times 10^{10} \text{ cm}^{-3}$ for Plumb and Ryan.

^b Plumb and Ryan (1986). Method of Troe (1979)

^c Reeves *et al* (1960)

^d Burgess *et al* (draft document, 1995). Constants adjusted for pressure.

^e Lloyd (1971)

The effect of changing power was incorporated in the model by changing the electron density, which was taken to be $1 \times 10^{12} \text{ cm}^{-3}$ at 700W. This was determined by adjusting the electron density till the model results matched one of the experiments conducted at 700W. This electron density was then linearly adjusted for all other powers and experimental conditions. A set of nonlinear homogeneous equations of the form

$$\frac{1}{\tau}([j]_o - [\bar{j}]) + \sum_l \sum_{m \geq l} v_{lm} k_{lm} [\bar{l}] [\bar{m}] + \sum_l v_l k_l [\bar{l}] = 0 \quad (5-30)$$

were solved to obtain the steady state values of each species. Here, τ is the residence time within the reactor, $[j]_o$ is the feed concentration of species, k_{lm} are the reaction rate coefficients of the second-order reactions involving species l and m , v_{lm} are the stoichiometric coefficients for the second-order reactions, and k_l and v_l are the first-order reaction analogues of k_{lm} and v_{lm} .

The results from this well-mixed model are shown below. For ease of comparison, the experimental results are plotted below the model output for each case. Fig 5-16 shows the comparison of % abatement, and the extents of reactions ϵ_{CO_2} and ϵ_{COF_2} as a function of fraction of C_2F_6 in inlet and power. Note that the model results are for a wider range than the experiments. The percentage of C_2F_6 in the gas feed was varied from 12% to 50% in the experiments, while the model results are shown for a ratio of 10% to 75%. The general trends for both the model and the experiments are similar. The model shows a maximum in abatement at about 48%, compared to 40% for the experiments. The variation in the extent of reaction observed experimentally is also observed in the model. However, the model underpredicts the extent ϵ_{CO_2} , and overpredicts extent ϵ_{COF_2} . This also explains why the maximum in abatement in the model is observed at 48% C_2F_6 in feed instead of the 40% observed experimentally.

Fig 5-17 shows the same plots as a function of flowrate and fraction of C_2F_6 in inlet. Again note that the range of parameter space depicted for the results from the model is wider than that for the experiments. The trends are again very similar for both the model and the experiments. The model however is unable to capture the sharp rise in ϵ_{CO_2} at low C_2F_6 fraction, and is also unable to capture the roll off in ϵ_{COF_2} at higher flowrates. Apart from that, the numbers and trends are similar.

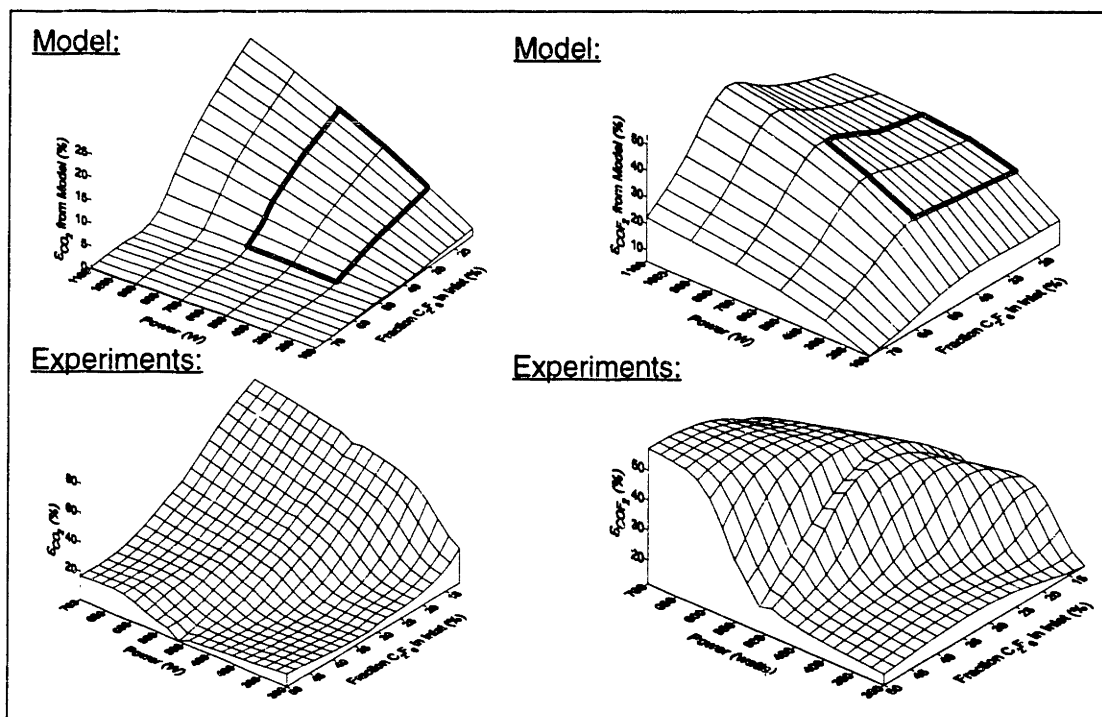


Figure 5-16: Comparison of Extents of reaction for model and experiments as a function of Power and Fraction C_2F_6 in inlet. The region over which experiments were carried out is shown in solid line in the Model plots. Fixed Conditions for the plots: Pressure at 6 torr and Flowrate at 800 sccm

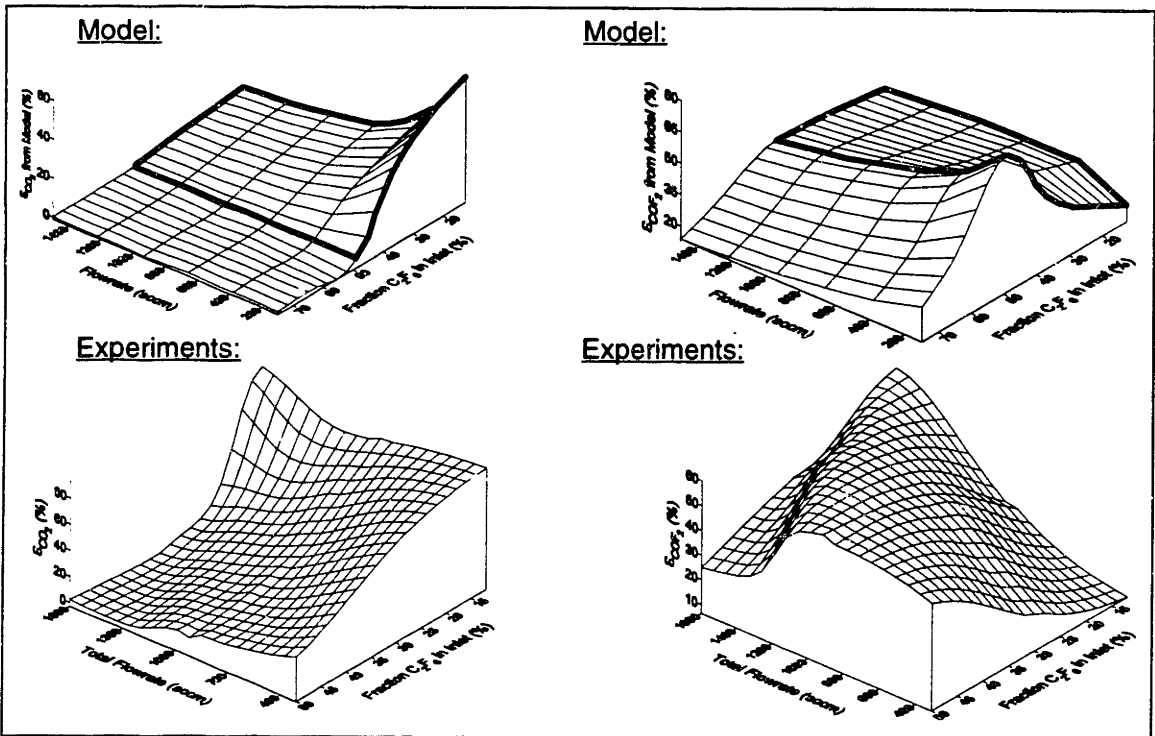


Figure 5-17: Comparison of Extents of reaction from model and experiments as a function of Flowrate and Fraction C_2F_6 in inlet. The region over which experiments were carried out is shown in solid line in the Model plots. Fixed Conditions for the plots: Pressure at 6 torr and Power at 700W

To summarize, although the simple well-mixed reactor model ignores all the complexities of flow in the reactor, it captures the essential trends fairly well. The model also predicts that most of the fluorine in the system leaves as F, and not as F_2 as observed by the mass spectrometer. In addition, the model also shows that all oxygen leaves in the atomic form. The concentration of CO is negligible compared to CO_2 , which is consistent with the equilibrium calculations carried out for these two species in other systems (Sekiguchi *et al.*, 1988). Those calculations show that the concentration of CO is negligible below temperatures of 2000K. The model also predicts much more COF_2 than COF, and some CF_3 . A sample concentration distribution from the model is shown in Table 5-5. As mentioned before, the presence of significant wall area before the effluent is injected into the mass spectrometer probably enables all of F, O and CF_3 to recombine to form F_2 , O_2 and C_2F_6 respectively.

Table 5-5: Steady state species concentrations for $C_2F_6 + O_2$ from the reactor model

<u>Plasma Parameters:</u>	<u>Steady State Results (cm^{-3}):</u>
Residence Time : 4.68 ms	C_2F_6 : 1.04×10^{16}
Electron Density : $1 \times 10^{12} cm^{-3}$	O_2 : 1.00×10^{12}
Pressure : 6 torr	CF_3 : 2.82×10^{14}
Temperature : 1000K	O : 6.48×10^{14}
C_2F_6 at inlet : $2.9 \times 10^{16} cm^{-3}$	COF_2 : 1.74×10^{16}
O_2 at inlet : $2.9 \times 10^{16} cm^{-3}$	COF : 4.39×10^{12}
	F : 1.87×10^{16}
	F_2 : 1.03×10^{13}
	CO_2 : 4.44×10^{14}
	CO : 9.12×10^{11}

5.8 Use of Abatement Unit in Integrated Circuit (IC) Fabrication Facilities

The experiments clearly show that this technology for abating C_2F_6 emissions is viable for use in a commercial IC fabrication facility. The degree of abatement is high, not only for C_2F_6 but also for other gases studied (see chapter 6). The stable products from the process can be scrubbed with water, eliminating all atmospheric emission. However, there are some issues when a technology is to be used in a commercial setting. Some of these issues are discussed in this section.

5.8.1 Deposition on Reactor Walls

During the initial experiments carried out in a standard ASTeX cavity which was not air cooled, significant black carbon-like deposition was observed on the alumina reactor walls after a C_2F_6 abatement process had run for a while. The experiments were all carried out at a $C_2F_6:O_2$ ratio of 50:50. This deposition was fairly well bonded to the reactor walls, and could not be scraped off the tube. It almost seemed to blend into the tube. This deposition is a serious concern for anybody entrusting this unit to operate in a

semiconductor fabrication facility. An XPS analysis of that residue (which sometimes grew to a thickness of about 1 mm) is shown in Fig 5-18.

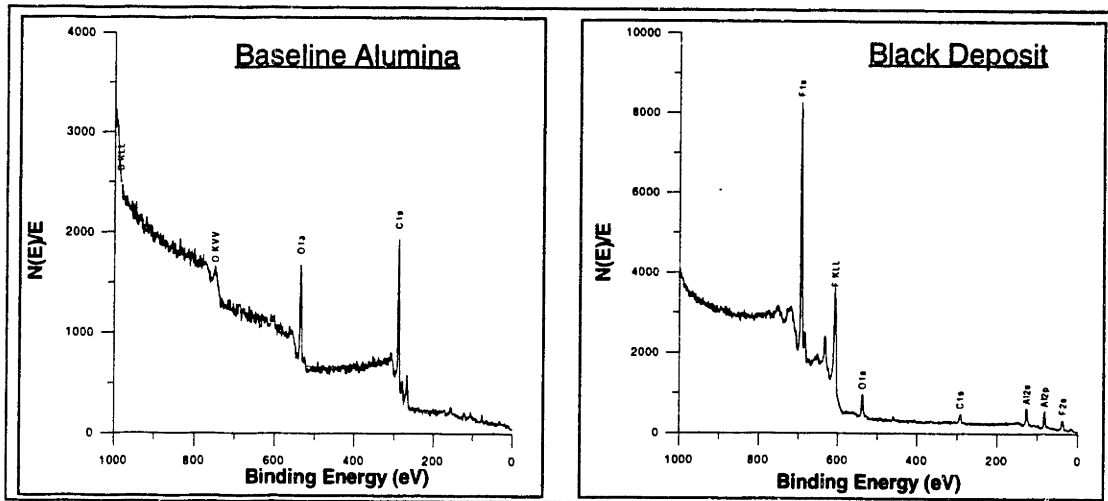


Figure 5-18: XPS analysis of black deposit on the inside of non-cooled alumina reactor wall

The XPS analysis indicated that most of the deposit comprised of F (C:F ratio of 12:88, and O:F ratio of 15:85). When air cooling was later added to the standard ASTeX applicator, deposition was still present; however, it was significantly reduced. The subsequent move to the ASTeX water cooled cavity all but eliminated the black deposition inside the tube. From these experiments it appeared that the deposition was a strong function of the inside tube temperature. The inside of the tube, which is in direct contact with the reacting mixture, is expected to get hot given the high measured temperature of the reacting gases. In fact, under conditions (*e.g.* very low power) where the plasma did not wet the entire circumference of the reactor tube, the non-wetted portion visibly glowed dull red on the inside when viewed through an axial viewport. Therefore it was quite plausible that the some form of heterogeneous cracking on the heated tube surface could be responsible for the deposition. The elimination of deposition in the water cooled cavity further supported this hypothesis.

An experiment was devised to test this hypothesis. A 0.25" alumina tube, closed on one end, was inserted into the reactor axially as depicted in Fig 5-19.

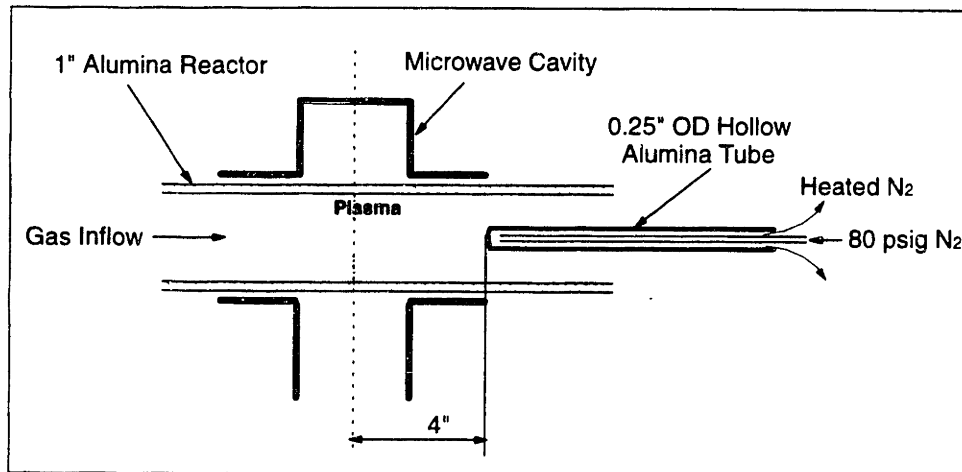


Figure 5-19: Experimental setup to determine the genesis of tube deposition

The end of the tube was located about 4" from the center of the reactor. A 50:50 mixture of C₂F₆ and O₂ was fed into the reactor and plasma was turned on at 700W for 10 minutes. After that time, the plasma and the pump were turned off and the tube extracted. There was visible pale brown deposition on the outside of the hollow tube from the process. This deposition was cleaned off using ethanol and the tube was re-inserted at the same position. This time however, a 0.125" open stainless steel (SS) tube was introduced coaxially into the alumina tube. Nitrogen at 80 psi was forced through the inner SS tube to keep the 0.25" alumina tube cool during the process. The plasma was turned on for 10 minutes. Gauging by the temperature of the N₂ escaping from the open end, the tube remained cool (10-15°C) during the entire run. The tube was re-examined after turning the plasma off, and this time no deposition was observed. When the tube was re-inserted without cooling, the deposition reappeared.

Therefore, the hypothesis that some form of heterogeneous high-temperature decomposition was responsible for the deposition was confirmed. From a manufacturing standpoint, using a water cooled ASTeX cavity should eliminate any form of deposition on the reactor tube wall.

5.8.2 Other Issues for Manufacturing

In addition to the deposition discussed above, there are other issues in the use of this unit in an IC fabrication facility. In a commercial setting, the input to the abatement unit would consist not only of C_2F_6 and O_2 , but also the products of C_2F_6 cleaning of SiO_2 CVD chambers — COF_2 , CO_2 , CO and SiF_4 (Guber and Kohler, 1995). The proportion of SiF_4 in the stream could approach 10%. There is a concern that any excess O_2 might react with SiF_4 to re-form SiO_2 which might manifest as sand particles. These “sand” particles, if formed, could pose problems for the roughing pump. This scenario is unlikely in the abatement unit however, because of the presence of excess F in the system. Fig 5-15 shows the abatement of C_2F_6 and consumption of O_2 as a function of flowrate and inlet feed composition. The C_2F_6 abatement remains near 100% even when 85% of the inlet gas is O_2 . Atomic F, which is a product of the abatement reaction, is consequently also present in the gas phase. Atomic F is known to etch SiO_2 spontaneously (Loewenstein, 1989). Therefore this F should prevent the formation of SiO_2 . If any SiO_2 does form however, this excess F should immediately react with it to form SiF_4 . Therefore, problems caused by SiO_2 formation are not expected in this setup.

Another potential concern is the issue of scale-up of the technology developed in this thesis to industrial situations. All the experiments in this thesis were carried out in a commercially available 1” diameter applicator at industrial flowrates. Therefore, the parameters are already at industrial levels and no scale-up is required. In addition, the pressure range studied is also the same as used in industry. There is the issue of plasma annularity which acts to restrict the effective plasma volume, and therefore the residence time. However, since increasing the power decreases annularity, this problem can be surmounted by increasing the applied power. In addition, if the residence time becomes important, two applicators in series could conceivably be employed to enhance the residence time.

There are some more issues in running the unit effectively. One is tuning the microwave power into the reactor. All experiments reported in this thesis used a three-stub manual tuner. It was difficult to strike the plasma under some conditions. However, once the optimal matching was achieved, only minor tuning was required to re-ignite the plasma. ASTeX has developed an auto-tuner which should be able to address the issue of tuning adequately. A more tricky problem is gauging the amount of additive O_2 required to achieve maximum abatement. There is however some process latitude here especially if the power can be increased. Excess O_2 can be added to the mixture, and the dilution effect can be countered by increasing the power. Alternately, an inline mass spectrometer can be used to gauge the composition of gas mixture into the unit, and a feedback algorithm can be used to add optimum quantity of O_2 .

A last point of importance is the fluorine emission budget of a fab. Although the emissions to air of C_2F_6 are cut down dramatically, thereby reducing the total F in the atmosphere (Zander *et al.* 1994), this process increases the fluorine emission in the water phase. This scrubbing water will have to be disposed off properly to ensure that F water emission budget is not exceeded. One alternative would be to treat this water with a base to precipitate out the fluorides in the form of a solid (*e.g.* CaF_2). This solid can then either be treated, or used in other chemical processes.

5.9 Conclusions

A simple and robust C_2F_6 abatement process has been developed and characterized. The process uses O_2 , which is already present in the mixtures used to clean PECVD chambers, as an additive gas. The gases are fed into a microwave tubular cavity where C_2F_6 is abated. The byproducts of this abatement process are CO_2 , COF_2 and F_2 , all of which can be easily scrubbed with water. The degree of C_2F_6 abatement is a strong function of the total power, residence time in the abatement unit and fraction of C_2F_6 in the inlet stream. It is directly proportional to power and inversely proportional to

residence time. An inlet composition of 40% C₂F₆ (and 60% O₂) seems to be optimal for maximum abatement. The process is also insensitive to pressure from 3-9 torr.

The abatement process developed holds commercial promise, and holds the potential to be easily transferred to IC fabrication facilities with the right choice of microwave reactor configuration.

Chapter 6: Abatement of Other Perfluorocompounds

In addition to C_2F_6 , other PFCs are also used in semiconductor fabrication. PFCs like CF_4 , SF_6 and CHF_3 are frequently used alone or as additive gases in SiO_2 etching processes. All these gases have long atmospheric lifetimes, and high global warming potentials. Therefore it would be desirable to either substitute these gases with non-PFCs, or abate them post-process to minimize their impact on the environment.

Since the microwave abatement unit was highly successful in abating C_2F_6 , we decided to study the abatement performance of the unit on three other PFCs — CF_4 , SF_6 and CHF_3 . Preliminary results on these gases were very encouraging. Therefore, a full set of design experiments was carried out to characterize the abatement of these gases as a function of four variables — Power, Pressure, Total Flowrate, and PFC: O_2 ratio in the inlet stream. The results of this study are presented in this chapter.

6.1 Abatement of CF_4

Preliminary experiments for CF_4 were carried out in an ASTeX water cooled cavity, using a 5kW microwave power supply. The HP GC/MS unit was used to analyze post-water scrubber effluent to characterize the abatement. The GC/MS column used (“M” deactivated Al_2O_3) was incapable to separating CF_4 from N_2 (used as a pump purge). Therefore Extracted Ion Chromatogram m/e 69 (CF_3^+) was used to determine the abatement. The initial experiments showed that CF_4 could be successfully abated in this unit using O_2 as an additive gas. In addition, the GC/MS did not detect any other by-products in the water-scrubbed plasma effluent. This was similar to C_2F_6 abatement, where the only species detected after water-scrubbing the effluent was C_2F_6 (in addition to purge N_2 of course). Subsequently, a set of designed experiments was carried out to characterize CF_4 abatement.

The experiments were designed and analyzed using NNAPER. The design variables studied were: Power (300-700 W), Pressure (3-9 torr), Total Flowrate (200-1400 sccm) and percent CF₄ in the inlet stream (25-75%). The rest of the inlet stream comprised of O₂. The experiments were conducted in the air-cooled ASTeX applicator. There was excellent agreement between the degree of abatement obtained using the MS and the GC/MS. Therefore the degree of abatement for these experiments was determined using the inline mass spectrometer and the peak intensity for CF₃⁺ (m/e 69) was used as a proxy for CF₄ concentration.

The results from the CF₄ designed experiments are compared to C₂F₆ results in Figures 6-1 through 6-3. The three plots show the degree of CF₄ abatement as a function of flowrate, percent CF₄ in inlet stream, pressure and power. Fig 6-1 shows the abatement as a function of flowrate and inlet stream composition at 6 torr and 700 W.

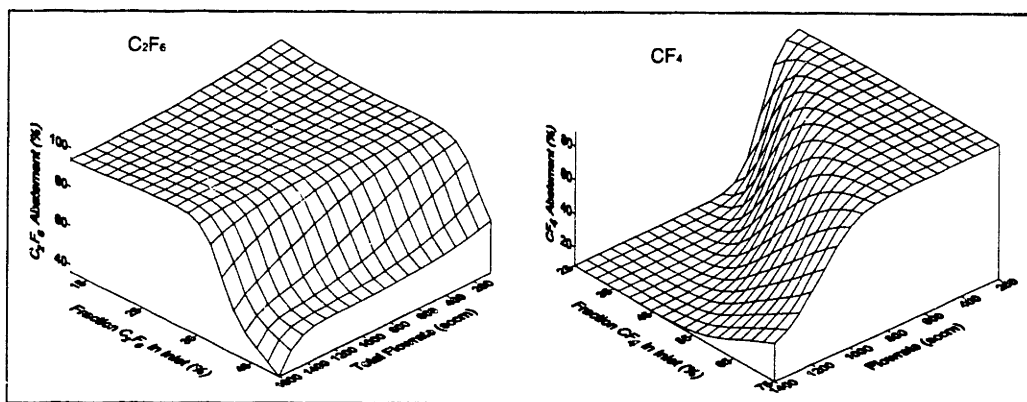


Figure 6-1: C₂F₆ vs. CF₄ abatement as a function of Fraction of PFC in Inlet and Flowrate. Fixed Conditions for the plots: Pressure at 6 torr and Power at 700W

As seen in Fig 6-1, flowrate seems to have a dramatic effect on abatement, with lower flowrates favoring abatement. The degree of abatement does not drop off until higher flowrates for CF₄ rich input streams. This behavior suggests that unlike C₂F₆ abatement, there is no optimal CF₄:O₂ ratio at least from 25-75% CF₄ in inlet. Lower fractions of O₂ actually aid the abatement process (at least till 25% O₂ in the feed). This

is probably because the Carbon to Fluorine ratio is lower in CF_4 than in C_2F_6 . The flowrate effect for CF_4 is not a simple residence time effect. This behavior is different from that of C_2F_6 . There is a limit till which the flowrate can be increased without a loss in abatement. If the flowrate is increased beyond this limit, the abatement drops off dramatically.

Fig 6-2 shows the effect of flowrate and pressure on abatement (at 700W and 75% fraction of CF_4 in inlet).

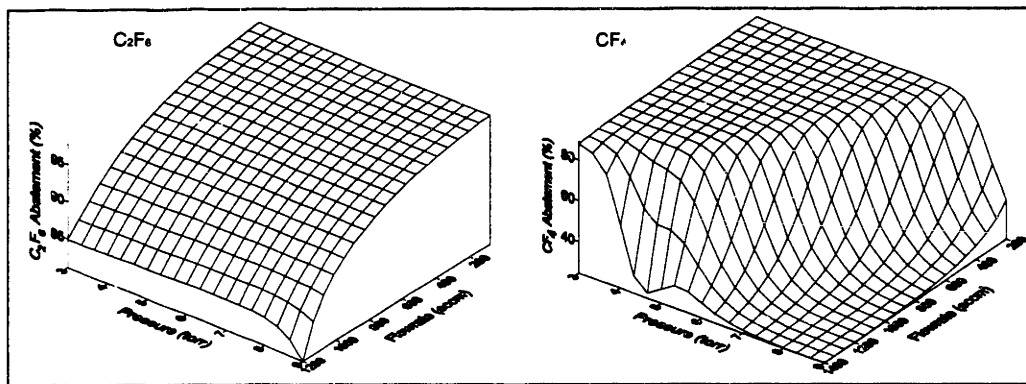


Figure 6-2: C_2F_6 vs. CF_4 abatement as a function of Pressure and Flowrate. Fixed Conditions for the plots: Power at 700W and Fraction of CF_4 in inlet at 75%

The flowrate behavior is similar to Fig 6-1. In addition, increasing pressure is detrimental to abatement, unlike for C_2F_6 where varying pressure from 3 to 9 torr had no impact on its abatement. Increasing pressure decreases CF_4 abatement in two ways. It increases the gas phase recombination rate, and also increases the annularity of the plasma causing a decrease in effective plasma volume. Fig 6-3 shows the effect of power and flowrate (75% CF_4 in inlet and 6 torr).

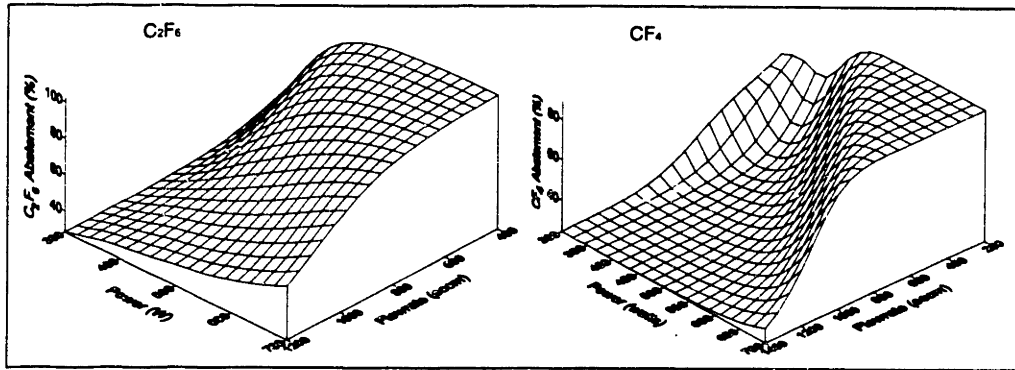


Figure 6-3: C_2F_6 vs. CF_4 abatement as a function of Power and Flowrate. Fixed Conditions for the plot: Pressure at 5 torr and Fraction of CF_4 in inlet at 75%

There is a saturation effect in power at lower flowrates. However, at higher flowrates (600-1000 sccm) the abatement is linear with increasing power initially, rapidly increases and then saturates again. At flowrates beyond 1000 sccm, the abatement is still linear with power. Again, this behavior is probably caused both by an increase in electron density (with increase in power), and by an increase in effective reactor volume as the plasma expands with increasing power.

In summary, the behavior of CF_4 abatement with a change in parameters is different from that of C_2F_6 . There is a strong pressure dependence (with lower pressures favorable to abatement), a flowrate threshold (beyond which the abatement rapidly decreases), and a power threshold (increasing the power beyond it does not affect abatement). In addition, there does not seem to be an optimum $CF_4:O_2$ ratio for abatement. CF_4 mixtures with 75% CF_4 seem to abate as well as those at 25%. Of course all these conclusions only apply within the parameter space investigated.

Fig 6-4 shows the mass spectra for CF_4 abatement, both with power off and on.

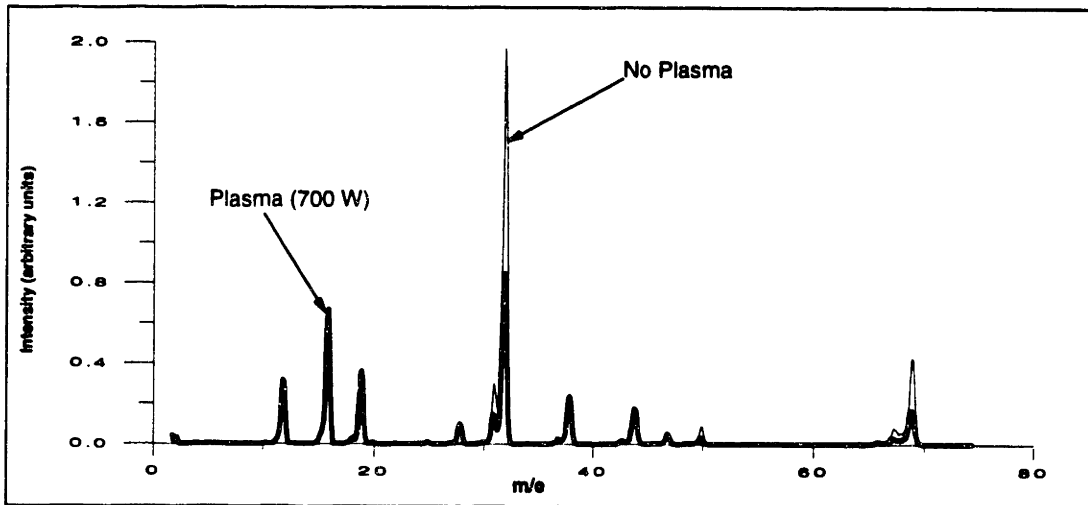
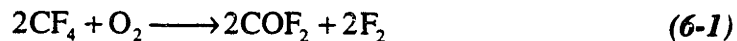


Figure 6-4: Mass spectrum for $CF_4 + O_2$ with and without plasma

The peak distribution is very similar to C_2F_6 abatement using O_2 , suggesting similar abatement mechanisms for both gases. This result is not surprising considering the similarities in the two molecules. While C_2F_6 disassociates to form CF_3 , CF_4 disassociates to form CF_2 , CF_3 and F (Plumb and Ryan, 1986). These radicals react with O (from dissociation of O_2) to form products similar to those from the reaction of CF_3 with O. Therefore, the abatement of CF_4 probably precedes via the aggregate reactions



It is easy to see why the optimal ratio of CF_4 in the input is no longer 40%. If reaction for the production of COF_2 dominates, the optimal ratio would be about 67%. However, neither of these reactions explain why this ratio would be greater than 75%, as observed experimentally.

The important conclusion from the mass spectrometer characterization of the effluent is that the major products from CF_4 abatement process are water soluble. This

was also corroborated by the GC/MS. Therefore, this abatement unit and process can be readily used to decrease the atmospheric emission of CF_4 .

6.2 Abatement of SF_6

The preliminary experiments for SF_6 gave promising abatement and also showed a strong dependence on flowrate and composition. Therefore design experiments were carried out using four design variables: Power (300-700 W), Pressure (3-9 torr), Flowrate (200-800 sccm) and Fraction of SF_6 in inlet stream (20-80%). Again O_2 was used as an additive gas. The inline Mass Spectrometer was used to characterize the abatement using peak m/e 127 (SF_5^+). Similar to C_2F_6 and CF_4 , there was again excellent agreement between the values obtained using the MS and those obtained using MTI portable GC equipped with an Al_2O_3 column. Therefore the UTI 100C MS was used for characterizing abatement.

The results from the experiments are shown in Fig 6-5 to 6-7. Fig 6-5 shows SF_6 abatement as a function of Flowrate and Fraction of SF_6 in inlet (at 6 torr and 500 W). There is a strong flowrate dependence especially at higher fractions of SF_6 in inlet. The abatement goes from near 100% at 400 sccm (at 80% SF_6 in inlet) to about 20% at 800 sccm. This effect is much stronger than can be explained by a simple residence time difference, and was also observed in the preliminary experiments where the analysis was done using the GC. Abatement is also impacted by the percent SF_6 in the inlet. At higher flowrates (greater than 500 sccm), abatement goes down with increased SF_6 in inlet, while it actually increases with fraction of SF_6 at lower flowrates. Similar to CF_4 , there is no clear optimum SF_6 to O_2 ratio. At lower flowrates, the abatement is favored by SF_6 rich streams, while at higher flowrates, lower SF_6 ratios are favorable. It should be mentioned that the flowrate effect is probably strongly dictated by the physical nature of the SF_6 plasma. The plasma for SF_6 abatement was visibly confined only to the extreme

1/16" periphery of the 0.75" ID reactor tube. Therefore, there was a significant annular region present through which the input gas could bypass the entire reaction zone.

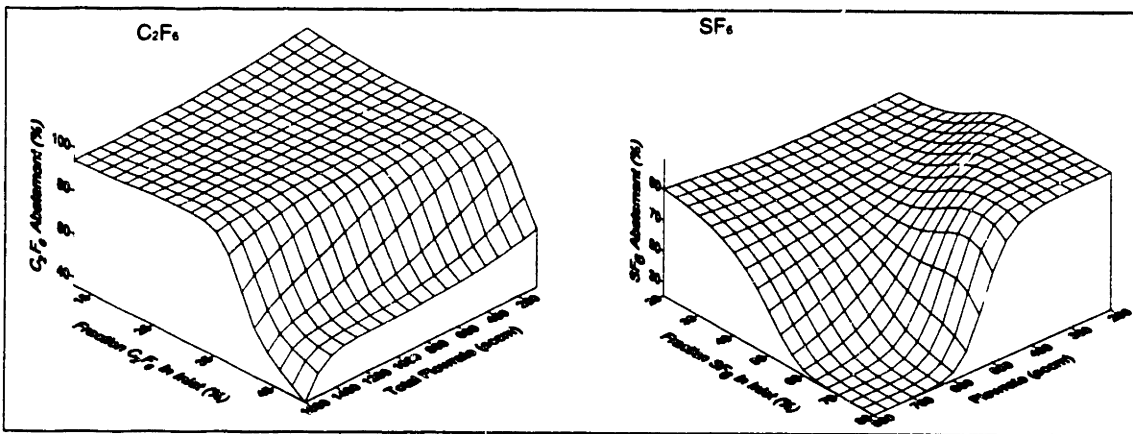


Figure 6-5: C_2F_6 vs. SF_6 abatement as a function of Flowrate and Fraction of SF_6 in inlet. Fixed conditions for plots: Pressure at 6 torr and Power at 500W

Fig 6-6 shows the abatement as a function of Pressure and Flowrate (at 500 W and 50% SF_6 concentration).

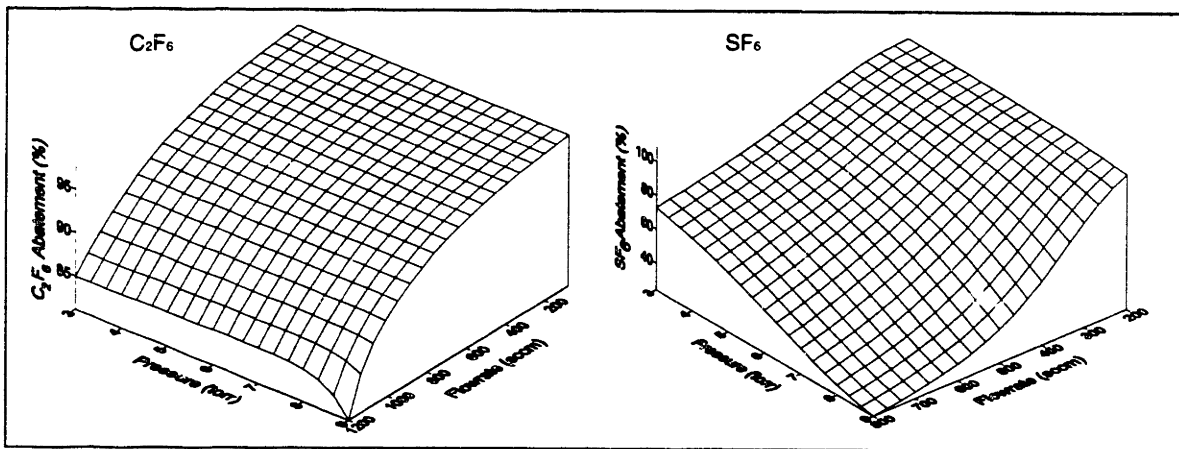


Figure 6-6: C_2F_6 vs. SF_6 abatement as a function of Pressure and Flowrate. Fixed conditions for plots: Power at 500W and Fraction of SF_6 in inlet at 50%

The strong dependence on flowrate is seen again. However, it is partially suppressed in the plot since it is drawn at 50% SF_6 concentration. As seen in Fig 6-5, the effect is really

pronounced at higher fractions of SF₆ in feed. There is a strong dependence of abatement on pressure, with the abatement dropping off by a factor of about 3.5 (from 70% to 20% at 800 sccm) as the pressure increases from 3 to 9 torr. Again, abatement is facilitated by lower pressures. This is either because gas phase recombination reactions start dominating at higher pressures, or because the plasma tends to fill less of the cross section at higher pressures. The latter is probably the dominant effect.

Fig 6-7 shows the effect of Power and Flowrate on SF₆ abatement (at 6 torr and 50% SF₆ in inlet).

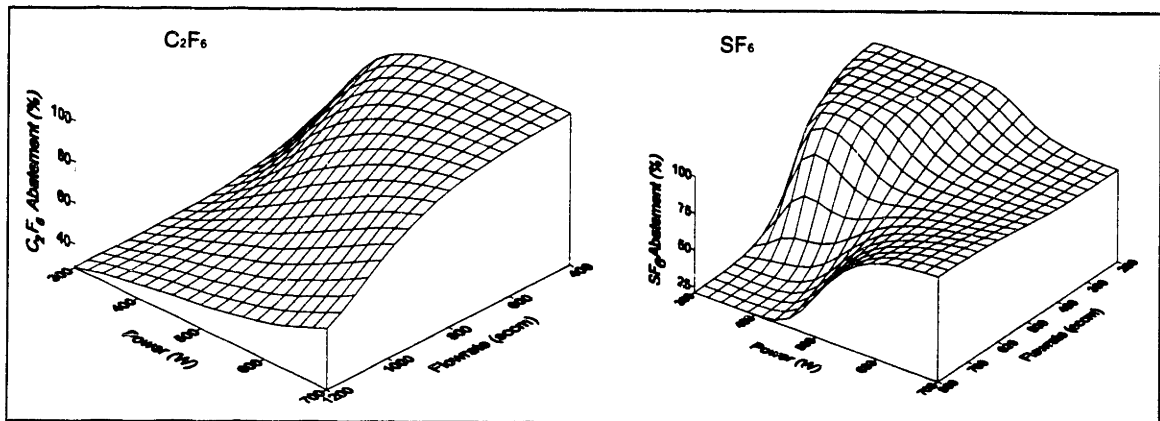
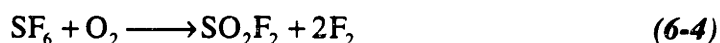


Figure 6-7: C₂F₆ vs. SF₆ abatement as a function of Power and Flowrate. Fixed conditions for plots: Pressure at 6 torr and Fraction of SF₆ in inlet at 50%

Power seems to have a dramatic effect at higher flowrates, with there being almost no abatement below 400 W (at 800 sccm). The abatement then ramps up and quickly approaches saturation. At lower flowrates, it almost appears that decreasing the power is beneficial. However, this is probably an artifact of the model, especially considering that the model predicts greater than 100% abatement in that region. Increasing power in the SF₆ system has two effects. It visually increases the effective reactor volume (and therefore residence time) by making the plasma less annular. In addition, it also leads to an enhancement in electron density, which in turn affects the electron impact dissociation reactions. Both these effects probably contribute to the observed behavior.

Fig 6-8 shows the mass spectrum for SF₆+O₂ system with and without a plasma. The species observed and their associated m/e were: O⁺ (16), F⁺ (19), O₂⁺ and S⁺ (32), SO⁺ (38), SF⁺ (51), SF₄⁺⁺ (54), SO₂⁺ (64), SFO⁺ (67), SF₂⁺ (70), SFO₂⁺ (83), SF₃⁺ (89), SF₂O₂⁺ (102), SF₄⁺ (108) and SF₅⁺ (127). No species were observed beyond m/e 127. From the Eight Peak Spectra (1995), the fewest products explaining all the peaks were SO₂, SO₂F₂ and F₂. Therefore, the postulated abatement mechanism for SF₆ is:



This reaction sequence suggests an optimal SF₆ ratio of 50% which was not observed experimentally. The overall mechanism is obviously much more complex than the one outlined above.

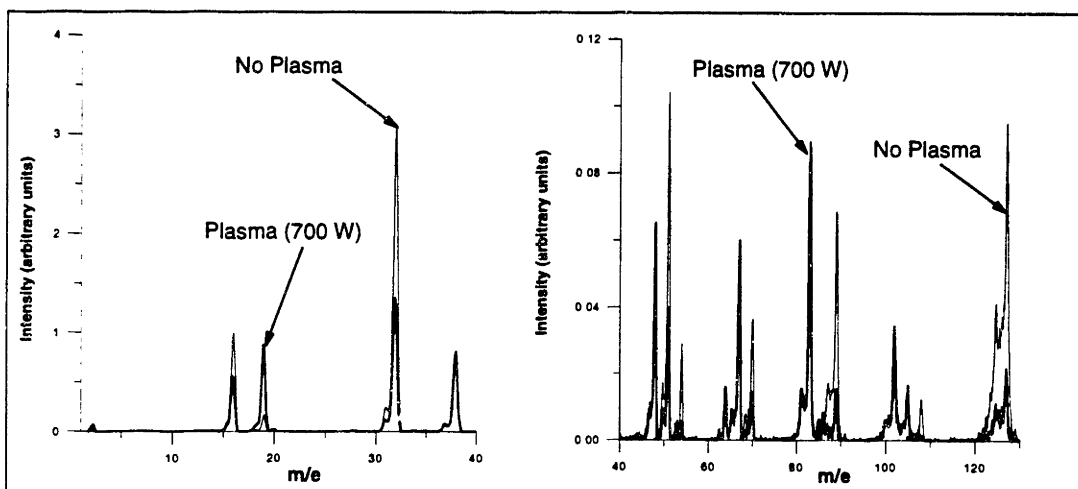


Figure 6-8: Mass spectrum for SF₆ + O₂ system with and without plasma

In summary, SF₆ abatement shows a strong flowrate dependence which is probably driven by the strong annular nature of the plasma. This annularity also results in the observed behavior with respect to power, which exhibits a similar trend as flowrate. The abatement is inversely proportional to pressure, which can also be explained by the

annular behavior of the plasma. The annularity of the plasma increases with pressure, which results in a smaller effective reactor volume. The main products from SF₆ abatement using O₂ are SO₂, SO₂F₂ and F₂, which are all water-soluble and therefore can be eliminated in a post plasma process water scrubber.

6.3 Abatement of CHF₃

The abatement of CHF₃ was investigated in the abatement reactor using O₂ as an additive gas. Fig 6-9 shows the abatement for two select conditions as characterized using the MTI P200 GC. The abatement was nearly 100% under all conditions investigated (the y-axis in the figure goes from 99% to 100%).

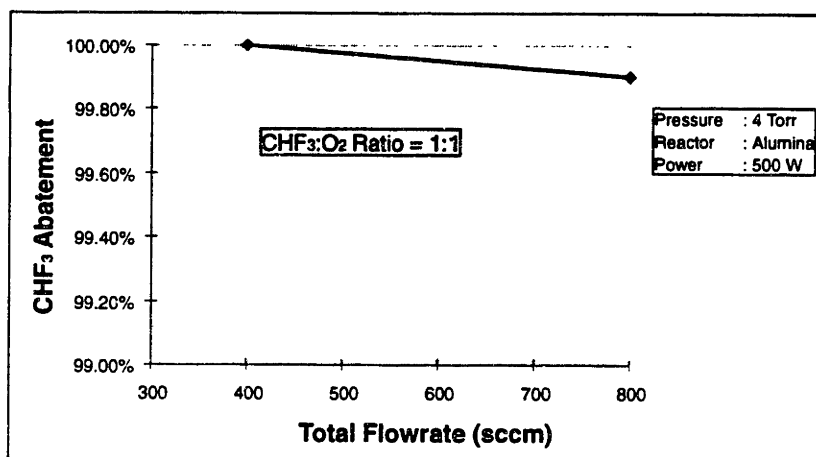


Figure 6-9: Abatement of CHF₃ in the microwave tubular reactor

The products from the abatement process were characterized using the mass spectrometer. The spectrum is shown in Fig 6-10, and indicates the presence of CO₂, COF₂, F₂ and HF as stable products. The spectrum is truncated at m/e 70 since there were no peaks beyond m/e 70.

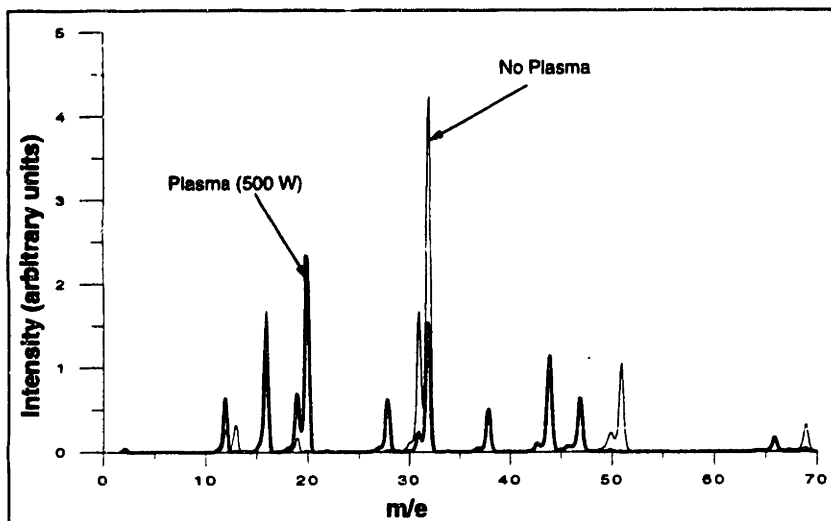
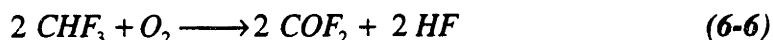
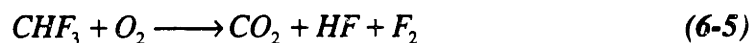


Figure 6-10: Mass spectrum for $\text{CHF}_3 + \text{O}_2$ system with and without plasma

Therefore the abatement of CHF_3 can be postulated to proceed via the following two reactions.



The actual abatement mechanism is obviously more complex than the one shown above.

6.5 Conclusions

The plasma abatement unit developed and characterized in this thesis has been used successfully to abate CF_4 , SF_6 and CHF_3 using O_2 as an additive gas. The products from the abatement of all these PFCs are water soluble. Therefore, the plasma abatement unit can be used in conjunction with a water scrubber to eliminate nearly all the emission of these PFCs to the atmosphere.

References

- Arno, J., J.W. Bevan, and M. Moisan, "Surface-wave Plasma Technology for Detoxification of Organic Waste Air Streams", *Workshop on the Treatment of Gaseous Emissions via Plasma Technologies*, NIST Gaithersburg (MD), March 19-21 (1995)
- Arnold, J. and D. Hartman, "Use of PFCs in Etching and Complexities of Identifying Alternatives", *SEMATECH PTAB Meeting*, Austin (1995)
- Bariya, A.J., H. Shan, C.W. Frank, S.A. Self, and J.P. McVittie, "The Etching of CHF_3 Plasma Polymer in Fluorine-containing Discharges", *J. Vac. Sci Technol. B*, **9** (1), 1 (1991)
- Benson, S.W., *Thermochemical Kinetics: Methods for Estimation of Thermochemical Data and Rate Parameters*, 2nd Edition, John Wiley & Sons, New York (1976)
- Barsotti, D., DuPont, *Personal Communication* (1995)
- Bhagat, P., "An Introduction to Neural Nets", *Chem. Eng. Progress*, **86** (8), 55 (1990)
- Bishop, C.M., "Neural Networks and their Applications", *Rev. Sci. Instrum.*, **65** (6), 1803 (1994)
- Burgess, D.R.F. Jr., M.R. Zachariah, W. Tsang, and P.R. Westmoreland, "Thermochemical and Chemical Kinetic Data for Fluorinated Hydrocarbons", NIST Draft Document (1995)
- Butterbaugh, J.W., D.C. Gray, and H.H. Sawin, "Plasma-surface Interactions in Fluorocarbon Etching of Silicon Dioxide", *J. Vac. Sci. Technol. B*, **9** (3), 1461 (1991)

- Chapman, B., *Glow Discharge processes: Sputtering and Plasma Etching*, John Wiley and Sons, New York (1980)
- "CFCs to Blame, it's conclusive", *Chemistry & Industry*, p3 (Jan 2, 1995)
- Coburn, J.W., and H.F. Winters, "Ion and Electron-Assisted Gas-Surface Chemistry — An Important Effect in Plasma Etching", *J. Appl. Phys.* **50** (5), 3189 (1979).
- Coburn, J.W., and M. Chen, "Dependence of f atom Density on Pressure and Flow rate in CF₄ Glow Discharges as determined by Emission Spectroscopy", *J. Vac. Sci. Technol.*, **18** (2), 353 (1981)
- Cooper, D.L., T.P. Cunningham, N.L. Allan, and A. McCulloch, "Potential CFC Replacements: Tropospheric Lifetimes of C₃ Hydrofluorocarbons and Hydrofluoroethers", *Atmospheric Environment*, **27A** (1), 117 (1993)
- Dalton, T.J., "Pattern Dependencies in the Plasma Etching of Polysilicon", *PhD Dissertation*, MIT, Cambridge (1994)
- Eight Peak Index of Mass Spectra*, The Royal Society of Chemistry (1991)
- Flamm, D.L., "Mechanisms of Radical Production in CF₃Cl, CF₃Br, and Related Plasma Etching Gases: The Role of Added Oxidants", *Plasma Chem. and Plasma Processing*, **1** (1), 37 (1981)
- Gierczak, T., R. Talukdar, G.L. Vaghjiani, E.R. Lovejoy, and A.R. Ravishankara, "Atmospheric Fate of Hydrofluoroethanes and Hydrofluorochloroethanes: I. Rate Coefficients for Reactions with OH", *J. Geophys. Res.*, **96** (D3), 5001(1991)
- Gray, D.C., "Beam Simulations Studies of Plasma-Surface Interactions in Fluorocarbon Etching of Si and SiO₂", *PhD Dissertation*, MIT, Cambridge(1992)
- Griffith, J.E., D.A. Grigg, M.J. Vasile, P.E. Russell, and E.A. Fitzgerald, "Scanning Force Metrology", *J. Vac. Sci. Technol. A*, **10** (4), 674 (1992)

- Griffith, J.E., D.A. Grigg, M.J. Vasile, P.E., Russell, and E.A. Fitzgerald, "Characterization of Scanning Probe Microscope Tips for Linewidth Measurements", *J. Vac. Sci. Technol. B*, **9** (6), 3586 (1991)
- Guber, A.E., and U.Kohler, "FTIR Spectroscopy for the Analysis of Selected Exhaust Gas Flows in Silicon Technology", *Journal of Molecular Structure*, 348, p209 (1995)
- Herzberg, G.H., *Molecular Spectra and Molecular Structure*, Van Nostrand Reinhold Company (New York, 1950)
- Hewlett Packard 5890 Series II Operating Manual (1994)
- Hu, Y-Z, "Scrubbing Characteristics of CCl_4 and C_2F_6 with a Titanium Sublimation Trap", *J. Vac. Sci. Technol. A*, **6** (3), 1255 (1988)
- Huppert, G.L., "2-D Simulations of RF Glow Discharges", *PhD Dissertation*, MIT, Cambridge (1995)
- Kiss, L.D.B., "Study of Plasma Chemical Kinetics by Modulated Power Relaxation", *PhD Dissertation*, MIT, Cambridge (1992)
- Kiss, L.D.B., and H.H. Sawin, "Comparison of CF_3Cl and $\text{C}_2\text{F}_6 + \text{Cl}_2$ Plasma Chemistry by Power Modulation", *J. Electrochem. Soc.*, **139** (5), 1414 (1992b)
- Kiss, L.D.B., and H.H. Sawin, "Evaluation of CF_4 Plasma Chemistry by Power Modulation", *Plasma Chem. Plasma Proc.*, **12** (4), 523 (1992a)
- Kiss, L.D.B., and H.H. Sawin, "Power Modulation Study of Chemical Kinetics in rf Discharges", *Plasma Chem. Plasma Proc.*, **12** (4), 495 (1992c)
- Kiss, L.D.B., J.P. Nicolai, W.T. Conner, and H.H. Sawin, "CF and CF_2 Actinometry in a CF_4/Ar Plasma", *J. Appl. Phys.*, **71** (7), 3186 (1992d)

- Kitamura, M., H. Akiya, and T. Urisu, "Polymer Deposition and Etching Mechanisms in C_2F_6 Radio-Frequency Plasma as Studied by Laser-Induced Fluorescence", *J. Vac. Sci. Technol. B*, **7** (1) 14 (1989)
- Lee, K.L., D.W. Abraham, F. Secord, and L. Landstein, "Submicron Si Trench Profiling with an Electron-Beam Fabricated Atomic Force Microscope Tip", *J. Vac. Sci. Technol. B*, **9** (6), 3562 (1991)
- Liu, J., "Scaling Relationships for Power Deposition and Ion Bombardment in Radio-Frequency Plasmas", *PhD Dissertation*, MIT, Cambridge (1992)
- Lloyd, A.C., "A Critical Review of the Kinetics of the Dissociation-Recombination Reactions of Fluorine and Chlorine", *International Journal of Chemical Kinetics*, Vol. **III**, 39-68 (1971)
- Loewenstein, L.M., "Temperature Dependence of Silicon Nitride Etching by Atomic Fluorine", *J. Appl. Phys.*, **65** (1), 386 (1989)
- Mantzaris, N.V., A. Boudouvis, and E. Gogolides, "Radio-Frequency Plasmas in CF_4 : Self-Consistent Modeling of the Plasma Physics and Chemistry", *J. Appl. Phys.*, **77** (12), 6169 (1995)
- Mocella, M.T., "PFC Emission Control: A Status Report on Options and technology", *Perfluorocompound (PFC) Technical Update*, SEMICON West Technical Seminar (1995)
- Mocella, M.T., J.A. Bondur, and T.R. Turner, "Process Module Metrology, Control and Clustering", *SPIE Proceedings*, **1594**, 232 (1992)
- Mocella, M.T., V. Mohindra, and H.H. Sawin, "Options for Environmentally Impacted Perfluorinated Gases Used in Plasma Processing", *Proceedings of the Tenth Symposium on Plasma Etching*, Vol **94-20**, p 192 The Electrochemical Society (1994)

- Mohindra, V., H.H. Sawin, M.T. Mocella, J.M. Cook, J. Flanner, and O. Turmel, "Alternatives to Perfluorocompounds as Plasma Processing Gases: SiO₂ Etching Using C₂F₅H and C₂F₄H₂", *Proceedings of the Tenth Symposium on Plasma Etching*, Vol **94-20**, p 300, The Electrochemical Society (1994)
- Moody, J., and C.J. Darken, "Fast Learning in Networks of Locally-Tuned Processing units", *Neural Computation*, **1**, 281 (1989)
- Newboe, B., "Warning: Is Your Product Made With CFCs?" *Semiconductor International*, p48 (Nov. 1993)
- Nordhaus, W.D., "An Optimal Transition Path for Controlling Greenhouse Gases", *Science*, **258** (20), 1315 (1992)
- Orlando, J.J., J.B. Burkholder, S.A. McKeen, and A.R. Ravishankara, "Atmospheric Fate of Several Hydrofluoroethanes and Hydrochloroethanes: 2. UV Absorption Cross Sections and Atmospheric Lifetimes", *J. Geophys. Res.*, **96** (D3), 5013 (1991)
- Plumb, I.C. and K.R. Ryan, "A Model of Chemical Processes occurring in CF₄/O₂ Discharges Used in Plasma Etching", *Plasma Chem. and Plasma Proc.*, **6** (3), 205 (1986)
- Ravishankara, A.R., A.A. Turnipseed, N.R. Jensen, S. Barone, M. Mills, C.J. Howard, and S. Solomon, "Do Hydrofluorocarbons Destroy Stratospheric Ozone?", *Science*, **263**, p71 (1994)
- Ravishankara, A.R., S. Solomon, A.A. Turnipseed, and R.F. Warren, "Atmospheric Lifetimes of Long-Lived Halogenated Species", *Science*, **259**, 194 (1993)
- Reeves, R.R., G. Mannella, and P. Harteck, "Rate of Recombination of Oxygen Atoms", *J. Chem. Phys.*, **32**, 632 (1960)
- Reid, R.C., J.M. Prausnitz, and T.K. Sherwood, *The Properties of Gases and Liquids*, 3rd Edition, McGraw-Hill Book Company, New York (1977)

- Ridgeway, R.G., J.G. Langan, P.J. Maroulis, and R.J. Richardson, "Strategy to Minimize Environmental Impact of PFC Gases Used in the Semiconductor Industry", *SEMATECH PTAB Meeting*, Austin (1995)
- Rotmans, J., *IMAGE: An Integrated Model to Assess the Greenhouse Effect*, Kluwer Academic Publishers (Boston, 1990)
- Sawin, H.H., and R. Reif, *Plasma Processing for Microelectronics Fabrication*, MIT (1995)
- Schneider, W.F., and T.J. Wallington, "Thermochemistry of COF₂ and Related Compounds", *J. of Physical Chemistry*, **98** (31), 7448 (1994)
- Sekiguchi, H., A. Kanzawa, and T. Honda, "Thermal Quenching Effects on Plasma Synthesis of NO and Plasma Decomposition of CO₂", *Plasma Chem. and Plasma Processing*, **9** (2), 257 (1989)
- Stephan, K., H. Deutsch, and T.D. Mark, "Absolute Partial and Total Electron Impact Ionization Cross Sections for CF₄ from Threshold up to 180 eV", *Journal of Chemical Physics*, **83** (11), 5712 (1985)
- Stix, T.H., "Removal of Chlorofluorocarbons from Earth's Atmosphere", *J. Appl. Phys.*, **66** (111), 5622 (1989)
- Stone, C.S., "Optimization of a PECVD Chamber Clean Process Utilizing C₃F₈ with Reduced Gas Flows", *SEMATECH PTAB Meeting*, Austin (1995)
- Striganov, A.R., and N.S. Sventitskii, *Tables of Spectral Lines of Neutral and Ionized Atoms*, Plenum (New York, 1968)
- Svehla, R.A., *Estimated Viscosities and Thermal Conductivities of Gases at High Temperatures*, NASA Technical Report R-132, Lewis Research Center, (1962)

Troe, J., "Predictive Possibilities of Unimolecular Rate Theory", *J. Physical Chemistry*, **83** (1) 114 (1979)

UTI 100C Operating and Service Manual (CA)

Walkup, R.E., K.L. Saenger, and G.S. Selwyn , "Studies of Atomic Oxygen in O₂ + CF₄ RF Discharges by Two-Photon Laser-Induced Fluorescence and Optical Emission Spectroscopy", *J. Chem. Phys.*, **84** (5), 2668 (1986)

Worth, W., SEMATECH, Pvt. Communication (1995).

Zander, R., C.P. Rinsland, E. Mahieu, M.R. Gunson, C.B. Farmer, M.C. Abrams, and M.K.W. Ko, "Increase in Carbonyl Fluoride (COF₂) in the Stratosphere and its Contribution to the 1992 Budget of Inorganic Fluorine in the Upper Stratosphere", *J. Geophysical Research*, **99** (D8), 16737 (1994)

Zau, G.C.H., J.W. Butterbaugh, P. Rummel, and H.H. Sawin, "Monitoring and Control of Real Power in RF Plasma Processing", *J. Electrochem. Soc.*, **138** (3), 872 (1991)

Zurer, P., "CFC Substitutes Proven Safe for Ozone Layer", *C&EN*, p5 (Jan 10, 1994)

Appendix A: Drawings for the Modulation Reactor

Figure A-0(a) 3" Symmetric Configuration

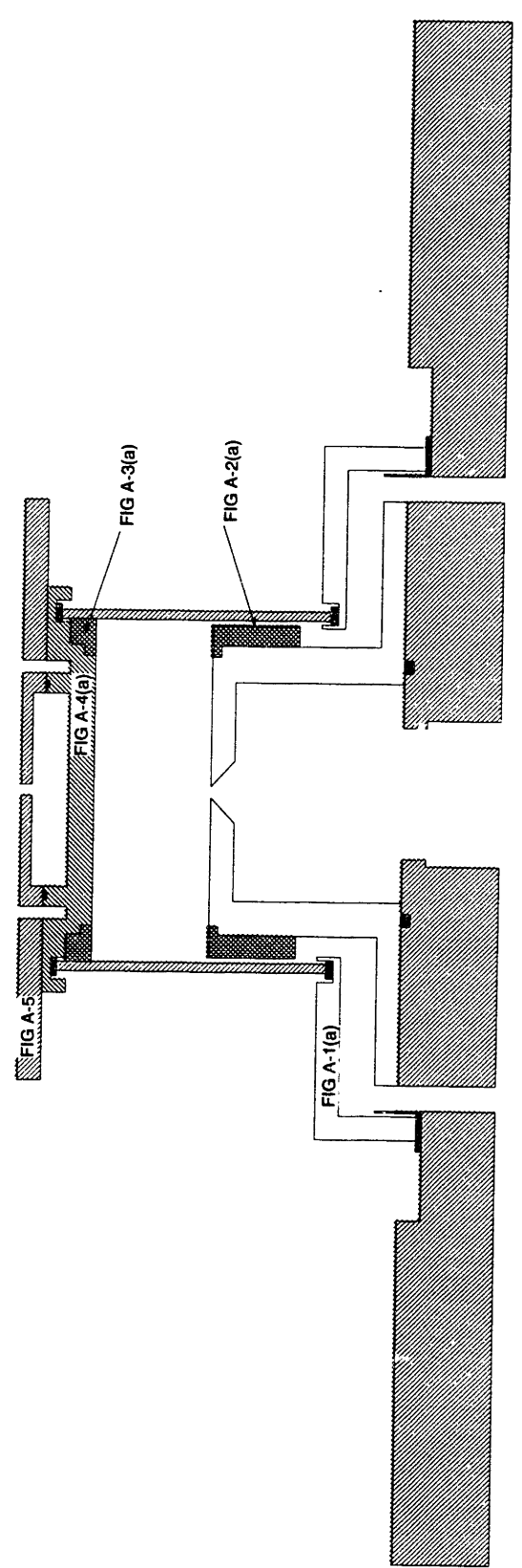


Figure A-0(b) 3"-4.5" Asymmetric Configuration

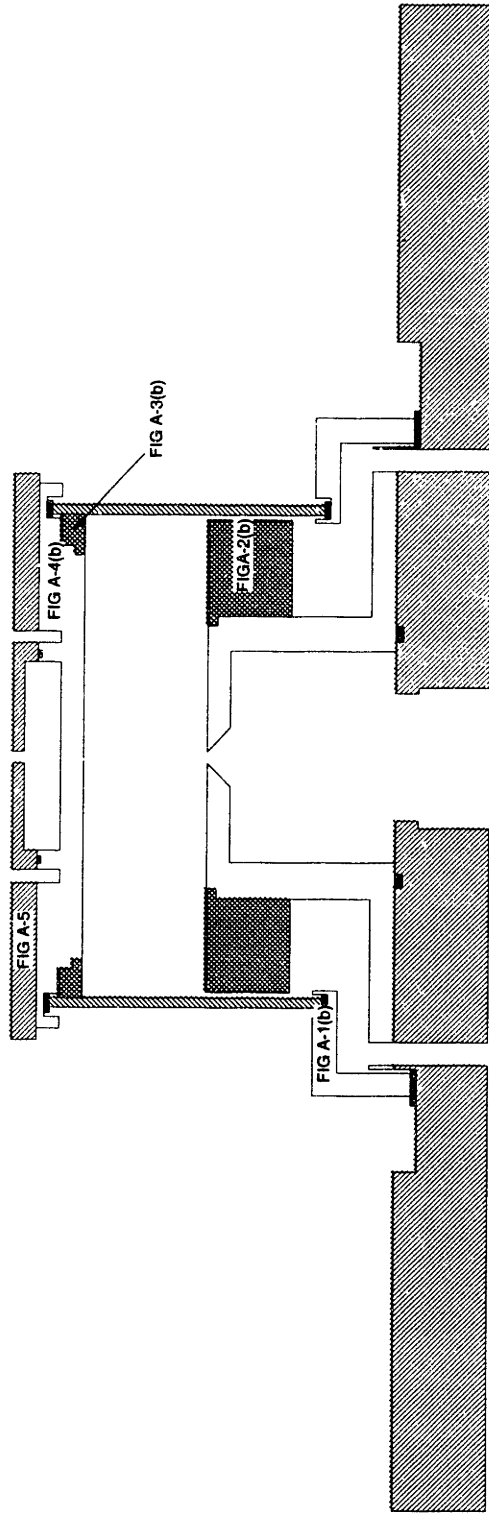


Figure A-0(c) 3" - 6" Asymmetric Configuration

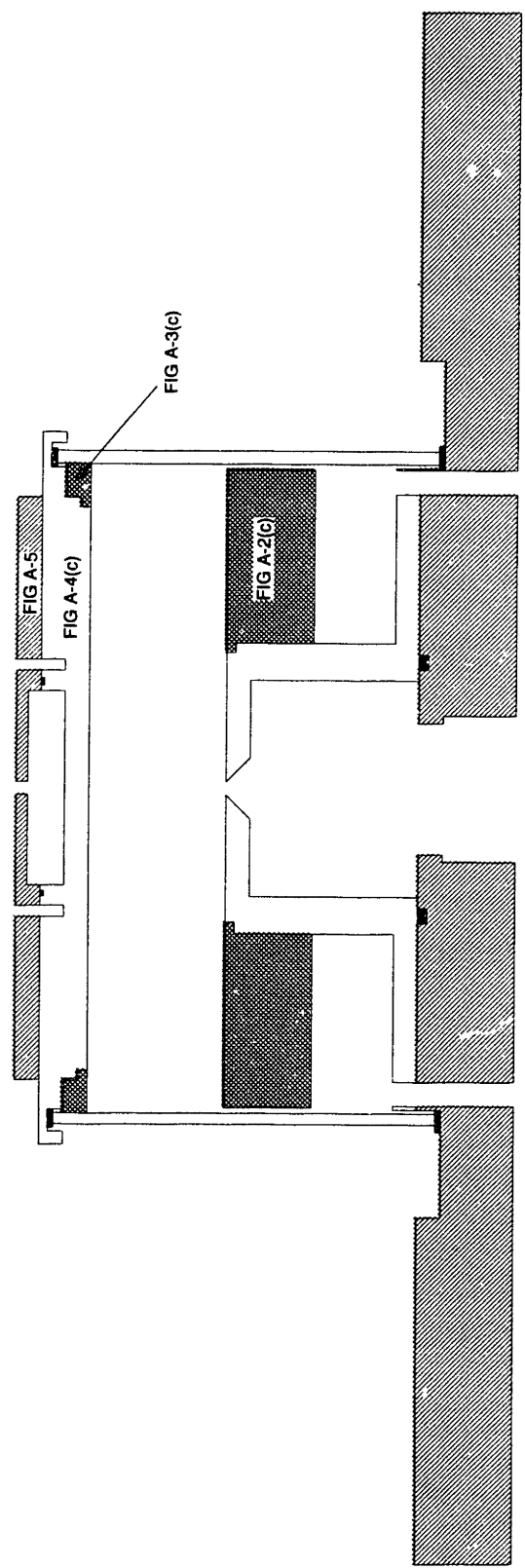
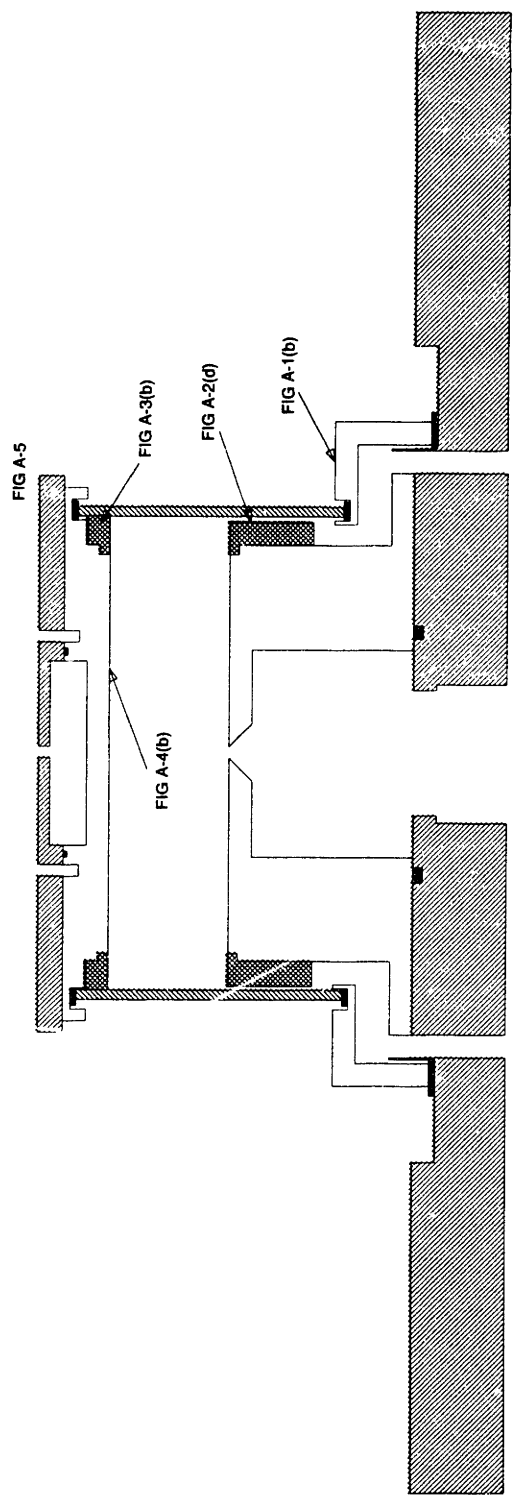


Fig A-0(d) 4.5" Symmetric Configuration



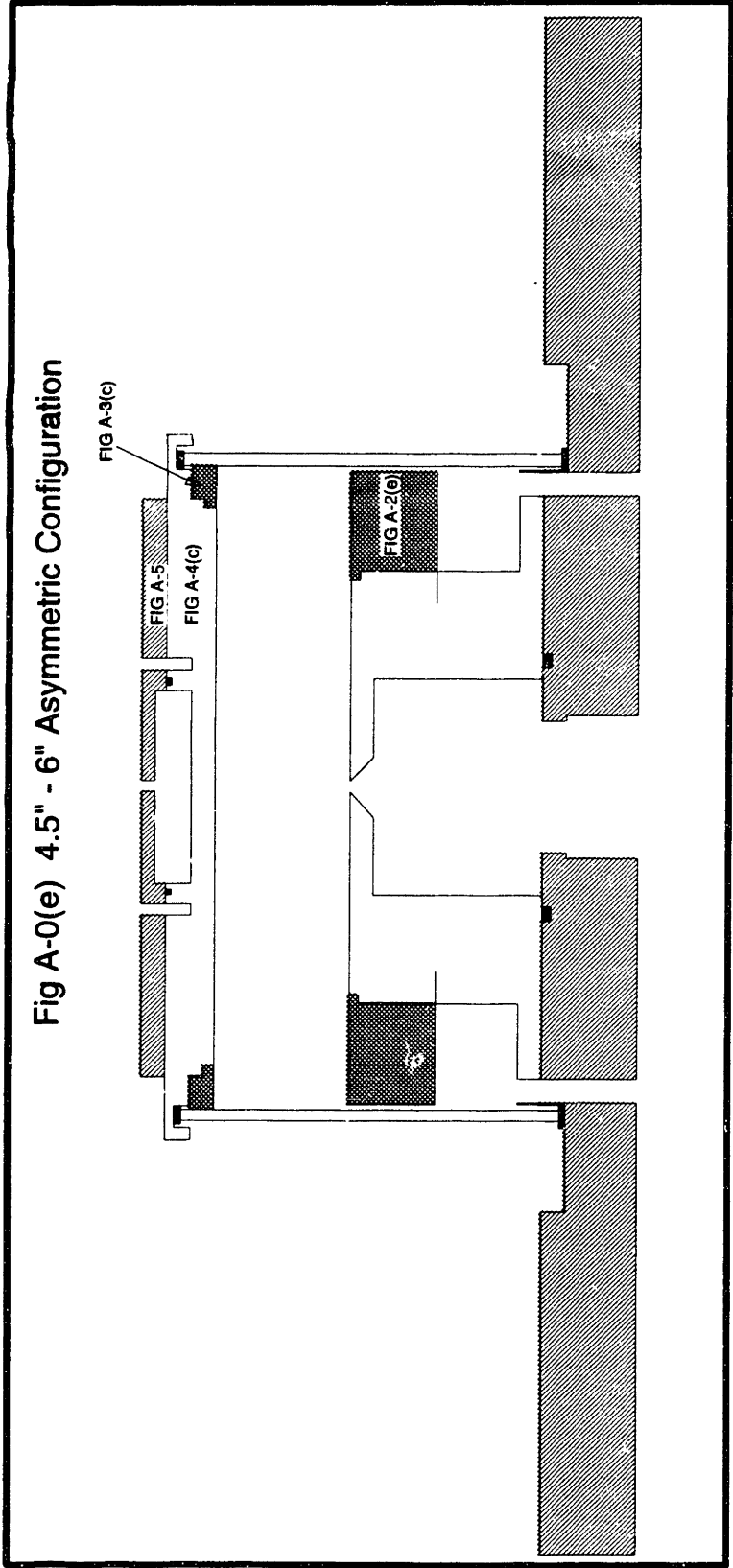
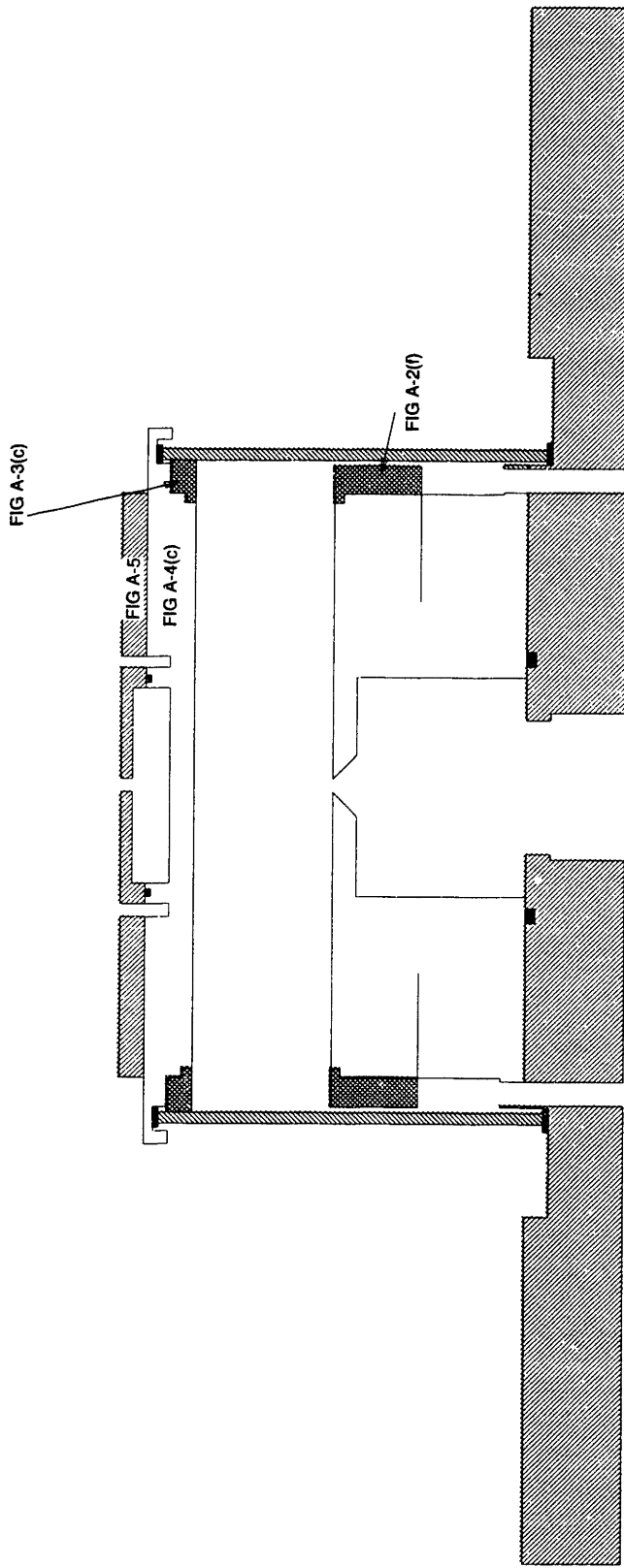


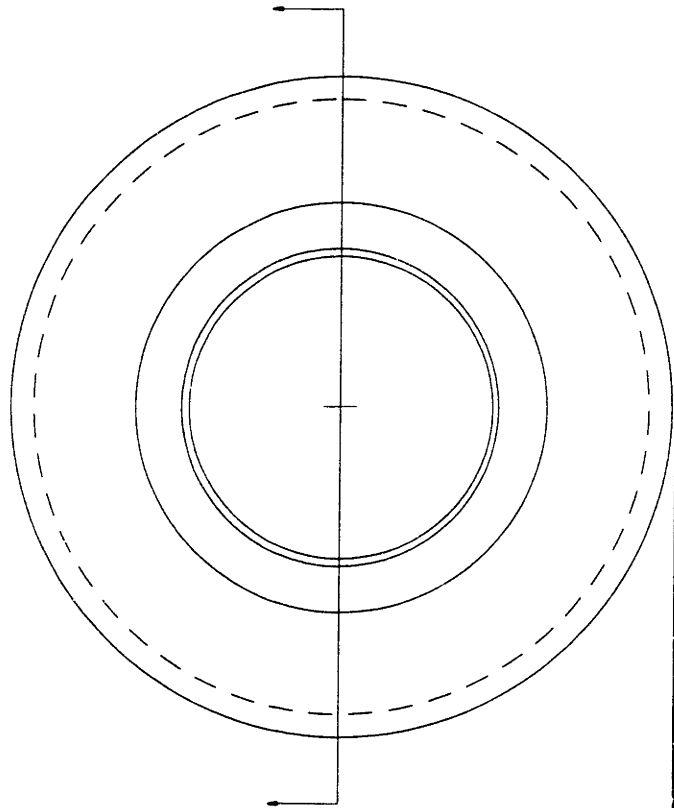
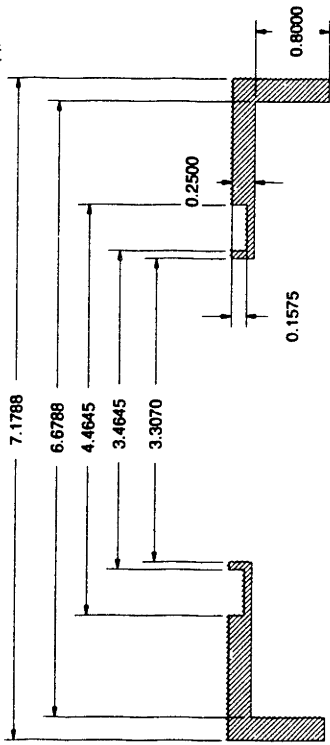
Fig A-0(f) 6" Symmetric Configuration



All Units in Inches
Material: Stainless Steel

Vivek Mohindra
66-217 MIT
Department of Chemical Engg
25 Ames Str, Cambridge, MA 02139
617-253-8912 (o), 617-253-9695

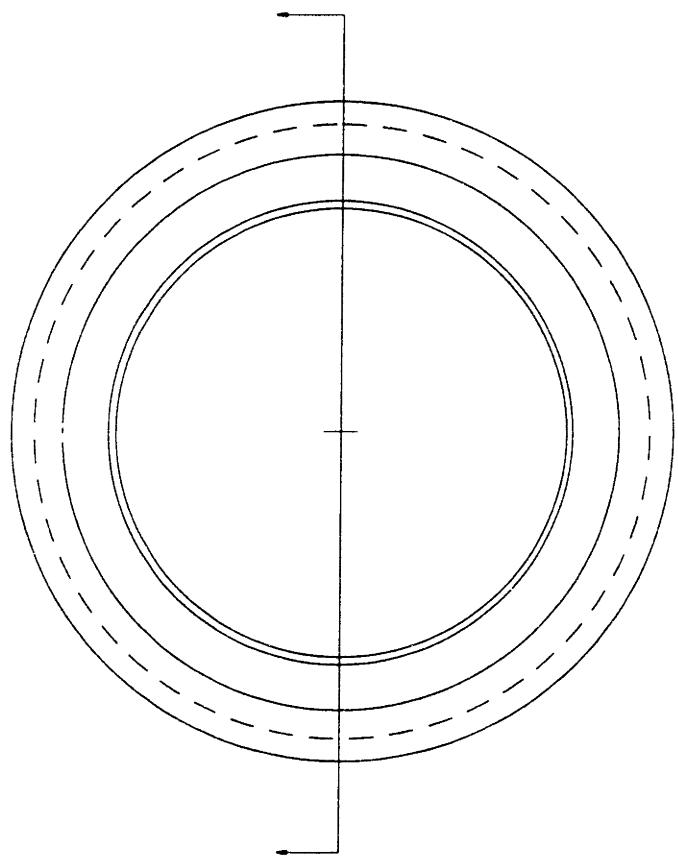
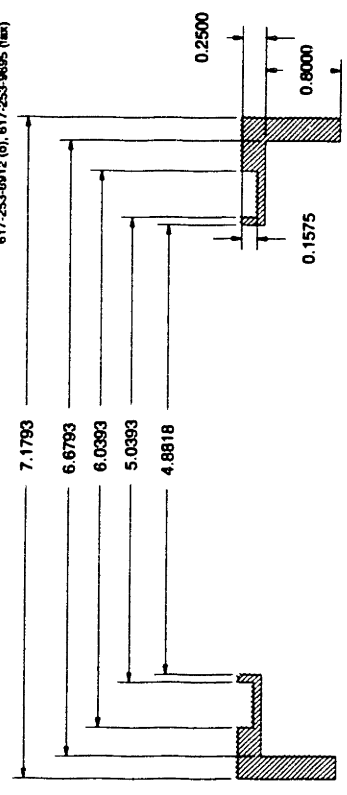
Figure A-1(a) Adapter-3"



All Units in Inches
Material: Stainless Steel

Vivek Mishra
66-217 MIT
Department of Chemical Engrg.
25 Amos St. Cambridge, MA 02139
617-253-8912 (e), 617-253-8695 (fax)

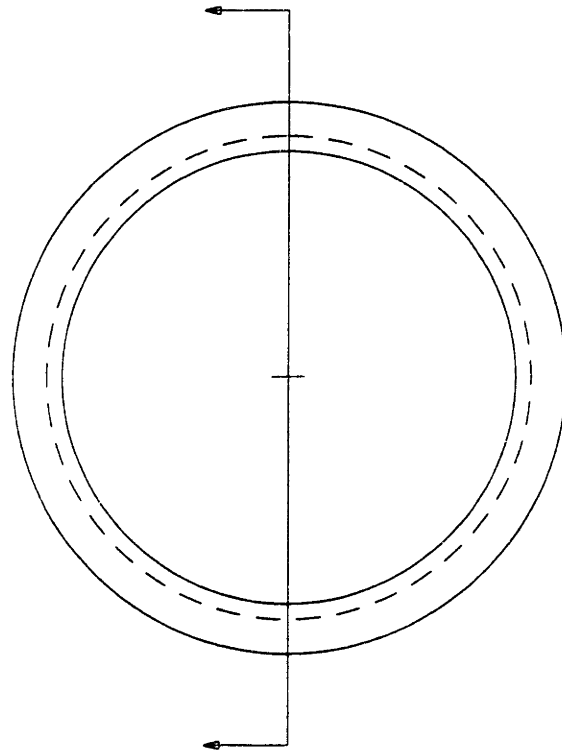
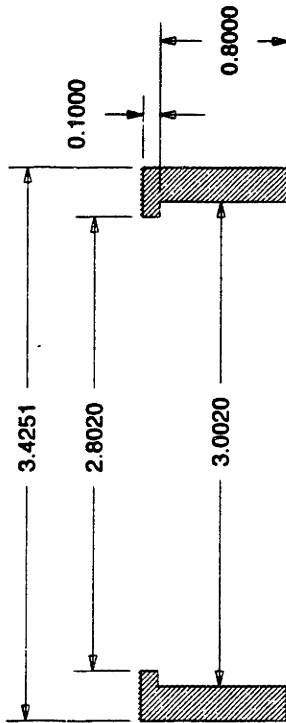
Figure A-1(b) Adapter-4.5"



All Units in Inches
Material: Teflon

Vivek Mohindra
66-217 MIT
Department of Chemical Engrg
25 Ames Str., Cambridge, MA 02139
617-253-8912 (o); 617-253-9695 (fax)

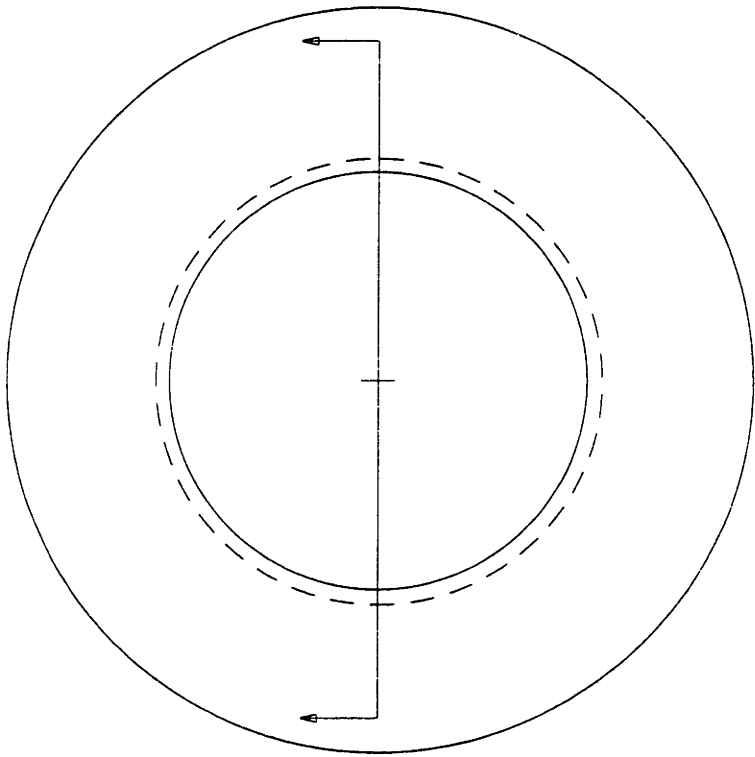
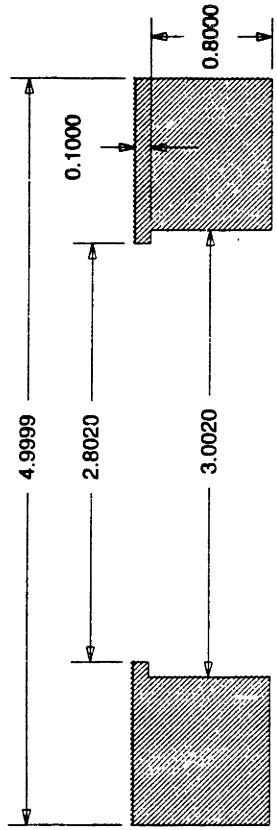
Figure A-2(a) Spacer 3"-3"



All Units in Inches
Material: Teflon

Vivek Mohindra
66-217 MIT
Department of Chemical Engg.
25 Ames St., Cambridge, MA 02139
617-253-6912 (c), 617-253-9695 (fax)

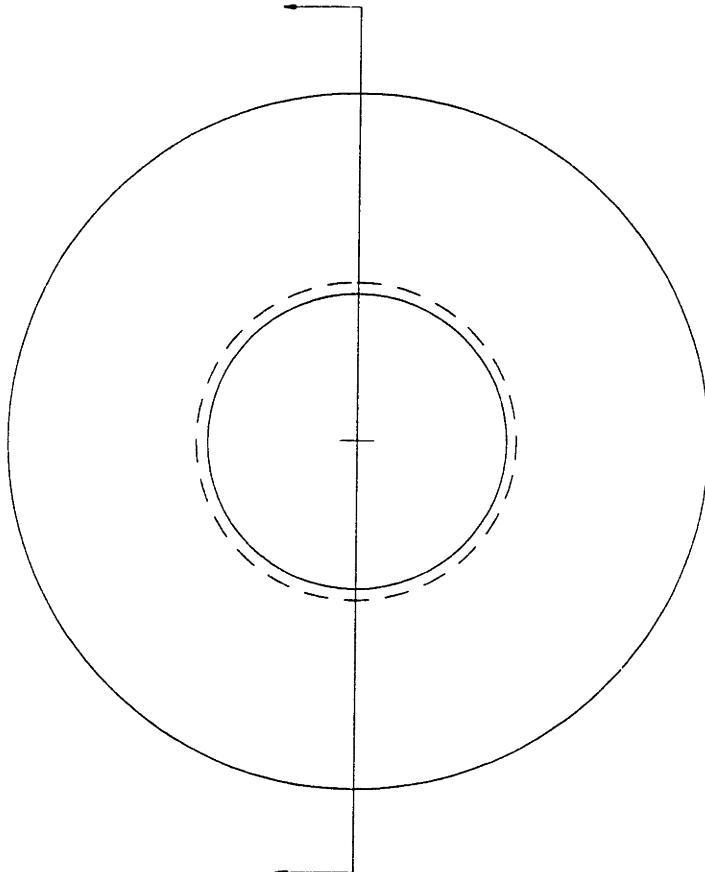
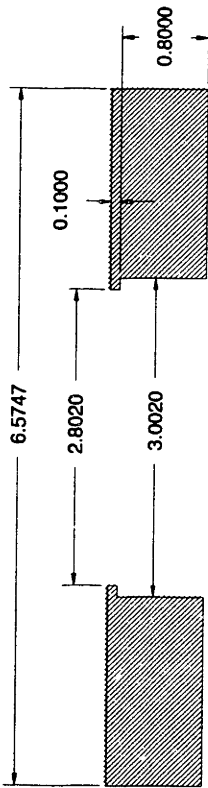
Figure A-2(b) Spacer 3"-4.5"



All Units in Inches
Material: Teflon

Vivek Mohindra
66-217 MIT
Department of Chemical Engrg.
25 Ames St., Cambridge, MA 02139
617-253-8912 (o); 617-253-9695 (fax)

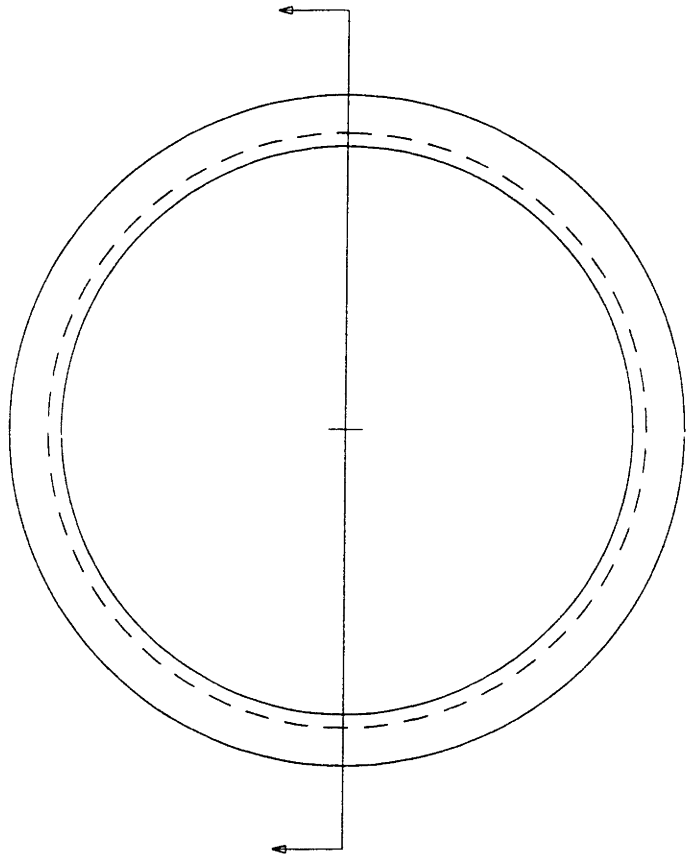
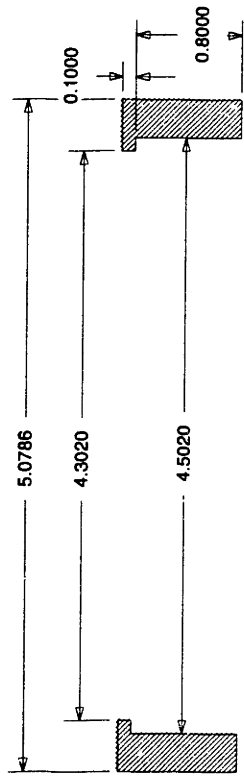
Figure A-2(c): Spacer 3"-6"



All Units in Inches
Material: Teflon
(0.5 mm clearance)

Vivek Mohindra
66-217 MIT
Department of Chemical Engg.
25 Ames Str, Cambridge, MA 02139
617-253-8912 (o); 617-253-9695 (fax)

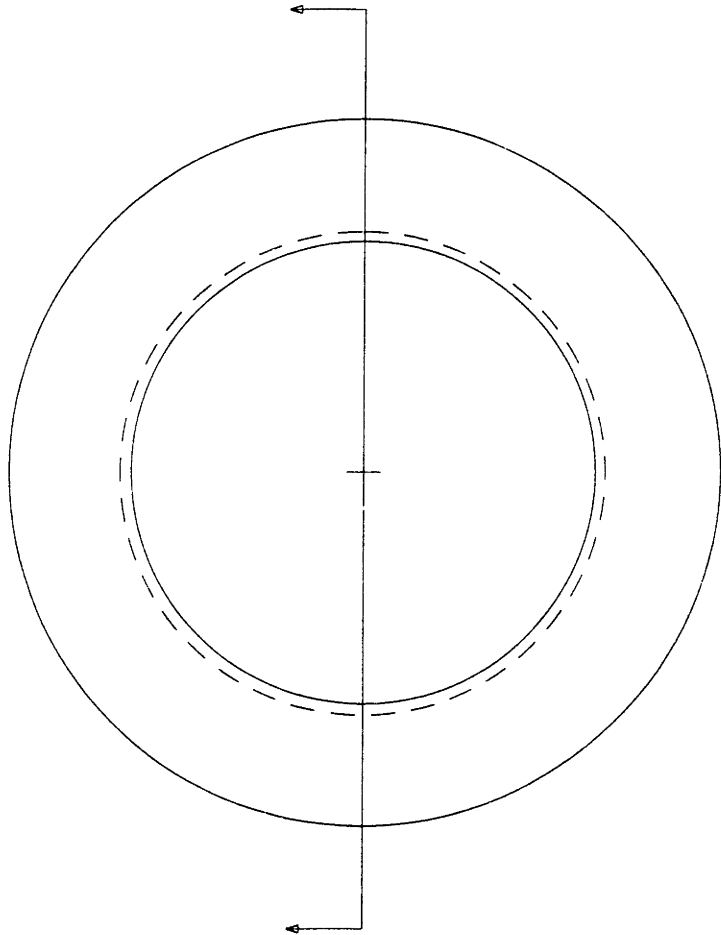
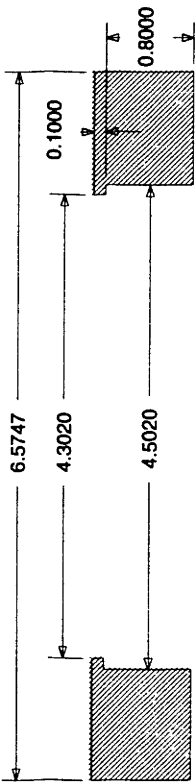
Fig 2(d): Spacer 4.5"-4.5"



All Units of Inches
Material: Teflon

Vivek Mohindra
66-217 MIT
Department of Chemical Engg.
25 Ames St, Cambridge, MA 02139
617-253-8912 (o); 617-253-9695 (fax)

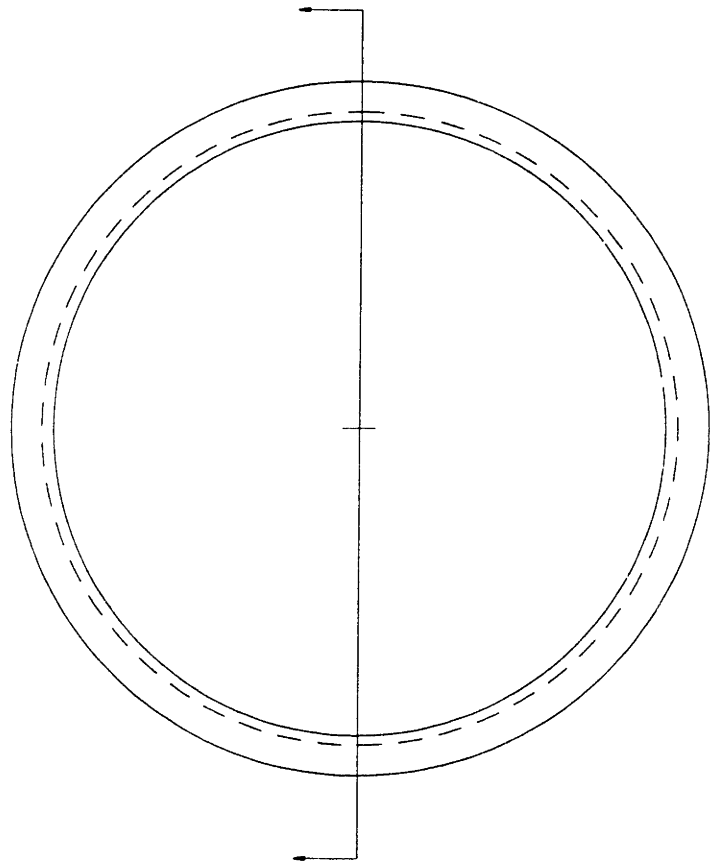
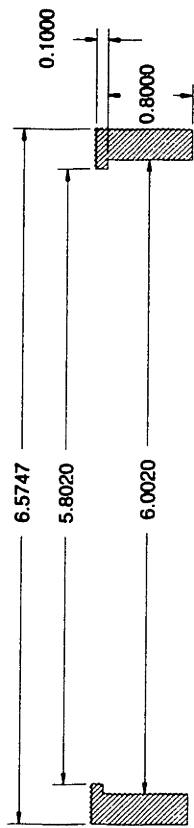
Figure A-2(e) Spacer 4.5"-6"



All Units in Inches
Material: Teflon

Virek Mohindra
66-217 MIT
Department of Chemical Engg
25 Ames St, Cambridge, MA 02139
617-253-8912 (o); 617-253-9895 (fax)

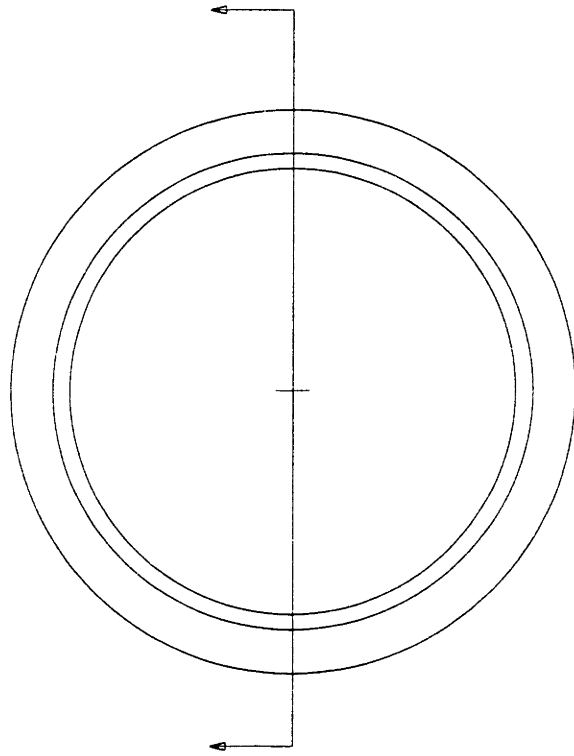
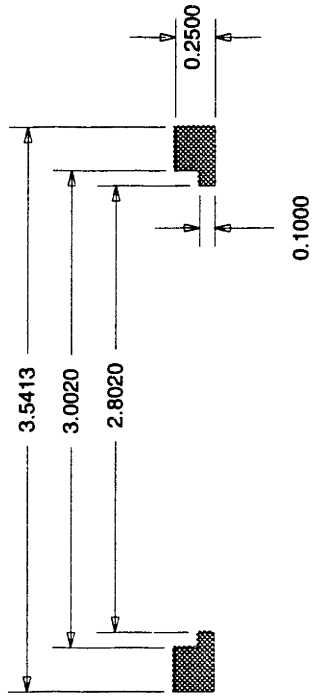
Figure A-2(f) Spacer 6"-6"



All Units in Inches
Material: Teflon

Vivek Mohindra
66-217 MIT
Department of Chemical Engg
25 Ames Str, Cambridge, MA 02139
617-253-8912 (o); 617-253-9695 (fax)

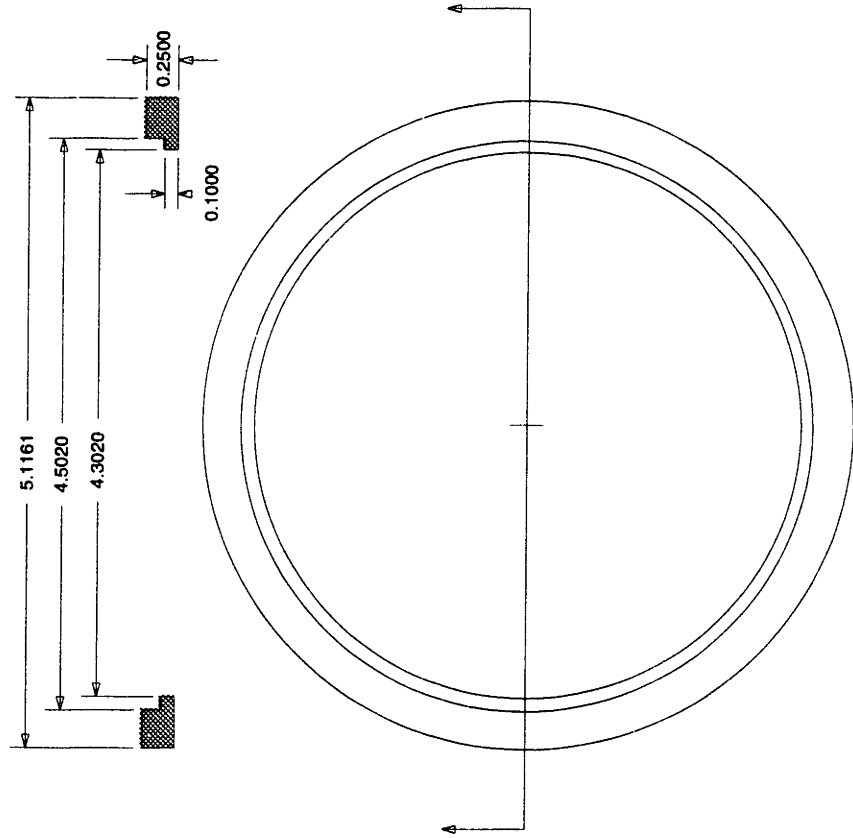
Figure A-3(a) Top Spacer 3"



All Units in Inches
Material: Teflon

Vivek Mohindra
66-217 MIT
Department of Chemical Engg
25 Ames Str, Cambridge, MA 02139
617-253-8912 (o); 617-253-9695 (fax)

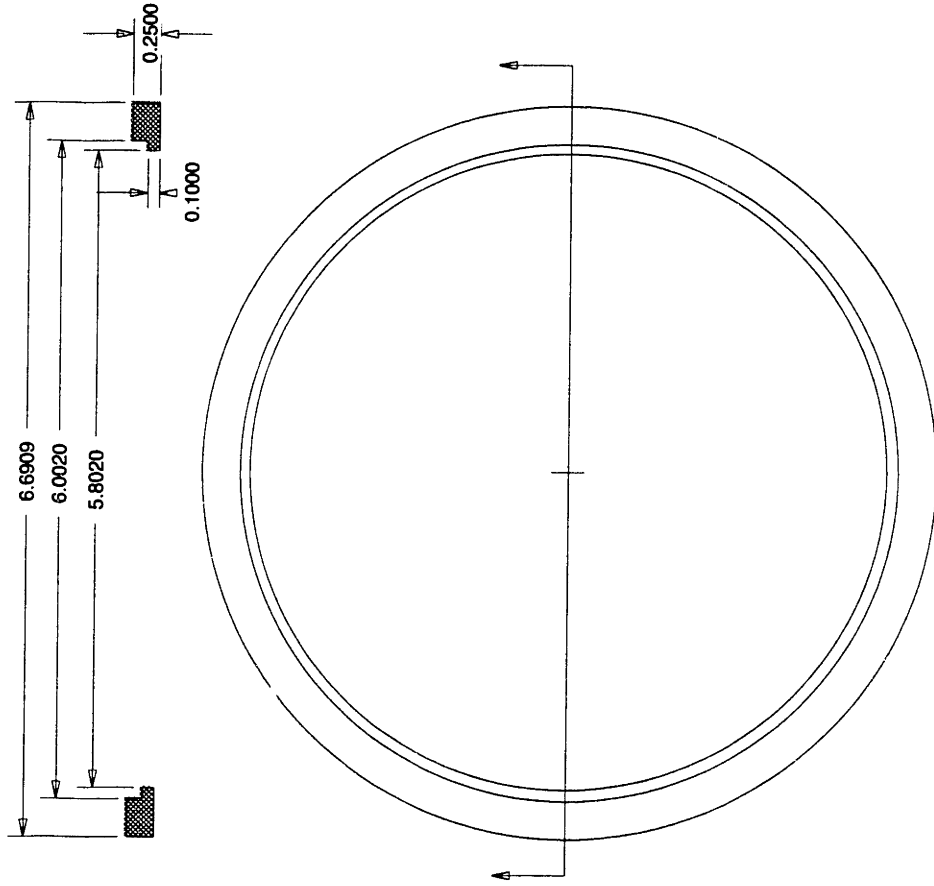
Figure A-3(b) Top Spacer 4"



All Units in Inches
Material: Teflon

Vivek Mohindra
66-217 MIT
Department of Chemical Engg
25 Ames Str, Cambridge, MA 02139
617-253-8912 (o); 617-253-9695 (fax)

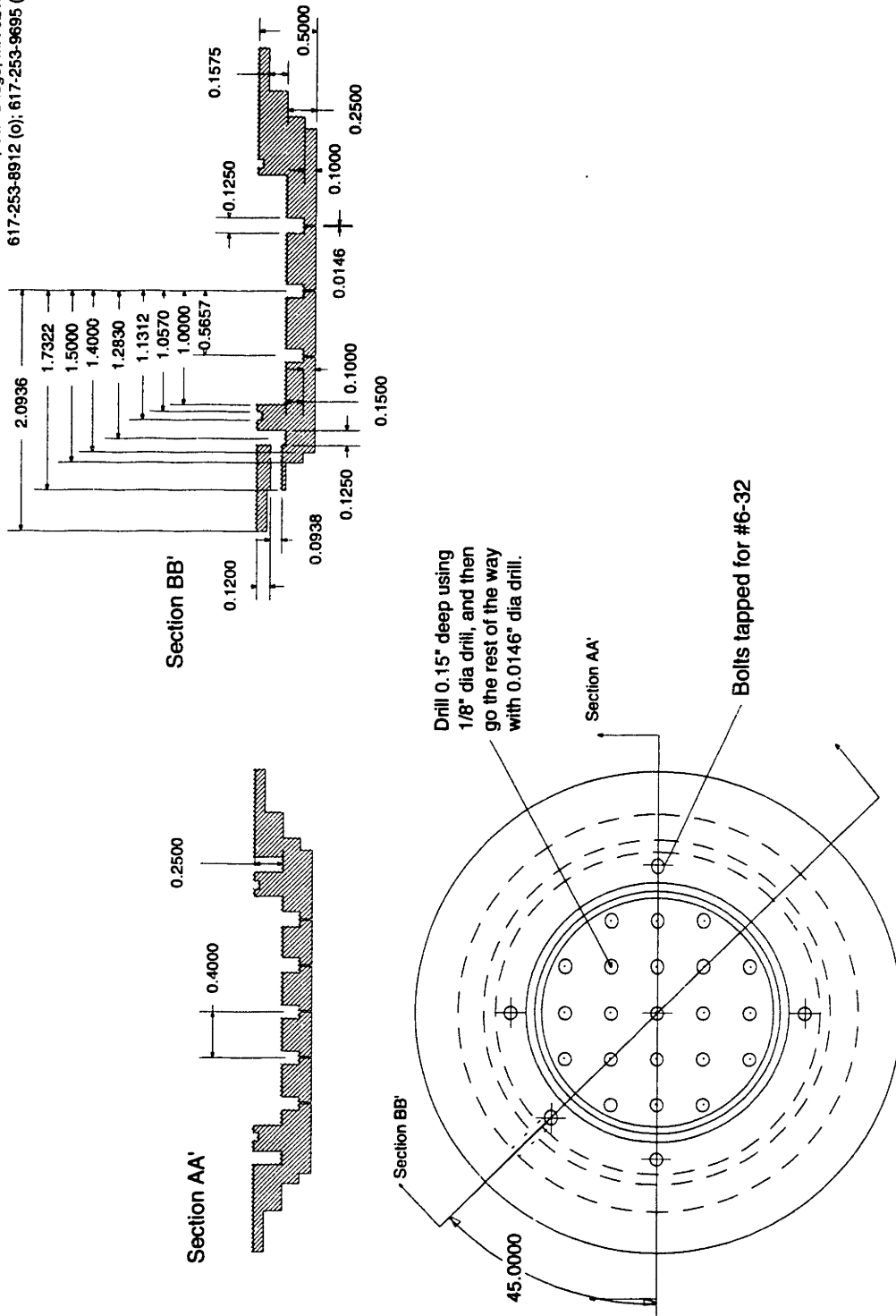
Figure A-3(c) Top Spacer 6"



All Units in Inches
 Material: Anodized Aluminum

Figure A-4(a): Anode 3"

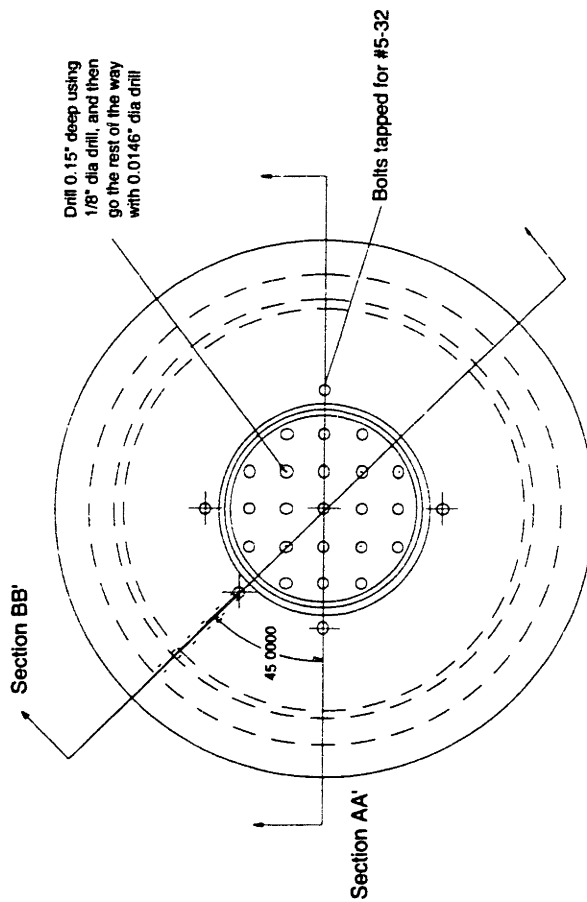
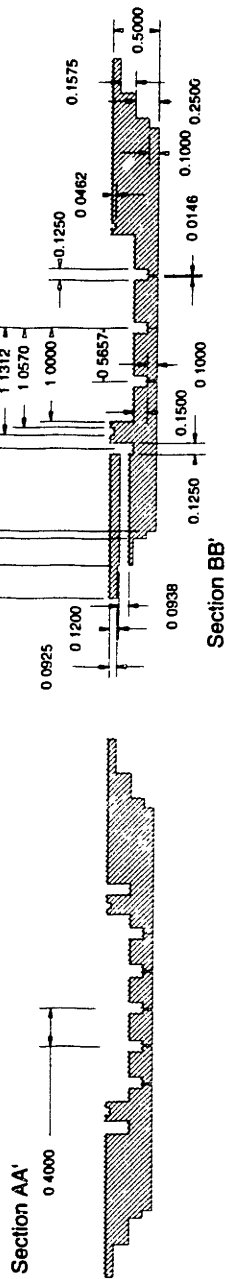
Vivek Mohindra
 66-217 MIT
 Department of Chemical Engg
 25 Ames Str, Cambridge, MA 02139
 617-253-8912 (O); 617-253-9695 (fax)



All Units in inches
 Material: Anodized Aluminum

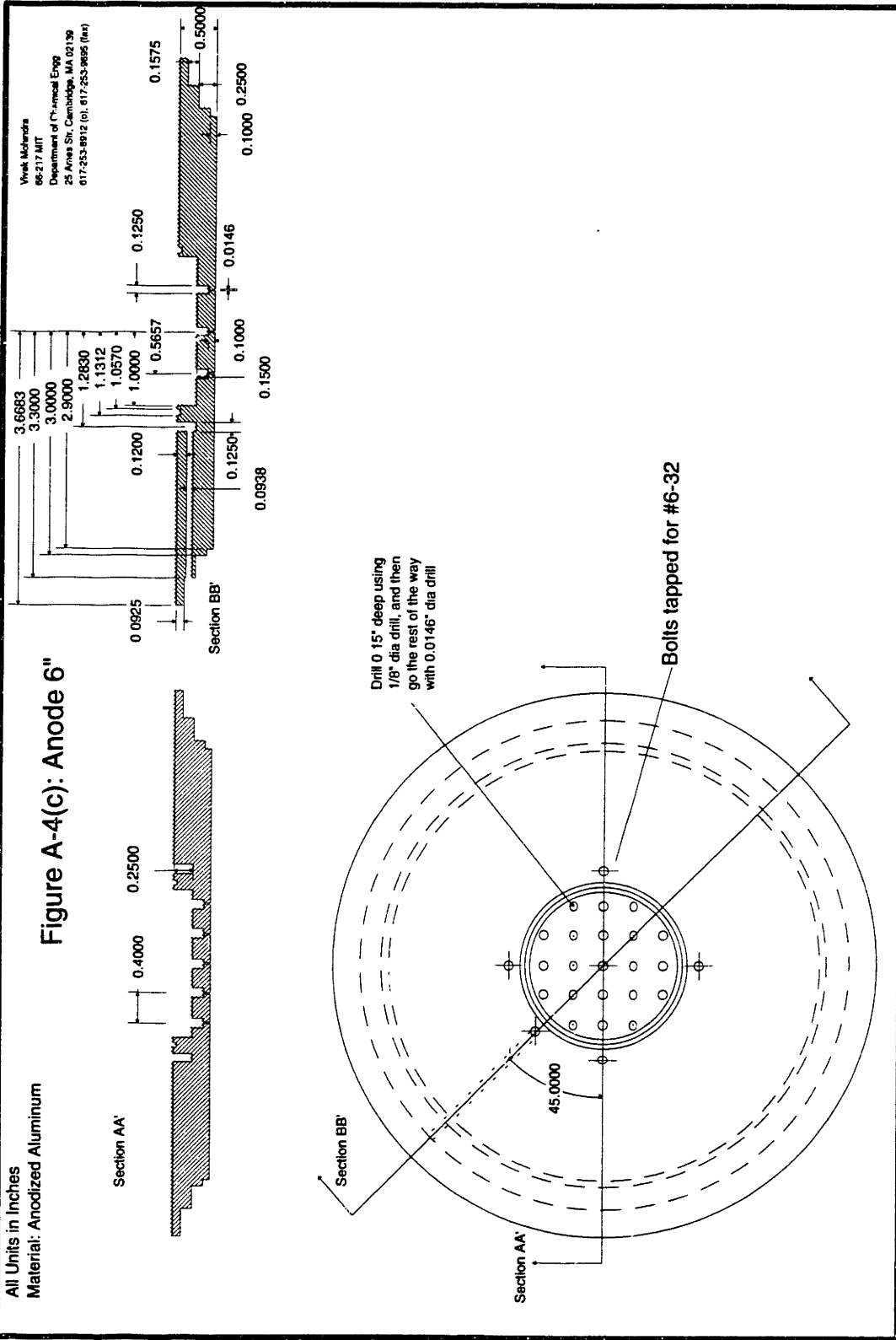
Figure A-4(b): Anode 4.5"

Vivek Mohindra
 66-217 MIT
 Department of Chemical Engg
 25 Ames St., Cambridge, MA 02139
 617-253-8912 (o), 617-253-8695 (fax)



All Units in Inches
 Material: Anodized Aluminum

Figure A-4(c): Anode 6"

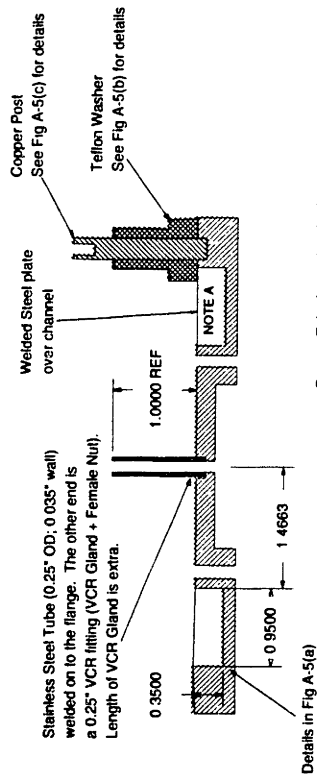


All Units in Inches

Material: Stainless Steel except where noted

Vincent Michonza
68-217 MIT
Department of Chemical Engg
25 Ames St., Cambridge, MA 02139
617-253-8912 (o), 617-253-9696 (fax)

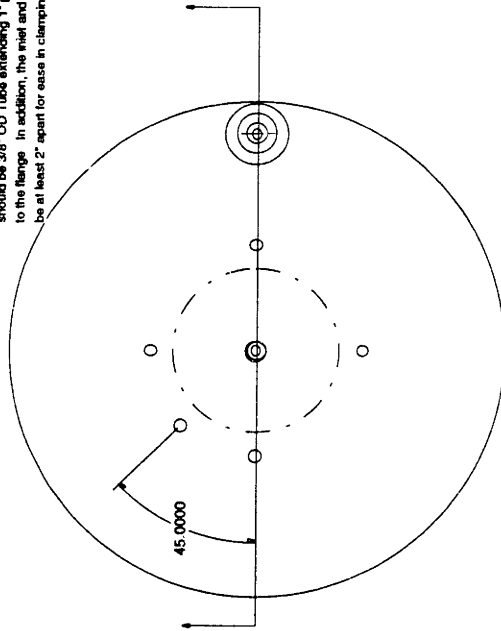
Figure A-5 Common Flange - Gas + Electric Feeds Overall Assembly



Copper Tube brazed to the flange

NOTE A

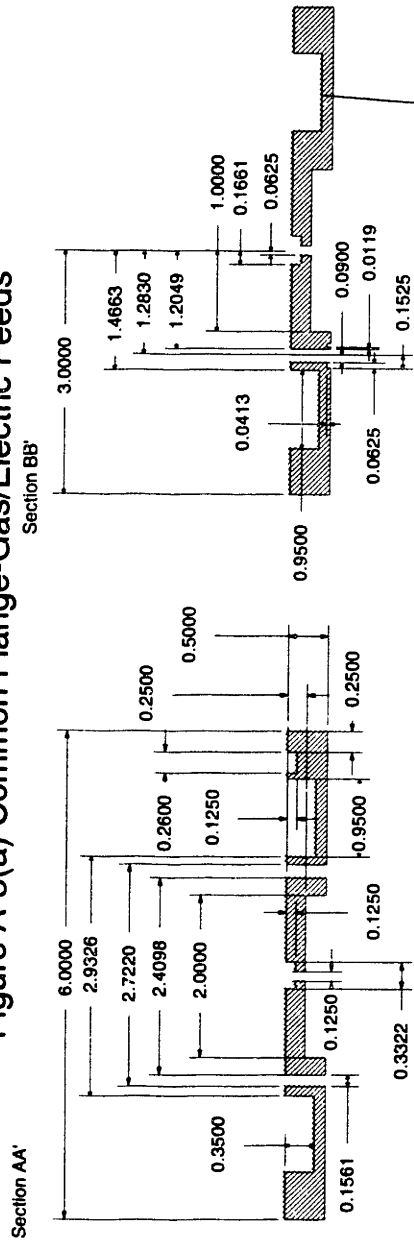
Space for internal groove with baffle for heat exchange. Maximize this space, and place inlet and outlet 180 degrees from the Copper post. The inlet and outlet should be 3/8" OD Tube extending 1" perpendicular to the flange. In addition, the inlet and outlet should be at least 2" apart for ease in clamping and unclamping.



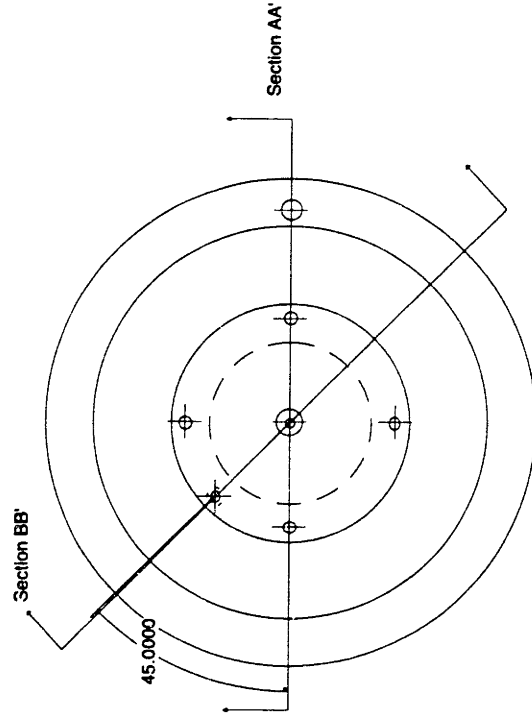
All Units in Inches
Material: Stainless Steel

Vincent Michels
66-217 MIT
Department of Chemical Engg
25 Amos St. Cambridge, MA 02139
617-253-9912 (6), 617-253-9992 (fax)

Figure A-5(a) Common Flange-Gas/Electric Feeds



Space for the internal channel.
The channel will be baffled to provide inlet and the outlet at the same end. Refer to Fig A-5 for further details.



All Units in Inches
Material: As specified

Vivek Mohindra
66-217 MIT
Department of Chemical Enrgs
25 Ames Str, Cambridge, MA 02139
617-253-8912 (o); 617-253-9695 (fax)

Figure A-5(b): Teflon Washer

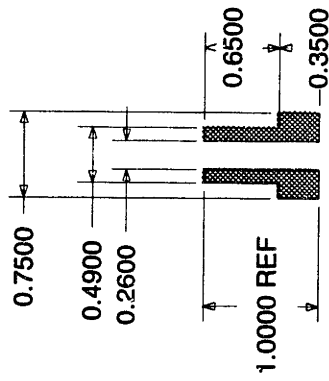
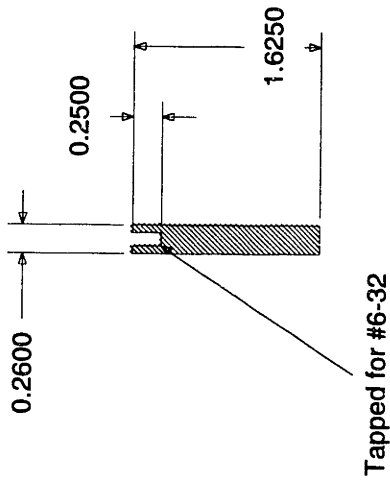


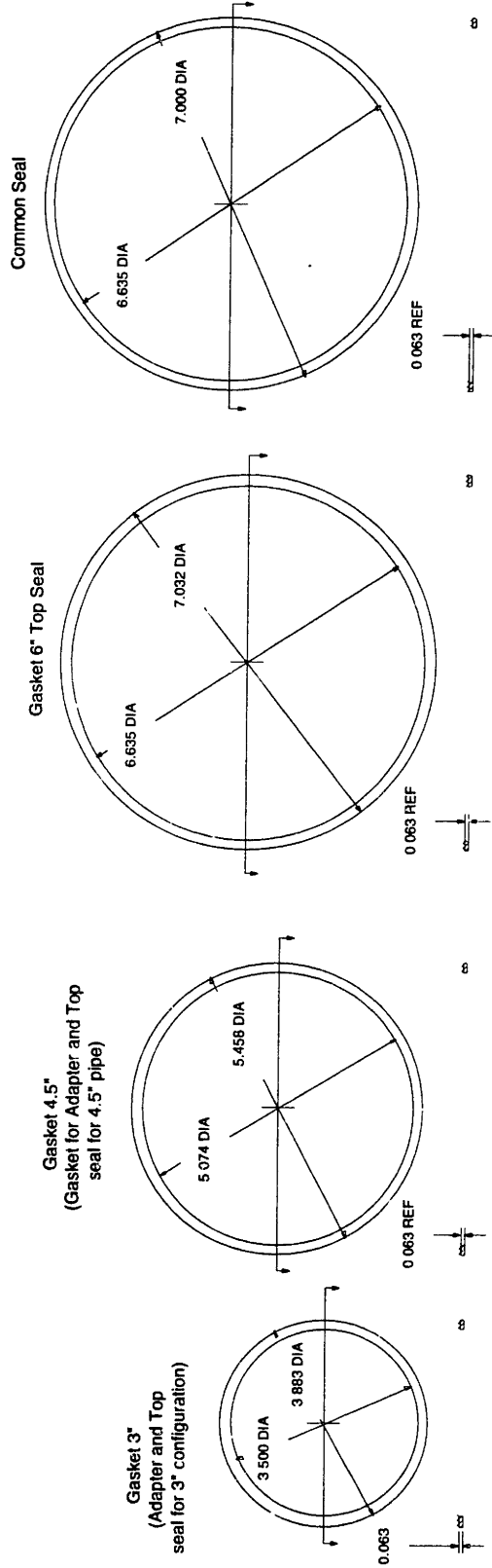
Figure A-5(c) Copper post



ALL Units in Inches
Material: Viton

Vivek Mohindra
66-217 MIT
25 Ames Str
Cambridge, MA 02139
617-253-8912 (ph); 617-253-9695 (fax)

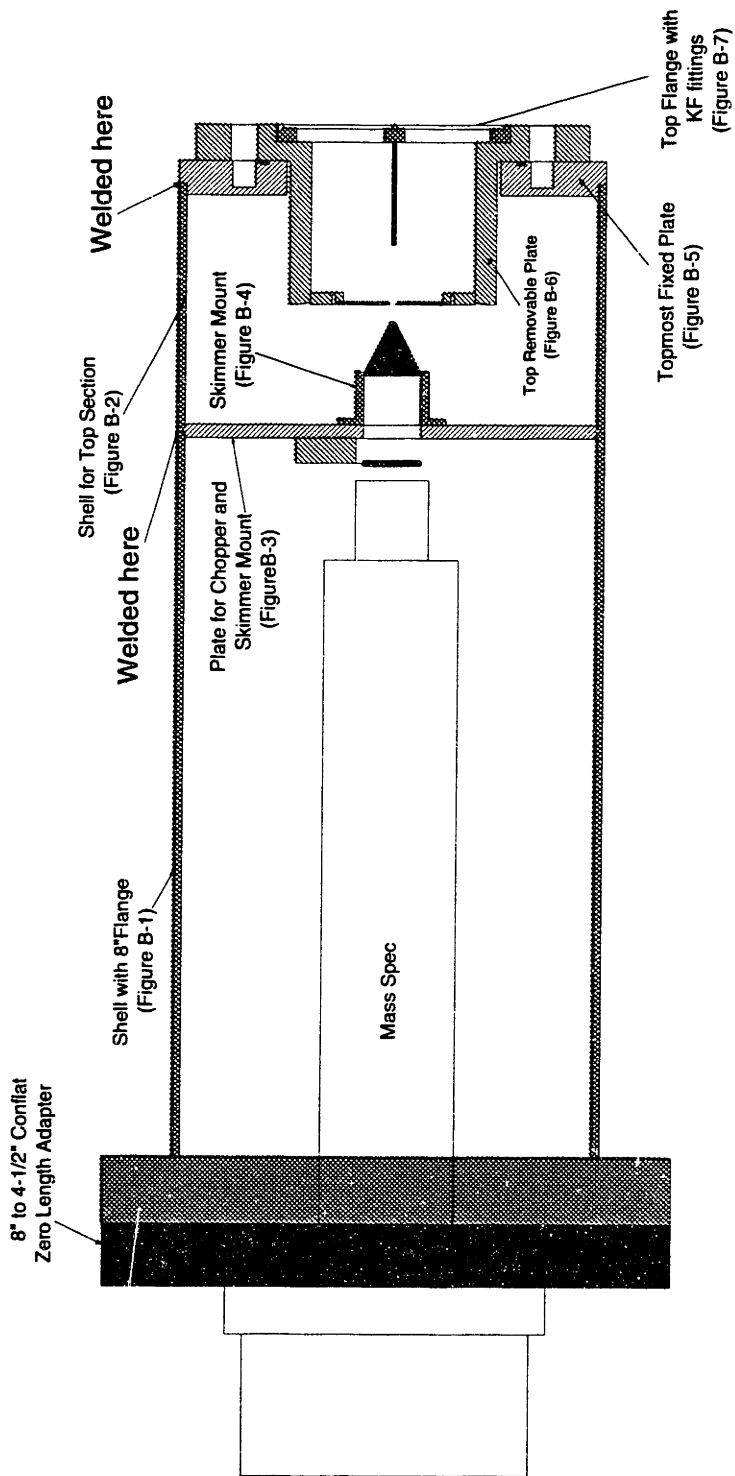
Figure A-6: Gaskets



Appendix B: Drawings for the UTI 100C Mass Spectrometer Assembly

Vivek Mohindra, 66-217 MIT
 Bldg 20 Receiving, 18 Vassar Str
 Cambridge, MA 02139
 617-253-8912 (o); 617-253-9695 (fax)

Figure B-0: Basic Layout of Mass Spec Assembly

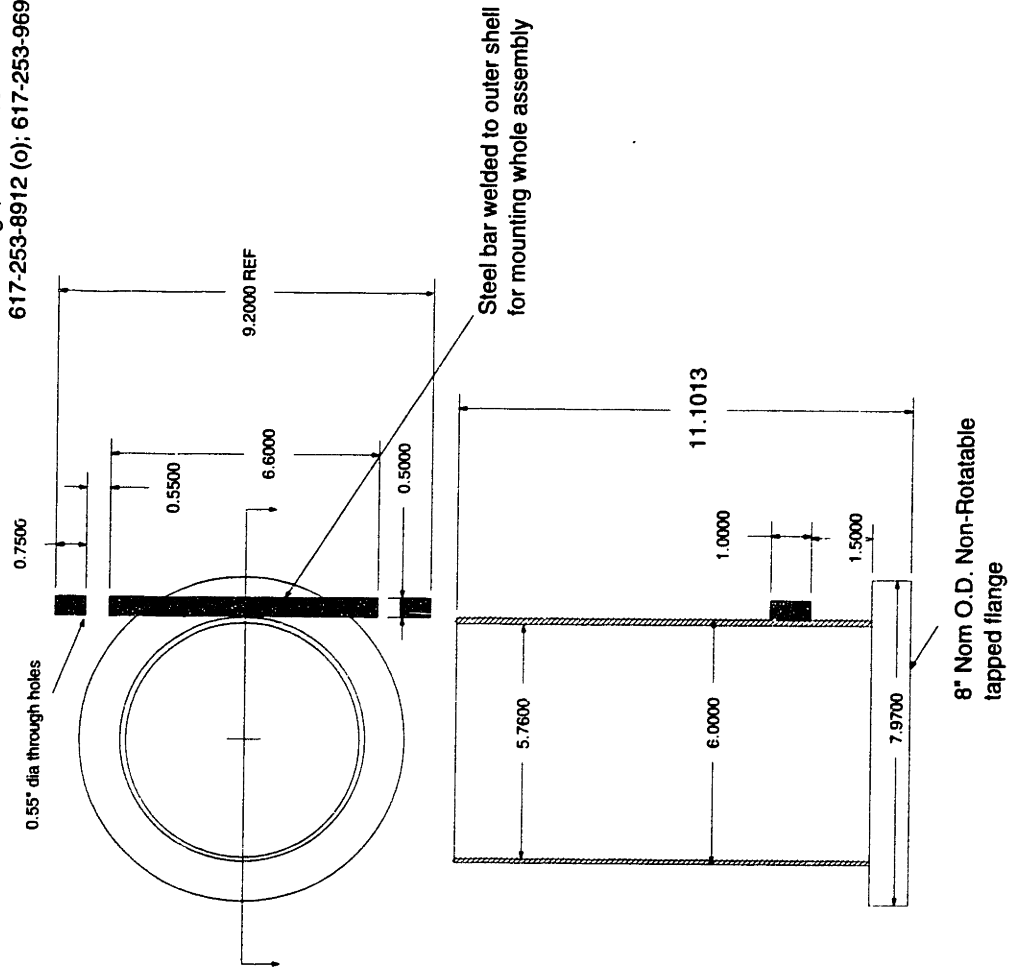


Note: External Flanges (Figure B-8) NOT shown on this drawing

All Dimensions in Inches
Material: Stainless Steel
(UHV Compatible)

Figure B-1: Shell With the 8" Flange

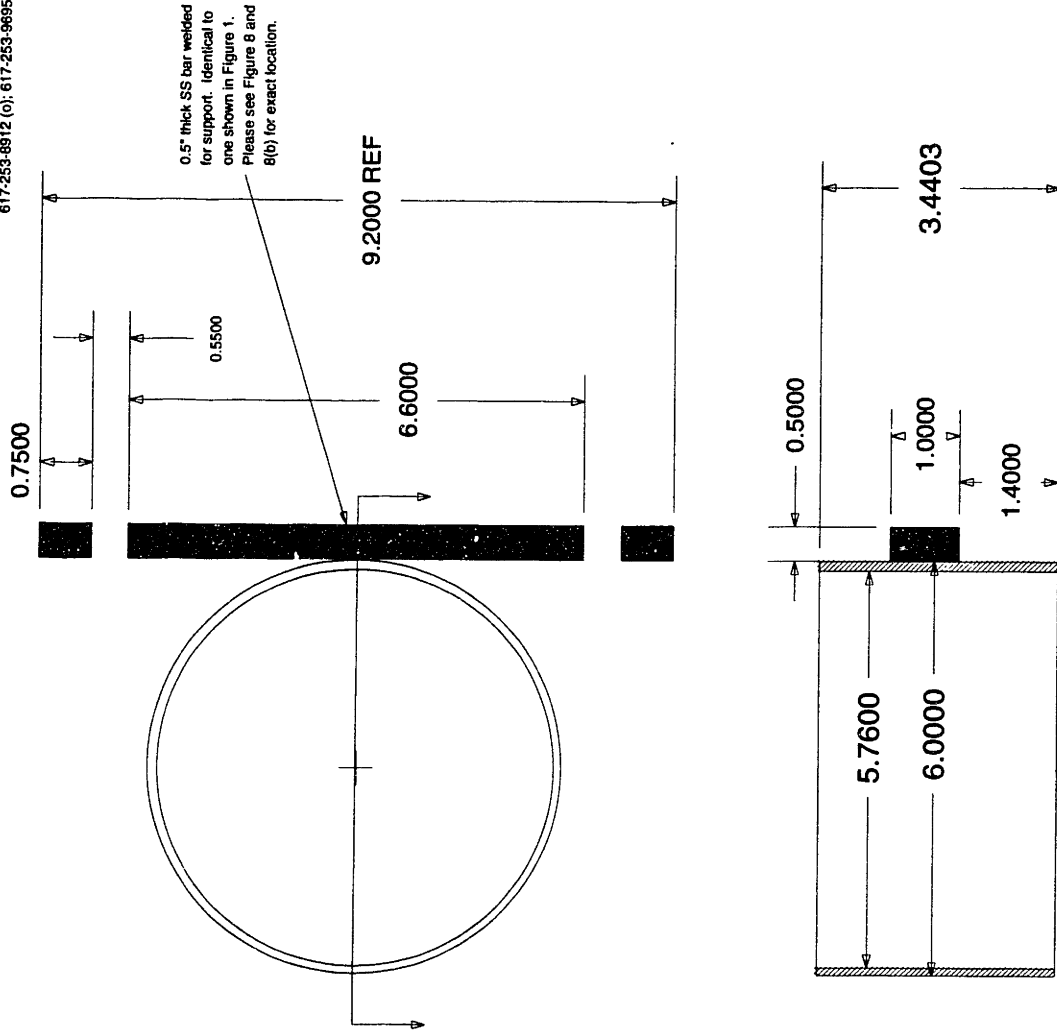
Vivek Mohindra 66-217 MIT
Bldg 20 Receiving, 18 Vassar Str
Cambridge, MA 02139
617-253-8912 (o); 617-253-9695 (fax)



All Dimensions in inches
Material: Stainless Steel
(UHV Compatible)

Figure B-2: Shell For the Top Section

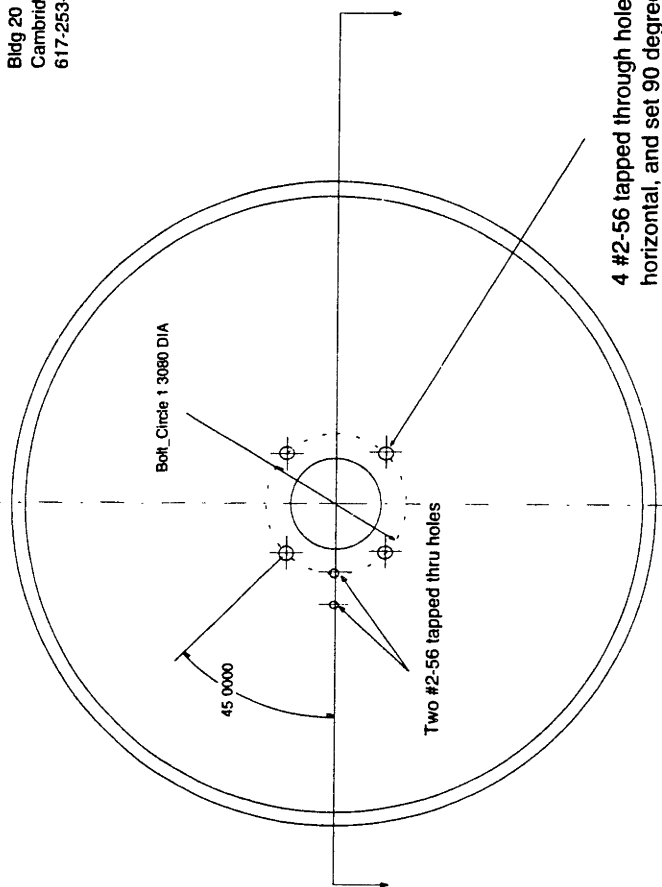
Vivek Mohindra 66-217 MIT
Bldg 20 Receiving, 18 Vassar St
Cambridge, MA 02139
617-253-8912 (o); 617-253-9695 (fax)



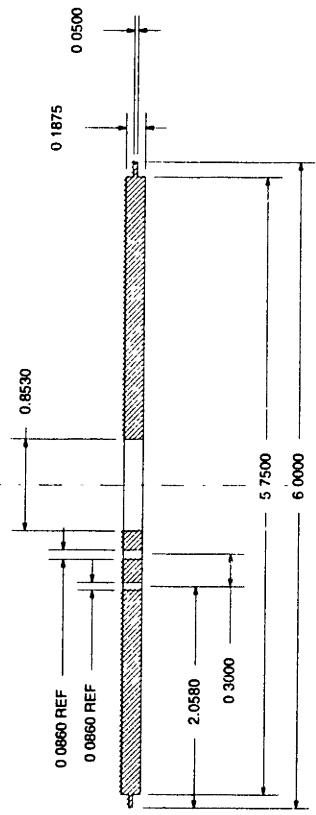
All Dimensions in Inches
Material: Stainless Steel
(UHV Compatible)

Figure B-3: Plate for Chopper and Skimmer Mount

Vivek Mohindra
66-217 MIT
Bldg 20, Receiving, 18 Vaassar Sir
Cambridge, MA 02139
617-253-8912 ; 617-253-9695 (fax)



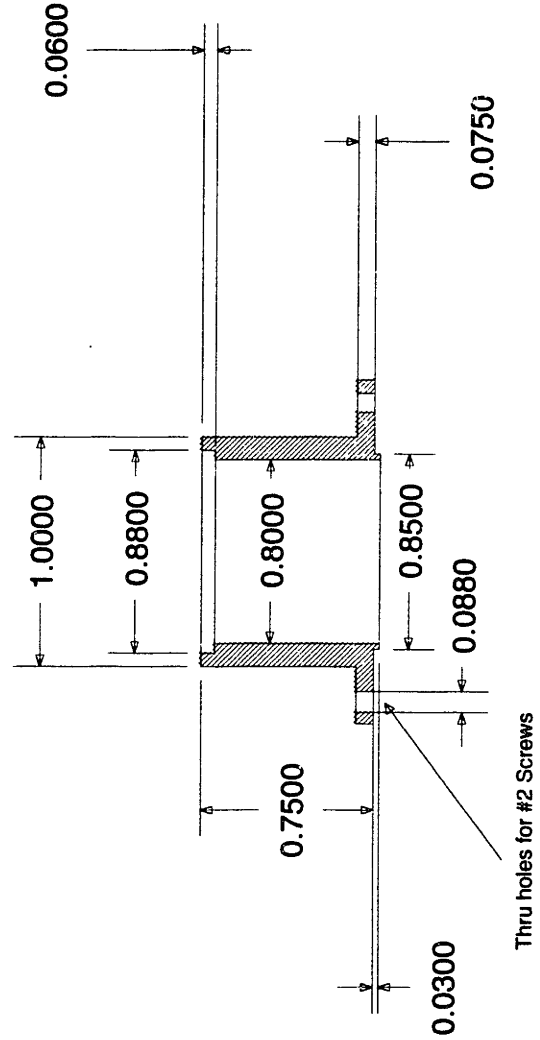
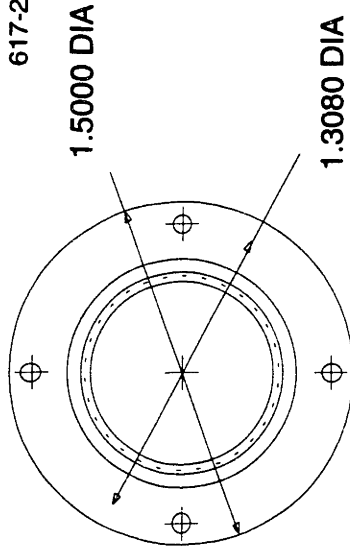
4 #2-56 tapped through holes, rotated 45 degrees from horizontal, and set 90 degrees from each other



All units at inches
Material: Stainless Steel
(UHV Compatible)

Figure B-4: Skimmer mount

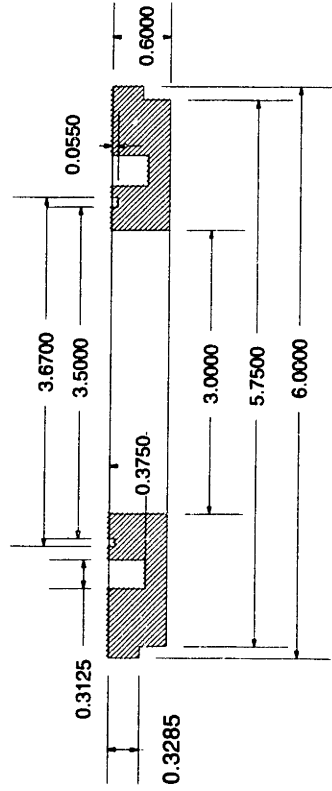
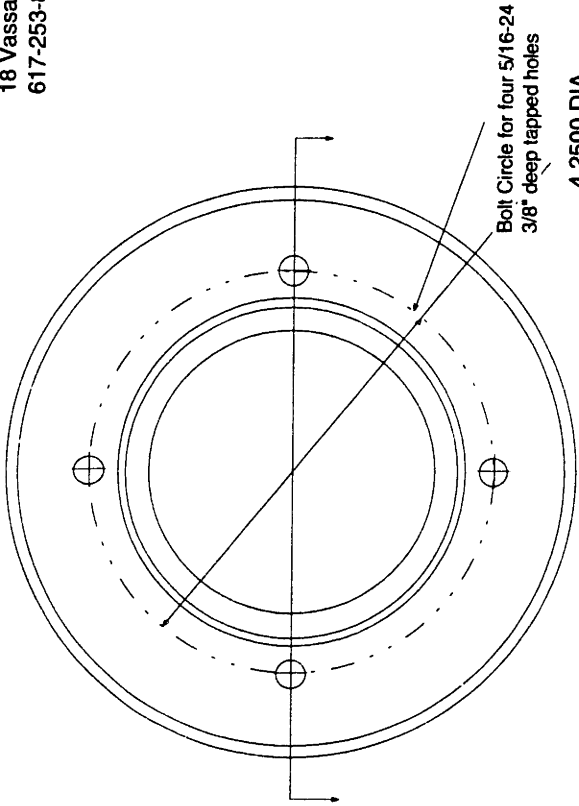
Vivek Mohindra 66-217, MIT
Bldg 20 Receiving, 18 Vassar Str
Cambridge, MA 02139
617-253-8912 (o); 617-253-9695 (fax)



All Dimensions in Inches
Material: Stainless Steel
(UHV Compatible)

Figure B-5: Topmost Fixed Plate

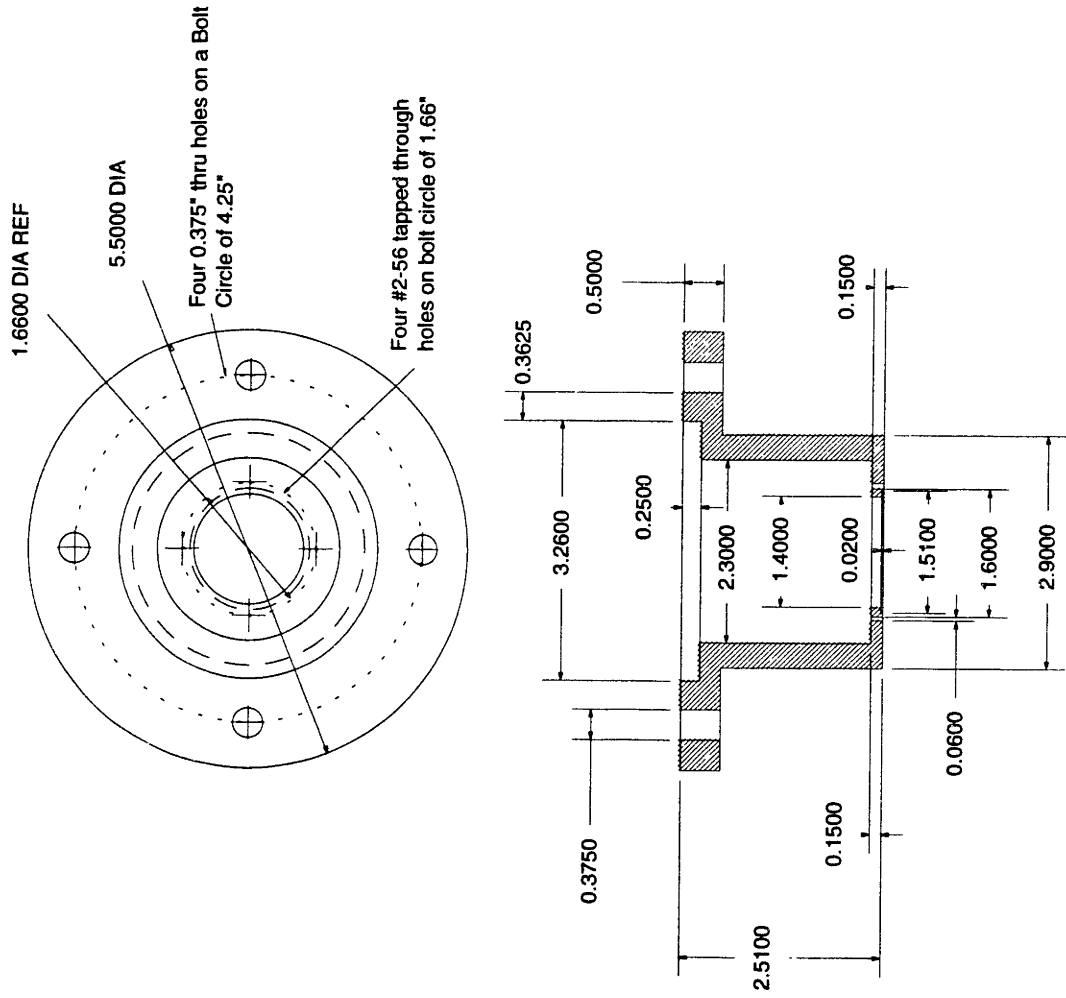
Vivek Mohindra, 66-217 MIT
Bldg 20 Receiving
18 Vassar Str, Camb. MA 02139
617-253-8912 (o); 617-253-9695 (fax)



All Dimensions in Inches
Material: Stainless Steel
(UHV Compatible)

Vivek Mohindra 66-217 MIT
Bldg 20 Receiving, 18 Vassar Str
Cambridge, MA 02139
617-253-8912 (o); 617-253-9695 (fax)

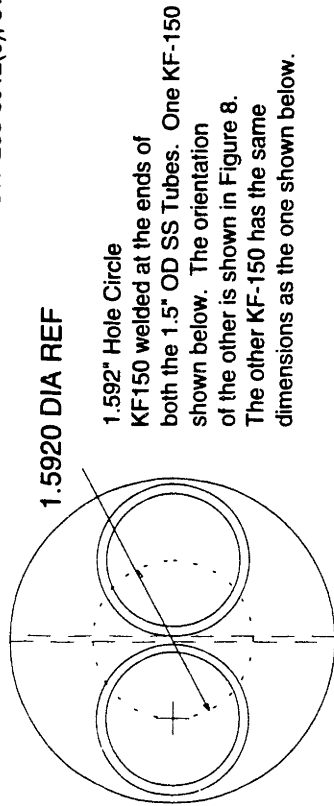
Figure B-6: Top Removable Plate



All Dimensions in Inches
 Material: Stainless Steel
 (UHV compatible)

Vivek Mohindra 66-217 MIT
 Bldg 18 Receiving, 18 Vassar Str
 Cambridge, MA 02139
 617-253-8912(o); 617-253-9696 (fax)

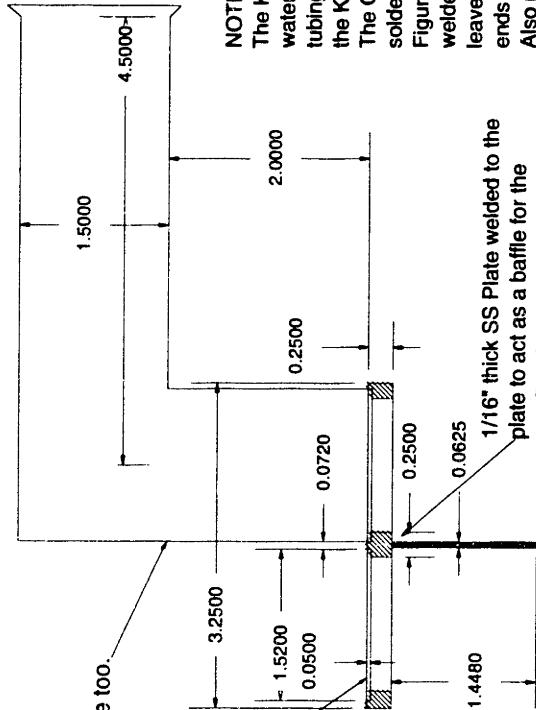
Figure B-7: Top Flange with KF Fittings



1.5920 DIA REF

1.592" Hole Circle

KF150 welded at the ends of both the 1.5" OD SS Tubes. One KF-150 shown below. The orientation of the other is shown in Figure 8. The other KF-150 has the same dimensions as the one shown below.



Similar KF fitting in this hole too.

NOTE:

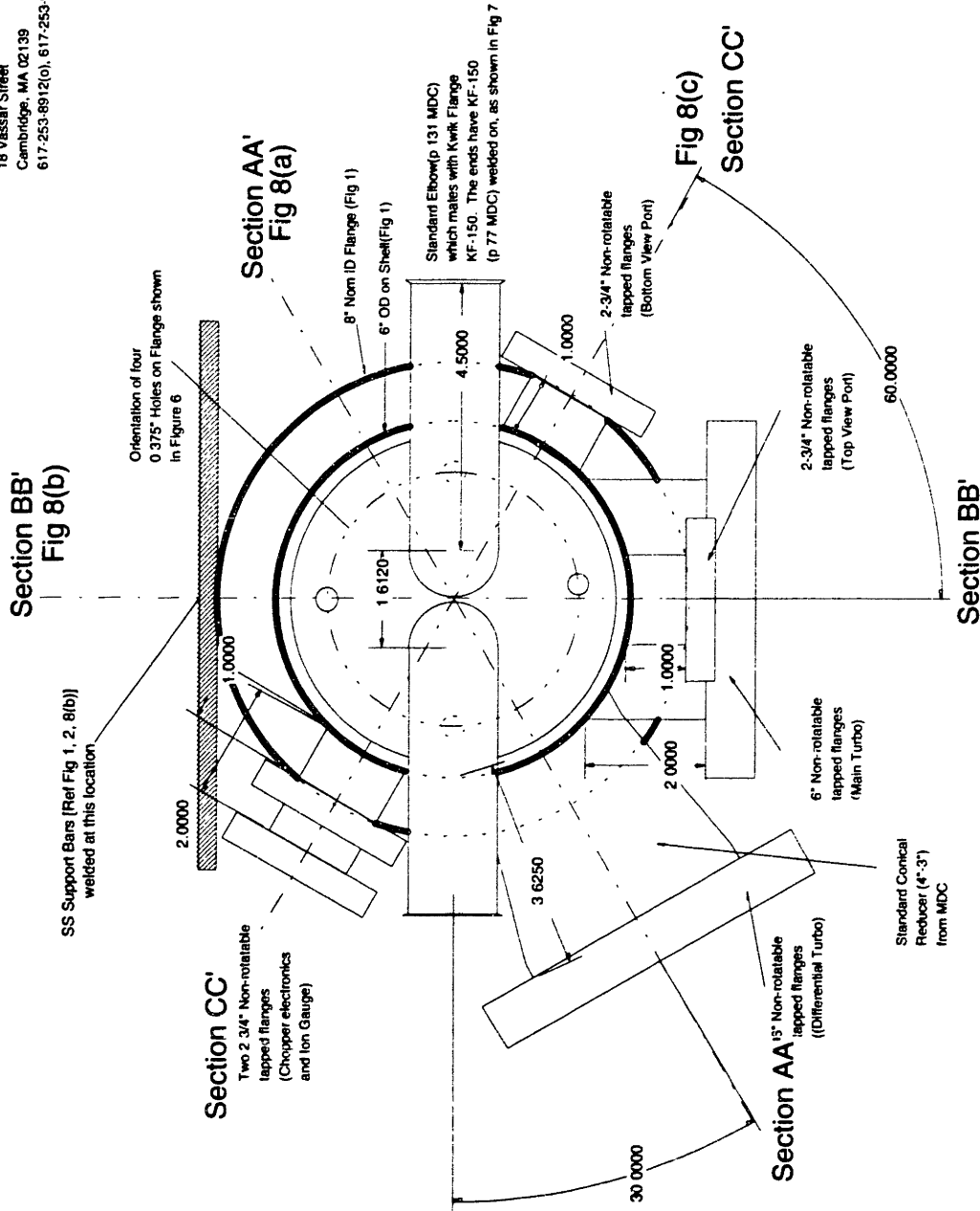
The Kwik Flanges need to be water cooled. 1/4" OD Copper tubing should be soldered onto the Kwik Flange pipe (outside). The Copper tube should also be soldered on top of the flange in Figure 6 (after this piece is welded onto that flange). Please leave 2" copper tube free at both ends for water hose connection. Also please leave 1" free near the open end of KF-150 fittings for ease of clamping.

1/16" thick SS Plate welded to the plate to act as a baffle for the gas flow from one KF fitting to the other.

All Dimensions in Inches
Material: Stainless Steel
(UHV application)

Figure B-8: Top View Showing Flange Location

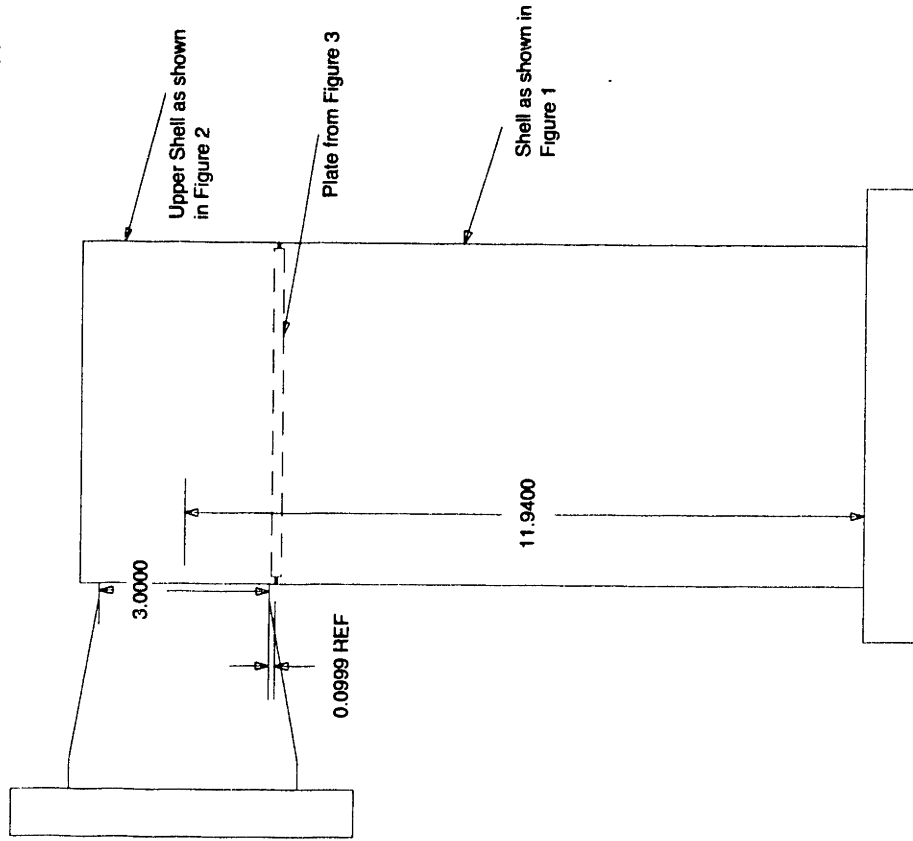
Vivek Mohindra 66-217 MIT
Bldg 20 Receiving
18 Vassar Street
Cambridge, MA 02139
617-253-8912(o), 617-253-9695 (fax)



All units in Inches
Material: Stainless Steel
(JHV Compatible)

Vivek Mohindra 66-217 MIT
Bldg 20 Receiving, 18 Vassar Str
Cambridge, MA 02139
617-253-8912 (o); 617-253-9695

Figure B-8(a): Section AA' : Flange Location

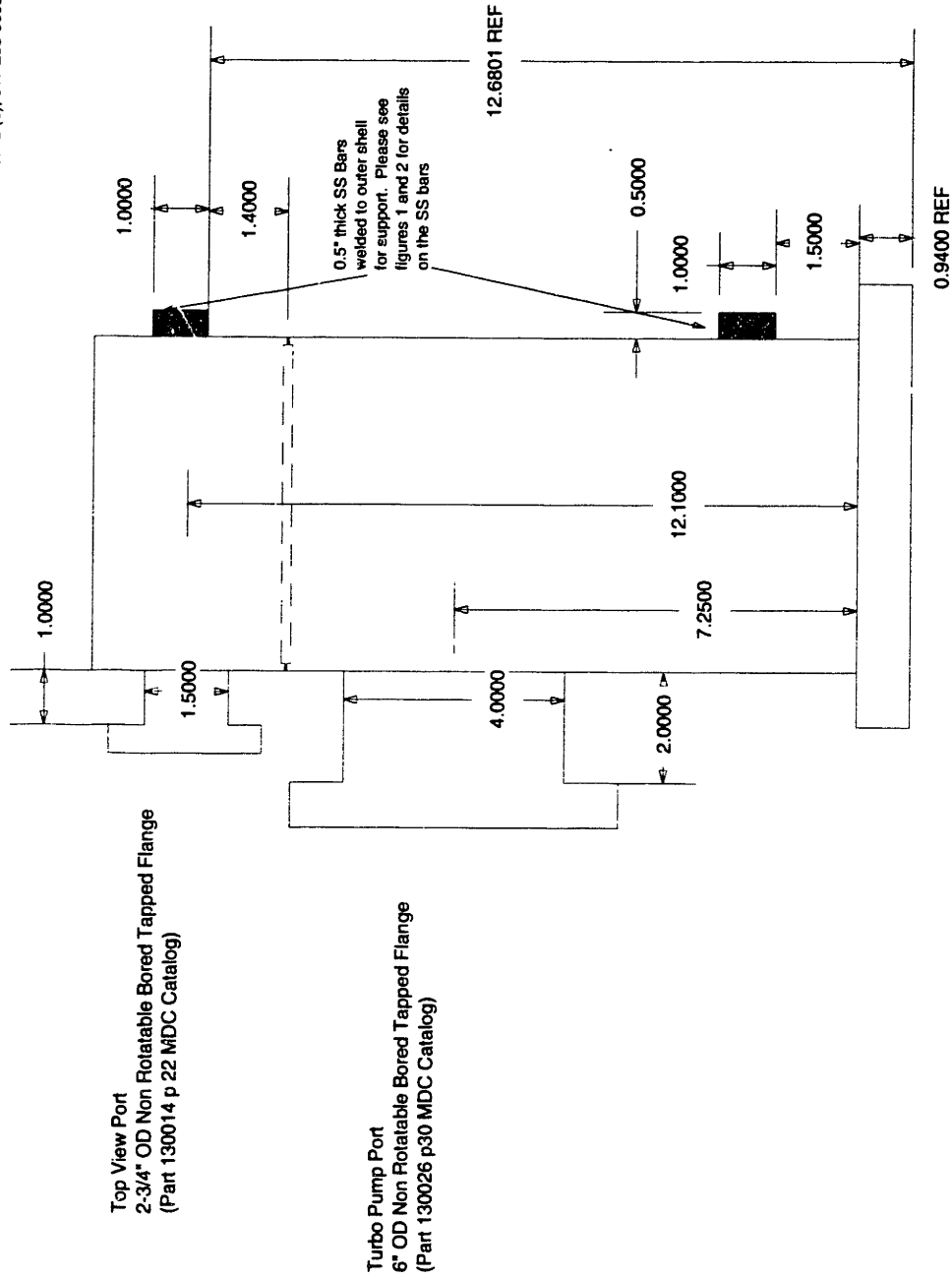


Turbo Pump Flange
Non-rotatable Bored Tapped 6" Flange
(Part 130026 p30 of MDC Catalog)
welded on to standard 4"-3" conical reducer
(Part 402512 p130 of MDC Catalog)

All units in Inches
Material: Stainless Steel
(UHV Compatible)

Vivek Mohindra 66-217 MIT
Bldg 20 Receiving, 18 Vassar St
Cambridge, MA 02139
617-253-8912 (o); 617-253-9695 (fax)

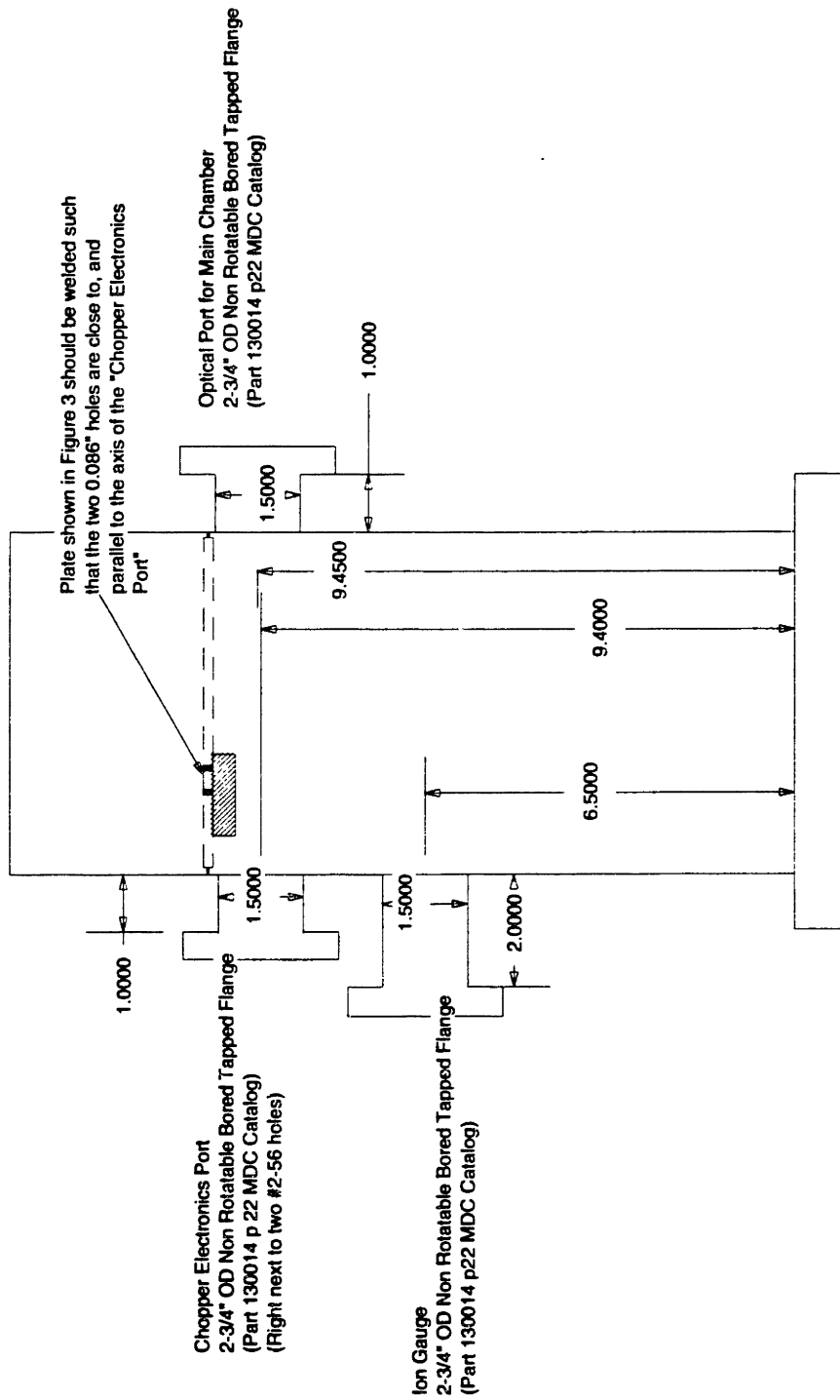
Figure B-8(b): Section BB' Flange Location



All units in inches
 Material: Stainless Steel
 (UHV Compatible)

Vivek Mohindra 66-217 MIT
 Bldg 20 Receiving, 18 Vassar Str
 Cambridge, MA 02139
 617-253-8912 (o); 617-253-9695 (fax)

Figure B-8(c): Section CC' Flange Location



Appendix C: Computer Code for Steady State Solution for $C_2F_6 + O_2$ Well-mixed Reactor Model

program SteadyState;

{Program for solving C2F6 + O2 system

- 1) $C_2F_6 + e^- \rightarrow CF_3 + CF_3 + e^-$
- 2) $CF_3 + CF_3 + M \rightarrow C_2F_6 + M$
- 3) $O_2 + e^- \rightarrow O + O + e^-$
- 4) $O + O + M \rightarrow O_2 + M$
- 5) $CF_3 + O \rightarrow COF_2 + F$
- 6) $COF_2 + e^- \rightarrow COF + F + e^-$
- 7) $COF + F \rightarrow COF_2$
- 8) $COF + O \rightarrow CO_2 + F$
- 9) $F + F + M \rightarrow F_2 + M$
- 10) $F_2 + e^- \rightarrow F + F + e^-$
- 11) $CO_2 + e^- \rightarrow CO + O + e^-$
- 12) $CO + F \rightarrow COF$
- 13) $CO + O + M \rightarrow CO_2 + M$

This program calculates the system of equations using a constant pressure condition. Any reaction may be turned "off" by setting the reaction rate, sticking coefficient, or electron temperature to zero.

The reaction set is solved using an iterative Newton-Raphson procedure. The convergence criteria is set as the sum of all the changes less than some epsilon. The program uses Gaussian elimination to solve the matrix equation: $J(\text{matrix}) \cdot \text{Del}(\text{vector}) = -R(\text{vector})$. The $J(\text{matrix})$ is the matrix of derivatives, the $-R(\text{vector})$ is the negative of the vector of reaction equations, and the $\text{Del}(\text{vector})$ is the change vector given by $X(k+1) - X(k)$, new-old. An initial solution guess is given in the file "C2F6Int.Par".

Two output files are given. The file "C2F6Out.Par" is a legacy file, including number of iterations required for solution, the iteration vector values, and the final solution. The file "C2F6Soln.Par" contains only the steady state solution terms in order, F, CF3, C2F6, F2, O, O2, CO, CO2, COF, COF2 and (1/residence time) --based on the outlet flow.

written by Vivek on 9-1-95 using Linda's program for CF4 as a backbone)

uses Dos,CRT,Common,Matrix;

const

```

NumVar:integer=11;      {Number of Variables}
R=1.036e-19;           {Gas Constant: (Torr.cm3)/(#molecules.K)}
Path='F:\vivek\linda\programs\mune\'; {Pathname for Files}
RateCoeffName='C2F6Rate.Par'; {Filename for Steady State Rate Coefficients}
ParamName='C2F6Plas.Par';   {Filename for Plasma Parameters}
InitialName='C2F6Int.Par';   {Filename for Initial Guess Values}
ResultsName='C2F6Soln.Par';  {Filename for Result Values}
TestEpsilon=1e-5;          {Convergence Test for Soln}
EDo=6e10;                  {ED for Plumb and Ryan's rate constants}
NewtonRelax=1;             {New Guess = Old + NewtonRelax*Deviation}
OutName='C2F6Out.Par';     {Output File for Checking Soln}
IterationName='C2F6IT.out'; {Iteration history for Newton Raphson}

```

type

```

Vector=TNVector;        {ArraySize for Variable Vector and
                          Matrix Dimension}
VMMatrix=TNMatrix;      {Matrix for Equation Solving}
KineticRec=Record
  k1,k2,ki2,Fc2,k2,k3,k4,k5,k6,kz7,ki7,Fc7,k7,k8,k9,k10,k11,
  kz12,ki12,Fc12,k12,k13:double;

```

```

                                { Kinetic Coefficients }
end;
PlasmaRec=Record
  Tau,ED,P,T,C2F6,O2o:double;
                                { Plasma Parameters: Residence Time (inlet
                                flowrate based on unreacted gas flow),
                                Electron Density, Pressure, Temperature
                                Initial Concentration of C2F6 (based on
                                constant pressure),
                                Initial conc of O2 (based on
                                constant pressure)}

end;

var
  Deriv:VMatrix;                { Partial Derivative Matrix }
  Eqn,Del,Old,New:Vector;       { Equation Vector, Difference Vector,
                                Old Guess Vector, New Guess Vector }
  i,j:integer;                  { Counter }
  KineticCoeff:KineticRec;      { Kinetic Coefficients }
  PlasmaParam:PlasmaRec;        { Plasma Parameters }
  SolnFound:Boolean;           { Test for Soln Found }
  GEEror:byte;                  { Error Flag for Gaussian Elimination }
  Output,IterationFile:Text;    { Printer File }

Procedure Initialize(var Old:Vector; var KineticCoeff:KineticRec;
  var PlasmaParam:PlasmaRec);

{ This procedure reads in parameters for the reaction system: Kinetic
Rate Coefficients, Plasma Parameters, Initial Guesses. }

var
  InitialFile,RateCoeffFile,ParamFile:Text; { File of Initial Guess Values,
                                              File of Rate Coefficients,
                                              File of Plasma Parameters }

begin

  { Get Initial Guess Values }

  Assign(InitialFile,Path+InitialName);
  Reset(InitialFile);
  i:=0;
  FillChar(Old,Sizeof(Old),0);
  While Not EOF(InitialFile) do begin
    i:=succ(i);
    readln(InitialFile,Old[i]);
  end;
  Close(InitialFile);

  { Get Kinetic Rate Coefficients }

  Assign(RateCoeffFile,Path+RateCoeffName);
  Reset(RateCoeffFile);
  FillChar(KineticCoeff,Sizeof(KineticCoeff),0);
  With KineticCoeff do begin
    { k1,k2,ki2,Fc2,k3,k4,k5,k6,kz7,ki7,Fc7,k8,k9,k10,k11,kz12,ki12,Fc12 }
    While Not EOF(RateCoeffFile) do begin
      Readln(RateCoeffFile,k1);
      Readln(RateCoeffFile,kz2);
      Readln(RateCoeffFile,ki2);
      Readln(RateCoeffFile,Fc2);
      Readln(RateCoeffFile,k3);
      Readln(RateCoeffFile,k4);
      Readln(RateCoeffFile,k5);
      Readln(RateCoeffFile,k6);
    end;
  end;

```

```

        Readln(RateCoeffFile,kz7);
        Readln(RateCoeffFile,ki7);
        Readln(RateCoeffFile,Fc7);
        Readln(RateCoeffFile,k8);
        Readln(RateCoeffFile,k9); {Multiply by [M] which is #/cc}
        Readln(RateCoeffFile,k10);
        Readln(RateCoeffFile,k11);
        Readln(RateCoeffFile,kz12);
        Readln(RateCoeffFile,ki12);
        Readln(RateCoeffFile,Fc12);
        Readln(RateCoeffFile,k13);
    end;
end;
Close(RateCoeffFile);

{Get Plasma Parameters}

Assign(ParamFile,Path+ParamName);
Reset(ParamFile);
FillChar(PlasmaParam,Sizeof(PlasmaParam),0);
With PlasmaParam do begin
    While Not EOF(ParamFile) do begin
        Readln(ParamFile,Tau);
        Readln(ParamFile,ED);
        Readln(ParamFile,P);
        Readln(ParamFile,T);
        Readln(ParamFile,C2F6o);
        Readln(ParamFile,O2o);
    end;
end;
Close(ParamFile);
end;

Procedure CalcFallOffRates(var KineticCoeff:KineticRec; PlasmaParam:PlasmaRec);

Var
    M,F:real; {number density,
               strong collision correction to 'Lindeman' trmt}

Begin
    With PlasmaParam do
        M:=P/(R*T);
    With KineticCoeff, PlasmaParam do begin
        if k1<>0 then k1:=k1*(ED/EDo);
        if kz2<>0 then begin
            F:=Exp((1/(1+ln(sqrt(kz2*M/ki2))/2.3026))*ln(Fc2));
            k2:=(kz2*M)/(1+(kz2*M)/ki2)*F;
        end else k2:=0;
        if k3<>0 then k3:=k3*(ED/EDo);
        if k4<>0 then k4:=k4*M;
        if k6<>0 then k6:=k6*(ED/EDo);
        if kz7<>0 then begin
            F:=Exp((1/(1+ln(sqrt(kz7*M/ki7))/2.3026))*ln(Fc7));
            k7:=(kz7*M)/(1+(kz7*M)/ki7)*F;
        end else k7:=0;
        if k9<>0 then k9:=k9*M;
        if k10<>0 then k10:=k10*(ED/EDo);
        if k11<>0 then k11:=k11*(ED/EDo);
        if kz12<>0 then begin
            F:=Exp((1/(1+ln(sqrt(kz12*M/ki12))/2.3026))*ln(Fc12));
            k12:=(kz12*M)/(1+(kz12*M)/ki12)*F;
        end else k12:=0;
        if k13<>0 then k13:=k13*PlasmaParam.P/760; {760 torrs in 1 atm}

    end;
End;

```

```

Procedure SetDerivMat(var Deriv:VMatrix; Old:Vector;
    KineticCoeff:KineticRec; PlasmaParam:PlasmaRec);

```

```

{This procedure sets the Derivative Matrix based on the last guess in the
Newton-Raphson iteration.}

```

```

var
M:real; {Total Gas Concentration:
          P/RT (#/cm3), thermal velocities of
          radicals (cm/s), Bohm ion loss}
i,j:integer; {Counter}

```

```
begin
```

```
{Initialize Derivative Matrix by setting all values to zero.}
```

```
FillChar(Deriv,Sizeof(Deriv),0);
```

```
{Calculate all non-zero matrix values using last guess}
```

```
With KineticCoeff,PlasmaParam do begin
```

```
M:=P/(R*T);
```

```
Deriv[1,1]:= -k1 - Old[11];
```

```
Deriv[1,3]:= 2*k2*Old[3];
```

```
Deriv [1,11]:= -Old[1];
```

```
Deriv[2,1]:= 2*k1;
```

```
Deriv[2,3]:= -4*k2*Old[3] - k5*Old[4] - Old [11];
```

```
Deriv[2,4]:= -k5*Old[3];
```

```
Denv[2,11]:= -Old[3];
```

```
Deriv[3,2]:= -k3 - Old[11];
```

```
Deriv[3,4]:= 2*k4*Old[4];
```

```
Denv[3,11]:= -Old[2];
```

```
Deriv[4,2]:= 2*k3;
```

```
Deriv[4,3]:= -k5*Old[4];
```

```
Deriv[4,4]:= -4*k4*Old[4] - k5*old[3] - k8*Old[6] - Old[11] - k13*Old[10];
```

```
Deriv[4,6]:= -k8*Old[4];
```

```
Deriv[4,9]:= k11;
```

```
Deriv[4,10]:= -k13*Old[4];
```

```
Deriv[4,11]:= -Old[4];
```

```
Deriv[5,3]:= k5*Old[4];
```

```
Deriv[5,4]:= k5*Old[3];
```

```
Deriv[5,5]:= -k6 - Old[11];
```

```
Deriv[5,6]:= k7*Old[7];
```

```
Deriv[5,7]:= k7*Old[6];
```

```
Deriv[5,11]:= -Old[5];
```

```
Deriv[6,3]:= k5*Old[4];
```

```
Denv[6,4]:= k5*Old[3] + k8*Old[6];
```

```
Deriv[6,5]:= k6;
```

```
Deriv[6,6]:= -k7*Old[7] + k8*Old[4];
```

```
Deriv[6,7]:= -k7*Old[6] - 4*k9*Old[7] - old[11] - k12*old[10];
```

```
Deriv[6,8]:= 2*k10;
```

```
Deriv[6,10]:= -k12*Old[7];
```

```
Deriv[6,11]:= -Old[7];
```

```
Deriv[7,4]:= -k8*old[6];
```

```
Denv[7,5]:= k6;
```

```
Deriv[7,6]:= -k7*old[7] - k8*Old[4] - Old[11];
```

```
Deriv[7,7]:= -k7*Old[6] + k12*Old[10];
```

```
Deriv[7,10]:= k12*Old[7];
```

```
Deriv[7,11]:= -Old[6];
```

```
Deriv[8,4]:= k8*Old[6] + k13*Old[10];
```

```
Deriv[8,6]:= k8*old[4];
```

```

Deriv[8,9]:=-k11 - Old[11];
Deriv[8,10]:=k13*Old[4];
Deriv[8,11]:=-Old[9];

```

```

Deriv[9,7]:= 2*k9*Old[7];
Deriv[9,8]:= -k10 - Old[11];
Deriv[9,11]:=-Old[8];

```

```

Deriv[10,4]:=-k13*Old[10];
Deriv[10,7]:= -k12 *Old[10];
Deriv[10,9]:= k11;
Deriv[10,10]:= -k12*Old[7] - Old[11] - k13*Old[4];
Deriv[10,11]:= -Old[10];

```

```

Deriv[11,1]:=1;
Deriv[11,2]:=1;
Deriv[11,3]:=1;
Deriv[11,4]:=1;
Deriv[11,5]:=1;
Deriv[11,6]:=1;
Deriv[11,7]:=1;
Deriv[11,8]=1;
Deriv[11,9]:=1;
Deriv[11,10]:=1;
Deriv[11,11]:=0;

```

```

end;
end,

```

```

Procedure SetEqnVector(var Eqn:Vector; Old:Vector;
KineticCoeff:KineticRec; PlasmaParam:PlasmaRec);

```

{ This procedure sets the -R(vector), the negative of the reaction equation system using the last guess of the Newton-Raphson iteration. }

```

var
M:real;           {Total Gas Concentration: P/RT}
i:integer;       {Counter}

```

```

begin

```

```

{ Initialize Equation Vector by setting all values to zero.}

```

```

FillChar(Eqn,Sizeof(Eqn),0);
With KineticCoeff,PlasmaParam do begin

```

```

M:=P/(R*T);

```

```

Eqn[1] :=-(1/TAU)*C2F6o - k1*Old[1] + k2*sqr(Old[3])
- Old[11]*Old[1]);
Eqn[2]:= -(2*k1*Old[1] - 2*k2*sqr(Old[3]) - k5*Old[3]*Old[4]
-Old[11]*Old[3]);
Eqn[3]:=-((1/tau)*O2o - k3*Old[2]+k4*sqr(Old[4]) -Old[11]*Old[2]);
Eqn[4]:=-(2*k3*Old[2] - 2*k4*sqr(Old[4]) - k5*Old[3]*Old[4]
-k8*old[6]*Old[4] + k11*Old[9] - Old[11]*Old[4]
-k13*Old[10]*Old[4]);
Eqn[5]:=-(k5*Old[3]*Old[4] - k6*Old[5] + k7*Old[6]*Old[7]
-Old[11]*Old[5]);
Eqn[6]:=-(k5*Old[3]*Old[4] + k6*Old[5] - k7*Old[6]*Old[7]
+k8*Old[6]*Old[4] - 2*k9*sqr(Old[7]) + 2*k10*Old[8]
-Old[11]*Old[7] -k12*Old[10]*Old[7]);
Eqn[7]:=-(k6*Old[5] - k7*Old[6]*Old[7] - k8*Old[6]*Old[4]
-Old[11]*Old[6] + k12*Old[10]*Old[7]);
Eqn[8]:=-(k8*Old[6]*Old[4] - k11 * Old[9] - Old[11]*Old[9]
+k13*Old[10]*Old[4]);
Eqn[9]:=-(k9*sqr(Old[7]) - k10*Old[8] - Old[11]*Old[8]).

```

```

Eqn[10]:= - (k11*Old[9] - k12 *Old[10]*Old[7] - Old[11]*Old[10]
-k13*Old[10]*Old[4]);
Eqn[11]:=(-M + Old[1] + Old[2] + Old[3] + Old[4] + Old[5] + Old[6]
+Old[7] + Old[8] + Old[9] + Old[10] );
end;
end;
{*****}

```

```

Procedure CheckNewGuess(var New,Old:Vector; Del:Vector; var SolnFound:Boolean);

```

```

{This procedure checks to see if the sum of the differences for the difference
vector is less than the required convergence test given by epsilon. This
difference test is the difference between the last guess and the new guess
given by Sqrt(Sum of Squares of differences) where a difference is given
by X(k+1)-X(k). If convergence has occurred results are written to the
appropriate output files.}

```

```

var
  DelSqrSum:double;      {Square Sum of Differences in Old & New}
  ResultsFile:Text;     {Text of Results}

```

```

begin

```

```

  {Calculate the Squareroot of the Sum of the Square of the Differences}

```

```

  DelSqrSum:=0,

```

```

  for i:=1 to NumVar do
    writeln(i, ' ',Del[i]);

```

```

    DelSqrSum:=DelSqrSum+Del[i]*Del[i],
    DelSqrSum:=Sqrt(DelSqrSum),
    writeln('Del Square Sum: ',DelSqrSum);

```

```

  {Check to see if this is less than the convergence epsilon}

```

```

  if DelSqrSum<TestEpsilon then begin
    SolnFound:=True;
    writeln('Solution Found -- DelSqrSum: ',DelSqrSum);
  end;

```

```

  {Calculate the New Guess for further iteration or for solution reporting}

```

```

  for i:=1 to NumVar do begin
    New[i]:=Old[i]+NewtonRelax*Del[i];
    Old[i]:=New[i];
  end;

```

```

  {Report solution to output files}

```

```

  if SolnFound then begin
    Assign(ResultsFile,Path+ResultsName);
    Rewrite(ResultsFile);
    writeln(Output,'Steady State Results: ');
    writeln(ResultsFile,New[1]);
    writeln(Output,'C2F6: ',New[1]);
    writeln(ResultsFile,New[2]);
    writeln(Output,' O2: ',New[2]);
    writeln(ResultsFile,New[3]);
    writeln(Output,' CF3: ',New[3]);
    writeln(ResultsFile,New[4]);
    writeln(Output,' O: ',New[4]);
    writeln(ResultsFile,New[5]);
    writeln(Output,'COF2: ',New[5]);
    writeln(ResultsFile,New[6]);
    writeln(Output,' COF: ',New[6]);
  end;

```

```

writeln(ResultsFile,New[7]);
writeln(Output,' F: ',New[7]);
writeln(ResultsFile,New[8]);
writeln(Output,' F2: ',New[8]);
writeln(ResultsFile,New[9]);
writeln(Output,' CO2: ',New[9]);
writeln(ResultsFile,New[10]);
writeln(Output,' CO: ',New[10]);
writeln(ResultsFile,New[11]);
writeln(Output,' TauOut: ',1/New[11]);
writeln(Output,' ');
writeln(Output,'Sum all: ',New[1]+New[2]+New[3]+New[4]+New[5]
+New[6]+New[7]+New[8]+New[9]+New[10]);
writeln(Output,'Carbon Balance: ',(1/PlasmaParam.Tau)*PlasmaParam.C2F6o*2,
' ', New[11]*(2*New[1] +1*(New[3]+New[5]+New[6]+New[9]
+New[10])););
writeln(Output,'Oxygen Balance: ', (1/PlasmaParam.Tau)*PlasmaParam.O2o*2,
' ', New[11]*(2*New[2] + 1*(New[4] + New[5] + New[6] + New[10] +
2*New[9])););
writeln(Output,'Fluorine Balance: ', (1/PlasmaParam.Tau)*PlasmaParam.C2F6o*6,
' ', New[11]*(6*New[1]+3*New[3] + 2*(New[5] + New[8] +New[6]+New[7])););
Close(ResultsFile);
end;
end;

```

BEGIN

{ Initialize iteration sequence }

```

SolnFound:=False;
j:=0;
Initialze(Old,KineticCoeff,PlasmaParam);
Assign(Output,Path+OutName);
Rewrite(Output);
CalcFallOffRates(KineticCoeff,PlasmaParam);
with KineticCoeff,PlasmaParam do begin
writeln(Output,'KineticCoeff: ');
writeln(Output,' k1: ',k1);
writeln(Output,' k2: ',k2,' kz2: ',kz2,' ki2: ',ki2,' Fc2: ',Fc2);
writeln(Output,' k3: ',k3);
writeln(Output,' k4: ',k4);
writeln(Output,' k5: ',k5);
writeln(Output,' k6: ',k6);
writeln(Output,' k7: ',k7,' kz7: ',kz7,' ki7: ',ki7,' Fc7: ',Fc7);
writeln(Output,' k8: ',k8);
writeln(Output,' k9: ',k9);
writeln(Output,' k10: ',k10);
writeln(Output,' k11: ',k11),
writeln(Output,' k12: ',k12,' kz12: ',kz12,' ki12: ',ki12,' Fc12: ',Fc12),
writeln(Output,' k13: ',k13);
writeln(Output);
writeln(Output,'Plasma Parameters: ');
writeln(Output,' Tau: ',Tau);
writeln(Output,' ED: ',ED);
writeln(Output,' P: ',P),
writeln(Output,' T: ',T);
writeln(Output,' C2F6o: ',C2F6o);
writeln(Output,' O2o: ',O2o),
writeln(Output,' ');
writeln(Output,'M:=',P/(R*T)),
writeln('KineticCoeff: ');
writeln(' k1: ',k1);
writeln(' k2: ',k2,' kz2: ',kz2,' ki2: ',ki2,' Fc2: ',Fc2);
writeln(' k3: ',k3);
writeln(' k4: ',k4);
writeln(' k5: ',k5);
writeln(' k6: ',k6);
writeln(' k7: ',k7,' kz7: ',kz7,' ki7: ',ki7,' Fc7: ',Fc7);

```

```

writeln(' k8: ',k8);
writeln(' k9: ',k9);
writeln(' k10: ',k10);
writeln(' k11: ',k11);
writeln(' k12: ',k12,' kz12: ',kz12,' ki12: ',ki12,' Fc12: ',Fc12);
writeln(' k13: ',k13);
writeln(Output);
writeln('Plasma Parameters: ');
writeln(' Tau: ',Tau);
writeln(' ED: ',ED);
writeln(' P: ',P);
writeln(' T: ',T);
writeln(' C2F6o: ',C2F6o);
writeln(' O2o: ',O2o);
writeln;

end;

{ Continue iterating starting from first guess until convergence test
has been reached }

While Not SolnFound do begin
  j:=succ(j);
  Writeln('Iteration: ',j);
  SetDerivMat(Deriv,Old,KineticCoeff,PlasmaParam);
  SetEqnVector(Eqn,Old,KineticCoeff,PlasmaParam);
  Gaussian_Elimination(NumVar,Deriv,Eqn,Del,GError);
  CheckNewGuess(New,Old,Del,SolnFound);
end;

{ Report number of iterations to solution to output file }

writeln(Output);
Writeln(Output,'Number of iterations to Soln: ',j);
Writeln('Number of iterations to Soln: ',j);
Close(Output);
END.

```


THESIS PROCESSING SLIP

FIXED FIELD ill _____ name _____

index _____ biblio _____

▶ COPIES Archives Aero Dewey Eng Hum
 Lindgren Music Rotch Science

TITLE VARIES ▶ _____

NAME VARIES ▶ _____

IMPRINT (COPYRIGHT) _____

▶ COLLATION 188 Q _____

▶ ADD DEGREE _____ ▶ DEPT _____

SUPERVISORS _____

NOTES

cat'r

date

▶ DEPT Chem. Eng

page
▶ F54

▶ YEAR 1996 ▶ DEGREE Ph.D.

▶ NAME MOHINDRA, Vivek